



저작자표시-비영리-변경금지 2.0 대한민국

이용자는 아래의 조건을 따르는 경우에 한하여 자유롭게

- 이 저작물을 복제, 배포, 전송, 전시, 공연 및 방송할 수 있습니다.

다음과 같은 조건을 따라야 합니다:



저작자표시. 귀하는 원저작자를 표시하여야 합니다.



비영리. 귀하는 이 저작물을 영리 목적으로 이용할 수 없습니다.



변경금지. 귀하는 이 저작물을 개작, 변형 또는 가공할 수 없습니다.

- 귀하는, 이 저작물의 재이용이나 배포의 경우, 이 저작물에 적용된 이용허락조건을 명확하게 나타내어야 합니다.
- 저작권자로부터 별도의 허가를 받으면 이러한 조건들은 적용되지 않습니다.

저작권법에 따른 이용자의 권리는 위의 내용에 의하여 영향을 받지 않습니다.

이것은 [이용허락규약\(Legal Code\)](#)을 이해하기 쉽게 요약한 것입니다.

[Disclaimer](#)

Doctor of Philosophy

**A Study on the Graphitic Carbon and
Metal/Metal Oxide Hybrid Structures for the
Glucose Sensing Materials**

The Graduate School of the University of Ulsan

School of Chemical Engineering

Yen-Linh Thi Ngo

*A Study on the Graphitic Carbon and Metal/Metal
Oxide Hybrid Structures for the Glucose Sensing
Materials*

Supervisor: Professor Seung Hyun Hur

A Dissertation

Submitted to

The Graduate School of the University of Ulsan

In partial Fulfillment of the Requirements

for the Degree of

Doctor of Philosophy

by

Yen-Linh Thi Ngo

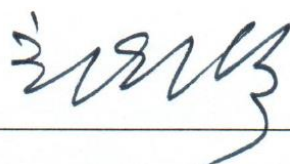
School of Chemical Engineering

Ulsan, South Korea

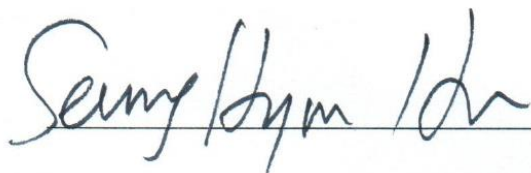
(November 2019)

*A Study on the Graphitic Carbon and Metal/Metal Oxide Hybrid
Structures for the Glucose Sensing Materials*

This certifies that the dissertation
of Yen-Linh Thi Ngo is approved.



Committee Chair Professor Won Mook Choi



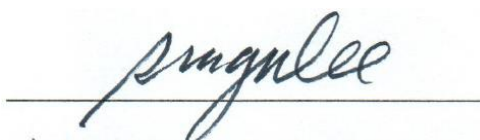
Committee Member Professor Seung Hyun Hur



Committee Member Professor Jin Suk Chung



Committee Member Professor Sung Gu Kang



Committee Member Professor Sun Gu Lee

School of Chemical Engineering

Ulsan, South Korea

(November 2019)

ABSTRACT

Diabetes mellitus is one of the most serious issues worldwide, causes serious damage to the eyes, kidneys, nerves, and heart. To reduce the health risk, early diagnosis and effective self-monitoring are crucial to controlling the glucose levels in the blood. Therefore, the development of suitable materials for the precise and reliable determination of glucose concentration is very important in many areas, including the food industry, biotechnology, and clinical diagnostics. Considerable efforts on glucose sensing have been made, consisting mainly of electrochemical, fluorescence and colorimetric methods.

In Part II related to enhance graphitic carbon sensing material by decorating transition metal/metal oxide based on non-enzymatic electrochemical glucose sensor, i.e. hybridizing silver – Ag, nickel oxide–NiO with reduced graphene oxide (rGO), decorating nickel manganese oxide–NiMn₂O₄ on rGO, and incorporating nickel oxide–NiO with graphitic carbon nitride (g-C₃N₄). The multi-dimensional Ag/NiO/rGO hybrid nanostructure exhibited good glucose sensing properties with sensitivity as high as 1869.4 $\mu\text{A mM}^{-1} \text{cm}^{-2}$. The synergistic effect of each component improved its electrocatalytic activity by enhancing electron transfer and increasing the specific surface area. Meanwhile, the presence of rGO in the composite inhibited the agglomeration of Ag and NiO nanoparticles regardless of the Ag and NiO content. rGO also played an important role as well as a charge transfer. In the other hand, the 3-dimensional rGO hydrogel (rGOH) network with NiMn₂O₄ was fabricated using a facile solvothermal synthesis, where the porous rGOH and NiMn₂O₄ provided a large surface area and excellent ion transportation. Moreover, rGOH provided numerous dispersion sites of NiMn₂O₄ and conductive pathways for electrons that are generated during the electrochemical reaction on an NiMn₂O₄ catalyst, which results in excellent glucose sensitivity. Recently, the g-C₃N₄ has become a potential candidate and replaced rGO based on its charge transfer ability in a range of applications, due to its unique electronic and optical properties, thermal/chemical stability, that improves the charge transfer in the electrochemical reaction. The NiO/g-C₃N₄ hybrid (NC) exhibited extremely

high glucose sensitivity, up to $5387.1 \mu\text{A mM}^{-1} \text{cm}^{-2}$, which is one of the highest values ever reported. These also show excellent selectivity, good-long term stability, and rapid response towards glucose.

In Part III studied of g-C₃N₄ quantum dot (g-CNQDs) and boronic acid for a highly selective and sensitive fluorescence glucose sensor, where g-CNQDs as a fluorescent and boronic acid as a quencher and receptor during glucose sensing. The g-CNQDs/phenylboronic acid (PBA) was prepared by a simple hydrothermal process, exhibited the high quantum yields, high glucose sensitivity and selectivity, low toxicity and good biocompatibility in the cell imaging test. The fluorescence quenching mechanism of this sensor can be attributed to some molecular interactions such as π - π stacking interaction between triazine rings of CNQDs and benzene rings of PBA, and hydrogen bonding between functional groups. Then, the fluorescence intensity (PL) was recovered in the presence of glucose due to PBA was released from g-CNQDs. On the other hand, the development of multi-chemical sensor was further investigated by introducing the covalent bonds between g-CNQDs and boronic acid groups. The functionalized of 3-amino phenylboronic acid (3APBA) on g-CNQDs caused strong enhancement of the fluorescence intensity, which acted as a fluorescent. When adding the glucose, the PL quenching of g-CNQDs/3APBA can be due to the formation of glucoboronate ester, meanwhile, the PL intensity of glucose added g-CNQDs/3APBA increased with increasing 1,2-propanediol concentration, which can be owing to the hydrolysis of glucoboronate ester in the presence of 1,2-propanediol at the boronic acid sites of g-CNQDs/3APBA. The g-CNQDs/3APBA exhibited high sensitivity and excellent selectivity with low detection limit towards glucose. This also can be applied to an effective multi-chemical sensor.

ACKNOWLEDGEMENT

Spending years for studying at the University of Ulsan, I have been blessed to have the pleasure of working and making friends with a lot of interesting individuals, who have made my experience as a joyful graduate student. I truly appreciate the support that they have given to me, both scientific and personal.

First and foremost, I would like to express my sincere gratitude and thanks to my advisor, Professor Seung Hyun Hur for giving me generous guidance, expert advice through all stages of this research as well as the preparation of all the manuscripts for publication and allowing me to grow into a research scientist. Your advice on both research as well as on my career have been priceless. Besides my advisor, I would like to thank all of my committee members, Professor Jin Suk Chung, Professor Won Mook Choi, Professor Sung Gu Kang and Professor Sun Gu Lee for their insightful comments and suggestions to this work.

Thanks to all my fellow labmates, Huynh Ngoc Tien, Le Thuy Hoa, Tran Van Phuc, Huynh Ngoc Diem, Hye-Jin Lee, Jayasmita Jana, and Linlin Wang for their professional supports in researching and their friendships. Also, I would like to thank my beloved friends, Dang Thi Thao, Thanh-Truc Pham, Kim Ngan Thi Tran, always beside me whether hard or cheerful, thank you for coming into my life and make it so interesting.

Last but not least, a deep gratitude to my family, my Dad, my Mom, and my older sister. Words cannot express how grateful I am to my family for all the sacrifices and encouragement they gave throughout my graduate study. Finally, I would like to special thanks to husband Nguyen Phi Luan for your love, care, advice, support me unconditionally and all the time we have been through together since the beginning. Thank you for your love and companionship, which have become an essential source of strength to me during the Ph.D. course.

With their wonderful helps, I can achieve my Ph.D. course. Thank you.

TABLE OF CONTENTS

PART I -	OVERVIEW OF DISSERTATION	I-1
Chapter 1. Introduction		I-1
1.1. Overview		I-1
1.1.1. <i>Diabetes and blood glucose monitoring</i>		I-1
1.1.2. <i>Glucose sensor</i>		I-4
1.1.2.1. Enzymatic glucose sensor		I-5
1.1.2.2. Non-enzymatic glucose sensors		I-7
1.1.3. <i>Motivation</i>		I-9
1.1.4. <i>Research objectives</i>		I-9
1.2. Outline of dissertation		I-10
1.3. Introduction of materials		I-12
1.3.1. <i>Graphitic carbon materials – layered structure</i>		I-12
1.3.1.1. Graphene oxide and reduced graphene oxide.....		I-12
1.3.1.2. Graphitic carbon nitride g-C ₃ N ₄		I-15
1.3.1.3. Boronic acid groups		I-16
1.3.2. <i>Nickel Oxide</i>		I-17
PART II -	Enhancement graphitic carbon material by decorating metal/metal oxide-based on non-enzymatic electrochemical sensor	II-19
Chapter 2. Multi-Dimensional Ag/NiO/Reduced Graphene Oxide Nanostructures for a Highly Sensitive Non-Enzymatic Glucose Sensor		II-19
2.1. Introduction		II-19
2.2. Experimental details		II-20
2.2.1. <i>Materials</i>		II-20
2.2.2. <i>Preparation of Ag/NiO/rGO</i>		II-21
2.2.3. <i>Preparation of Ag/NiO/rGO modified electrodes</i>		II-22
2.2.4. <i>Instrumental analysis</i>		II-22
2.3. Results and Discussion		II-23
2.3.1. <i>Characterization of Ag/NiO/rGO</i>		II-23
2.3.2. <i>Electrochemical behavior of Ag/NiO/rGO towards glucose</i>		II-28
2.3.3. <i>Stability and effect of the interfering species of the Ag/NiO/rGO electrode</i>		II-35
2.3.4. <i>Real sample analysis</i>		II-36
2.4. Conclusions		II-37
2.5. Supporting information		II-38

Chapter 3. NiMn₂O₄ Spinel Binary Nanostructure Decorated on Three-Dimensional Reduced Graphene Oxide Hydrogel for Bifunctional Materials in Non-enzymatic Glucose Sensor	II-44
3.1. Introduction	II-44
3.2. Experimental details	II-45
3.2.1. <i>Materials</i>	II-45
3.2.2. <i>Preparation of NiMn₂O₄/rGOH</i>	II-45
3.2.3. <i>Preparation of NiMn₂O₄/rGOH modified electrodes</i>	II-46
3.2.4. <i>Instrumental analysis</i>	II-47
3.3. Results and Discussion	II-48
3.3.1. <i>Characterization of rGOH, NiMn₂O₄, and NiMn₂O₄/rGOH</i>	II-48
3.3.2. <i>Electrochemical behaviors of NiMn₂O₄/rGOH towards glucose</i>	II-53
3.3.3. <i>Stability and effect of the interfering species of the NiMn₂O₄/rGOH electrode</i>	II-58
3.3.4. <i>Real blood test</i>	II-59
3.4. Conclusions	II-60
3.5. Supporting Information	II-61
Chapter 4. Highly Sensitive Non-Enzymatic Electrochemical Glucose Sensor based on Multi-functional NiO/g-C₃N₄ Hybrid Nanostructures	II-72
4.1. Introduction	II-72
4.2. Experimental details	II-73
4.2.1. <i>Materials</i>	II-73
4.2.2. <i>Synthesis of NiO/ g-C₃N₄ hybrid materials</i>	II-73
4.2.3. <i>Preparation of the NiO/g-C₃N₄ modified electrodes</i>	II-74
4.2.4. <i>Instrumental analysis</i>	II-75
4.3. Results and Discussion	II-75
4.3.1. <i>Characterization of pristine g-C₃N₄, NiO and NiO/g-C₃N₄</i>	II-75
4.3.2. <i>Electrochemical glucose sensing with NiO/g-C₃N₄ electrodes</i>	II-81
4.3.3. <i>Stability, reproducibility and anti-interference property of the NiO/g-C₃N₄ electrode</i>	II-85
4.3.4. <i>Real sample test</i>	II-86
4.3.5. <i>Flexible glucose sensor based on NiO/g-C₃N₄</i>	II-87
4.4. Conclusions	II-89
4.5. Supporting Information	II-89

PART III - Glucose-sensitive fluorescence sensor based on graphitic carbon nitride quantum dots	III-96
Chapter 5. Highly Biocompatible Phenylboronic acid-functionalized Graphitic Carbon Nitride Quantum Dots for the Selective Glucose Sensor	III-96
5.1. Introduction	III-96
5.2. Experimental details	III-97
5.2.1. <i>Materials</i>	III-97
5.2.2. <i>Synthesis of g-CNQDs/PBA</i>	III-98
5.2.3. <i>Glucose sensing</i>	III-99
5.2.4. <i>Measurement of the quantum yields</i>	III-99
5.2.5. <i>Cell culture and fluorescence imaging</i>	III-99
5.2.6. <i>Cytotoxicity assay of g-CNQDs</i>	III-100
5.2.7. <i>Instrumental analysis</i>	III-100
5.3. Results and discussion.....	III-101
5.3.1. <i>Characterization of g-CNQDs and g-CNQDs/PBA</i>	III-101
5.3.2. <i>Fluorescence properties of g-CNQDs</i>	III-106
5.3.3. <i>Glucose sensing of g-CNQDs/PBA</i>	III-108
5.3.4. <i>Detection of glucose in real blood</i>	III-111
5.3.5. <i>Bio-imaging and Cytotoxicity test</i>	III-112
5.4. Conclusions	III-113
5.5. Supporting Information	III-113
Chapter 6. Aminoboronic Acid-functionalized Graphitic Carbon Nitride Quantum Dots for the Photoluminescence Multi-chemical Sensing Probe.....	III-120
6.1. Introduction	III-120
6.2. Experimental details	III-121
6.2.1. <i>Materials</i>	III-121
6.2.2. <i>g-CNQDs/3APBA quantum dots preparation</i>	III-122
6.2.3. <i>Detection of Glucose</i>	III-123
6.2.4. <i>Instrumental analysis</i>	III-123
6.3. Results and discussion.....	III-124
6.3.1. <i>Characterization of quantum dots</i>	III-124
6.3.2. <i>Optical properties of g-CNQDs/3APBA</i>	III-128
6.3.3. <i>Fluorescence glucose detection of g-CNQDs/3APBA</i>	III-129
6.3.4. <i>Measurement of the glucose concentration in real blood serums</i>	III-133
6.3.5. <i>Cell imaging and cytotoxicity test</i>	III-134

6.3.6. <i>Paper-based glucose sensor</i>	III-136
6.4. Conclusions	III-137
6.5. Supporting Information	III-138
PART IV - SUMMARY	IV-148
PART V - RECOMMENDATIONS FOR FUTURE WORK.....	V-150
REFERENCES	V-151
LIST OF PUBLICATIONS.....	V-171

LIST OF FIGURES

Figure 1.1. Percentage of deaths attributed to high blood glucose that occur at ages 20–69 years, by sex and country income group, 2012 (Source: Global report on diabetes, WHO).	I-2
Figure 1.2. Trends in prevalence of diabetes, 1980–2014, by country income group (Source: Global report on diabetes, WHO).	I-2
Figure 1.3. Percentage of countries reporting basic technologies generally available in publicly funded primary health-care facilities (Source: Global report on diabetes, WHO).	I-3
Figure 1.4. Summary of enzymatic glucose oxidation mechanisms, presented as first, second and third-generation sensors [7].	I-6
Figure 1.5. A schematic illustration of the IHOAM model in which M^* is the reductive metal I-8	
Figure 1.6. The main structure of dissertation.	I-11
Figure 1.7. Graphene from graphite: Graphite is a basic material found in nature. When taken apart graphite sheets become graphene. A rolled-up layer of graphene forms a carbon nanotube, folded up it becomes a small football, fullerene. Hidden inside graphite, graphene was waiting to be discovered (Source: Nobel Foundation. "Nobel Prize in Physics 2010 for graphene -- 'two-dimensional' material." ScienceDaily. ScienceDaily, 5 October 2010).	I-13
Figure 1.8. (A) Graphitic top-down approach and (B) molecular carbon precursor bottom-up approach for producing wide variety of graphene-based materials in large quantities [15]. ...	I-14
Figure 1.9. (A) Triazine and (B) tri-s-triazine (heptazine) structures of $g-C_3N_4$	I-15
Figure 1.10. The binding process between phenylboronic acid and diol.	I-17
Figure 2.1. Schematic diagram of the fabrication steps of Ag/NiO/rGO.	II-22
Figure 2.2. Schematic diagram of electrochemical measurement systems and reactions on the electrode surface.	II-23
Figure 2.3. XPS spectrum of 5Ag/NiO/rGO (A) survey spectra with pure GO, (B) Ni 2p, (C) Ag 3d, (D) C 1s and C 1s of GO (inset).	II-24
Figure 2.4. Raman spectra of GO, pure rGO, Ag/NiO, and 5Ag/NiO/rGO.	II-25

Figure 2.5. FE-SEM images of (A) pure rGO, (B) Ag/NiO, (C) 5Ag/NiO/rGO, and (D) the EDS result of 5Ag/NiO/rGO.....	II-26
Figure 2.6. (A) HR-TEM images of 5Ag/NiO/rGO. Corresponding FFT patterns (B) rGO, (C) NiO and (D) Ag nanoparticles.....	II-27
Figure 2.7. Cyclic voltammograms of (A) pure rGO, (B) Ag/NiO and NiO (inset), (C) NiO/rGO, and (D) 5Ag/NiO/rGO modified electrode in 0.1 M NaOH in the absence (black) and presence of 1 mM glucose (red), respectively. The scan rate is 50 mV s ⁻¹	II-29
Figure 2.8. CV curves of the 5Ag/NiO/rGO in 0.1 M NaOH with 1 mM glucose at different scan rates ranging from 10 mV s ⁻¹ to 100 mV s ⁻¹ . The inset presents a plot of the peak current versus square root of the scan at an applied potential of +0.6 V.	II-32
Figure 2.9. (A) CV curves of the 5Ag/NiO/rGO electrode at various glucose concentrations in a 0.1 M NaOH solution at a scan rate of 50 mV s ⁻¹ . (B) Calibration curve showing the response of 5Ag/NiO/rGO to a wide range of glucose concentrations, 50 μM to 25 mM. The error bars indicate the standard deviations for triplicate measurements at each glucose concentration.	II-34
Figure 2.10. Amperometric test of 5Ag/NiO/rGO electrode recorded at + 0.6 V towards the successive addition of 1 mM glucose in 0.1 M NaOH.	II-35
Figure 2.11. Amperometric response of the Ag/NiO/rGO electrode with the successive injection of 5 mM glucose (twice), then 0.5 mM interfering species of (A) UA, AA, DA and (B) fructose, lactose, sucrose, and 5 mM glucose into 0.1 M NaOH under + 0.6 V.	II-36
Figure 3.1. Schematic diagram of the preparation steps of NiMn ₂ O ₄ /rGOH.	II-46
Figure 3.2. XRD patterns of (A) rGOH, (B) NiMn ₂ O ₄ and (C-F) NiMn ₂ O ₄ /rGOH with various NiMn ₂ O ₄ contents.....	II-48
Figure 3.3. Raman spectra of (A) GO, (B) NiMn ₂ O ₄ , (C) rGOH and (D-G) NiMn ₂ O ₄ /rGOHs with various NiMn ₂ O ₄ contents.	II-49
Figure 3.4. (A) XPS survey spectra of 1.0NiMn ₂ O ₄ /rGOH and GO. The XPS spectra of (B) Mn 2p, (C) Ni 2p, and (D) C 1s. The inset shows the XPS spectra of C1s of GO.....	II-50

Figure 3.5. FE-SEM images of (A) pure rGOH, (B) NiMn ₂ O ₄ , and (C) 1.0NiMn ₂ O ₄ /rGOH. HR-TEM images of NiMn ₂ O ₄ /rGOH (D and E) and corresponding FFT patterns of (F) rGOH and (G) NiMn ₂ O ₄ .	II-52
Figure 3.6. CV curves of (A) rGOH, NiMn ₂ O ₄ and 1.0NiMn ₂ O ₄ /rGOH in the absence of glucose. CV curves of (B) rGOH, (C) NiMn ₂ O ₄ , and (D) 1.0NiMn ₂ O ₄ /rGOH modified electrode in 0.1 M NaOH in the absence (black) and presence of 0.5 mM glucose (red), respectively. The scan rate was 50 mV s ⁻¹ .	II-54
Figure 3.7. (A) CV curves of the 1.0NiMn ₂ O ₄ /rGOH in 0.1 M NaOH with 1 mM glucose at different scan rates ranging from 10 mV s ⁻¹ to 100 mV s ⁻¹ . (B) Plot of the peak current versus square root of the scan rate at an applied potential of +0.62 V.	II-55
Figure 3.8. (A) CV curves of 1.0NiMn ₂ O ₄ /rGOH with different glucose concentrations in a 0.1 M NaOH solution at a scan rate of 50 mV s ⁻¹ . (B) Calibration curve of 1.0NiMn ₂ O ₄ /rGOH at a wide range of glucose concentrations from 0 μM to 20 mM. The error bars indicate the standard deviations for triplicate measurements at each glucose concentration.	II-56
Figure 3.9. Amperometric test of the 1.0NiMn ₂ O ₄ /rGOH electrode recorded at +0.62 V towards the successive addition of 1 mM glucose in the 0.1 M NaOH electrolyte at every 90 s.	II-57
Figure 3.10. Amperometric response to successive injections of 1 mM glucose and 5 mM interferences of (A) UA, AA, DA, and SB, and (B) galactose, fructose, lactose, and sucrose of the 1.0NiMn ₂ O ₄ /rGOH electrode in 0.1 M NaOH electrolyte at an applied voltage of +0.62 V.	II-58
Figure 4.1. Schematic diagram of the preparation process of NiO/g-C ₃ N ₄ hybrid materials (NC) and NC based electrodes.	II-74
Figure 4.2. FT-IR spectra of pure g-C ₃ N ₄ and NC(x) with various Ni(OH) ₂ and melamine mass ratios.	II-76
Figure 4.3. XRD patterns of (A) g-C ₃ N ₄ (calcined at 370 °C), (B) g-C ₃ N ₄ (calcined at 550 °C), (C) NiO and (D-H) various NC(x) with x = 0.5, 1, 2, 3, 4 corresponding to D, E, F, G and H, respectively.	II-77

Figure 4.4. (A) XPS survey and high-resolution (B) C 1s, (C) N 1s, and (D) Ni 2p XPS spectra of pristine g-C₃N₄ and NC(1) composite II-78

Figure 4.5. FE-SEM images of (A) pristine g-C₃N₄ (calcined at 370 °C), (B) NiO and (C) NC(1). (D) EDS spectrum of NC(1). (E) TEM and (F) HR-TEM images of NC(1) and the inset images are the FFT patterns of g-C₃N₄ and NiO..... II-80

Figure 4.6. CV curves of pure g-C₃N₄, NiO and NC(1) in 0.1 M NaOH at a scan rate of 50 mV s⁻¹ with (solid line) and without (dash dot line) 500 μM glucose, respectively. II-82

Figure 4.7. (A) CV curves of the NC(1) in 0.1 M NaOH with 1 mM glucose at different scan rates 10 – 100 mV s⁻¹. (B) Plot of the peak current versus the square root of the scan rate at an applied potential of +0.68 V..... II-83

Figure 4.8. (A) CV curves of the NC(1) and (B) calibration curve from CV of NC(1) at a wide range of glucose concentrations from 500 nM to 20 mM. (C) Typical amperometric current response recorded at +0.68 V and (D) calibration curves vs. glucose concentration from amperometric with the successive addition of various glucose concentrations at 60 s intervals. Conditions: scan rate of 50 mV s⁻¹, 0.1 M NaOH electrolyte. Inset: (C) the response time to achieve steady-state current. The error bars indicate the standard deviations for triplicate measurements at each glucose concentration. Inset: (B) and (D) calibration curves at low glucose concentrations..... II-84

Figure 4.9. Typical amperometric response of NC(1) to the sequential addition of 1 mM glucose and 0.1 mM interferences of UA, AA, Sor, DP, Lys, Glys, galactose, fructose, lactose, maltose, and sucrose in 0.1 M NaOH electrolyte at an applied voltage of + 0.68 V II-86

Figure 4.10. (A) CV test of NC(1)/flexible electrode in the presence of various glucose concentrations in 0.1 M NaOH at a scan rate of 50 mV s⁻¹. (B) Amperometric response of NC(1)/flexible sensor at + 0.64 V with the successive addition of glucose in 0.1 M NaOH at every 60 s. (C) Calibration curve of NC(1)/flexible sensor with the linear fitting result. (D) Current response with different bending times in 0.1 M NaOH. The inset shows a digital picture of bent NC(1) electrode. II-88

Figure 5.1. Schematic diagram of g-CNQDs/ PBA fabrication from melamine.	III-98
Figure 5.2. TEM images of (A-B) bulk g-C ₃ N ₄ , (C) g-CNQDs, (E) g-CNQDs/PBA. (D) Size distribution of g-CNQDs. (F) Tyndall effect of g-CNQDs dispersion with the red laser light passing through. Inset: (B) FFT patterns of g-C ₃ N ₄ , (C) HR-TEM images of g-CNQDs.	III-102
Figure 5.3. XRD patterns of melamine, bulk g-C ₃ N ₄ and g-CNQDs.	III-103
Figure 5.4. FT-IR spectra of bulk g-C ₃ N ₄ , g-CNQDs and g-CNQDs/PBA.	III-104
Figure 5.5. (A) XPS survey spectra of melamine, bulk g-C ₃ N ₄ , g-CNQDs, and g-CNQDs/PBA. The high-resolution XPS spectra of (B) C 1s, (C) N 1s, (D) O 1s, and (E) B 1s for g-CNQDs/PBA.	III-105
Figure 5.6. UV-Vis absorption and photoluminescence (PL) emission and excitation spectra of g-CNQDs; the inset shows a digital photo of g-CNQDs under visible (left) and UV lights (right). (B) PL spectra of g-CNQDs at various excitation wavelengths.	III-107
Figure 5.7. Proposed glucose-sensing mechanism based on g-CNQDs/PBA as a fluorescent and PBA as a receptor.	III-109
Figure 5.8. (A) PL emission spectra of g-CNQDs and g-CNQDs /PBA at various glucose concentrations (from bottom to top: 0 – 1 mM). (B) Plots of the relative PL intensity (F/F ₀) versus glucose concentration. F and F ₀ are the PL intensity of g-CNQDs/PBA in the absence and presence of glucose, respectively. The inset shows a linear curve over the concentration range from 25 nM to 1 μM. Measurement conditions: g-CNQDs = 2 mg/mL, PBA = 0.25 M, pH = 7.2, and λ _{ex} = 310 nm. The error bars imply the standard deviations for triplicate determinations at each concentration.	III-109
Figure 5.9. Relative PL intensity ((F-F ₀)/(F _{Glu} -F ₀)) of g-CNQDs/PBA in the presence of various interfering species. F and F ₀ represent the PL intensity of g-CNQDs/PBA with and without 5 mM of interfering species, respectively. F _{Glu} is the PL intensity at 1 mM of glucose. The data shown here describe the average of three experiments for each interfering species.	III-110

Figure 5.10. Confocal fluorescence images of HeLa cells incubated with g-CNQDs under (A) bright field, and excitation at (B) 405 nm, and (C) 488 nm. The scale bar represents 30 μm ...	III-112
Figure 6.1. Schematic diagram of g-CNQDs/ 3APBA synthesis process from melamine.	III-122
Figure 6.2. FT-IR spectra of g-C ₃ N ₄ (at), g-CNQDs and g-CNQDs/3APBA.	III-124
Figure 6.3. (A) XPS survey spectra and high-resolution XPS spectra of (B) C 1s, (C) N 1s, (D) O 1s of g-C ₃ N ₄ (at), g-CNQDs, and g-CNQDs/3APBA and (E) B 1s of g-CNQDs/3APBA. ..	III-126
Figure 6.4. TEM images of (A) g-CNQDs, (C) g-CNQDs/3APBA. HR-TEM images of (B) g-CNQDs and (D) g-CNQDs/3APBA.	III-127
Figure 6.5. Sensing mechanism of g-CNQDs/3APBA based fluorescence sensor “on-off” for glucose and “on-off-on” for propylene glycol.....	III-130
Figure 6.6. (A) PL emission spectra of g-CNQDs/3APBA in the presence of different glucose concentrations. (B) Plots of the relationship between the relative PL intensity (F_0/F) and glucose concentration. F_0 and F are the PL intensity of g-CNQDs/3APBA in the absence and presence of glucose, respectively. The inset shows a linear curve over the concentration range from 25 nM to 1 μM . Measurement conditions: g-CNQDs/3APBA = 0.5 mg/mL, pH = 10, and λ_{ex} = 320 nm.	III-131
Figure 6.7. (A) PL response of g-CNQDs/3APBA in the presence of 10 mM glucose and different concentrations of propylene glycol. (B) Plot of the linear range of relative PL intensity (F/F_0) vs concentration of propylene glycol, with F_0 and F being the PL intensity in the absence and presence of propylene glycol.	III-133
Figure 6.8. Cellular cytotoxicity of g-CNQDs/3APBA towards HeLa cells evaluated by using the MTT assay.	III-135
Figure 6.9. Confocal fluorescence images of HeLa cells under laser excitation at (A) 405 nm, and (B) 488 nm of g-CNQDs/3APBA. The scale bar represents 20 μm	III-135

Figure 6.10. Fluorescence images of test paper in the absence and presence of glucose under visible light and a 365 nm UV lamp.....III-136

Figure 6.11. Correct total cell fluorescence (CTCF) of each sample. The bar describes the average of three experiments for each sample.....III-137

Supporting Information

Figure S2.1. (A-F) CV curves of the Ag/NiO/rGO electrode with different Ag contents at various glucose concentrations in a 0.1 M NaOH at a scan rate of 50 mV s⁻¹ II-38

Figure S2.2. Calibration curves of current density vs. glucose concentration at various Ag contents..... II-39

Figure S2.3. Calibration curves of current density vs. concentration of glucose at difference solution ratio of Ag/NiO and rGO..... II-39

Figure S2.4. The sensitivity of 5Ag/NiO/rGO at different temperature..... II-40

Figure S2.5. Raman spectra of (A) Ag/NiO/rGO at various Ag contents and (B) Ag/NiO/rGO at different solution ratio of Ag/NiO and GO. II-40

Figure S2.6. The CV curves of 5Ag/NiO/rGO modified electrode in presence of 0.5 mM concentration of various interfering species and glucose in 0.1 M NaOH. The inset obviously presents the CV curves of different interfering species. Scan rate is 50 mV s⁻¹. II-41

Figure S2.7. Stability of the Ag/NiO/rGO glucose sensor at room temperature. The current was measured every 3 days for one month. II-41

Figure S3.1. (A-F) CV curves of rGOH (A), NiMn₂O₄ (B), and the NiMn₂O₄/rGOHs (C-F) modified electrodes synthesized at different NiMn₂O₄ contents at various glucose concentrations in a 0.1 M NaOH at a scan rate of 50 mV s⁻¹. II-61

Figure S3.2. Calibration curves of sensitivity vs. concentration of glucose of the NiMn₂O₄/rGOH synthesized at different NiMn₂O₄ contents in a 0.1 M NaOH at a scan rate of 50 mV s⁻¹. II-62

Figure S3.3. (A-C-E) CV curves and (B-D-F) corresponding calibration curves of sensitivity vs. concentration of glucose of the 1.0NiMn₂O₄/rGOH electrodes synthesized at different solvothermal temperature in a 0.1 M NaOH at a scan rate of 50 mV s⁻¹. II-63

Figure S3.4. The images of various NiMn₂O₄/rGOH prepared at different solvothermal temperature. Only above 130 °C the hydrogel can be properly formed and at too high temperature hydrogel becomes hard and thus the specific area decreases (Table S3.2). Therefore, we fabricated all samples for further study in this manuscript at 160 °C..... II-64

Figure S3.5. The XPS survey spectra of various xNiMn₂O₄/rGOH fabricated at 160 °C..... II-65

Figure S3.6. FE-SEM images of (A) rGOH, (B) NiMn₂O₄, and FE-SEM/EDAX images for Ni, Mn, C and O elements of (C-D) 0.5NiMn₂O₄/rGOH, (E-F) 0.75NiMn₂O₄/rGOH, (G-H) 1.0NiMn₂O₄/rGOH and (I-J) 1.25NiMn₂O₄/rGOH. II-66

Figure S3.7. HR-TEM images of (A-C) NiMn₂O₄, (D-F) 0.5NiMn₂O₄/rGOH, (G-I) 0.75NiMn₂O₄/rGOH, (J-L) 1.0NiMn₂O₄/rGOH and (M-O) 1.25NiMn₂O₄/rGOH at various resolution..... II-67

Figure S3.8. The current increase of 1.0NiMn₂O₄/rGOH electrode when 5 mM of each interfering species was injected in 0.1 M NaOH electrolyte at the applied voltage of +0.62 V. The error bars indicate the standard deviation of triplicate determination of each interfering species. II-68

Figure S3.9. Stability of the 1.0NiMn₂O₄/rGOH based on glucose sensor at room temperature. The current was measured every 3 days for one month. II-68

Figure S3.10. Amperometric tests of 1.0NiMn₂O₄/rGOH in 0.1 M NaOH at +0.62 V with the successive addition of (A) Horse and (B) Rabbit serum. II-69

Figure S4.1. Thermal treatment process was simulated under nitrogen flow gas by TGA (top) and (DTA) analyses for melamine and as-synthesized NiO/g-C₃N₄ composites. II-89

Figure S4.2. XRD patterns of (A) melamine, g-C₃N₄ calcinated at 370 and 500 °C; (B) Ni(OH)₂ and NiO. II-90

Figure S4.3. FE-SEM images of various composite (A) NC(0.5), (B) NC(2), (C) NC(3) and (D) NC(4)..... II-90

Figure S4.4. (A) N₂ adsorption-desorption (BET isotherm) of g-C₃N₄, NiO, and NC(1); (B) BJH pore size distribution of NC(1)..... II-91

Figure S4.5. Plot of calibration curves of NiO and composites NC(x) with various glucose concentration in 0.1 M NaOH at a scan rate of 50 mV s ⁻¹	II-91
Figure S4.6. Stability of NC(1) based glucose sensor at room temperature. The current was recorded every 3 days in 30 days.....	II-92
Figure S4.7. Amperometric tests and calibration curves of NC(1) in 0.1 M NaOH at an applied potential +0.68 V with the successive addition of real serum samples (A-B) Horse serum and (C-D) Rabbit serum.....	II-92
Figure S4.8. Schematic illustration of the fabrication process of flexible NC(1) sensor.	II-93
Figure S5.1. The optimized concentration of g-C ₃ N ₄ . PL emission spectra of g-CNQDs with the different concentration of g-C ₃ N ₄ under excitation wavelength at 310 nm, buffer pH = 7.2.	III-113
Figure S5.2. The optimized concentration of PBA. (A-B) PL emission spectra of g-CNQDs/PBA in PBS buffer with the addition of various PBA concentrations increasing from 0 to 0.25 M (top to bottom). Inset: the linear plot of the PL intensity for g-CNQDs/PBA versus the PBA concentration. The PL spectra were by using 2 mg/mL g-CNQDs recorded in PBS buffer (pH 7.2) under $\lambda_{ex} = 310$ nm, $\lambda_{em} = 434$ nm. The error bars imply the standard deviations for triple measurement at each concentration.	III-114
Figure S5.3. Simulated the optimized conditions including temperature and time for hydrothermal process by MATLAB simulation of the 3D-scattering intensity distribution.	III-114
Figure S5.4. Plots of integrated PL intensity of g-CNQDs and quinine sulfate (reference dye) as a function of optical absorbance at 310 nm and relevant data.	III-115
Figure S5.5. The XPS spectrum (A) C 1s, (B) N 1s, (C) O 1s of melamine, bulk g-C ₃ N ₄ , g-CNQDs and g-CNQDs/PBA.	III-116
Figure S5.6. The effect of pH on the PL intensity of g-CNQDs in the range from 2 to 13. The experiment was measured in g-CNQDs (2 mg/mL) solution at excitation wavelength of 310 nm. The error bars imply the standard deviations for triple measurement at each pH value.	III-117

Figure S5.7. The UV-vis spectrum of PBA (red curve), and emission spectrum of the g–CNQDs ($\lambda_{\text{ex}} = 310$ nm) (black curve).	III-117
Figure S5.8. PL emission spectra of g–CNQDs/PBA towards the real serum (A) Horse serum, (B) Rabbit serum. The inset pictures show the relative PL intensity vs various concentration of serum. The error bars imply the standard deviations for triple determination at each concentration.	III-118
Figure S5.9. Cellular cytotoxicity of g–CNQDs towards HeLa cells evaluated by using the MTT assay.	III-118
Figure S6.1. Simulated the optimize conditions including temperature and time for hydrothermal process for fabricated g-CNQDs/3APBA by MATLAB simulation of the 3D-scattering intensity distribution.....	III-138
Figure S6.2. TEM and HR-TEM image of g-C ₃ N ₄ after acid treatment process.....	III-138
Figure S6.3. (A) UV-Vis absorption and photoluminescence (PL) emission spectra of g-CNQDs/3APBA at various excitation wavelengths; the inset photo represents the g-CNQDs/3APBA suspension under visible (left) and UV light (right). (B) PL emission spectra at the wide range of excitation wavelength from 280 – 520 nm.	III-139
Figure S6.4. Plots integrated PL intensity of quinine sulfate (reference dye) and g-CNQDs/3APBA as a function of optical absorbance at 320 nm and relevant data.....	III-139
Figure S6.5. Time-resolved fluorescence decay spectra of g-CNQDs/3APBA and inserted shows two-exponential analysis results.....	III-140
Figure S6.6. Tyndall effect of g-CNQDs/3APBA in the aqueous dispersion obtained by red laser passing through solution.....	III-140
Figure S6.7. (A) PL emission spectra of g-CNQDs/3APBA in PBS solution with pH = 7 and 10; (B) the relative PL intensity of g-CNQDs/3APBA versus the glucose concentration; (C-D) PL emission of g-CNQDs/3APBA with the addition of various glucose concentration increasing from 25 nM to 10 mM in PBS pH = 7 and 10, respectively. The PL spectra was by using 0.5 mg/mL g-CNQDs/3APBA recorded in PBS buffer under $\lambda_{\text{ex}} = 320$ nm, $\lambda_{\text{em}} = 374$ nm.	III-141

Figure S6.8. (A) PL emission spectra of g-CNQDs and g-CNQDs/3APBA/EDC at the various excitation wavelength; (B) The PL emission of g-CNQDs, g-CNQDs/3APBA, g-CNQDs/3APBA with glucose and g-CNQDs/3APBA/Glucose with propylene glycol (diol).III-142

Figure S6.9. Relative PL intensity $((F-F_0)/(F_{Glu}-F_0))$ of g-CNQDs/3APBA after the addition of various interfering species. F and F_0 represent the PL intensity of g-CNQDs/3APBA with and without 5 mM of interfering species, respectively. F_{Glu} is the PL intensity at 1 mM of glucose.III-142

Figure S6.10. (A) PL emission spectra and (B) Relative PL intensity $((F-F_0)/(F_{PG}-F_0))$ of g-CNQDs/3APBA/Glucose in the presence of different diol groups. F and F_0 represent the PL intensity of g-CNQDs/3APBA/Glucose with and without 1 mM of interfering species, respectively. F_{PG} is the PL intensity at 1 mM of propylene glycol. The data shown here describe the average of three experiments for each interfering species.III-143

Figure S6.11. PL emission spectra of g-CNQDs/3APBA towards the real serum (A) Horse serum, (B) Rabbit serum. The inset pictures show the relative PL intensity vs various concentration of serum. The error bars imply the standard deviations for triple measurement at each concentration.III-143

LIST OF TABLES

Table 1.1. Technologies under development for glucose sensors.....	I-4
Table 2.1. Sensitivity of Ag/NiO/rGO at various contents of Ag.....	II-33
Table 2.2. The sensitivity of Ag/NiO/rGO at different ratio between Ag/NiO and rGO solutions	II-33
Table 2.3. Amperometric determination of the glucose concentration in real blood samples.....	II-37
Table 3.1. Glucose sensitivity of various samples fabricated in this study.....	II-56
Table 3.2. Comparison of the glucose concentration between the commercial enzymatic glucometer and 1.0NiMn ₂ O ₄ /rGOH measured at various glucose concentrations.	II-59
Table 4.1. Comparison of the glucose level between NiO/g-C ₃ N ₄ and commercial glucometer.	II-87
Table 5.1. Comparison of the glucose concentration between the commercial glucometer and g-CNQDs/PBA measured at various glucose concentrations.....	III-111
Table 6.1. Comparison of a commercial glucometer with the sensor based on g-CNQDs/3APBA for glucose determination at various serum concentrations.	III-134

Supporting Information

Table S2.1. BET surface areas of pure rGO, NiO/rGO and various Ag/NiO/rGOs with different Ag contents.....	II-42
Table S2.2. BET surface areas of various 5Ag/NiO/rGO fabricated with different solution ratio of Ag/NiO and GO.	II-42
Table S2.3. The glucose sensing results of our study compared to the previous nickel oxide- based studies.....	II-43
Table S3.1. BET surface area of rGOH, NiMn ₂ O ₄ and various NiMn ₂ O ₄ /rGOHs of different NiMn ₂ O ₄ contents.....	II-70
Table S3.2. BET surface areas of various 1.0NiMn ₂ O ₄ /rGOHs synthesized at different solvothelmal temperatures.....	II-70

Table S3.3. The glucose sensing results of our study compared to those of the previous nickel/manganese oxide-based studies.	II-70
Table S4.1. Relative ratio of C=C, HC-O, N-C=N and N-C=O/O-C=O of all samples by C 1s spectra analysis.....	II-93
Table S4.2. Relative ratio of C-N=C (N ₁), N-(C) ₃ and HN-(C) ₂ (tertiary - N ₂), C - NH (quaternary - N ₃) of all samples by N 1s spectra analysis.....	II-93
Table S4.3. The BET surface area and glucose sensitivity of various samples fabricated in this study.	II-94
Table S4.4. Performance comparison of NiO/g-C ₃ N ₄ based electrode and other non-enzymatic glucose sensor.....	II-94
Table S5.1. Comparison of performance of some previous studies based on fluorescent sensor for glucose.....	III-119
Table S6.1. Detail of functional groups in FT-IR results of g-CNQDs/3APBA.	III-144
Table S6.2. Relative ratio of C=C, HC-O, N-C=N and N-C=O of all samples by C 1s spectra analysis.	III-145
Table S6.3. Relative ration of C-N=C (N ₁), N-(C) ₃ and HN-(C) ₂ (tertiary - N ₂), C - NH (quaternary - N ₃) of all samples by N 1s spectra analysis.....	III-145
Table S6.4. Comparison of quantum yield performance based on g-CNQDs.	III-146
Table S6.5. Comparison of performance of some previous studies based on g-C ₃ N ₄ for glucose sensor.....	III-147

NOMENCLATURES

Abbreviations

3-APBA	3-Amino Phenylboronic Acid
BET	Brunauer-Emmett-Teller Equation
CD	Galvanostatic Charge-Discharge
CV	Cyclic Voltammetry
EDS	Energy Dispersive X-ray spectra
EIS	Electrochemical Impedance Spectroscopy
FE-SEM	Field-Emission Scanning Electron Microscopy
FFT	Fast Fourier Transform
FT-IR	Fourier Transform Infrared Spectra
GCE	Glassy Carbon Electrode
GO	Graphene Oxide
GOx	Glucose Oxidase
g-C ₃ N ₄	Graphitic Carbon Nitride
g-CNQDs	Graphitic Carbon Nitride Quantum dots
HR-TEM	High Resolution Transmission Electron Microscopy
HS	Horse Serum
LOD	Limit of Detection
rGO	Reduced Graphene Oxide
RS	Rabbit Serum
TGA	Thermal Gravimetric Analysis

TMB	3,3',5,5'-Tetramethylbenzidine
PBA	Phenylboronic acid
PBS	Phosphate Buffer Solution
PL	Photoluminescence Spectra
UV-Vis	Ultraviolet – visible
XPS	X-ray Photoelectron Spectroscopy
XRD	X-ray Diffraction

Roman and Greek letters

QYs	Quantum yields (%)
Sensitivity	Sensitivity ($\mu\text{A mM}^{-1} \text{cm}^{-2}$)
S_{BET}	Specific surface area ($\text{m}^2 \text{g}^{-1}$)
λ	Wavelength (nm)

PART I - OVERVIEW OF DISSERTATION

Chapter 1. Introduction

1.1. Overview

1.1.1. Diabetes and blood glucose monitoring

Diabetes mellitus, more commonly known as diabetes, is a metabolic disease that characterized by elevated levels of blood glucose [1]. Diabetes is caused by a lack of insulin, either due to the destruction of insulin producing beta cells in the pancreas, or due to insulin resistance, a condition in which the body's muscle, fat and liver cells do not use insulin effectively. There are three types of diabetes: Type 1 diabetes, where in the body's own immune system attacks and destroys the cells in the pancreas where insulin is made, rendering the affected person unable to produce insulin naturally; Type 2 diabetes, which is a result from decrease in the body's ability to respond to insulin; and gestational diabetes, which occurs in women during pregnancy [2]. Symptoms of diabetes are excessive excretion of urine, thirst, constant hunger, weight loss, blurry vision and extreme fatigue. If left untreated diabetes can eventually damage the heart, blood, vessels, eyes, kidneys and nerves, leading to disability and premature death.

Risk of death for adults with diabetes is 50% higher than for adults without diabetes. According to the World Health Organization (WHO) and the International Diabetes Federation, there were 1.5 million deaths worldwide directly caused by diabetes in 2012. Notably, >80% diabetic patients live in low and middle-income countries [2]. As shown in **Figure 1.1**, diabetes prevalence has risen faster in low- and middle-income countries than in high-income countries. Higher-than-optimal blood glucose was responsible for an additional 2.2 million deaths as a result of increased risks of cardiovascular and other diseases, for a total of 3.7 million deaths related to blood glucose levels in 2012. Forty-three percent of all deaths attributable to high blood glucose occur prematurely, before the age of 70 years – an estimated 1.6 million deaths worldwide. Globally, high blood glucose causes about 7% of deaths among men aged 20–69 and 8% among

women aged 20–69. **Figure 1.2** shows that the percentage of premature deaths attributable to high blood glucose is higher in low- and middle-income countries than in high-income countries, and higher among men than women [3].

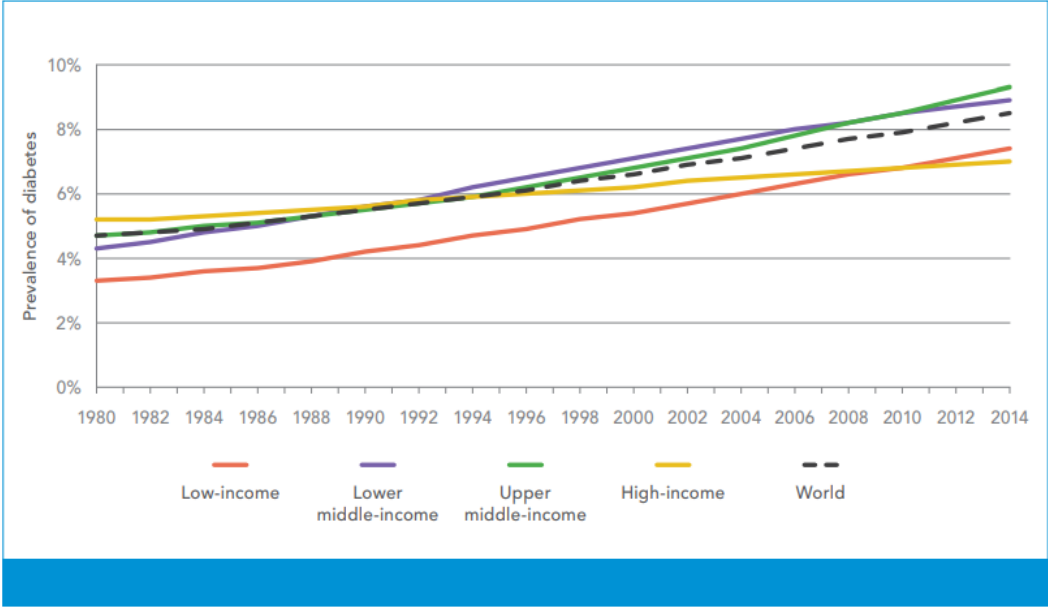


Figure 1.1. Percentage of deaths attributed to high blood glucose that occur at ages 20–69 years, by sex and country income group, 2012 (Source: Global report on diabetes, WHO).

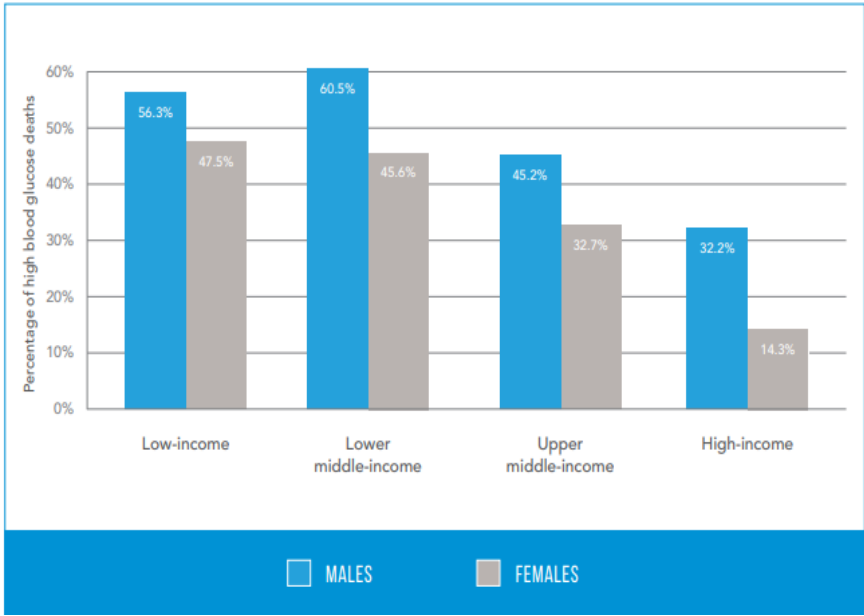


Figure 1.2. Trends in prevalence of diabetes, 1980–2014, by country income group (Source: Global report on diabetes, WHO).

Diabetes can be prevented or delayed through regular physical activity, healthy diet, and appropriate use of insulin and oral medications to lower blood sugar levels. Moreover, diabetes management also includes reducing cardiovascular disease risk factors, such as high blood pressure, high lipid levels [3]. Well-structured health services can provide the key interventions and regular follow-up necessary to help people with diabetes live long and relatively healthy lives, even though it is a chronic, progressive disease. Thus, essential technologies necessary for early detection, diagnosis and monitoring of diabetes in primary health care include weighing machines, measurement tapes, glucometers, blood glucose test strips, urine protein test strips and urine ketone test strips. However, basic technologies for early detection, diagnosis and monitoring of diabetes in primary care settings are generally not available in low-income and lower middle-income countries (**Figure 1.3**).

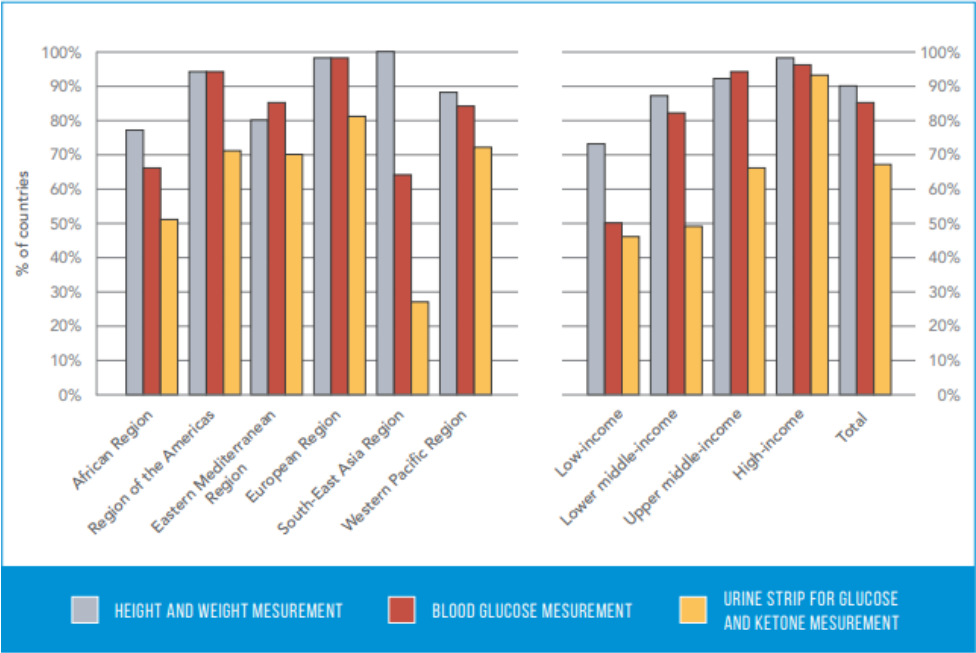


Figure 1.3. Percentage of countries reporting basic technologies generally available in publicly funded primary health-care facilities (Source: Global report on diabetes, WHO).

Figure 1.3 shows the proportion of countries reporting the general availability of height and weight measurement, blood glucose measurement, and urine strips for glucose and ketone measurement. Among low- and lower middle-income countries, only one in three (35% and 36%

of countries respectively) can report that the most basic technologies to measure height and weight, blood glucose, and urine strips for glucose and ketone measurement are generally available in primary care facilities. This lack of access to basic technologies and essential medicines stands in sharp contrast to the reported widespread availability of these items in high-income countries.

1.1.2. Glucose sensor

Despite the lack of any known cure for diabetes, we have managed to improve treatment efficiency to palliate its symptoms and diminish its complications through appropriate medication and blood sugar monitoring, to improve treatment decisions and glucose control. Therefore, glucose sensors are an attractive field of sensor and accounting for about 85% of the biosensor industry [4]. Glucose sensor systems are classified into two groups based on duration of measurement method and time: the point sample test and the continuous glucose monitor (CGM) (Table 1.1) [5].

Table 1.1. Technologies under development for glucose sensors

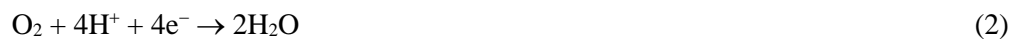
Glucose sensor	Point sample test	Urine dipstick
		Finger prick glucometer
	Continuous glucose monitor	Invasive <ul style="list-style-type: none"> • Subcutaneous amperometric electrodes • Microdialysis • Intravenous implantable devices • Micropores
		Noninvasive <ul style="list-style-type: none"> • Transdermal: reverse iontophoresis, sonophoresis, etc • Optical: fluorescence, infrared spectroscopy, Raman spectroscopy, etc

Most glucose sensors are enzyme-based, whereas others are non-enzyme-based. Non-enzymatic glucose sensors utilize metal as electrodes, these electrodes can be made from variety of element – nickel, silver, copper, etc. with different morphology [6]. The sensitivity of these system is quite good and wide linear detection range. While non-enzymatic glucose detection methods rely on the direct oxidation on the elements electrodes enzymatic glucose sensor

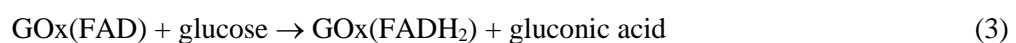
working based on the catalytic activity of enzyme such as GOx to oxidize glucose. The high selectivity and relative non-toxicity of enzyme-based electrodes has retained the focus commercially available glucose sensors on enzymatic systems. However, over the past decade the development of non-enzymatic glucose sensor has risen at a considerable rate.

1.1.2.1. Enzymatic glucose sensor

Up to now, enzymatic glucose sensors dominate the biosensing industry, especially glucose oxidase (GOx) is used as the enzyme in the most sensor owing to its high sensitivity and selectivity. The primary mechanism of enzymatic glucose sensor was introduced by Clark and Lyons in 1962 [7], in which oxygen consumption was monitored based on the catalytic oxidation of glucose in the presence of oxygen. The GOx entrapped over an oxygen electrode and then, a negative electrode potential was applied to the cathode to detect oxygen consumption as the following reactions [8,9]:



However, the various amounts of background oxygen in the sample affected the accuracy and precision of GOx-based electrode. Updike and Hicks were solved the problems which corrected for background oxygen levels by developing of the oxygen sensor and measuring current differences. Then, in 1973, the first amperometric enzyme glucose GOx-based glucose detection, in which the production of hydrogen peroxide was monitored instead of the highly variable oxygen reduction current, was suggested by Guibault and Lubrano [10]. The key component in glucose oxidation reaction is the redox center, flavin adenine dinucleotide (FAD). The biocatalytic reaction of GOx involves the reduction of the flavin group in the enzyme GOx(FAD) by reacting with glucose, thus producing the redox product of enzyme GOx(FADH₂) and gluconic acid, followed by the re-oxidation of GOx(FADH₂) by electron acceptor (Med_{ox}) to regenerate the oxidized form of the enzyme GOx(FAD) [8,11].





According to the nature of Med_{ox} , the enzymatic glucose sensors can be classified into the three following generations: the physiological mediator O_2 , the synthetic electron acceptor, and the electrode potentiostated at a potential positive of the formal potential of GOx , which are used as the Med_{ox} to regenerate $\text{GOx}(\text{FAD})$ in the first, second, and third generation glucose sensors, respectively [8]. They are also summarized in **Figure 1.4**.

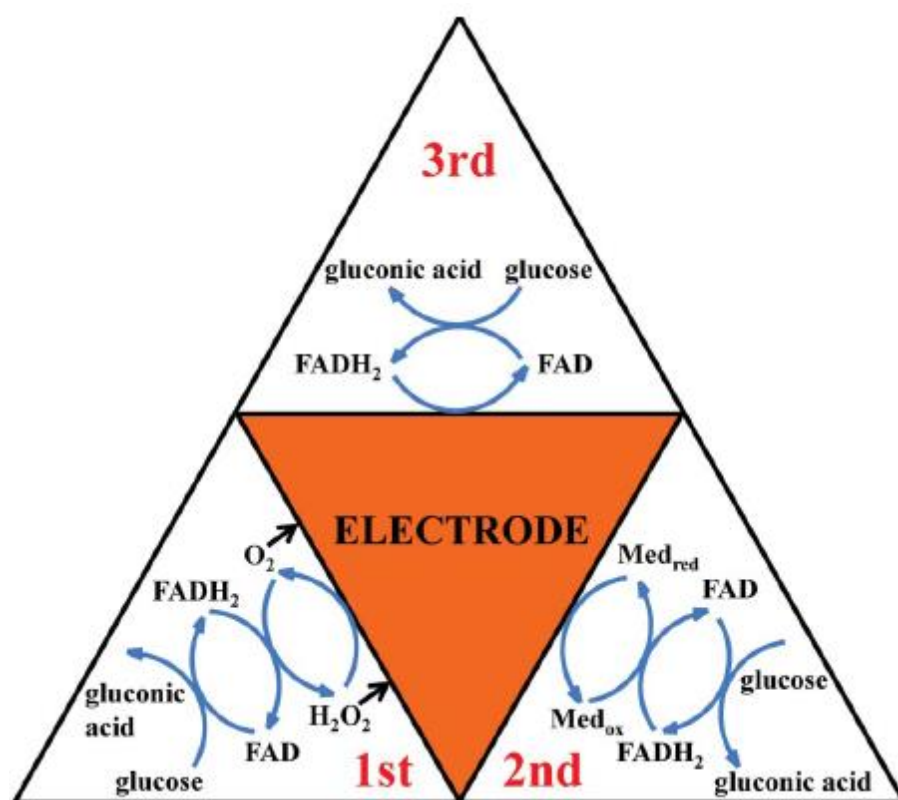


Figure 1.4. Summary of enzymatic glucose oxidation mechanisms, presented as first, second and third-generation sensors [8].

Overall, enzymatic glucose sensors remain a balance of advantages versus disadvantages of which both are significant. Despite dominating the glucose sensor industry, enzymatic systems have some drawbacks. Stability issues that surround enzymatic systems in all fields of science also hinder the development and application of enzymatic glucose sensors. Despite numerous attributes to relative stability, GOx is still constrained to pH ranges of 2-8, temperatures below 44°C , and ambient humidity levels [11]. As diabetes continues to rise in developing countries,

such as high-cost fabrication processes and short shelf-life of sensors become less viable. Even though these disadvantages, enzymatic glucose sensors remain commercially unchallenged. This is understandable given the high selectivity of the enzyme towards glucose.

1.1.2.2. Non-enzymatic glucose sensors

Due to easily affected by environment conditions, and elaborated fabrication procedures (including adsorption, cross-linking, entrapment, and electropolymerization) which are required to immobilize enzyme on a solid electrode, leading to a decrease in the activity of the enzyme [12]. Thus, the use of non-enzymatic glucose sensors potentially promises the fourth generation to analytical glucose oxidation, because of their high stability, simplicity, reproducibility and free from oxygen limitation. The non-enzymatic glucose sensor worked based on the direct electrochemistry of glucose (oxidation or reduction). Noble metals (Ag, Au, Pd, Pt, etc.), transition metals and their oxide, composite (Co, Cu, Ni, Ti, etc.) were usually chosen to develop the non-enzymatic glucose in recently research.

An “Incipient Hydrous Oxide Adatom Mediator” (IHOAM) model was proposed by Burke and the hydroxide pre-monolayer formation was demonstrated to be one of the key points for the electrocatalytic process of glucose [11]. The importance of the “active” hydroxide anions in the vicinity of the electrode surface produced by the dissociation of water (Eqn. (5)) to the electro-oxidation of glucose and many other organic molecules is well known. The oxidative adsorbed hydroxide radical expressed as MOH_{ads} is formed by the chemisorption of hydroxide anions to the reductive metal adsorption site (expressed as M as shown in Eqn. (6)) and is believed to be the catalytic component of electrocatalysts for glucose.



It can be seen that the mediate oxidation MOH_{ads} of the adsorbed species at potentials takes part in the step of glucose oxidation. The redox process of glucose at the surface is illustrated in **Figure 1.5**. As is seen in the above equations, the increased concentration of OH^-

promotes the formation of MOH_{ads} [13]. So non-enzymatic glucose sensors are dependent on pH and alkaline environment, which is the reason why a higher sensitivity of non-enzymatic glucose sensor is investigated in a higher pH environment. However, various nanomaterials supported on the graphitic carbon, which exhibited the fast electron transportation, high thermal conductivity, good biocompatibility and excellent flexibility; were developed as excellent electrocatalyst for non-enzymatic glucose sensing. As can be seen, various metal/metal oxide, and graphitic carbon nanomaterials can be utilized for non-enzymatic glucose sensing in alkaline media because of the stability and excellent catalysis of these materials or their oxides/hydroxides under high pH conditions. Therefore, the hybrid of graphitic carbon with metal/metal oxide can solve the problems that exist in the direct oxidation of glucose on a conventional metal as electrode [8,12].

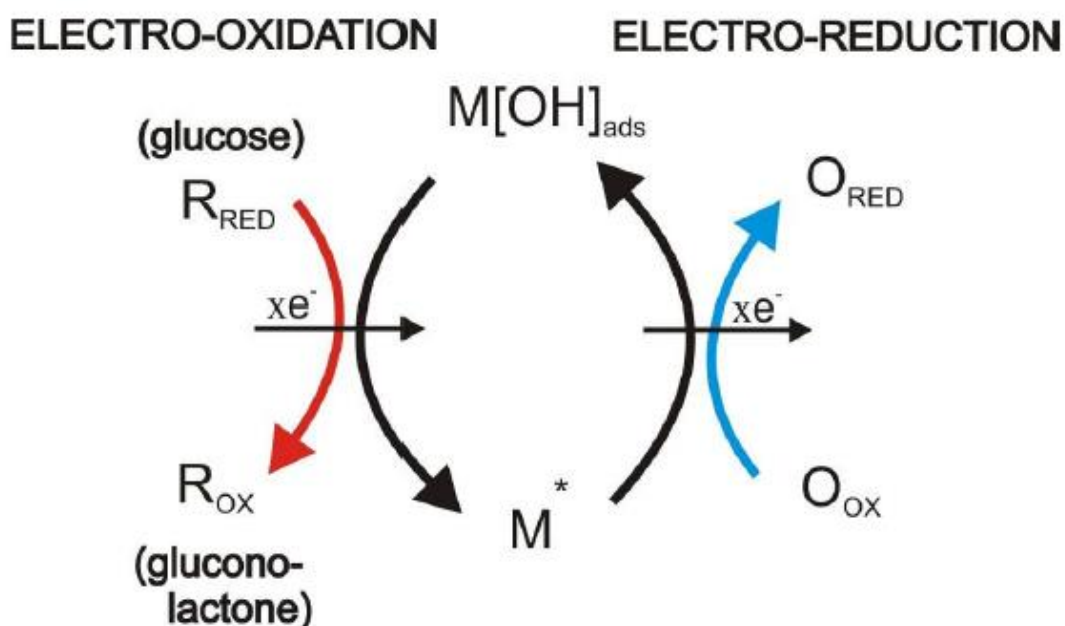


Figure 1.5. A schematic illustration of the IHOAM model in which M^* is the reductive metal adsorption site, and MOH_{ads} is the oxidative adsorbed hydroxide radical. The scheme shows how both oxidative and reductive processes are catalysts at the metal surface [11].

Nowadays, numerous efforts have been made on the development of enzyme-less or enzyme-free glucose sensors involving nanostructured electrodes to oxidize glucose directly on the surface. However, chloride fouling following a long detection period remains problematic. Another alternative method for enzyme-free glucose sensors is synthetic boronic acid-based

receptors. The probe technology can employ fluorescence, fluorescence lifetime, colorimetric, or polarization-based method.

1.1.3. Motivation

As stated above, diabetes prevalence has been rising more rapidly in middle- and low-income countries. It represents that the lack of resources in infrastructure and trained personnel of these regions. This has motivated a demand for low-cost, high sensitivity, reliable and easy-to-use platforms for the monitoring and diagnosis, in order to provide the results even in the most limited facilities. With a regard to contributing to developing the glucose sensor technologies, our research investigates involving nanostructure materials based on modification of graphitic carbon structure to provide rapid and accurate measurements of glucose.

1.1.4. Research objectives

The overall goal of the research is to improve the sensitivity as well as selectivity towards glucose of graphitic carbon-based composite electrocatalyst and quantum dots fluorescence. The graphitic carbon was first chosen based on the following points:

- (i) High electronic surface area than bulk metal/metal oxide based on electrodes,
- (ii) Improve the electron transfer kinetics with other materials,
- (iii) High catalytic activity,
- (iv) Chemical stability.

This research is focused on the fabrication of metal/metal oxide-decorated/graphitic carbon (reduced graphene oxide or graphitic carbon nitride) composite based on non-enzymatic electrochemical glucose sensor and boronic acid/graphitic carbon nitride quantum dots (g-CNQDs) based on fluorescence sensor. Each type of glucose sensor exhibits some advantages to overcome the natural disadvantage of metal/metal oxide/reduced graphene oxide or graphitic carbon nitride, and boronic acid/g-CNQDs, thus contribute to enhancing the sensitivity toward glucose.

1.2. Outline of dissertation

This study is focused on the development of graphitic carbon-based sensing material and their application in glucose sensor. The structure of this dissertation contains three main parts as following:

❖ *Part I. Overview of dissertation*

Chapter 1 presents diabetes affection for human life, the classification of a glucose sensor, followed by the introduction of basic mechanism of enzyme and non-enzyme glucose sensor. The objectives and overview of the dissertation are presented. The next part in this chapter gives an introduction of graphitic carbon including graphene oxide and graphitic carbon nitride, metal/metal oxide and their role in the electrochemical reaction. It also gives a brief introduction of boronic acid, composing with graphitic carbon nitride, which is promising candidate in fluorescence glucose sensor. Here also present drawbacks of this material and review some methods to overcome those disadvantages.

❖ *Part II. Enhancement graphitic carbon material by decorating metal/metal oxide-based on non-enzymatic electrochemical sensor*

Chapter 2 gives an introduction of reduced graphene oxide, nickel oxide, silver and their role in the electrochemical reactions. Since nickel oxide has some drawbacks as low electrical conductivity and surface area, there are many attempts have been made by creating a nanostructured to improve the glucose sensitivity without enzymes through the synergistic effects of each component.

Chapter 3 studied of nickel manganese oxide/ reduced graphene oxide composites with porous hydrogel structure, the synergistic effect of nickel manganese with reduced graphene oxide. Nickel manganese oxide plays a role as an electrocatalytic in the glucose oxidation reaction; whereas reduced graphene oxide promotes the charges transfer in reactions.

Chapter 4 is a study of enhancement sensitivity by incorporation between nickel oxide and graphitic carbon nitride. The interesting point in this research is the reduced graphene oxide

replaced by graphitic carbon nitride due to its unique electronic and electrical properties, that improves the charge transfer in the electrochemical reaction, which confirms via sensitivity towards glucose.

❖ *Part III. Glucose-sensitive fluorescence sensor based on graphitic carbon nitride quantum dots*

Chapter 5 gives an introduction of graphitic carbon nitride, boronic acid functional group are used for fluorescent sensor. With the excellent properties, this study reported a highly selective and sensitive glucose sensor by using graphitic carbon nitride as a fluorescent and boronic acid as a quencher and receptor during glucose sensing.

Chapter 6 focus on the improved sensor from the study in Chapter 5 based on graphitic carbon nitride and derivative of boronic acid. By introducing properly designed chemical bonding to this structure, more chemical can be detected by the “on-off-on” mechanism. This research reports an effective fluorescence “on-off-on” sensor for the determination of glucose and propylene glycol-based on the reversible covalent bonds of boronic acid with 1,2-diols groups.

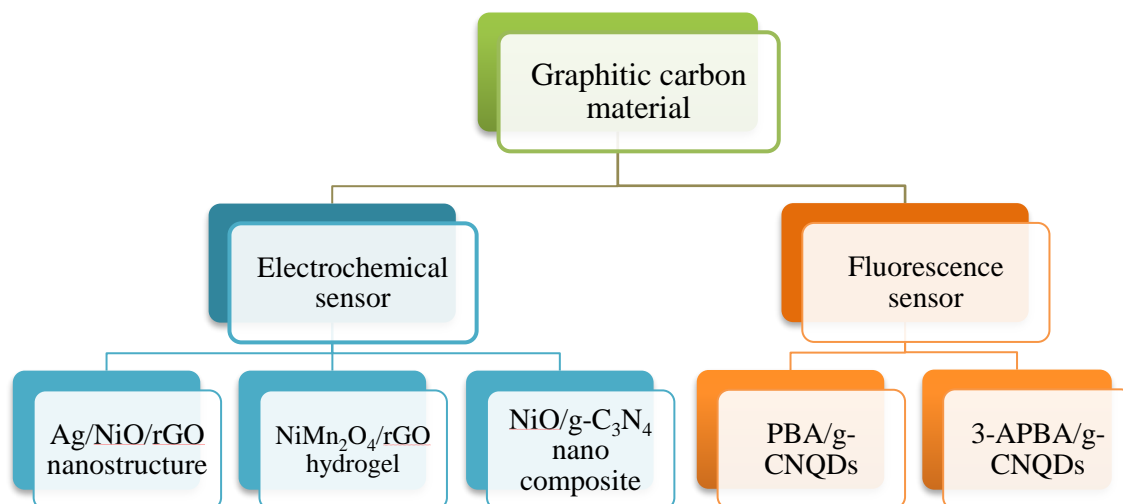


Figure 1.6. The main structure of dissertation.

1.3. Introduction of materials

1.3.1. Graphitic carbon materials – layered structure

1.3.1.1. Graphene oxide and reduced graphene oxide

Graphene, discovered in 2004, is a rising star in the field of material science. Graphene, one of the allotropes (carbon nanotube, fullerene, diamond) of elemental carbon, is a planar monolayer with a two-dimension (2D) sp^2 -bonded carbon atoms (**Figure 1.7**). Graphene has demonstrated a variety of intriguing properties including high electron mobility at room temperature ($250,000 \text{ cm}^2 \text{ V}^{-1} \text{ s}^{-1}$) exceptional thermal conductivity ($5000 \text{ Wm}^{-1} \text{ K}^{-1}$) and superior mechanical properties with Young's modulus of 1 TPa [14,15]. With extraordinary physical and chemical properties, graphene has ignited extensive research in nanoelectronics, supercapacitors, fuel-cells, batteries, sensing, catalysis, etc. [14,16].

Until 2008, Dai's group overcome the issue of aggregation of graphene by using oxidized formed – graphene oxide (GO). In comparison to other carbon-based materials such as carbon nanotube (CNT), fullerene, nanoribbons, GO exhibits some merits like “low cost of productions, extremely large surface area for efficient drug binding and lesser toxic metallic impurities from fabrication process” [17]. Several large-scale processing methods have been involved for different graphene-based materials through either graphitic top-down or molecular carbon precursor bottom-up approaches, as summarized in **Figure 1.8** [16]. On a relatively large scale, graphene is mostly obtained from graphite precursors through subsequent dispersion and oxidation– exfoliation–reduction in water or suitable organic solvents, i.e. in the form of GO as schematically shown in **Figure 1.8**. Moreover, GO can be easily reduced to remove oxygen containing groups to graphene-like sheets form, named reduced graphene oxide (rGO). In the case of nanocomposite this study, GO and rGO were prepared by modified Hummers method are mostly due to their low cost, easy synthesis, and high performance [18,19]. The GO structure contains abundant oxygen-rich functional groups; hydroxyl and epoxy groups on the basal plane

and carbonyl and carboxyl groups on edges of the graphene sheets. Thus, GO and rGO have been widely used as based material for nanocomposites and supported materials for real applications.

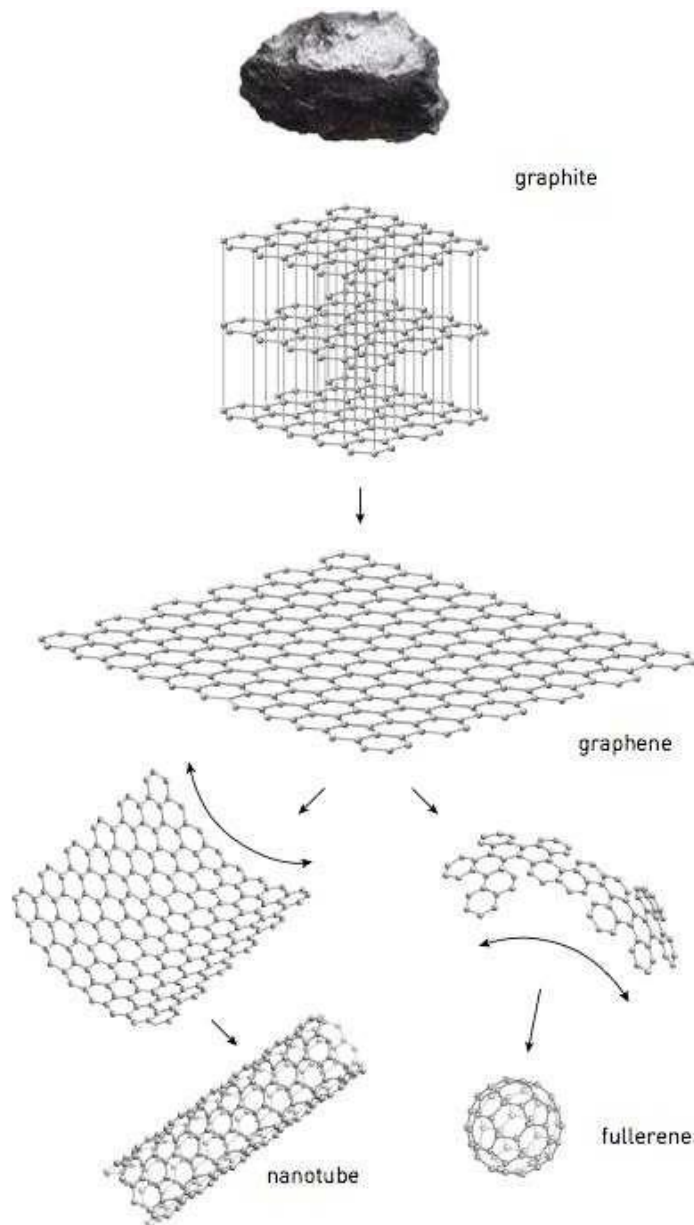
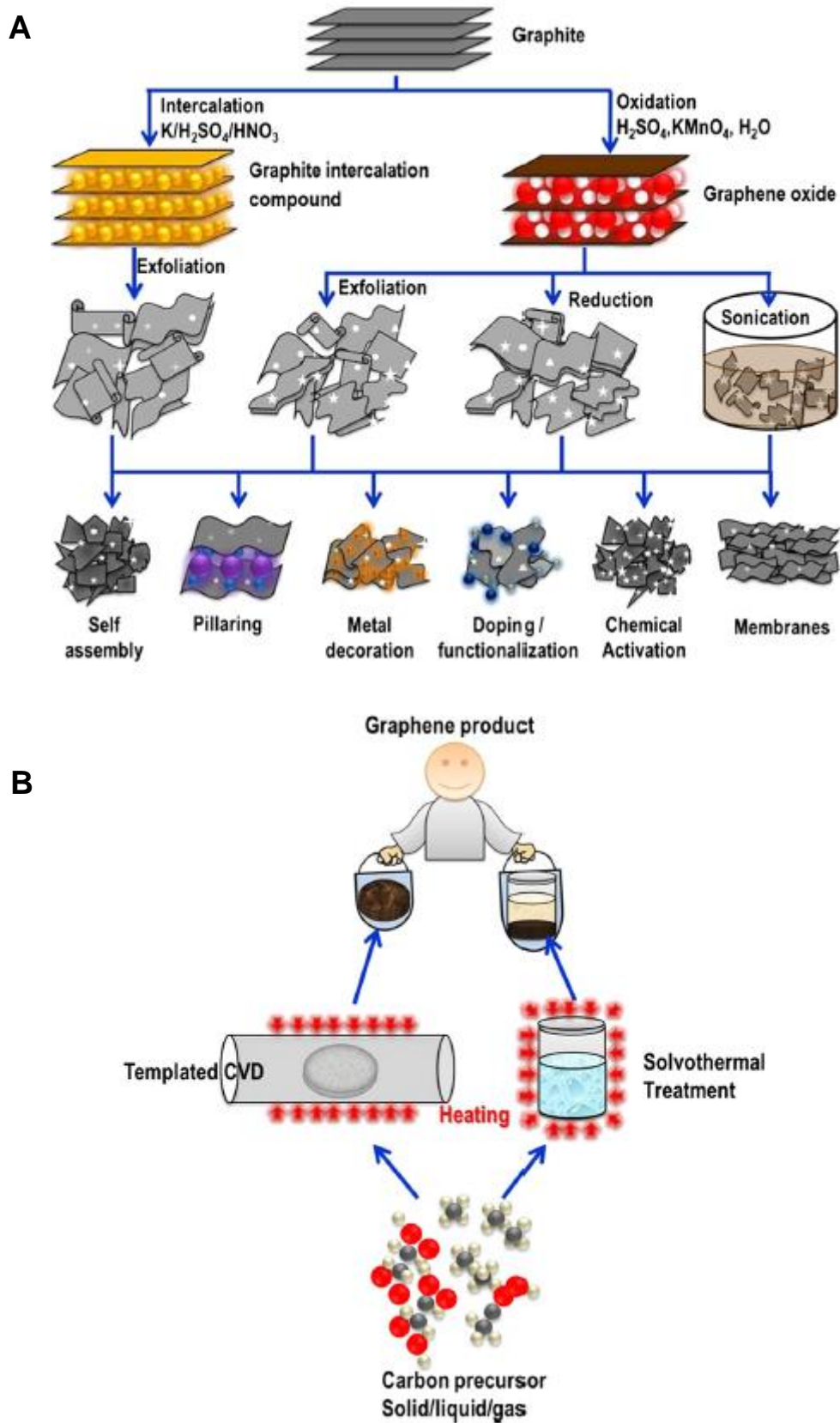


Figure 1.7. Graphene from graphite: Graphite is a basic material found in nature. When taken apart graphite sheets become graphene. A rolled-up layer of graphene forms a carbon nanotube, folded up it becomes a small football, fullerene. Hidden inside graphite, graphene was waiting to be discovered (Source: Nobel Foundation. "Nobel Prize in Physics 2010 for graphene -- 'two-dimensional' material." ScienceDaily. ScienceDaily, 5 October 2010).



1.3.1.2. Graphitic carbon nitride $g\text{-C}_3\text{N}_4$

Graphitic carbon nitride ($g\text{-C}_3\text{N}_4$) is not only the most stable allotrope of carbon nitrides and metal-free polymeric semiconductors; but it also has excellent properties such as low toxicity, excellent biocompatibility, eco-friendly, great photostability, and distinct optical features that are attractive for many applications due to the presence of basic surface sites [20]. $g\text{-C}_3\text{N}_4$ has a two-dimensional structure and exhibits a highly π -conjugated electronic structure due to the rigorous C-N plane along with the separate layers. In addition, $g\text{-C}_3\text{N}_4$ is abundant and easily prepared via one-step polymerization of cheap feedstocks like cyanamide, urea, thiourea, melamine, and dicyandiamide. Thus, the structure of $g\text{-C}_3\text{N}_4$ was found that the basic tectonic units to establish a single layer allotrope of $g\text{-C}_3\text{N}_4$ are triazine (C_3N_3) and tri-s-triazine/heptazine (C_6N_7) rings, as shown in **Figure 1.9**. However, the tri-s-triazine is generally recognized as the building block for the typical formation of $g\text{-C}_3\text{N}_4$ due to its superior stability [21-24].

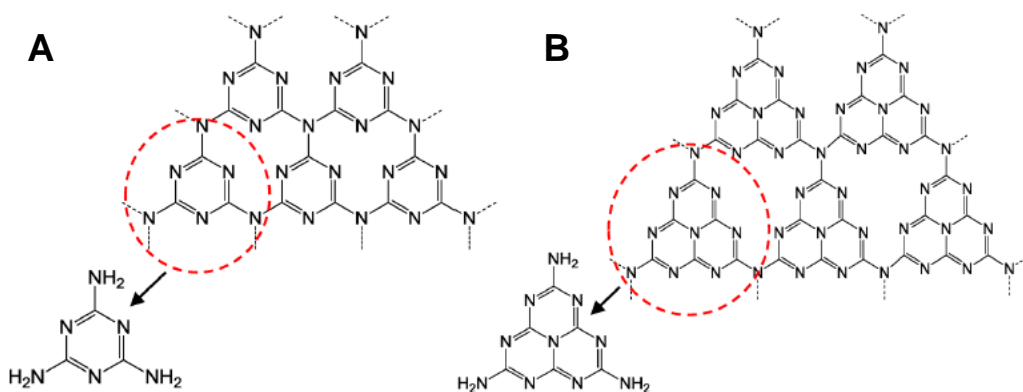


Figure 1.9. (A) Triazine and (B) tri-s-triazine (heptazine) structures of $g\text{-C}_3\text{N}_4$.

Recently, nanoscale $g\text{-C}_3\text{N}_4$, such as $g\text{-C}_3\text{N}_4$ nanocomposite, fluorescent $g\text{-C}_3\text{N}_4$ nanosheets ($g\text{-CNNS}$) and $g\text{-C}_3\text{N}_4$ quantum dots ($g\text{-CNQDs}$) have been assessed for various applications such as biosensor [25], photocatalysts [24], water splitting [26], bioimaging and drug delivery [27], and oxygen reduction [28]. The $g\text{-C}_3\text{N}_4$ has a unique two-dimensional layered structure, thus, which is favorable for hybridizing with other components. Among these approaches, the formation of heterostructures demonstrates a great potential to promote the electrocatalytic performance of $g\text{-C}_3\text{N}_4$ because the electron-hole pairs can be efficiently separated, and charge carriers could transfer across the interface

of the heterostructure to restrain the recombination [29]. On the other hand, it has many studies to fabricate g-CNQDs, which exhibits improved quantum yield and sensitivity for specific target materials, such as glucose [30].

1.3.1.3. Boronic acid groups

The boronic acid moiety represents an ideal recognition element for the determination of saccharides. Boronic acids have been known for over 100 years, but the interaction between boronic acids and diols first being reported in 1959 [31]. Then, boronic acid and various derivatives containing boronic acid functional group are used widely fluorescent biosensors to detect glucose based on the fluorescence, UV absorption, and surface plasmon resonance [32]. Boronic acids react with 1,2-diols or 1,3-diols in aqueous solution to create five- or six-membered cyclic esters via reversible covalent interactions in aqueous media [33,34]. The rigid cis-diols found in many saccharides generally form stronger complexes than acyclic diols like ethylene glycol and trans-diols. Boronic acids act as weak Lewis acids. Consequently, they are capable of reacting with water to turn from the neutral trigonal form into the anionic tetrahedral form. This is also true for the respective boronic acid complexes and the boronate esters. The binding process of phenylboronic acids with diols is illustrated in **Figure 1.10**. The formation of a cyclic boronate ester via interaction with a diol intensifies the electrophilicity of the boronic acid group and thereby reduces its pKa value (from approximately 9 to about 6). Hence, at pH values between 6.5 and 8.5, the boronic acid exists in its trigonal form, but in the presence of a saccharide, it passes into its tetrahedral anionic form. When attached to a fluorescent, this changes the characteristic features of fluorescent emission. This can induce changes in intensity, decay time and polarization. For these reasons, the boronic acid group provides an ideal tool for the development of reversibly acting molecular probes for saccharides [33].

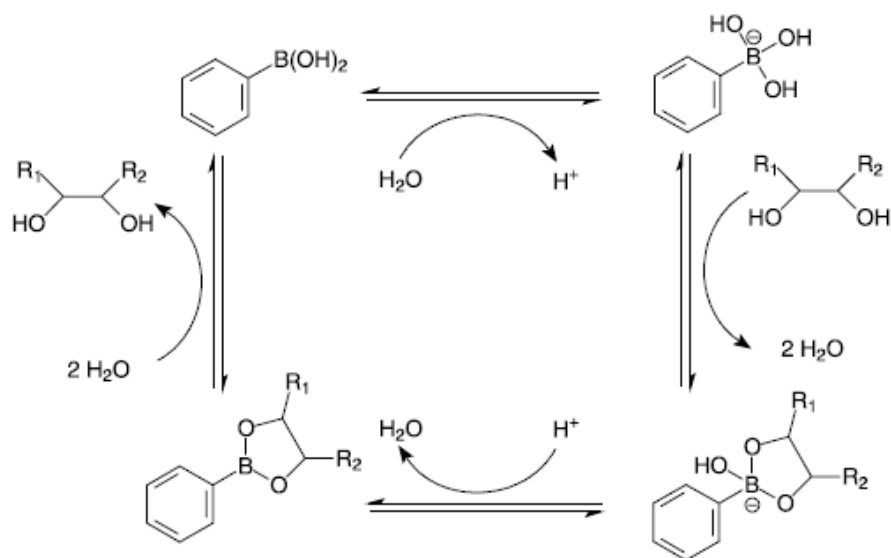
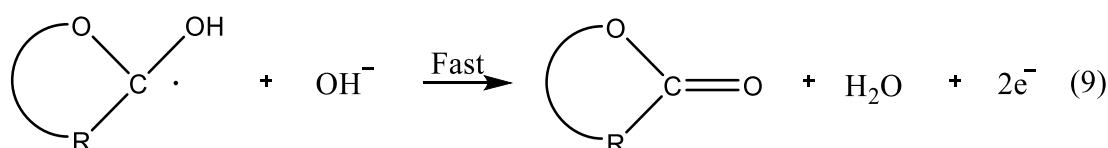


Figure 1.10. The binding process between phenylboronic acid and diol.

1.3.2. Nickel Oxide

Among the various cost-effective metal oxides, nickel oxide (NiO) is used widely in many applications, including supercapacitors, gas sensors, biosensors, lithium batteries, and catalysts, owing to its unique optical, electrical, and electrocatalytic properties. Fleishmann et al. [35] reported a thorough investigation into the behavior of a nickel-based anode electrode on the electrochemical reaction of organic materials, including glucose. In agreement with a number of other works [11], the catalytic component is a Ni(III) oxyhydroxide species, the oxidized partner to the Ni(OH)₂/NiOOH redox couple. The surface bound change of the nickel oxidation state and mechanism for the oxidation of glucose at nickel electrode in alkaline, may be represented by the equations:



Immersion of NiO-based electrode into an alkaline electrolyte, leading to the formation of nickel oxyhydroxide by electrooxidation. As presented in Eqn. (7), NiO is oxidized to catalytically active NiOOH, then, glucose oxidation immediately after the formation of the Ni(III) species at the surface to form a radical intermediate and reforming the Ni(OH)₂ species (Eqn. (8)) which in turn reacts with active hydroxyl radicals in the NiOOH surface. The reaction product of electrooxidation with the Ni(III) catalyst is gluconolactone and subsequently gluconic acid.

Although NiO has attracted attention for non-enzymatic glucose sensors owing to high its high electrocatalytic activity, electron transfer capability, and good biocompatibility. However, they still have some drawbacks that currently prevent their application of glucose sensors such as low electrical conductivity and specific surface area. Thus far, different morphologies of NiO has been demonstrated using a range or preparation methods and their morphology-dependent properties have also been widely studied [36-38]. On the other hand, the low conductivity and sensitivity of the pristine NiO electrode should be solved before NiO can be used as an electrode material for glucose detection. In this regard, a hybrid of NiO with highly conductive materials can lead to improve electrical and electrochemical properties.

PART II - ENHANCEMENT GRAPHITIC CARBON MATERIAL BY DECORATING METAL/METAL OXIDE- BASED ON NON-ENZYMATIC ELECTROCHEMICAL SENSOR

Chapter 2. Multi-Dimensional Ag/NiO/Reduced Graphene Oxide Nanostructures for a Highly Sensitive Non-Enzymatic Glucose Sensor

2.1. Introduction

Many studies have focused on the development of effective glucose sensor technologies since the invention of the first glucose enzyme electrodes by Clark and Lyons [7]. Enzymatic sensors based on immobilized glucose oxidase (GOx) are used widely for glucose detection owing to their excellent sensitivity and selectivity over interference materials, such as ascorbic acid and uric acid. On the other hand, there are many problems induced by biomaterials, such as poor stability, high cost of enzymes, and weakness to environmental conditions, including pH, temperature, humidity, and the interferences caused by other substances [39,40]. To solve these problems, non-enzymatic electrodes have been explored widely, which allows glucose to be oxidized directly on the electrode surface without enzymes. Recent studies have shown that electrodes modified with noble metals (Ag, Pt, Au) [41,42], metal alloys (Pt, Au, Ir, Pd, Cu, and Co) [43,44], transition metals (Ni, Pd) [45,46] and metal oxides can be used effectively to detect glucose in the absence of GOx.

Among the various cost-effective metal oxides, nickel oxide (NiO) is used widely in many applications, including supercapacitor [47], gas sensors [48], biosensor [49], lithium batteries [50] and catalysts [51], owing to its unique optical, electrical, and electrocatalytic properties. Although NiO has attracted attention for non-enzymatic glucose sensors owing to its high electrocatalytic activity, electron transfer capability, and good biocompatibility, its low

glucose sensitivity due to the low electrical conductivity and surface area should be solved. To overcome these drawbacks, many attempts have been made to enhance the glucose sensitivity by creating a range of nanostructured [37,52,53]. Therefore, the design of a hybrid system composed of multi-components with the multi-dimensional structures can be a promising strategy because the final properties can be improved dramatically by the synergistic effects of each component.

This paper reports a non-enzymatic glucose sensor that shows the highest glucose sensitivity ever reported, as well as excellent selectivity and stability by hybridizing 0-dimensional (0D) silver (Ag) nanoparticles, 2D reduced graphene oxides (rGO), and 3D NiO nanoflower structures fabricated by a simple hydrothermal synthesis. Ag nanoparticles can increase the electrocatalytic activity by enhancing charge separation during the electro-oxidation/reduction reactions [54] with less poisoning by the chemisorbed intermediates generated by the electrooxidation of glucose compared to other metals. In addition, rGO can enhance the glucose sensitivity by increasing the surface area and electrical conductivity, enhancing glucose adsorption and charge transfer, and providing numerous anchoring and dispersion sites for metal and metal oxide nanostructures because it has abundant functional groups and restored electron pathways after reduction.

2.2. Experimental details

2.2.1. Materials

Nickel(II) nitrate hexahydrate ($\text{NiNO}_3 \cdot 6\text{H}_2\text{O}$), ammonium hydroxide (NH_4OH), silver nitrate (AgNO_3), potassium permanganate (KMnO_4), hydrogen peroxide (H_2O_2) (30 wt. %), sulfuric acid 98% (H_2SO_4), sodium hydroxide (NaOH), ethanol ($\text{C}_2\text{H}_5\text{OH}$), polyvinylpyrrolidone (PVP, $\text{C}_6\text{H}_9\text{NO}$)_n, nafion, isopropanol (IPA), D-(+)-glucose, D-fructose, lactose, sucrose, ascorbic acid (AA), uric acid (UA), dopamine (DA), horse serum (HS), and rabbit serum (RS) were purchased from Sigma-Aldrich Co. (USA). Expandable graphite powder was obtained from Asbury Graphite Mills Inc. (USA). All chemicals were used as received. Deionized (DI) water was used to wash the samples in all experiments.

2.2.2. Preparation of Ag/NiO/rGO

A GO suspension was prepared by the oxidation of expanded graphite powder by a modified Hummer's method, as described elsewhere [55]. To fabricate Ag/NiO/rGO, 0.1 mmol of $\text{NiNO}_3 \cdot 6\text{H}_2\text{O}$ and a pre-calculated amount of AgNO_3 was added to 10 mL of DI water and stirred at room temperature. A 1 mL sample of NH_4OH and 5 mg of PVP was introduced to the mixture and stirred continuously for 1 h. The mixed solution was then added to 5 mL of an aqueous GO slurry with a 5 mg/mL solid content. Various amounts of AgNO_3 were tested, as described in **Figures S2.1-2** (Supporting Information), and the optimal amount was found to be 5% AgNO_3 (mole percentage to NiO). The various volume ratios between Ag/NiO and GO were also tested, as shown in **Figure S2.3** (Supporting Information), and the optimal ratio was found to be 1:1. The samples were transferred to a Teflon-lined stainless steel autoclave, heated to 140 °C and maintained at that temperature for 12 h to build a network structure of GO. The optimal hydrothermal temperature was selected after testing over a wide range of temperatures, as shown in the **Figure S4** (Supporting Information). After the autoclave was cooled slowly to room temperature, the obtained samples were submerged with deionized water (DI) to eliminate all the unreacted chemicals followed by freeze drying at -37 °C for 2 days to remove the water without destroying the networks. Finally, the Ag/NiO/rGO was calcined at 400 °C for 3 h in flowing nitrogen to convert $\text{Ni}(\text{OH})_2$ to NiO and obtain the multi-dimensional hybrid structure with enhanced electrical conductivity by the reduction of GO to rGO.

The samples prepared in this study were labeled $x\text{Ag/NiO/rGO}$ and $y:z\text{Ag/NiO/rGO}$, where x indicates the percentage moles of Ag at a fixed volume ratio of Ag/NiO and rGO solutions, and y:z is the volume ratio of the Ag/NiO and rGO solutions at a fixed Ag content. **Figure 2.1** presents a detailed schematic of the preparation steps of Ag/NiO/rGO.

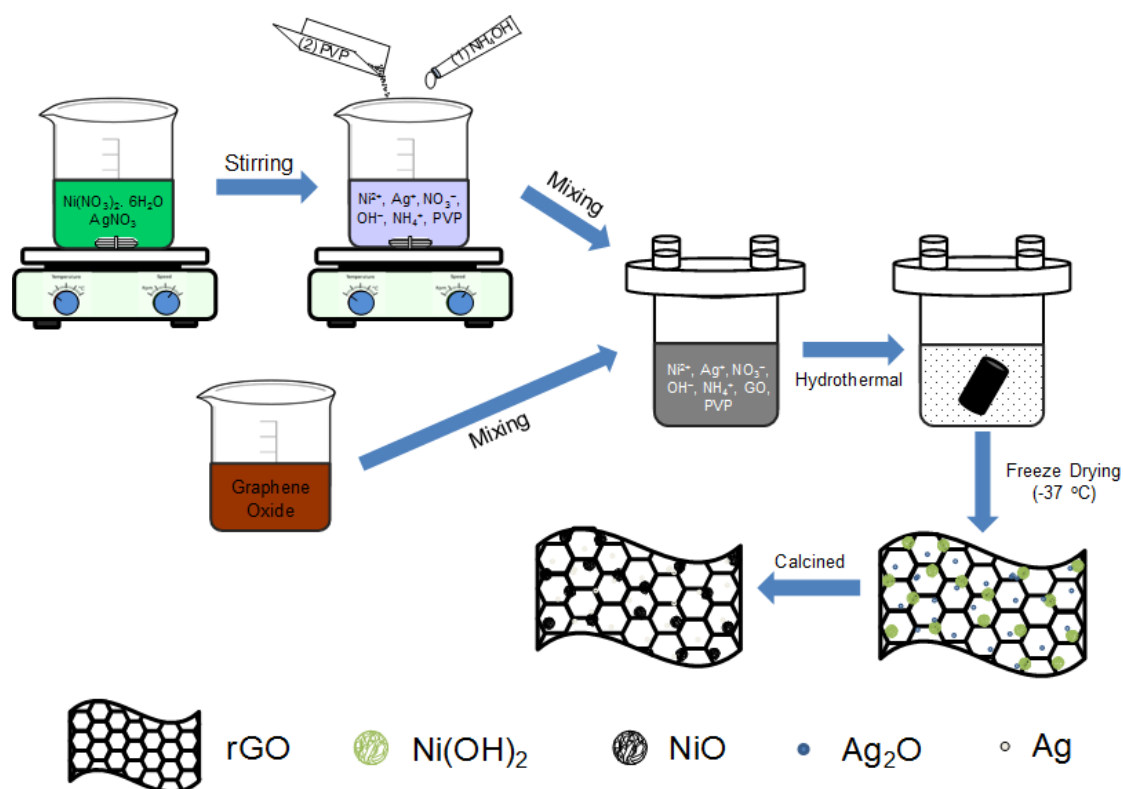


Figure 2.1. Schematic diagram of the fabrication steps of Ag/NiO/rGO.

2.2.3. Preparation of Ag/NiO/rGO modified electrodes

Before loading the Ag/NiO/rGOs, a glassy carbon electrode (GCE, 3 mm of diameter) was polished sequentially with 0.05 μm alumina slurries and 1 μm diamond slurries, then rinsed with DI water. The electrode was then sonicated, washed with ethanol and DI, and dried with nitrogen. To produce a slurry, 10 mg of Ag/NiO/rGO was mixed with 0.5 mL of a 5 wt.% nafion solution in isopropanol (IPA). Finally, 10 μL of the prepared solution was coated on a GCE and dried at room temperature by lightly blowing with a N_2 gun (**Figure 2.2**).

2.2.4. Instrumental analysis

Raman spectroscopy (Thermo Fisher Scientific, USA) was performed using a Raman microscope with an incident laser light with a wavelength of 532 nm. The oxidation state and elemental composition of the samples were examined by X-ray photoelectron spectroscopy (XPS, K-Alpha, Thermo Fisher Scientific ESCALAB 250Xi, USA) using an $\text{Al K}\alpha$ X-ray source

(1486.6 eV). In addition, the morphology was visualized by high-resolution transmission electron microscopy (HR-TEM, JEOL JEM-2100F, USA), field-emission scanning electron microscopy (FE-SEM, JEOL JSM-7600F, Japan). An energy dispersive X-ray spectrometer (EDS) connected to the SEM was used to determine the X-ray mapping images of the elements with a working voltage of 20 kV. The specific surface area was measured using a surface area and porosity analyzer (Micromeritics, ASAP 2020, USA) with the calculations performed using the Brunauer-Emmett-Teller (BET) equation.

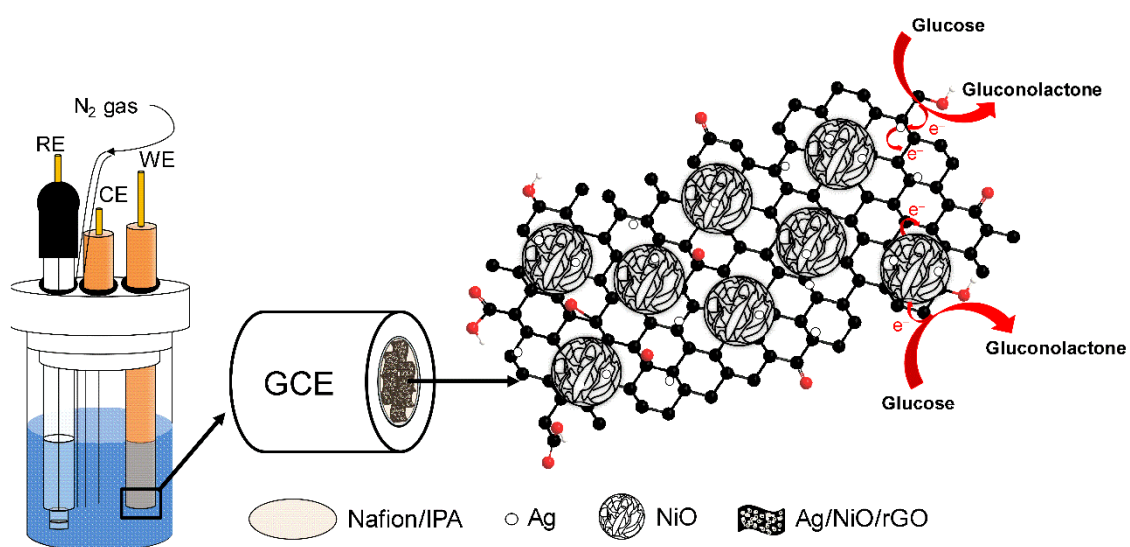


Figure 2.2. Schematic diagram of electrochemical measurement systems and reactions on the electrode surface.

2.3. Results and Discussion

2.3.1. Characterization of Ag/NiO/rGO

As shown in **Figure 2.3(A)**, the XPS survey spectra of both pure GO and 5Ag/NiO/rGO exhibited two sharp peaks of 530.07 eV and 284.71 eV, which can be attributed to O 1s and C 1s, respectively. In the 5Ag/NiO/rGO, more peaks were observed, which are associated with Ni²⁺ (Ni 2p) and Ag⁰ (Ag 3d), indicating the presence of NiO and metallic Ag in the sample. As shown in the high resolution XPS (**Figure 2.3(B)**), the Ni 2p spectrum of 5Ag/NiO/rGO revealed two strong peaks at approximately 854.05 eV and 872 eV, which can be attributed to the Ni 2p_{3/2} and

Ni $2p_{1/2}$ spin-orbit of NiO, respectively [55]. The Ag $3d_{5/2}$ and Ag $3d_{3/2}$ peaks of metallic Ag were also observed at approximately 368 eV and 374 eV, respectively (Figure 2.3(C)) [56].

As shown in Figure 2.3(D), in contrast to C 1s of pristine GO (inset), the C 1s peaks for 5Ag/NiO/rGO exhibited a reduced intensity at 285.51, 286.20, and 288.05 eV, which were assigned to C-O (epoxy and alkoxy), C=O (carbonyl group), and O-C=O (carboxyl group), respectively, and an increased intensity at 284.36 eV, which corresponds to C=C (sp^2 carbon) in aromatic rings, which clearly indicates the reduction of functional groups and restoration of the sp^2 networks after the hydrothermal and thermal process during 5Ag/NiO/rGO preparation.

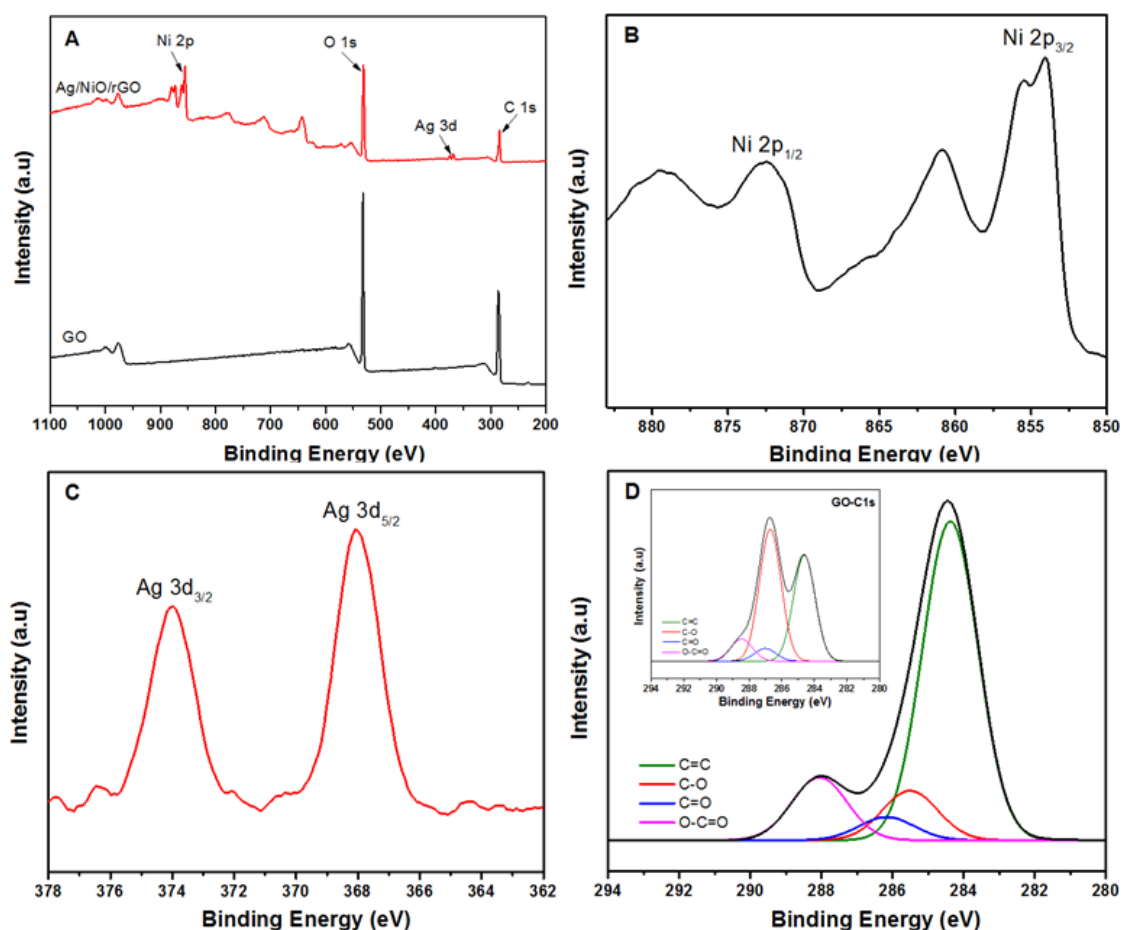


Figure 2.3. XPS spectrum of 5Ag/NiO/rGO (A) survey spectra with pure GO, (B) Ni 2p, (C) Ag 3d, (D) C 1s and C 1s of GO (inset).

To verify the heterostructure of the samples, the Raman spectra were obtained, as shown in Figure 2.4. In pristine GO, the G-band and D-band at $\sim 1605\text{ cm}^{-1}$ and $\sim 1353\text{ cm}^{-1}$ were

observed, which can be assigned to the bond stretching of all pairs of C sp^2 atoms in-plane (E_{2g} -vibration mode) and the breathing mode of k-point photons with A_{1g} symmetry [57,58]. The intensity of the ratio between the D and G band (I_D/I_G) for the Ag/NiO/rGO (1.017) increased significantly compared to those of pristine GO (0.884) and rGO (0.965), which indicates a reduction of the functional groups and restoration of the graphitic domains. Moreover, the G-band of Ag/NiO/rGO (1601 cm^{-1}) shifts approximately 4 cm^{-1} to a lower frequency than that of pristine GO (1605 cm^{-1}), which also indicates the reduction of GO to rGO. Note that Ag/NiO/rGO exhibited new broad peaks centered at $\sim 546\text{ cm}^{-1}$ and $\sim 1090\text{ cm}^{-1}$, which were assigned to the oscillation of Ni–O [55], and a sharp peak at $\sim 1001\text{ cm}^{-1}$, which corresponds to the vibration modes of Ag nanoparticles, respectively [59].

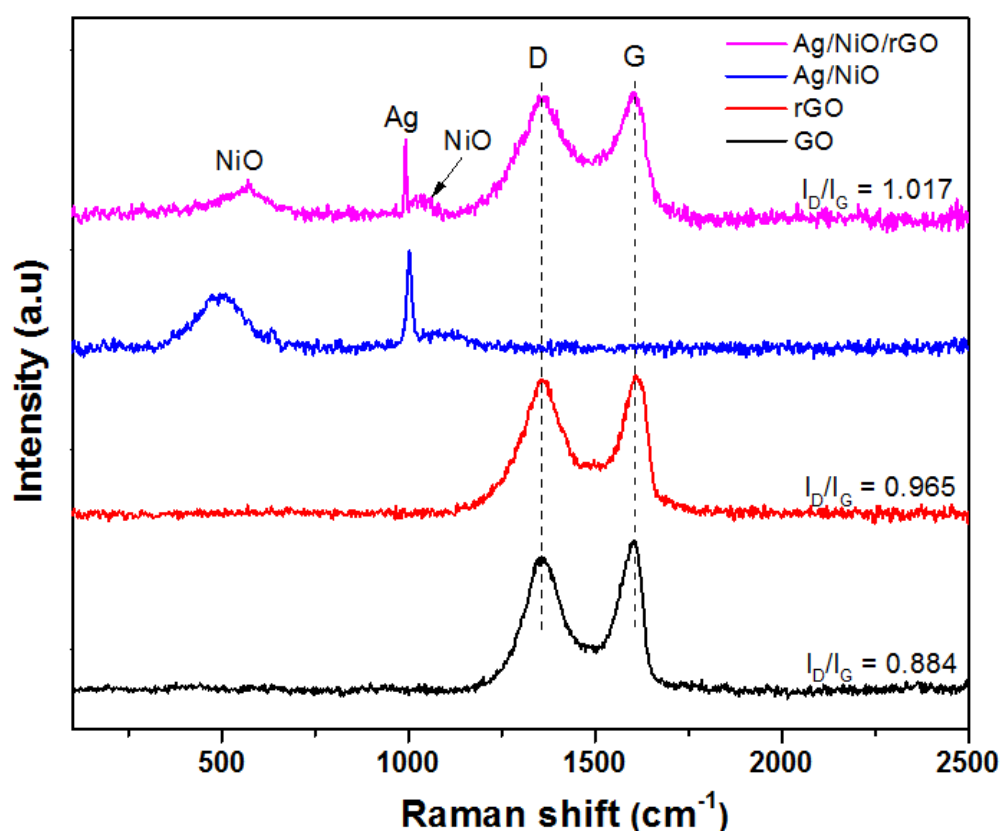


Figure 2.4. Raman spectra of GO, pure rGO, Ag/NiO, and 5Ag/NiO/rGO.

The Raman spectra of Ag/NiO/rGO at various Ag loadings (0%, 5%, 10%, 15% and 20%) are shown in **Figure S2.5(A)** (Supporting Information). The intensity of the peak at $\sim 1000\text{ cm}^{-1}$,

which was assigned to the vibration of Ag, increased with increasing Ag content. In addition, as the ratio between of Ag/NiO and GO was increased from 1:3 to 3:1, the intensity of the absorption peaks related to both Ag and NiO increased accordingly (**Figure S2.5(B)** – Supporting Information). No noticeable change in I_D/I_G among the various ratios was observed, which indicates the reduction of GO to rGO under all conditions.

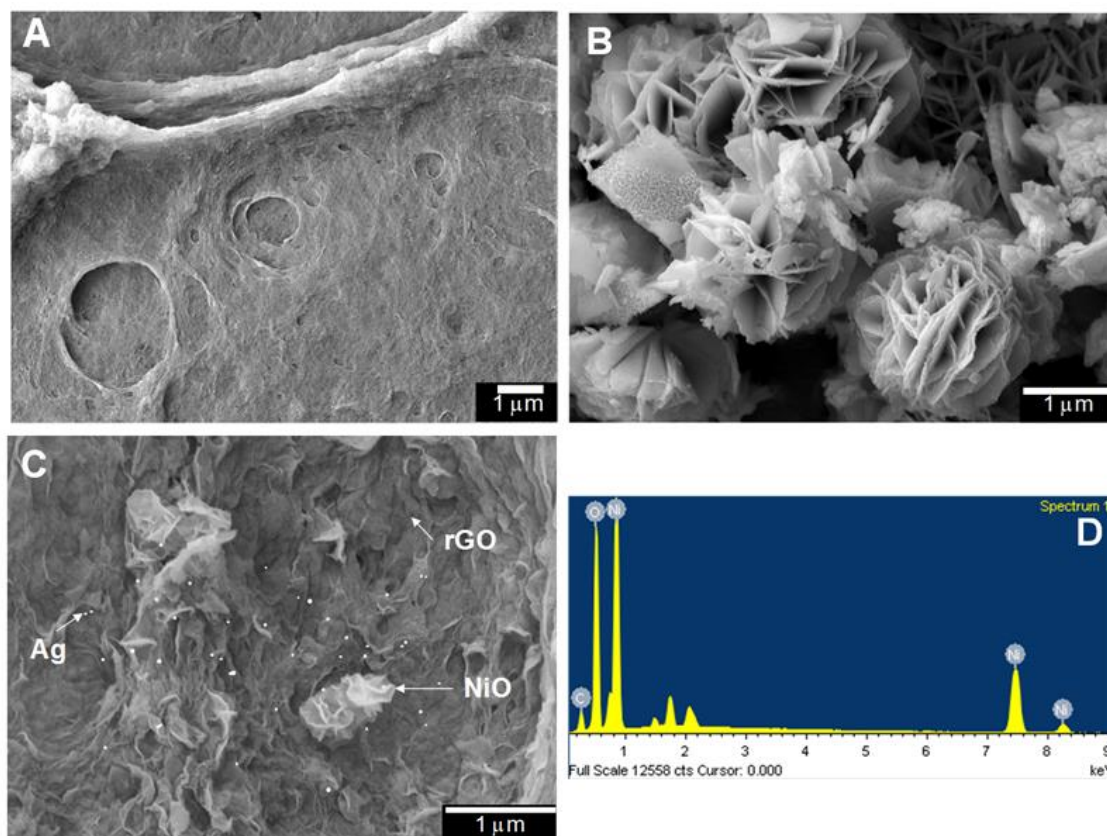


Figure 2.5. FE-SEM images of (A) pure rGO, (B) Ag/NiO, (C) 5Ag/NiO/rGO, and (D) the EDS result of 5Ag/NiO/rGO.

Figure 2.5 presents the surface morphology and atomic composition of the as-synthesized rGO, Ag/NiO and Ag/NiO/rGO examined by FE-SEM and EDS. rGO showed a smooth 2D surface and stacked morphology after the hydrothermal reduction (**Figure 2.5(A)**). Instead, the rGO in Ag/NiO/rGO (**Figure 2.5(B)**) became more corrugated due to the presence of 0D Ag nanoparticles and 3D NiO flower-like nanostructures (**Figure 2.5(C)**). The mean size of the NiO flowers was significantly smaller in Ag/NiO/rGO than in pristine NiO, which indicates an interaction between NiO and rGO during hydrothermal synthesis. As shown in

Figure 2.5(D), EDS confirmed the existence of all elements, such as Ni, O, C, and Ag in Ag/NiO/rGO.

The lattice structures of Ag/NiO/rGO were verified by HR-TEM, as shown in **Figure 2.6**. As shown in **Figure 2.6(A)**, the metal structures were well dispersed over the rGO surface and each section was magnified to observe the lattice structures. The Fast Fourier Transform (FFT) patterns in **Figures 2.6(B-D)** can be indexed to the (002) plane ($d = 3.5 \text{ \AA}$) of the hexagonal graphite phase from rGO, (111) and (222) crystal plane of the trigonal NiO phase (the interplanar distance are 2.5 \AA and 1.2 \AA), and (111) planes of cubic Ag, respectively [60].

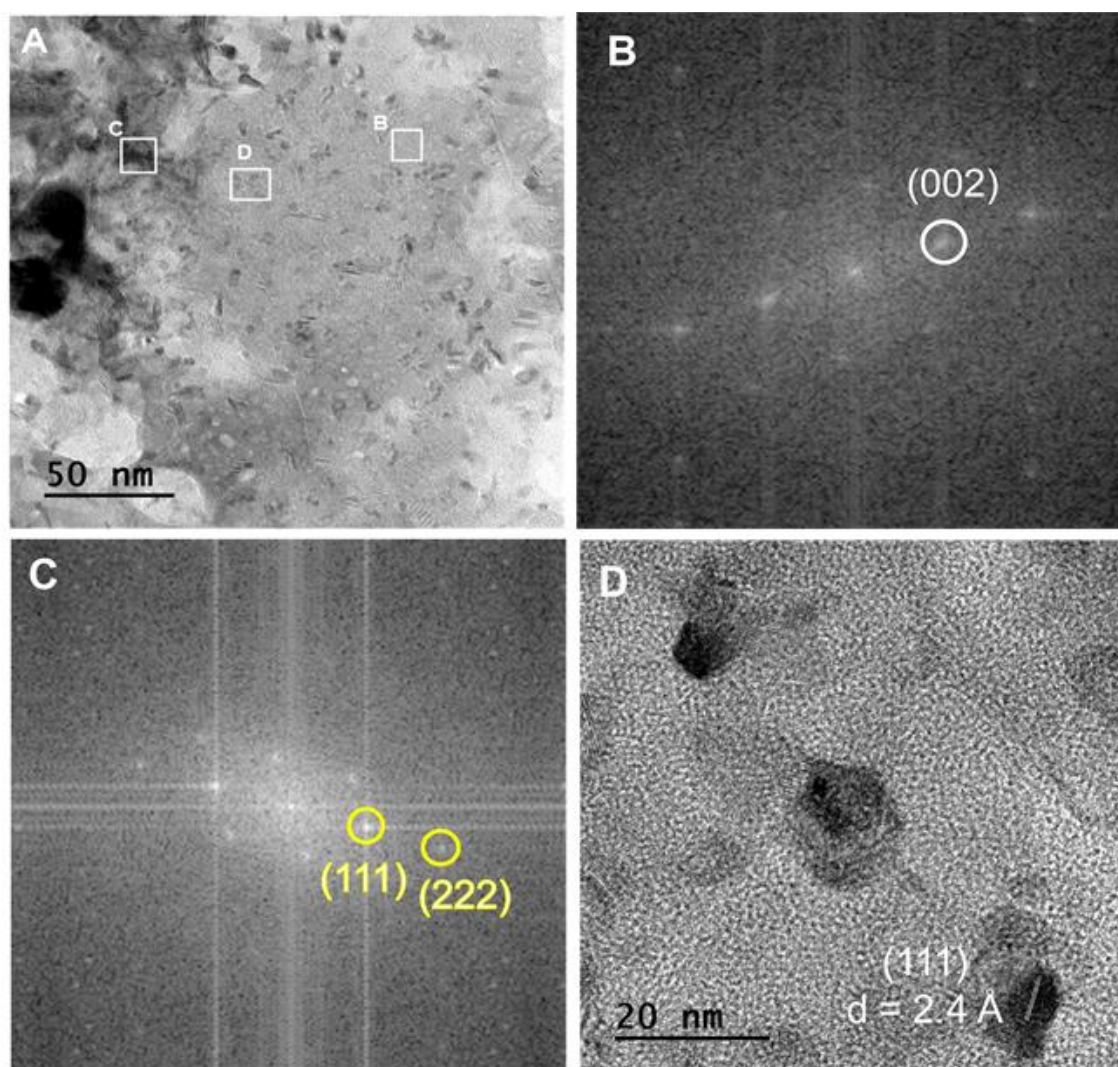


Figure 2.6. (A) HR-TEM images of 5Ag/NiO/rGO. Corresponding FFT patterns (B) rGO, (C) NiO and (D) Ag nanoparticles.

The surface area of all the samples with different Ag contents and Ag/NiO:rGO ratios were measured using a BET apparatus and summarized in **Tables S2.1 and S2.2** (Supporting Information). As the Ag content was increased to 5%, the surface area increased due to the less agglomeration of rGO sheets. At an excessively high Ag content, as the excess Ag just contributes the increase in total mass, the surface area decreased. The change in surface area at various Ag/NiO:rGO volume ratios showed similar results. An optimal rGO content exists and an excessively high GO content results in a decrease in surface area due to more agglomeration between the rGO sheets. At a 5% Ag content and 1:1 Ag/NiO:rGO ratio, Ag/NiO/rGO exhibited a specific surface area as high as $776.85 \text{ m}^2 \text{ g}^{-1}$, which is expected to contribute to the high glucose adsorption and excellent mass transfer observed during the glucose redox cycles on the electrode surface.

2.3.2. Electrochemical behavior of Ag/NiO/rGO towards glucose

The electrochemical behaviors of rGO and 5Ag/NiO/rGO electrodes were evaluated by cyclic voltammetry (CV) in a 0.2 M KCl solution containing 5 mM $\text{K}_3(\text{Fe}(\text{CN})_6)$ as the supporting electrolyte at a scan rate 50 mV s^{-1} . The sensing electroactive surface area (A) was calculated using the Randles-Sevcik equation [61]:

$$I_p = 2.69 \times 10^5 \cdot A \cdot n^{3/2} \cdot D^{1/2} \cdot C \cdot \nu^{1/2} \quad (\text{i})$$

where I_p is the oxidation potential current (A), n is the number of electrons participating in the redox reaction ($= 1$), C is the concentration of the redox probe molecule in the solution (mol/cm^3), D is the diffusion coefficient ($0.76 \times 10^{-5} \text{ cm}^2 \text{ s}^{-1}$), and ν is the scan rate of the potential (0.05 V s^{-1}). The electroactive surface areas of 5Ag/NiO/rGO ($1.768 \times 10^{-3} \text{ cm}^2$) was calculated to be ~ 5 times larger than that of pure rGO ($0.352 \times 10^{-3} \text{ cm}^2$), which can be due to the increased physical surface area (BET surface area) and the electrocatalytic contribution of the Ag and NiO nanostructures.

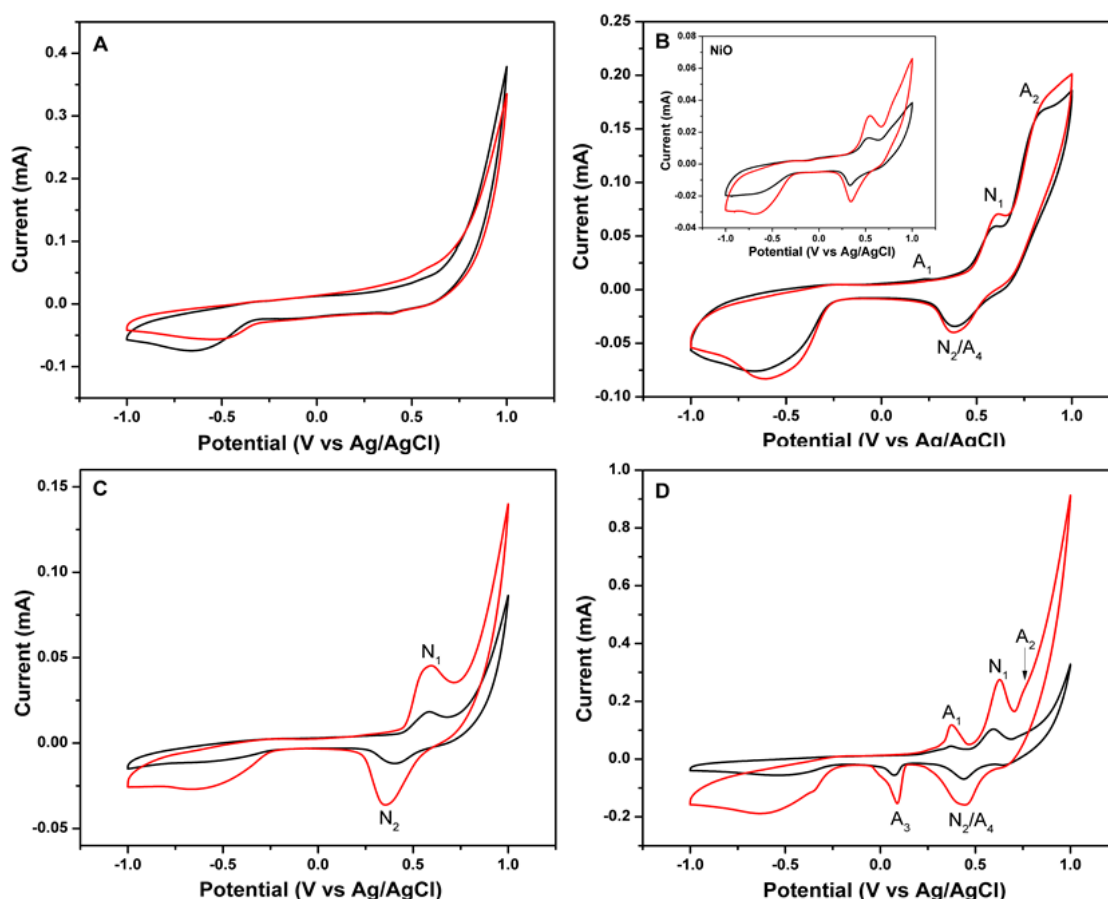


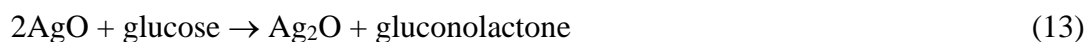
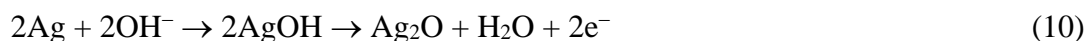
Figure 2.7. Cyclic voltammograms of (A) pure rGO, (B) Ag/NiO and NiO (inset), (C) NiO/rGO, and (D) 5Ag/NiO/rGO modified electrode in 0.1 M NaOH in the absence (black) and presence of 1 mM glucose (red), respectively. The scan rate is 50 mV s^{-1} .

The glucose sensing characteristics of bare rGO, pure NiO, 5Ag/NiO, NiO/rGO and 5Ag/NiO/rGO were evaluated by CV measurements in the absence and presence of 1mM glucose in a 0.1 M NaOH electrolyte at a scan rate of 50 mV s^{-1} from -1 V to 1 V . As shown in **Figure 2.7**, the background current of 5Ag/NiO/rGO was higher than those of any other samples over the given potential range of -1 V to 1 V in the absence of a glucose solution, which can be attributed to the increased electroactive surface area and high electrical conductivity of rGO. Pure rGO (**Figure 2.7(A)**) did not show noticeable oxidation or reduction peaks, even when glucose was dissolved in the electrolyte; however, Ag/NiO exhibited anodic peaks at $+0.6 \text{ V}$, $+0.27 \text{ V}$, and $+0.84 \text{ V}$, which are related to the oxidation peaks of Ni^{2+} (denoted as N_1), Ag^0 (A_1) and Ag^+ (A_2), respectively [62]. During a reverse scan, it showed a cathodic peak of Ni^{3+} (N_2) at $+0.4 \text{ V}$,

which could be overlapped with the reduction peak of Ag^{2+} (A_4) due to their similar reduction potentials [56]. As shown in **Figure 2.7(C)**, when NiO nanostructures were hybridized with rGO, the N_1 peak increased significantly compared to those of pure NiO (the inset in **Figure 2.7(B)**) and Ag/NiO, which indicates the synergetic effects between NiO and rGO for the electrochemical reactions.

The enhanced glucose response was observed more clearly when 5Ag/NiO/rGO was used as an electrode. As shown in **Figure 2.7(D)**, all oxidation and reduction peaks could be observed distinctively with a peak current enhanced several times. Two strong oxidation peaks at +0.63 V and +0.37 V were assigned to N_1 and A_1 , respectively, and one weak oxidation peak at +0.76 V can corresponded to A_2 . The peak for the $\text{Ag}^+/\text{Ag}^{2+}$ redox pair could be observed more clearly at a higher Ag content, as shown in **Figure S2.1** (Supporting Information). The two cathodic peaks, N_2 and A_4 , overlapped each other, which can result in an enhanced glucose response compared to that of the single component.

The electrochemical reactions during the oxidation scan in the presence of glucose on the Ag/NiO/rGO electrode can be described as follows [62,63]:



When the potential of electrode was increased in the alkaline solution, Ag and NiO in the electrodes could be oxidized to Ag_2O , AgO, and NiOOH (Eqns. 10–12), which results in

oxidation peaks, even in the absence of glucose. In the presence of glucose, each component could be reduced by the oxidation of glucose to gluconolactone (Eqns. 13–15), which enhances the peak intensity by facilitating redox cycles, especially for NiO. When Ag nanoparticles are present on the NiO surface, electron transfer can be improved during the glucose redox reactions on insulated NiO due to the highly conductive Ag nanoparticles, which results in enhanced glucose sensing of the Ag/NiO electrode [60]. In the same way, the highly conductive and large 2D surfaced rGO can also dissipate charges accumulated on the NiO surface, which results in strongly enhanced glucose sensitivity of Ag/NiO/rGO. In turn, rGO improves the glucose sensing not only by physical effects, such as a large surface area and better dispersion of NiO nanostructures, but also by electrical effects, such as high electrical conductivity and charge transfer capability.

Figure 2.8 illustrates the CVs of the Ag/NiO/rGO at different scan rates in the presence of 1 mM glucose in 0.1 M NaOH. The anodic (I_{pa}) and cathodic (I_{pc}) peak current increased significantly as the scan rate was varied from 10 to 100 mV s^{-1} . As shown in the inset in **Figure 2.8**, a linear relationship with the square roots of the scan rate was established with a correlation coefficient (R^2) of 0.9975 (I_{pa}) and 0.9919 (I_{pc}), indicating that electrochemical oxidation is quite stable on the Ag/NiO/rGO surface, even at high scan rates. The high electrical conductivity and large surface area of Ag/NiO/rGO can minimize the electron and mass transfer resistance, which might result in a rapid response.

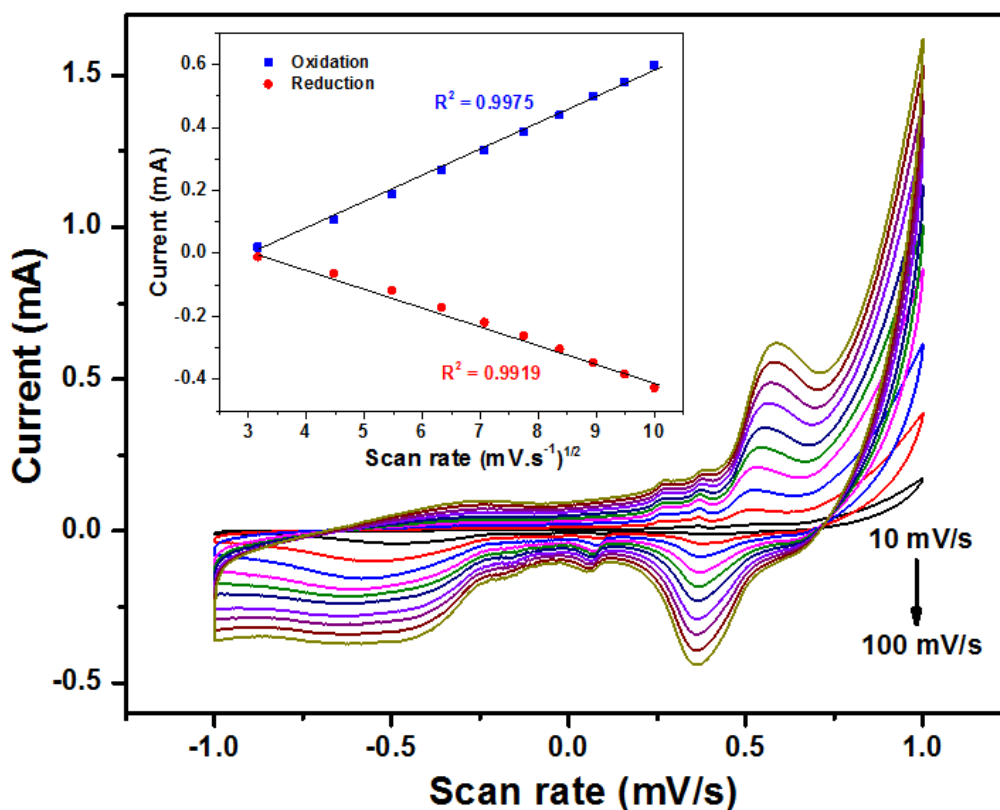


Figure 2.8. CV curves of the 5Ag/NiO/rGO in 0.1 M NaOH with 1 mM glucose at different scan rates ranging from 10 mV s⁻¹ to 100 mV s⁻¹. The inset presents a plot of the peak current versus square root of the scan at an applied potential of +0.6 V.

To examine the glucose sensitivity of the Ag/NiO/rGO electrode further, the CV was measured at various glucose concentrations at a scan rate 50 mV s⁻¹ in a 0.1 M NaOH solution, as shown in **Figure 2.9(A)**. The oxidation peak current increased gradually with increasing glucose concentration from 50 μM to 7.5 mM without any significant peak shift, even at high glucose concentrations, which indicates an excellent and stable glucose response, even at very low and high glucose concentrations. The sensitivity can be calculated using the following equation:

$$\begin{aligned} & \text{Sensitivity } (\mu\text{A} \cdot \text{mM}^{-1} \cdot \text{cm}^{-2}) \\ &= \frac{\Delta \text{current } (\mu\text{A})}{\Delta \text{glucose concentration (mM)} \times \text{electrode area (cm}^2\text{)}} \quad (\text{ii}) \end{aligned}$$

As summarized in **Tables 2.1 and 2.2**, 5Ag/NiO/rGO with a 1:1 Ag/NiO:rGO ratio exhibited the highest glucose sensitivity of $1869.4 \mu\text{A.mM}^{-1}.\text{cm}^{-2}$, which was approximately 3.3 times greater than that of NiO/rGO ($565.8 \mu\text{A.mM}^{-1}.\text{cm}^{-2}$) and one of the highest glucose sensitivities ever reported from NiO-based glucose sensors, as compared in **Table S2.3** (Supporting Information). The increase in the glucose sensitivity of 5Ag/NiO/rGO can be attributed to the increased specific surface area, better dispersion of NiO, effective charge transfer among Ag, NiO, and rGO, and the excellent conductivity of rGO. The excess Ag decreased the glucose sensitivity due to the low electrocatalytic activity of Ag alone and the decreased specific surface area.

Table 2.1. Sensitivity of Ag/NiO/rGO at various contents of Ag.

Samples	Content of Ag (%)	Sensitivity ($\mu\text{A.mM}^{-1}.\text{cm}^{-2}$)	Correlation coefficient (R^2)
Ag/NiO/rGO	0	565.8	0.9973
	1	997.5	0.9982
	3	1243.5	0.9983
	5	1869.4	0.9990
	7	1565.5	0.9988
	10	1448.7	0.9968
	15	1218.7	0.9985
	20	1043.2	0.9990

Table 2.2. The sensitivity of Ag/NiO/rGO at different ratio between Ag/NiO and rGO solutions

Samples	Ratio of volume	Sensitivity ($\mu\text{A.mM}^{-1}.\text{cm}^{-2}$)	Correlation coefficient (R^2)
Ag/NiO/rGO	3:1	1353.7	0.9968
	2:1	1464.8	0.9989
	1:1	1869.4	0.9990
	1:2	1535.0	0.9980
	1:3	1445.3	0.9927

The calibration curve of 5Ag/NiO/rGO was plotted to investigate the linear range and detection limit. As shown in **Figure 2.9(B)**, two linear ranges were identified with one at a low glucose level from 50 μM to 7.5 mM with a regression coefficient (R^2) of 0.999 and a slope of 1869.4 $\mu\text{A}\cdot\text{mM}^{-1}\cdot\text{cm}^{-2}$ and the other at high glucose concentration from 10 mM to 25 mM with a regression coefficient (R^2) of 0.998 and a slope of 115.8 $\mu\text{A}\cdot\text{mM}^{-1}\cdot\text{cm}^{-2}$, which indicates wide detection range with stable high glucose sensitivity. The detection limit of glucose sensing was estimated to be as low as 2.44 μM ($S/N = 3$).

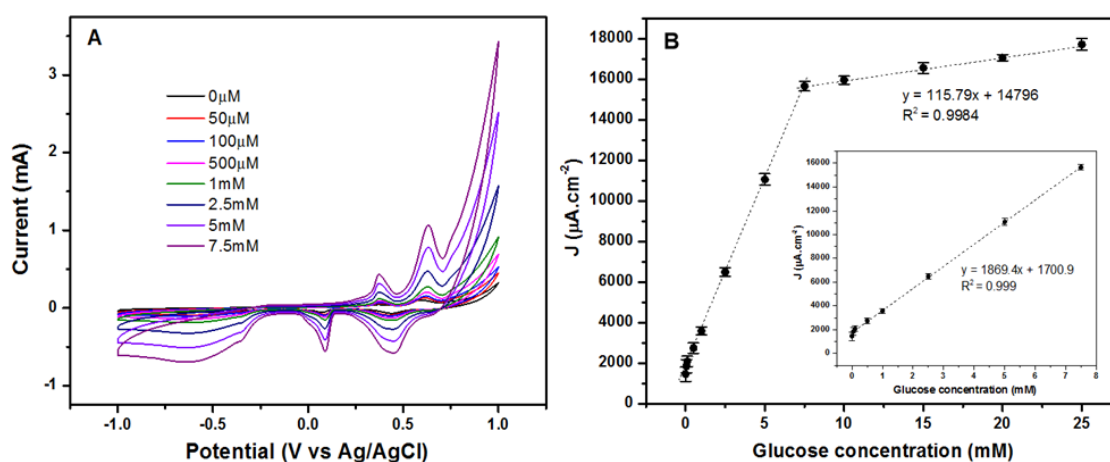


Figure 2.9. (A) CV curves of the 5Ag/NiO/rGO electrode at various glucose concentrations in a 0.1 M NaOH solution at a scan rate of 50 mV s^{-1} . (B) Calibration curve showing the response of 5Ag/NiO/rGO to a wide range of glucose concentrations, 50 μM to 25 mM. The error bars indicate the standard deviations for triplicate measurements at each glucose concentration.

Figure 2.10 shows a typical amperometric response of Ag/NiO/rGO to glucose with a constant applied potential of +0.6 V in a 0.1 M NaOH electrolyte. When 1 mM of glucose was injected directly into the stirred NaOH solution at every 90 s, the Ag/NiO/rGO exhibited a rapid response time ($< 4\text{s}$) and the successive addition of glucose results in a linear increase in current, which demonstrates the fast and wide range glucose sensing capability of Ag/NiO/rGO fabricated in this study.

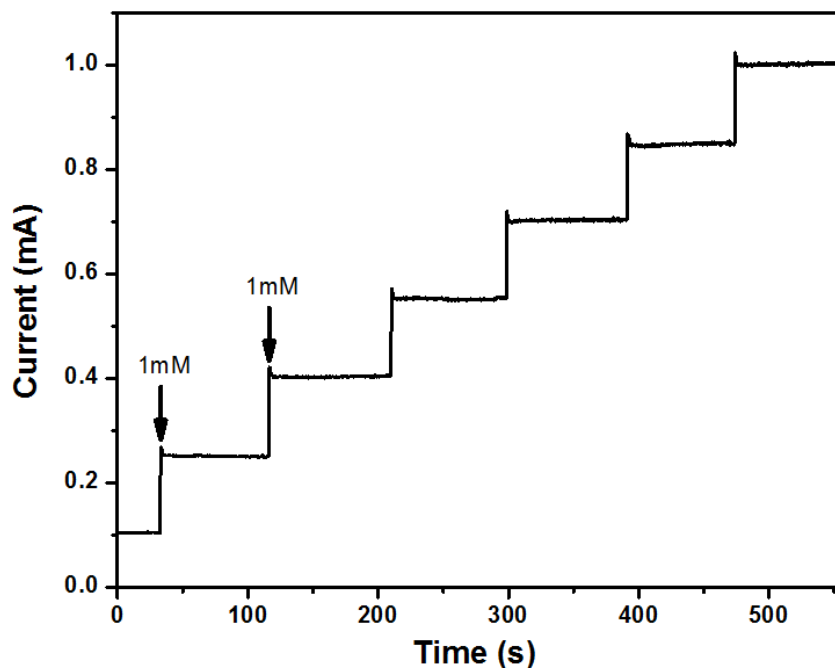


Figure 2.10. Amperometric test of 5Ag/NiO/rGO electrode recorded at +0.6 V towards the successive addition of 1 mM glucose in 0.1 M NaOH.

2.3.3. Stability and effect of the interfering species of the Ag/NiO/rGO electrode

Selectivity is also one of the most important factors of a glucose sensor because there are many interfering species, such as uric acid (UA), ascorbic acid (AA), dopamine (DA), and other carbohydrate compounds, such as fructose, lactose, and sucrose in real blood samples. The anti-interference study was carried out by the sequential addition of 5.0 mM glucose and 0.5 mM of each interfering species under amperometric test conditions. In addition, the CV test of 5Ag/NiO/rGO composite also was measured at same concentration of various interfering species in 0.1 M NaOH (**Figure S2.6**-Supporting information). As shown in **Figure 2.11**, no significant response from interfering species were observed, which demonstrates the excellent selectivity of Ag/NiO/rGO towards glucose.

The long-term stability of the sensor was also evaluated by measuring the change in current over 30 days period (**Figure S2.7**-Supporting Information). The sensor electrodes were stored in air at room temperature and their sensitivity was investigated every three days after injecting 1 mM glucose to 0.1 M NaOH electrolyte. The current was decreased by only 8% from

its original current and became saturated after 30 days, which suggests that the Ag/NiO/rGO fabricated in this study has a high environmental stability than that of enzymatic glucose sensors.

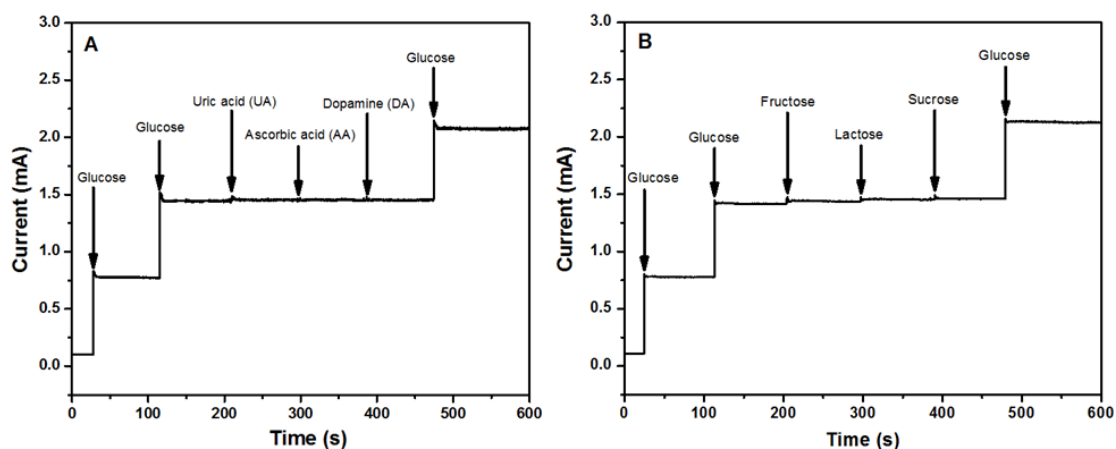


Figure 2.11. Amperometric response of the Ag/NiO/rGO electrode with the successive injection of 5 mM glucose (twice), then 0.5 mM interfering species of (A) UA, AA, DA and (B) fructose, lactose, sucrose, and 5 mM glucose into 0.1 M NaOH under + 0.6 V.

2.3.4. Real sample analysis

To validate the feasibility of the sensor for practical applications, the Ag/NiO/rGO electrode was applied to determine the glucose concentration in rabbit (RS) and horse (HS) blood serum samples, in which the original glucose concentrations are known. At the CV measurement, 50 μ L of the serum sample (diluted in the water at a 1:1, 1:2, 1:3, 1:4 and 1:5 ratio) was injected to a 0.1 M NaOH solution and the current response was recorded. The glucose concentrations in the RS and HS were compared with those measured by a commercial ACCU-CHEK[®] Performa Blood Glucose Meter. As summarized in the **Table 2.3**, the percentage difference between both measurements of the concentration was only 1.206 % for RS and 1.254 % for HS, which confirms that the Ag/NiO/rGO sensor fabricated in this study allows the excellent detection of glucose, even in real blood samples.

Table 2.3. Amperometric determination of the glucose concentration in real blood samples

Dilution ratio of serums in DI water	Horse blood serum (mM)		Rabbit blood serum (mM)	
	Ag/NiO/rGO	Glucometer	Ag/NiO/rGO	Glucometer
pure	3.765	3.774	7.669	7.770
1:1	2.540	2.553	4.646	4.662
1:2	1.875	1.887	3.577	3.552
1:3	1.495	1.554	2.980	3.053
1:4	1.180	1.166	2.351	2.331
1:5	1.010	0.999	2.088	2.054
Relative Error (%)	1.254		1.206	

2.4. Conclusions

Multi-dimensional Ag/NiO/rGO hybrid structures were fabricated successfully by a facile hydrothermal process followed by thermal annealing, which was then used for the non-enzymatic glucose sensor. The 0D Ag nanoparticles and 3D-NiO flower-like nanostructures were decorated on rGO network, which enhanced the electrocatalytic activity by enhancing electron transfer and increasing the specific and electroactive surface areas. Ag/NiO/rGO exhibited excellent glucose sensing properties, such as high sensitivity, rapid response, low detection limit, and long-term stability. Moreover, the sensor could detect glucose over a wide range of glucose concentrations from 50 μM to 7.5 mM with sensitivity as high as $1869.4 \mu\text{A.mM}^{-1}.\text{cm}^{-2}$, which is one of the highest glucose sensitivity ever reported for NiO based glucose sensors. The sensor also exhibited excellent anti-interference properties and comparable sensing capability to commercial enzymatic glucose sensors for real blood samples.

2.5. Supporting information

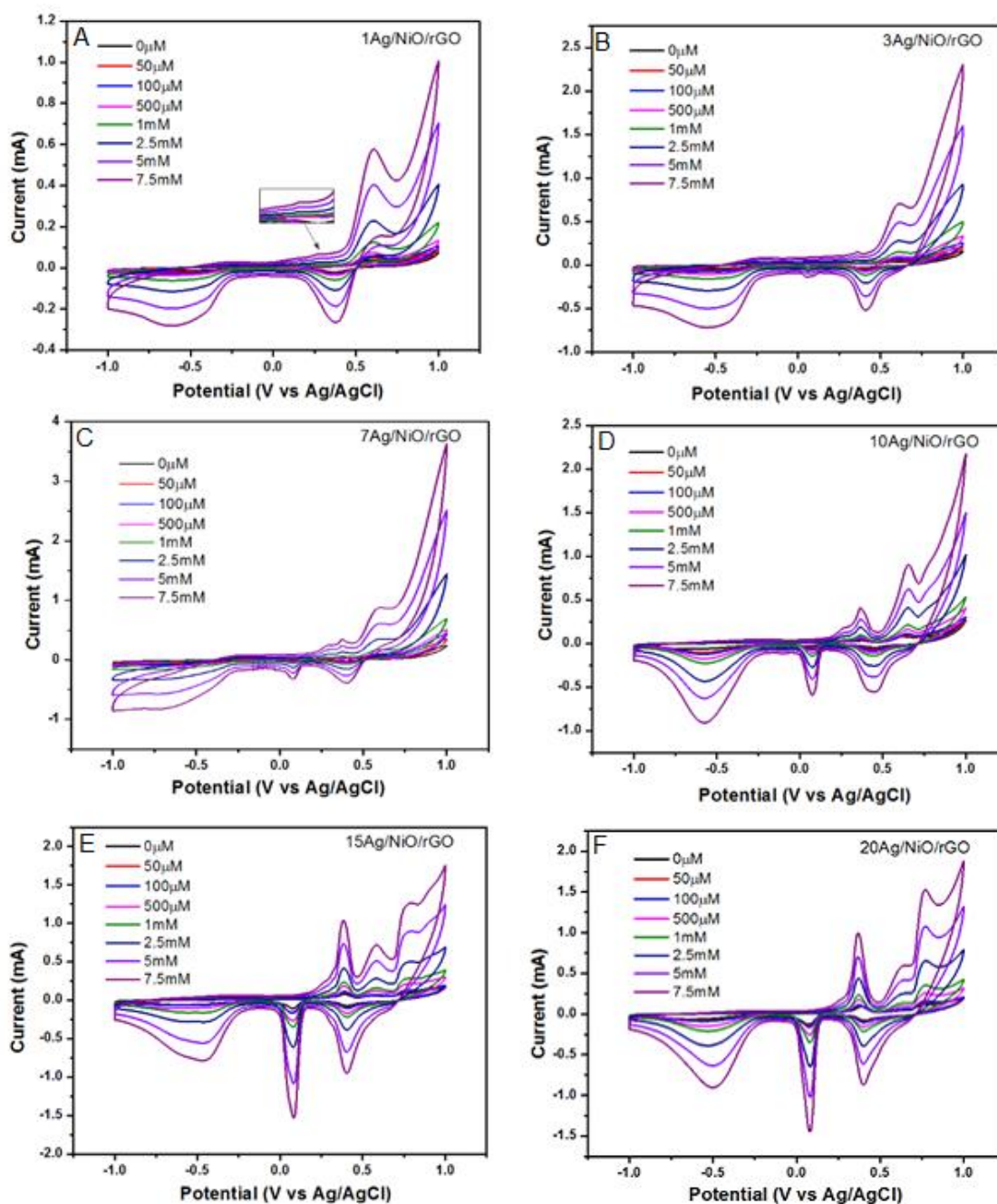


Figure S2.1. (A-F) CV curves of the Ag/NiO/rGO electrode with different Ag contents at various glucose concentrations in a 0.1 M NaOH at a scan rate of 50 mV s^{-1} .

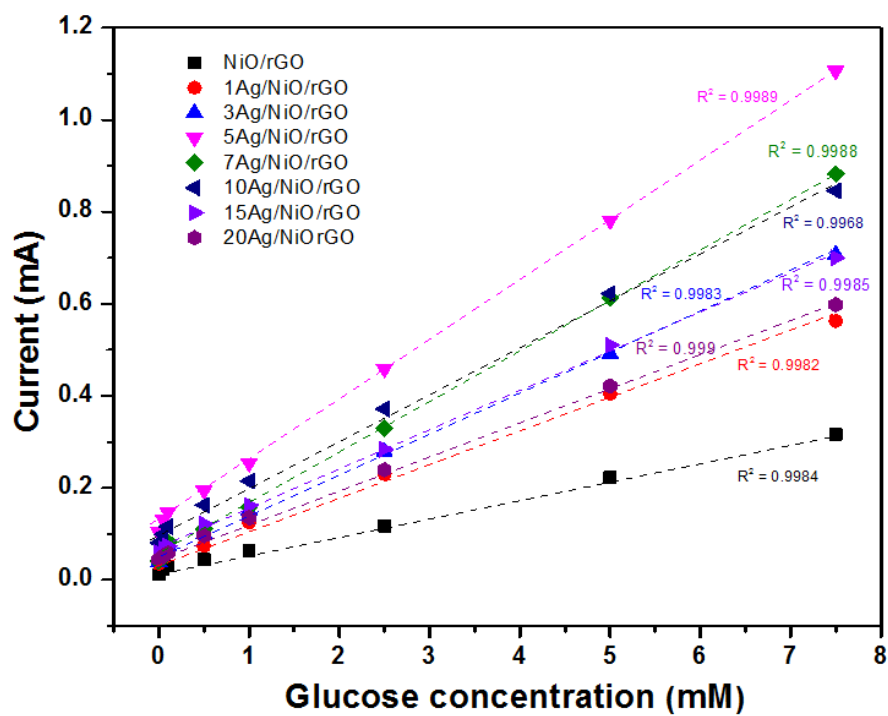


Figure S2.2. Calibration curves of current density vs. glucose concentration at various Ag contents.

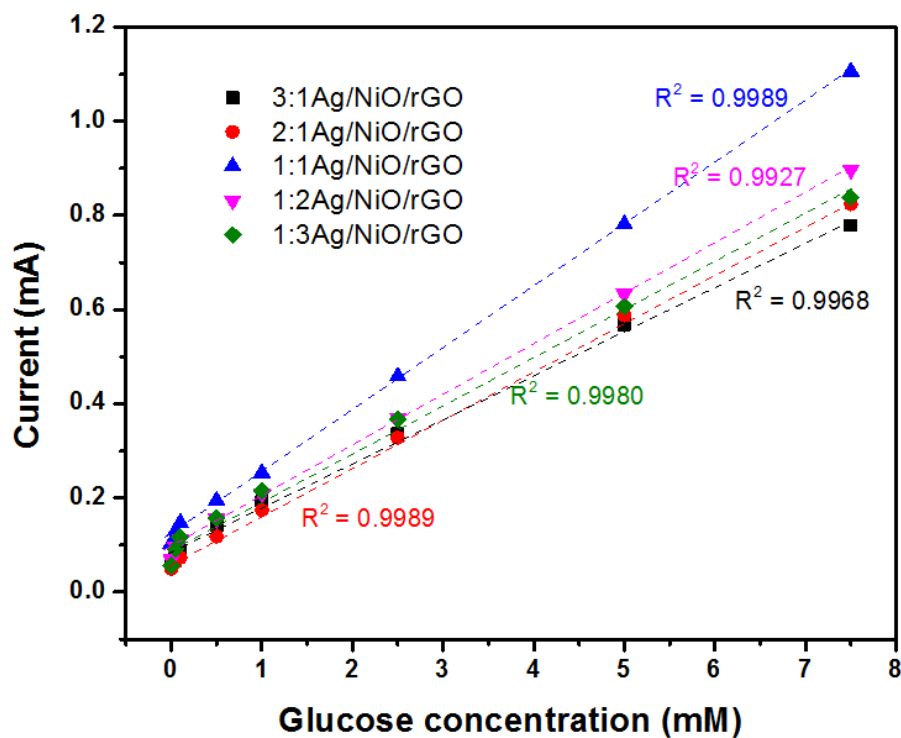


Figure S2.3. Calibration curves of current density vs. concentration of glucose at different solution ratio of Ag/NiO and rGO.

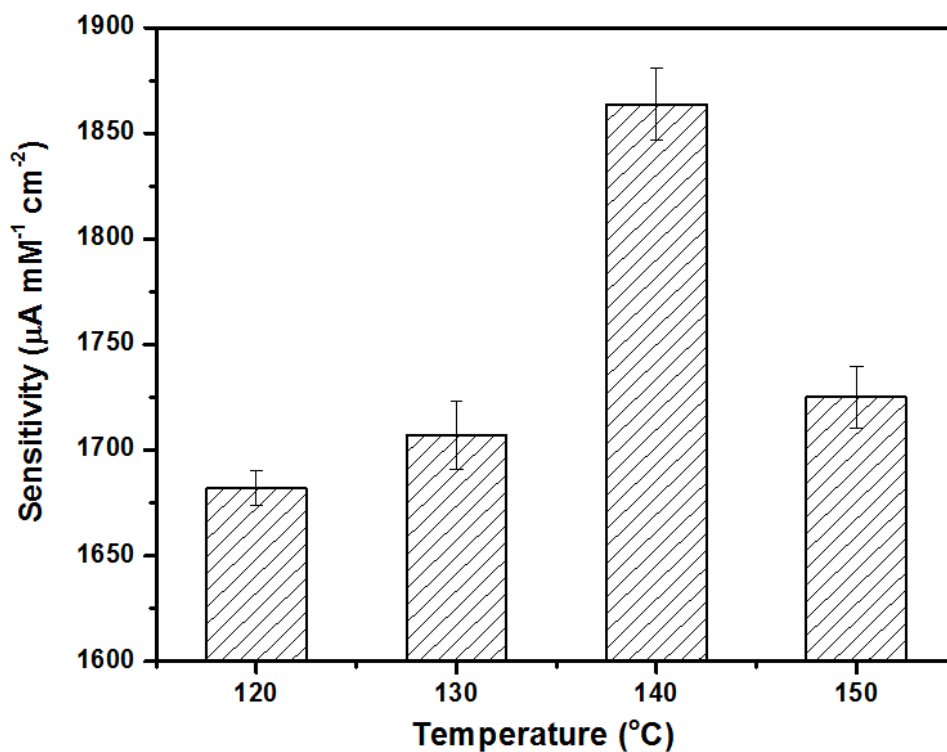


Figure S2.4. The sensitivity of 5Ag/NiO/rGO at different temperature.

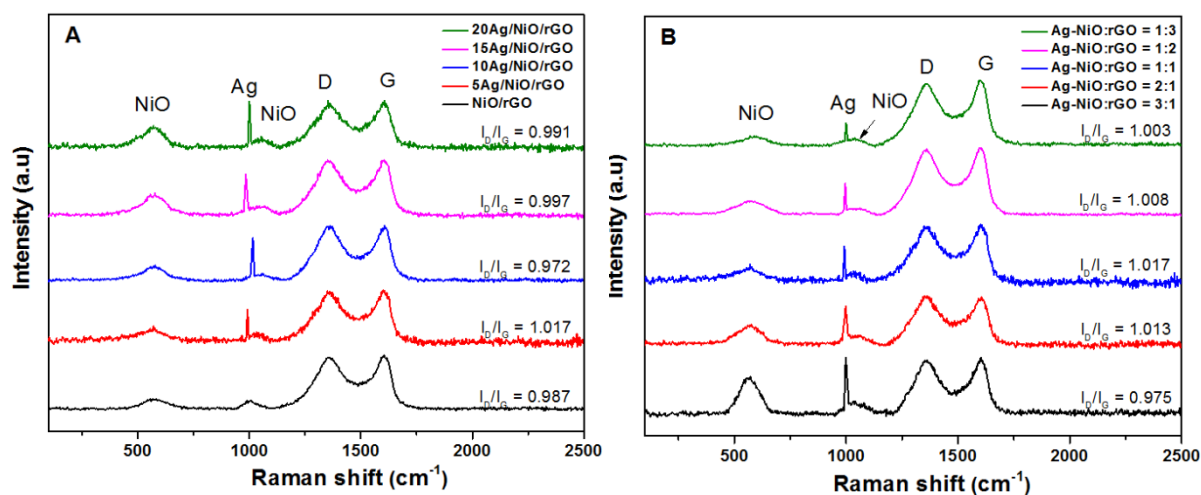


Figure S2.5. Raman spectra of (A) Ag/NiO/rGO at various Ag contents and (B) Ag/NiO/rGO at different solution ratio of Ag/NiO and GO.

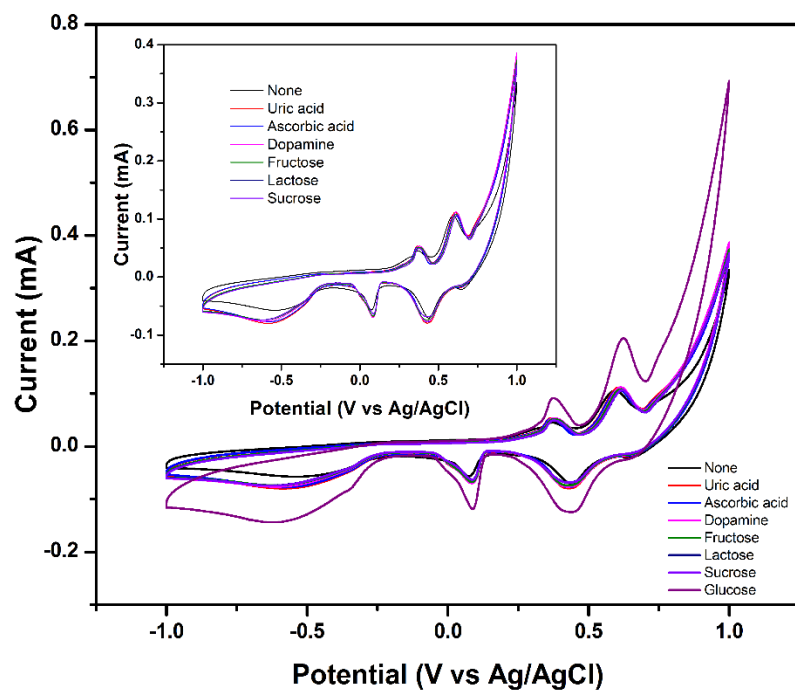


Figure S2.6. The CV curves of 5Ag/NiO/rGO modified electrode in presence of 0.5 mM concentration of various interfering species and glucose in 0.1 M NaOH. The inset obviously presents the CV curves of different interfering species. Scan rate is 50 mV s^{-1} .

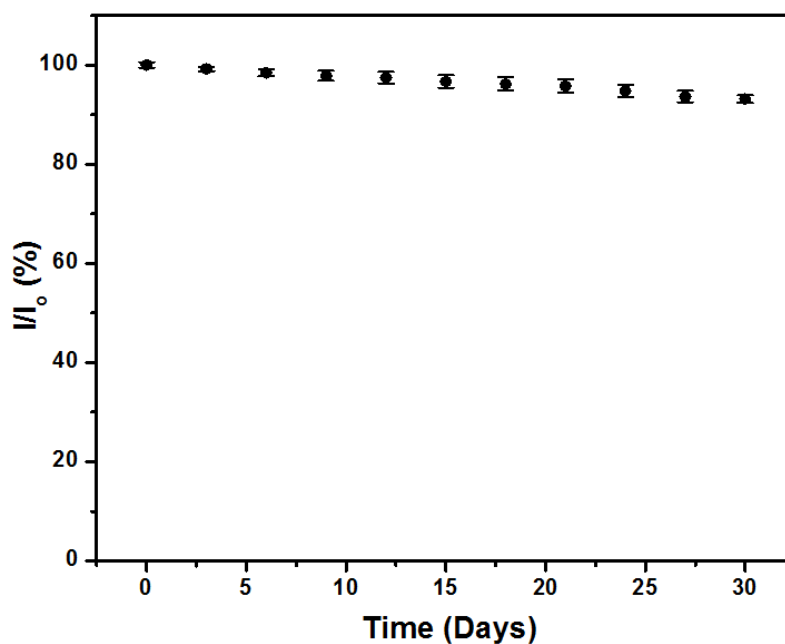


Figure S2.7. Stability of the Ag/NiO/rGO glucose sensor at room temperature. The current was measured every 3 days for one month.

Table S2.1. BET surface areas of pure rGO, NiO/rGO and various Ag/NiO/rGOs with different Ag contents.

Sample	Content of Ag (%)	BET surface area (m ² g ⁻¹)
rGO	0	374.90
NiO/rGO	0	651.80
1Ag/NiO/rGO	1	693.74
3Ag/NiO/rGO	3	701.37
5Ag/NiO/rGO	5	776.85
7Ag/NiO/rGO	7	619.55
10Ag/NiO/rGO	10	574.12
15Ag/NiO/rGO	15	489.07
20Ag/NiO/rGO	20	425.94

Table S2.2. BET surface areas of various 5Ag/NiO/rGO fabricated with different solution ratio of Ag/NiO and GO.

Sample	Ratio of volume (Ag/NiO:GO)	BET surface area (m ² g ⁻¹)
3:1Ag/NiO/rGO	3:1	498.12
2:1Ag/NiO/rGO	2:1	623.40
1:1Ag/NiO/rGO	1:1	776.85
1:2Ag/NiO/rGO	1:2	654.97
1:3Ag/NiO/rGO	1:3	605.73

Table S2.3. The glucose sensing results of our study compared to the previous nickel oxide-based studies.

Material electrode	Linear range	Sensitivity ($\mu\text{A}\cdot\text{mM}^{-1}\text{cm}^{-2}$)	Low detection limit (LOD)	Response time (s)	Ref.
Hedgehog-NiO	0.1–5 μM	1052.8	1.2 μM	–	[64]
NiO@Ag NWs*	0–1.28 mM	67.51	1.01 μM	7	[60]
Pt/NiO/rGO	0.05–5.66 mM	668.2	0.2 μM	2.5	[63]
Ag/Ag ₂ O-rGO	0.2–8mM	32	0.06 mM	–	[62]
NiO/rGO	3.13 μM –3.05 mM	1087	1 μM	~ 10	[65]
NiO@Polypyrrole NWs	0.01–0.5 mM; 1-20 mM	1094.8 62.87	0.33 μM 5.77 μM	–	[66]
NiO NFs**/ rGO	0.002–0.6 mM	1100	0.77 μM	< 5	[53]
Ag/NiO/rGO	50 μM –7.5 mM; 10 mM –25 mM	1807.2 115.8	2.44 μM 1.22 mM	< 4	This work

*NWs: nanowires. **NFs: nanofibers.

Chapter 3. NiMn₂O₄ Spinel Binary Nanostructure Decorated on Three-Dimensional Reduced Graphene Oxide Hydrogel for Bifunctional Materials in Non-enzymatic Glucose Sensor

3.1. Introduction

Recently, nickel-manganese spinel oxide (NiMn₂O₄) has attracted considerable attention as an electrode material in electrochemical reactions because of its low-cost, good electrochemical reactivity, and outstanding electrochemical capacitance [67]. In addition, NiMn₂O₄ has been investigated extensively in many fields, such as gas sensors [68], catalysis [69], negative temperature coefficient thermistors [70], magnetism [71], and energy storage [72]. The applications of NiMn₂O₄ in energy storage devices are often impeded by its poor electrical conductivity and many attempts have been made to improve this [73]. For example, controlling the structure and morphology related to the increase in specific surface area and electrical conductivity or hybridizing it with highly conductive materials to improve the electrical and electrochemical properties [74].

Graphene has intriguing properties, including extraordinary electrical conductivity, unusual mechanical strength, and large specific surface area [75,76], and has been used in many fields, such as field-effect transistors [77,78], transparent conductors [79,80], solar cell [81,82], fuel cell [83,84], energy storage devices [85,86], and bio/gas sensors [15,87]. As one of the graphene derivatives, graphene oxide (GO) has been used as a substitute for pristine graphene, particularly in the fabrication of hybrid materials because of its high density of surface functional groups, which act as anchoring sites with metal or metal oxide materials. Moreover, after the reduction of functional groups, GO can be transformed into reduced GO (rGO), which exhibits excellent electrical properties, such as good electrical conductivity, and effective charge transfer with other materials [88].

In this study, a 3-dimensional (D) rGO hydrogel network (rGOH) with NiMn₂O₄ was fabricated using a facile solvothermal synthesis, where the porous rGOH provides numerous dispersion sites of NiMn₂O₄ and conductive pathways for electrons that are generated during the electrochemical reaction (i.e., glucose oxidation/reduction) on a NiMn₂O₄ catalyst, which results in excellent glucose sensitivity. The NiMn₂O₄/rGOH fabricated in this study exhibited glucose sensitivity as high as 1310.8 $\mu\text{A}\cdot\text{mM}^{-1}\text{cm}^{-2}$, which is one of the highest values ever reported on a NiMn₂O₄-based glucose sensor.

3.2. Experimental details

3.2.1. Materials

Expandable graphite was obtained from Asbury Graphite Mills Inc. (USA). Nickel (II) acetate tetrahydrate (Ni(OCOCH₃)₂·4H₂O), manganese (II) acetate tetrahydrate (CH₃COO)₂Mn·4H₂O, citric acid monohydrate (C₆H₈O₇·H₂O), potassium permanganate (KMnO₄), hydrogen peroxide (H₂O₂) (30 wt. %), sulfuric acid 98% (H₂SO₄), potassium hydroxide (KOH), sodium hydroxide (NaOH), ethanol 99.9% (C₂H₅OH), nafion, isopropanol (IPA), D-(+)-glucose, D-(-)-fructose, galactose, lactose, sucrose, ascorbic acid (AA), uric acid (UA), dopamine (DA), sorbitol (SB), horse serum (HS), and rabbit serum (RS) were purchased from Sigma-Aldrich Co. (USA). All chemicals were used as received. Deionized (DI) water was used to wash the samples in all experiments.

3.2.2. Preparation of NiMn₂O₄/rGOH

The NiMn₂O₄/rGOH was fabricated using a facile one-step solvothermal method. Typically, 0.250 g of Ni(OCOCH₃)₂·4H₂O, 0.490 g of (CH₃COO)₂Mn·4H₂O, and 1.267 g of C₆H₈O₇·H₂O were dissolved in 10 mL of ethanol (C₂H₅OH) with vigorous stirring for 30 min. The resulting mixture was then added to 5 mL of an aqueous GO slurry with a 5 mg/mL solid content that was synthesized by Hummer's method, as described elsewhere [55]. The mixture was transferred to a Teflon-lined stainless steel autoclave and maintained at 160 °C for 12 h to

fabricate a porous 3D network structure of NiMn₂O₄/rGOH. As shown in **Figures S3.1-S3.4** (Supporting Information) the optimal concentration of Ni(OCOCH₃)₂·4H₂O was 1 mmol at a Ni²⁺:Mn²⁺ ratio of 1:2, and the optimal solvothermal temperature was 160 °C. After the autoclave was cooled slowly to room temperature, the product was washed with DI water to eliminate all the unreacted chemicals followed by freeze drying at -37 °C for 2 days to remove the water without destroying the porous network. Finally, the synthesized products were treated thermally at 350 °C for 3 h in a nitrogen atmosphere to form spinel xNiMn₂O₄ and reduce GO to rGO by removing the functional groups. The samples prepared in this study were labeled xNiMn₂O₄/rGOH, where x indicates the number of moles of Ni(OCOCH₃)₂·4H₂O at a fixed volume ratio of nickel-manganese salt solution and GO slurry. **Figure 3.1** illustrates the fabrication procedure of NiMn₂O₄/rGOH.

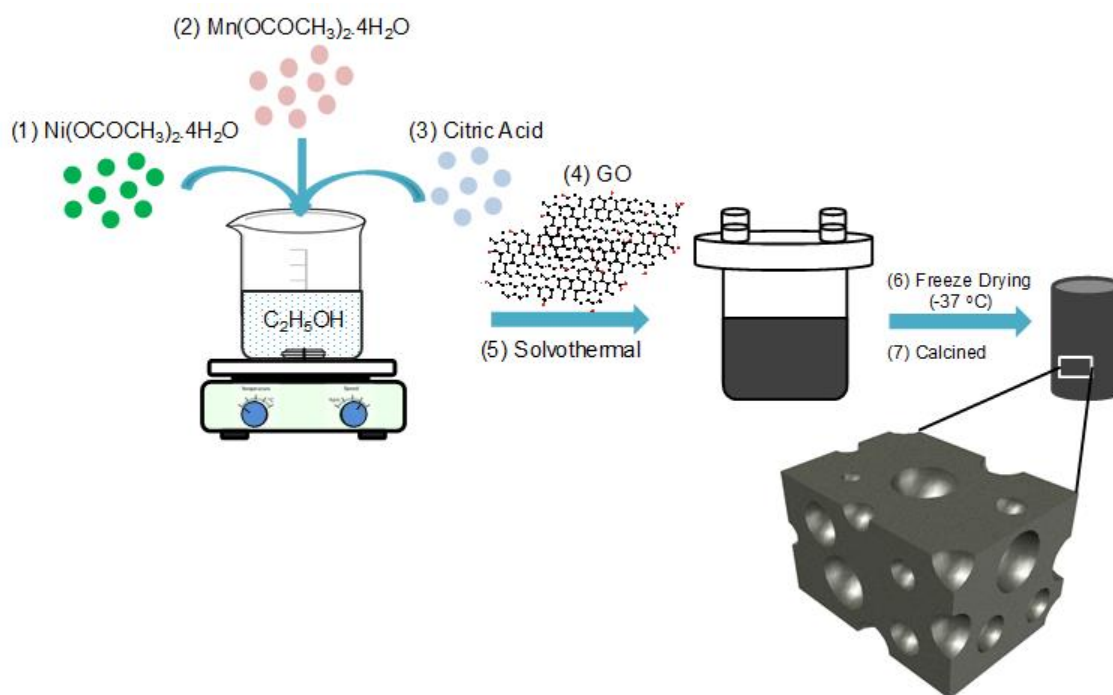


Figure 3.1. Schematic diagram of the preparation steps of NiMn₂O₄/rGOH.

3.2.3. Preparation of NiMn₂O₄/rGOH modified electrodes

A glassy carbon electrode (GCE, 3 mm of diameter), the glucose electrode, was polished sequentially with 0.05 μm alumina and 1 μm diamond slurries and rinsed with DI water. The

electrode was sonicated, washed with ethanol and DI, and dried with a N₂ gun. To produce a slurry, 10 mg of NiMn₂O₄/rGOH was mixed with 0.5 mL of a 5 wt. % nafion solution in isopropanol (IPA). Finally, 10 μL of the prepared solution was coated on a GCE and dried at room temperature with a N₂ gun.

3.2.4. Instrumental analysis

The morphology and surface properties of the prepared samples were visualized by high-resolution transmission electron microscopy (HR-TEM, JEOL JEM-2100F, USA) and field-emission scanning electron microscopy (FE-SEM, JEOL JSM-7600F, Japan). X-ray elements mapping images were obtained by an energy dispersive X-ray spectrometer (EDS) at working voltage of 15 kV. X-Ray diffraction (XRD, Rigaku, D/MAZX 2500V/PC model, Japan) was performed using Cu K α radiation (40 kV, 30 mA, $\lambda = 1.5415 \text{ \AA}$) at scanning angles (2θ) ranging from 10 – 90° 2θ at a scan rate of 2 θ per min. Raman spectroscopy (Thermo Fisher Scientific, DXR Raman Microscope, USA) was obtained using incident laser light at a wavelength of 532 nm. The chemical composition and oxidation state of the samples were examined by X-ray photoelectron spectroscopy (XPS, K-Alpha, Thermo Fisher Scientific ESCALAB 250Xi, USA) using an Al K α X-ray source (1486.6 eV). The specific surface area was measured from the surface area and porosity analyzer (Micromeritics, ASAP 2020, USA) data using the Brunauer-Emmett-Teller (BET) equation.

Electrochemical measurements were carried out using an electrochemical workstation (Bio-Logic, SP-50, USA), which was a standard three-electrode cell composed of NiMn₂O₄/rGOH/GCE, platinum wire, and Ag/AgCl (3 M NaCl) as the working, counter, and reference electrodes, respectively. All electrochemical measurements for the glucose sensor were taken in a 0.1 M NaOH solution at room temperature.

3.3. Results and Discussion

3.3.1. Characterization of rGOH, NiMn₂O₄, and NiMn₂O₄/rGOH

The crystallographic phase and structure information of the samples were identified by XRD. **Figure 3.2** presents the XRD pattern of rGOH, NiMn₂O₄, 0.5NiMn₂O₄/rGOH, 0.75NiMn₂O₄/rGOH, 1.0NiMn₂O₄/rGOH and 1.25NiMn₂O₄/rGOH. The XRD peaks for NiMn₂O₄/rGOH at 18.3, 29.8, 35.6, 43.6, 56.8, and 63.6° 2θ were assigned to the (111), (220), (311), (400), (511), and (440) planes of cubic phase NiMn₂O₄ (JCPDS Card No. 71-0852) and another peak shown at 25.2° was attributed to the (002) plane of the graphene sheets [55], indicating the successful formation of spinel NiMn₂O₄ even with rGOH under these experimental conditions.

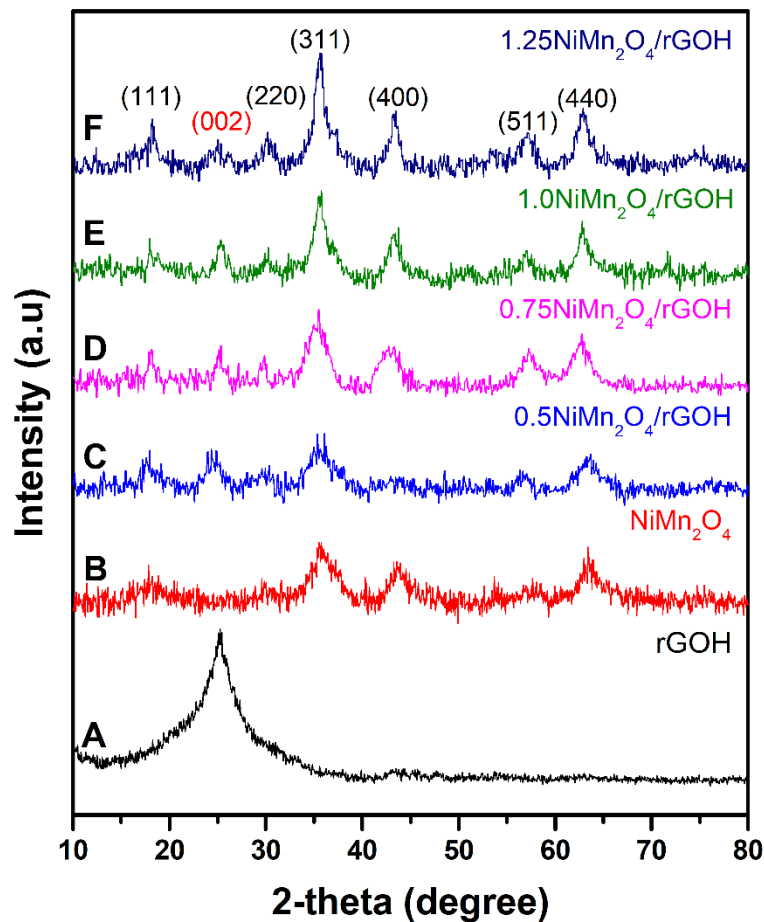


Figure 3.2. XRD patterns of (A) rGOH, (B) NiMn₂O₄ and (C-F) NiMn₂O₄/rGOH with various NiMn₂O₄ contents.

The phase composition of the GO, NiMn₂O₄, rGOH and various NiMn₂O₄/rGOHs were examined by Raman spectroscopy, as shown in **Figure 3.3**. Two characteristic broad peaks in the high wavenumber region at ~1346 cm⁻¹ and ~1598 cm⁻¹ were observed, which were assigned to the bond stretching of all pairs of C sp² atoms in-plane E_{2g}-vibration mode (D-band) and the breathing mode of k-point photons with A_{1g} symmetry (G-band), respectively [89]. The intensity ratio between the D and G bands (I_D/I_G) for NiMn₂O₄/rGOH was significantly higher than that of pristine GO, confirming the reduction of the functional groups and the restoration of numerous graphitic domains. No noticeable difference in the I_D/I_G ratio among the various NiMn₂O₄/rGOHs was observed, indicating that the degree of reduction of GO to rGOH is similar under all compositions. Two other peaks of NiMn₂O₄/rGOH observed at the low wavenumber region were assigned to the oscillations of Ni–O and Mn–O [90].

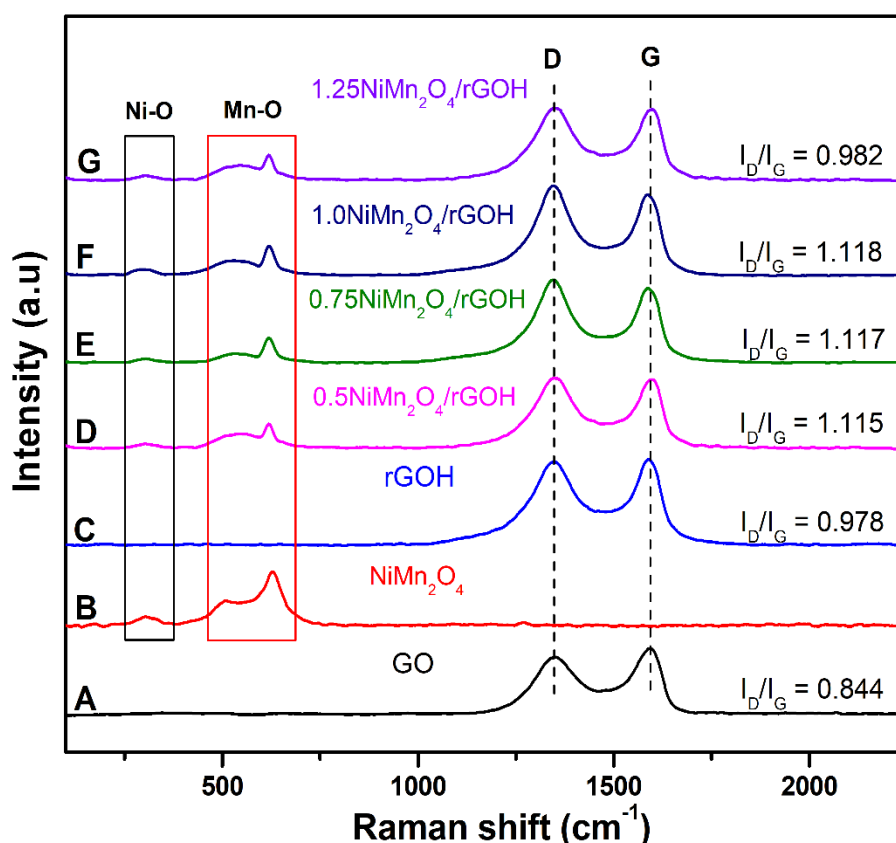


Figure 3.3. Raman spectra of (A) GO, (B) NiMn₂O₄, (C) rGOH and (D-G) NiMn₂O₄/rGOHs with various NiMn₂O₄ contents.

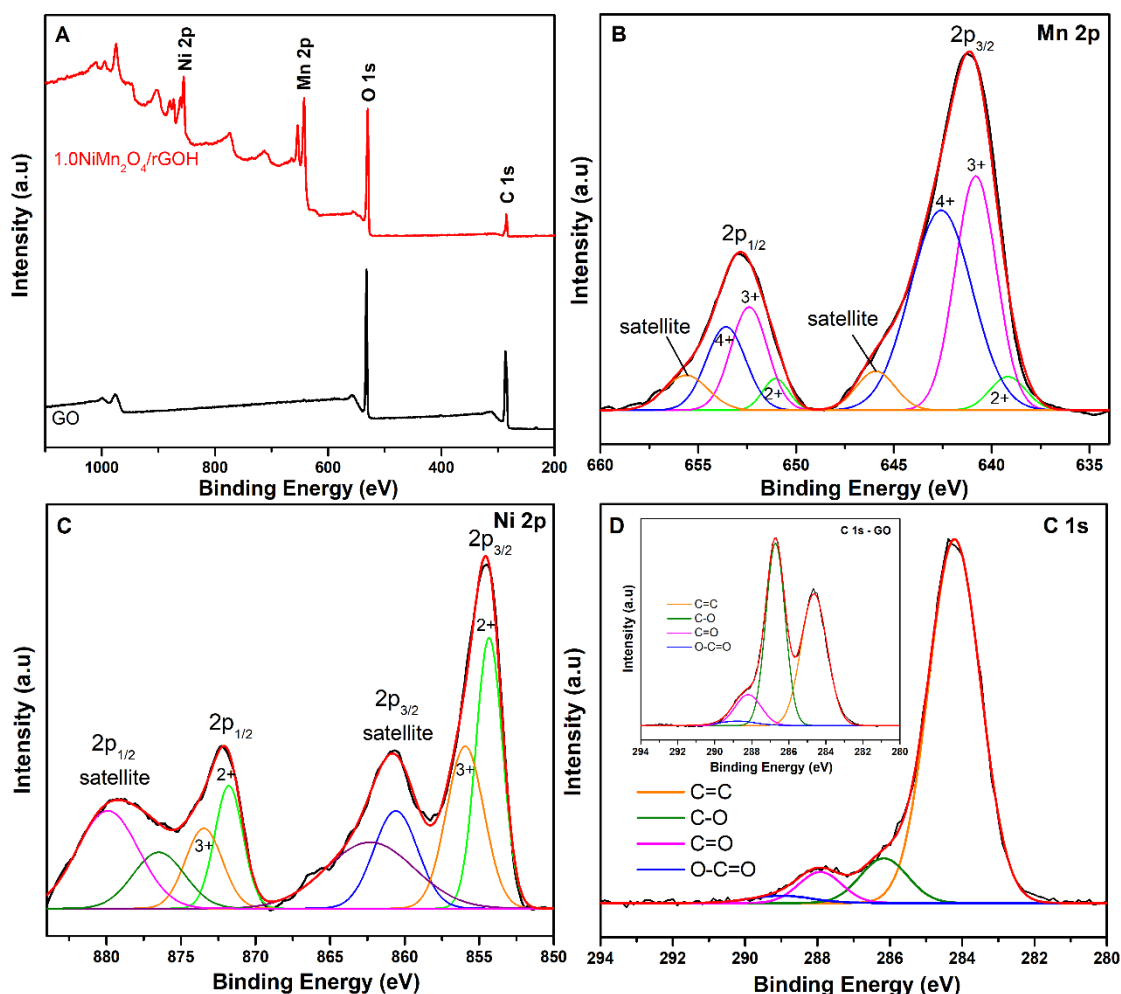


Figure 3.4. (A) XPS survey spectra of 1.0NiMn₂O₄/rGOH and GO. The XPS spectra of (B) Mn 2p, (C) Ni 2p, and (D) C 1s. The inset shows the XPS spectra of C1s of GO.

The composition and oxidation state for each element of NiMn₂O₄/rGOH were examined by XPS. As shown in **Figure 3.4(A)**, the peaks related to Ni, Mn, C, and O were all observed in the survey spectra of NiMn₂O₄/rGOH but only those of C and O were observed for rGOH. As shown in **Figure S3.5** (Supporting Information), the XPS peak intensities of Ni and Mn increase as the amount of metal precursor increases and that of C decreases accordingly, which indicates that the final composition of NiMn₂O₄/rGOH was well-controlled by the initial conditions. **Figures 3.4(B–D)** shows the high-resolution XPS spectra of Mn 2p, Ni 2p and C 1s. The Mn 2p spectrum exhibited three types of Mn oxidation states (+2, +3 and +4). The strong peaks for Mn³⁺ and Mn⁴⁺ are located at 652.37 & 640.77 eV and 653.59 & 642.58 eV, respectively. The Mn 2p spectra exhibit a charge transfer satellite which demonstrated the existence of Coulomb

interactions between the 3d electron of the transition metal and vigorous hybridization between the ligand O 2p and transition metal 3d orbitals [91]. Ni 2p also showed more complicated peaks. The peaks for Ni²⁺ and Ni³⁺ were located at 871.80 & 854.27 eV and 873.53 eV & 855.96 eV, respectively. In addition, broad satellite peaks centered at 879.26 eV and 860.72 eV were also observed. These peaks agree with those reported in previous results [55]. The Ni/ Mn elemental ratio obtained from XPS was 1/1.95, which is close to the formula of NiMn₂O₄.

The C 1s spectrum of pristine GO exhibited several peaks at 284.35, 286.18, 287.91, and 288.82 eV, which were assigned to the C–C (sp² carbon), C–O (epoxy and alkoxy), C–O (carbonyl group), and O–C=O (carboxyl group), respectively. After the solvothermal process, the peak associated with C–C in aromatic rings (284.35 eV) becomes predominant while the others related to the oxygen functional groups are reduced considerably, which clearly indicates that most of the oxygen-containing functional groups are reduced and the sp² carbon network is restored during NiMn₂O₄/rGOH fabrication.

Figures 3.5(A–C) show FE-SEM images of the surface morphology and structure of the as-obtained rGOH, NiMn₂O₄, and NiMn₂O₄/rGOH. Pure rGOH (**Figure 3.5(A)**) showed a well-developed 3D porous structure and pristine NiMn₂O₄ (**Figure 3.5(B)**) exhibited a smooth surface with many holes. Instead, NiMn₂O₄/rGOH (**Figure 3.5(C)**) became more corrugated and roughened, which suggests an interaction between NiMn₂O₄ and rGOH during the solvothermal synthesis. As shown in **Figure S3.6** (Supporting Information), the elements of Ni, Mn, C, and O are homogeneously dispersed in NiMn₂O₄/rGOH, which indicates that the NiMn₂O₄/rGOH fabricated in this study is a well-developed 3D structure with homogeneous composition.

Figures 3.5(D-E) presents the HR-TEM images. The rGOH and NiMn₂O₄ were mixed together. As shown in **Figures 3.5(F-G)**, the fast Fourier transform (FFT) of selected regions in **Figure 3.5(E)** reveal the crystals indexed to the (002) plane ($d = 3.2 \text{ \AA}$) of the hexagonal graphite phase from rGOH and (111) and (222) crystal plane of the cubic NiMn₂O₄ phase ($d = 4.8$ and 2.4 \AA), indicating the formation of a hybrid nanostructure of NiMn₂O₄/rGOH. The HR-TEM images of xNiMn₂O₄/rGOH (**Figure S3.7** -Supporting Information) show that as the NiMn₂O₄ content

increases its coverage on the GO increases and NiMn_2O_4 is uniformly dispersed up-to a 1:1 ratio ($1.0\text{NiMn}_2\text{O}_4/\text{rGOH}$). But it starts to agglomerate at a 1.25:1 ratio, which might result in decreased surface area and glucose sensitivity by blocking pores of rGOH.

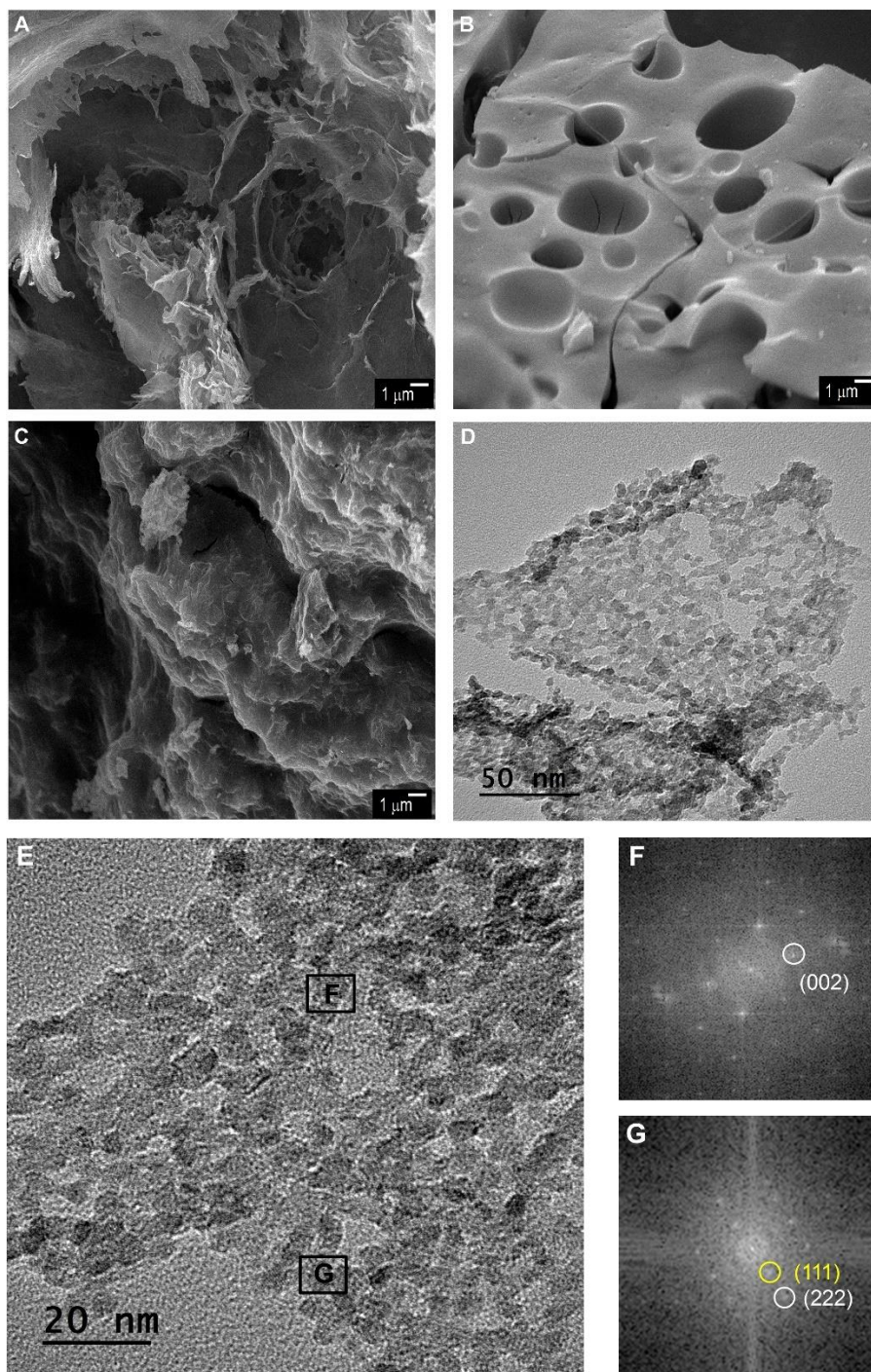
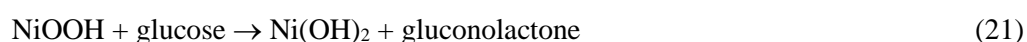
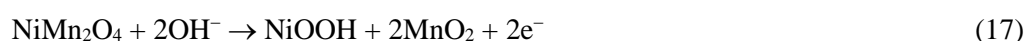


Figure 3.5. FE-SEM images of (A) pure rGOH, (B) NiMn_2O_4 , and (C) $1.0\text{NiMn}_2\text{O}_4/\text{rGOH}$. HR-TEM images of $\text{NiMn}_2\text{O}_4/\text{rGOH}$ (D and E) and corresponding FFT patterns of (F) rGOH and (G) NiMn_2O_4 .

3.3.2. Electrochemical behaviors of NiMn₂O₄/rGOH towards glucose

The glucose sensing characteristics of NiMn₂O₄/rGOH were monitored by CV in a 0.1 M NaOH electrolyte in the presence or absence of 0.5 mM glucose at a scan rate of 50 mV s⁻¹ and scan range from -1 V to 1 V, as shown in **Figure 3.6**. In the absence of a glucose solution, the background current of 1.0NiMn₂O₄/ rGOH was higher than those of the other samples, which indicates the highest electrochemical active surface area of 1.0NiMn₂O₄/rGOH among them due to the increased specific surface area (**Table S3.1** - Supporting Information) and high electrical conductivity of 1.0NiMn₂O₄/ rGOH (**Figure 3.6(A)**). No obvious oxidation or reduction peaks were observed in the case of pure rGOH (**Figure 3.6(B)**). Instead, NiMn₂O₄ showed noticeable reduction–oxidation (redox) peaks (**Figure 3.6(C)**), confirming that the electrocatalytic current originated primarily from the catalytic redox reaction of glucose on NiMn₂O₄. As shown in **Figure 3.6(D)**, NiMn₂O₄/rGOH exhibits two anodic peaks at +0.12 and +0.62 V, which corresponds to the oxidation peaks of Mn³⁺ and Ni²⁺, respectively. At a higher potential, MnO₂ can be oxidized further to MnO₄²⁻ [92]. During a reverse scan, the reduction peaks of Ni³⁺ and Mn⁶⁺ were observed at +0.3 V, and another peak for Mn⁴⁺ was observed at -0.5 V. Especially, a pair of redox peaks of Ni²⁺/Ni³⁺ could be overlapped with the redox peak of Mn⁴⁺/Mn⁶⁺ due to their similar redox potentials [93]. When 0.5 mM of glucose was added, the redox current increased except for rGOH alone and the following equations suggest the electrochemical mechanism during the redox scan in the presence or absence of glucose on the NiMn₂O₄/rGOH electrode [92]:



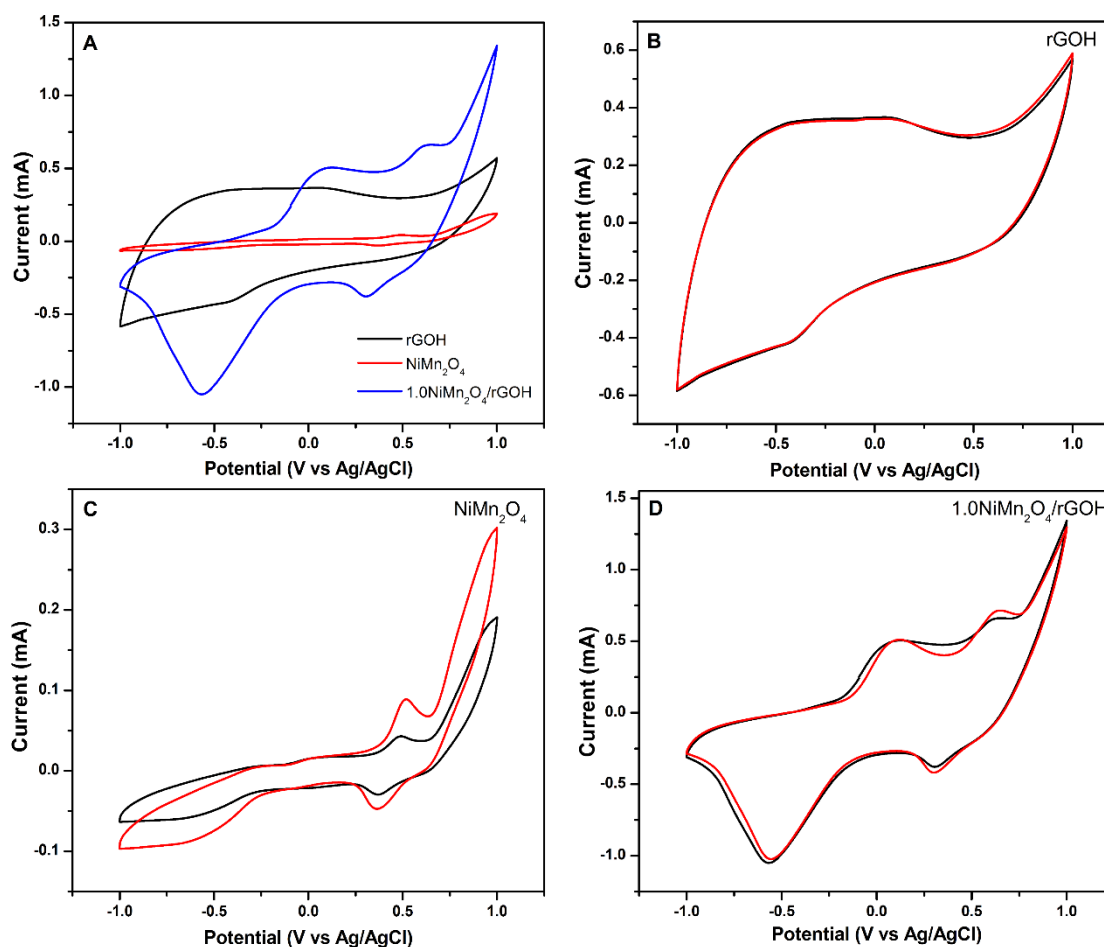
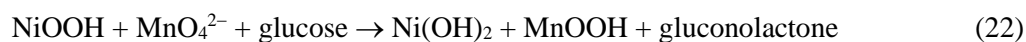


Figure 3.6. CV curves of (A) rGOH, NiMn₂O₄ and 1.0NiMn₂O₄/rGOH in the absence of glucose. CV curves of (B) rGOH, (C) NiMn₂O₄, and (D) 1.0NiMn₂O₄/rGOH modified electrode in 0.1 M NaOH in the absence (black) and presence of 0.5 mM glucose (red), respectively. The scan rate was 50 mV s⁻¹.

According to the Incipient Hydrated Oxide Adatom Mediator (IHOAM) model, during the anodic scan, the oxidized metal oxide catalysts can oxidize glucose to gluconolactone (Eqns. 19-21), which can increase the total current at a given potential, and *vice versa* during the cathodic scan [94]. The slightly positive shift of the anodic peak in the presence of glucose can be attributed to the lower reaction kinetics of the electrocatalytic process by the adsorption of glucose and the oxidized intermediates on the active sites of the catalyst.

The effect of the scan rate was also examined in the presence of 1 mM glucose, as shown in **Figures 3.7(A-B)**, to investigate the electrochemical redox reaction mechanism of glucose. Obviously, the oxidation (anodic – I_{pa}) and reduction (cathodic – I_{pc}) peak currents were both directly proportional to the square root of the scan rate in the range, 10–100 mV s^{-1} , with a very high correlation coefficient (R^2) of 0.9934 (I_{pa}) and 0.9875 (I_{pc}), indicating that the glucose redox reaction is a diffusion-controlled process involving OH^- from the electrolyte to the electrode surface during the reduction step and reversed during the oxidation step [66]. Moreover, a positive shift of the oxidation peak and negative shift of the reduction peak with increasing scan rate also indicates that the adsorption of glucose and oxidized intermediates control the kinetics of the electrochemical reactions [63].

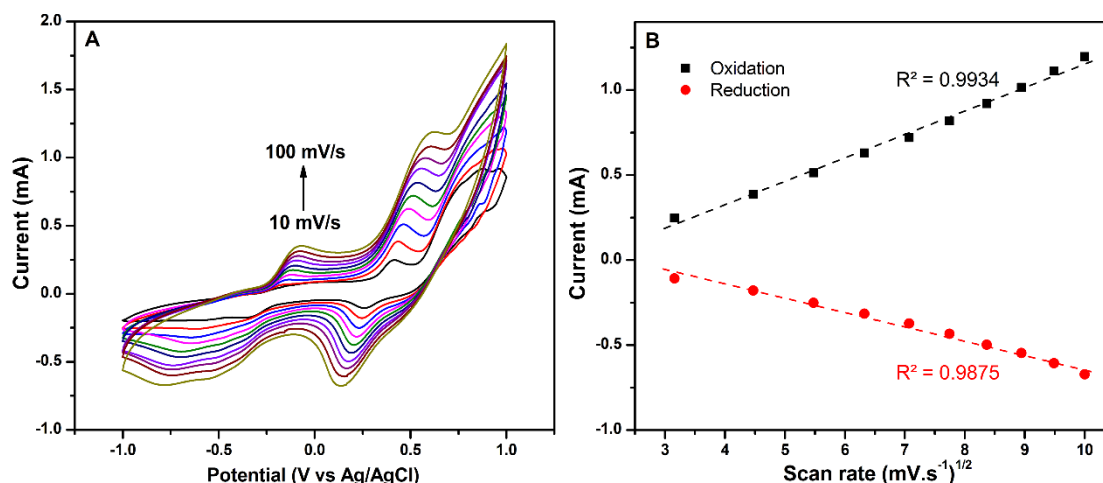


Figure 3.7. (A) CV curves of the 1.0NiMn₂O₄/rGOH in 0.1 M NaOH with 1 mM glucose at different scan rates ranging from 10 mV s^{-1} to 100 mV s^{-1} . (B) Plot of the peak current versus square root of the scan rate at an applied potential of +0.62 V.

The glucose sensing characteristics of the 1.0NiMn₂O₄/rGOH electrode were examined further at glucose concentrations ranging from 10 μM to 20 mM at a scan rate of 50 mV s^{-1} in a solution containing 0.1 M NaOH, as shown in **Figure 3.8**. As the glucose concentration increases, the redox peaks increased gradually and linearly without a significant peak shift. Two linear ranges from 10 μM to 1 mM and 1 mM to 20 mM were observed, which indicates a low detection limit and a wide detection range of 1.0NiMn₂O₄/rGOH fabricated in this study. The detection

limit of 1.0NiMn₂O₄/rGOH was as low as 1.78 μM and various NiMn₂O₄/rGOHs with different ratios were measured and summarized in **Table 3.1**. The glucose sensitivity was calculated using the following eqn. (ii) as displayed in **Chapter 2**.

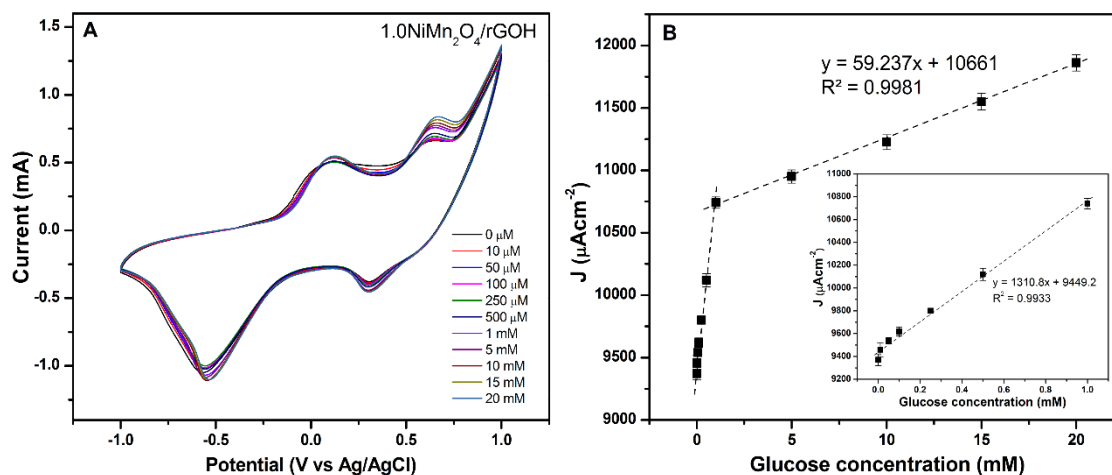


Figure 3.8. (A) CV curves of 1.0NiMn₂O₄/rGOH with different glucose concentrations in a 0.1 M NaOH solution at a scan rate of 50 mV s⁻¹. (B) Calibration curve of 1.0NiMn₂O₄/rGOH at a wide range of glucose concentrations from 0 μM to 20 mM. The error bars indicate the standard deviations for triplicate measurements at each glucose concentration.

Table 3.1. Glucose sensitivity of various samples fabricated in this study.

Samples	Sensitivity (μA·mM ⁻¹ ·cm ⁻²)	Correlation coefficient (R ²)
rGOH	592.82	0.9863
NiMn ₂ O ₄	766.96	0.9827
0.5NiMn ₂ O ₄ /rGOH	874.67	0.9898
0.75NiMn ₂ O ₄ /rGOH	1089.9	0.9880
1.0NiMn ₂ O ₄ /rGOH	1310.8	0.9933
1.25NiMn ₂ O ₄ /rGOH	1172.1	0.9901

Among the samples, the 1.0NiMn₂O₄/rGOH exhibited the highest glucose sensitivity of 1310.8 μA mM⁻¹ cm⁻², which is approximately 2.2 and 1.7 times higher than those of rGOH and NiMn₂O₄, respectively. Furthermore, this is also one of the highest glucose sensitivities ever reported for NiO/MnO₂-based glucose sensors, as shown in **Table S3.3** (Supporting Information).

The excellent glucose sensitivity of 1.0NiMn₂O₄/rGOH can be attributed to the increased specific surface area by the formation of porous 3D structures, improved effective charge transfer between NiMn₂O₄ and rGOH, and the excellent electrical conductivity of rGOH after reduction.

Figure 3.9 presents a typical amperometric response of 1.0NiMn₂O₄/rGOH to glucose with a constant applied potential of +0.62 V in a solution containing the 0.1 M NaOH electrolyte. The measurement was carried out by the direct injection of 1 mM glucose into the stirred NaOH solution at every 90 s. With the successive injections of glucose, the response of the 1.0NiMn₂O₄/rGOH electrode towards glucose increased immediately and reached a steady state within 3.5 s. The amperometric signal after glucose injection showed a linear increase in current and rapid stabilization, demonstrating the fast and wide range glucose sensing capability of the NiMn₂O₄/rGOH electrode fabricated in this study. The high electrical conductivity and large surface area of NiMn₂O₄/rGOH can minimize the electron and mass transfer resistance, which might result in a rapid and stable response.

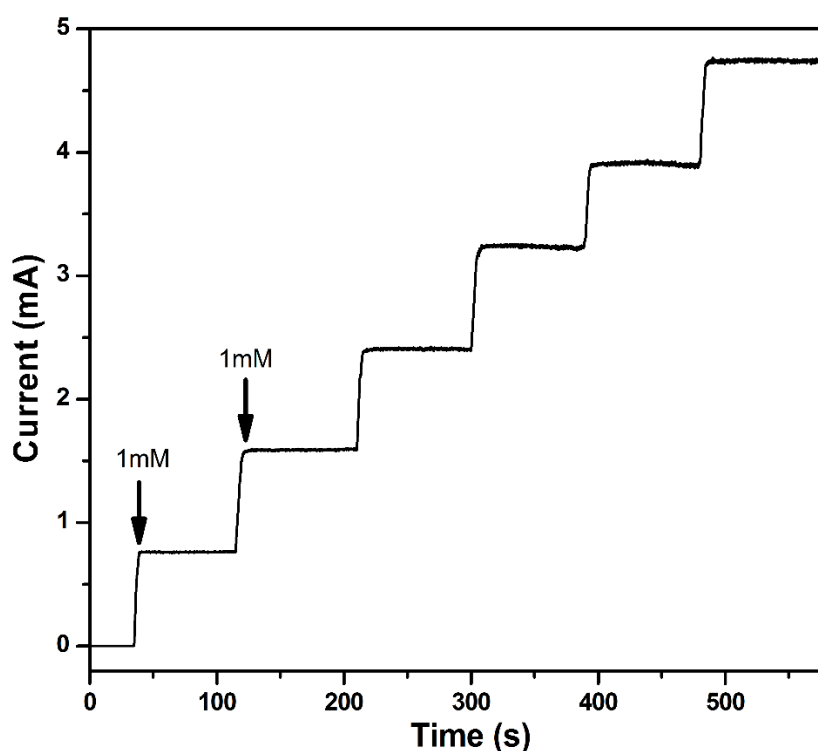


Figure 3.9. Amperometric test of the 1.0NiMn₂O₄/rGOH electrode recorded at +0.62 V towards the successive addition of 1 mM glucose in the 0.1 M NaOH electrolyte at every 90 s.

3.3.3. Stability and effect of the interfering species of the NiMn₂O₄/rGOH electrode

The detection of glucose in real blood can be disturbed by interfering species, such as uric acid (UA), ascorbic acid (AA), dopamine (DA), sorbitol (SB), and other carbohydrate compounds, including galactose, fructose, lactose, and sucrose. The anti-interference effect of NiMn₂O₄/rGOH to the interfering reagents were evaluated by the sequential addition of 1.0 mM glucose and 5 mM of each of the interfering species under amperometric test conditions. As shown in **Figure 3.10**, a well-defined glucose response was observed, whereas there was no significant response from any interfering reagents even with a 5 times higher concentration than that of glucose. All the interfering species exhibited a two order of magnitude lower current than that of glucose (**Figure S3.8** – Supporting Information), highlighting the excellent selectivity of NiMn₂O₄/rGOH for glucose detection.

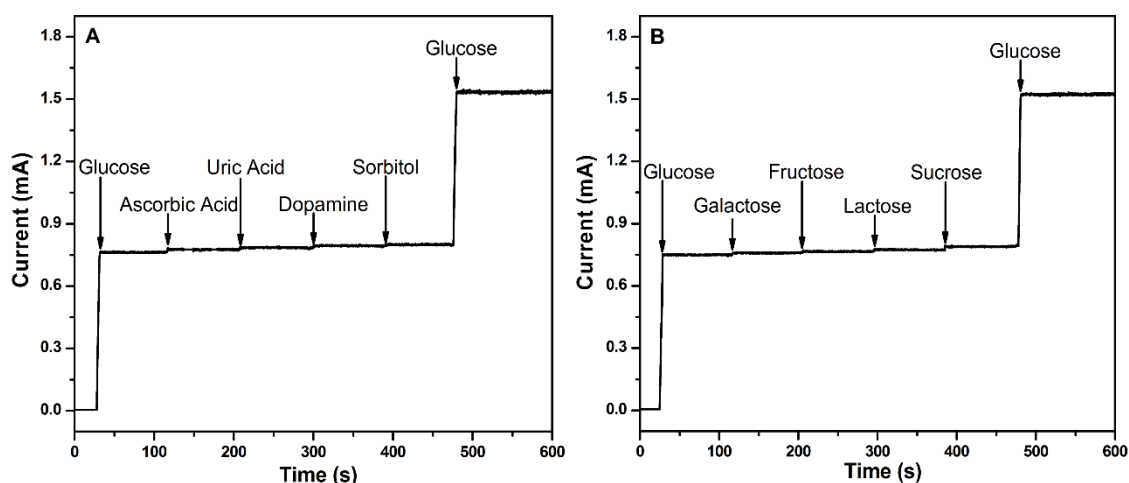


Figure 3.10. Amperometric response to successive injections of 1 mM glucose and 5 mM interferents of (A) UA, AA, DA, and SB, and (B) galactose, fructose, lactose, and sucrose of the 1.0NiMn₂O₄/rGOH electrode in 0.1 M NaOH electrolyte at an applied voltage of +0.62 V.

The stability of the NiMn₂O₄/rGOH sensor was also evaluated by measuring the change in current over a 30 days experimental period. The NiMn₂O₄/rGOH electrodes were kept in air at room temperature and their sensitivity was monitored every three days by injecting 1 mM glucose into a 0.1 M NaOH electrolyte solution. As shown in **Figure. S3.9** (Supporting Information), even after 30 days, the NiMn₂O₄/rGOH electrode maintained approximately 93.07%

of its initial current and saturated in the continuous tests for one month, suggesting that the NiMn₂O₄/rGOH fabricated in this study has excellent long-term stability.

3.3.4. Real blood test

The feasibility of the NiMn₂O₄/rGOH glucose sensor for practical applications was evaluated by amperometric measurements by the successive injection of horse (HS) and rabbit (RS) blood sera, whose glucose concentration is already known. As shown in **Figure S3.10** (Supporting Information) the NiMn₂O₄/rGOH electrode exhibited a linear and rapid response to both sera. To evaluate the accuracy of the glucose sensing performance of the NiMn₂O₄/rGOH electrode, various glucose concentrations of HS and RS were prepared and their concentrations were measured using a commercial ACCU-CHEK® Performa Blood Glucose Meter and 1.0NiMn₂O₄/rGOH electrode. As summarized in **Table 3.2**, the NiMn₂O₄/rGOH sensor had negligible error compared to those of the commercial glucometer, where the percentage difference between both measurements was only 1.230% for HS and 1.197% for RS, which confirmed that NiMn₂O₄/rGOH can monitor a wide range of glucose concentrations effectively with the same accuracy as the commercial enzymatic glucometer.

Table 3.2. Comparison of the glucose concentration between the commercial enzymatic glucometer and 1.0NiMn₂O₄/rGOH measured at various glucose concentrations.

Dilution ratio of serums in DI water	Horse blood serum (mM)		Rabbit blood serum (mM)	
	1.0NiMn ₂ O ₄ /rGOH	Glucometer	1.0NiMn ₂ O ₄ /rGOH	Glucometer
pure	3.405	3.441	6.148	6.216
1:1	2.303	2.275	3.796	3.830
1:2	1.908	1.887	2.585	2.553
1:3	1.461	1.443	2.176	2.220
1:4	1.131	1.111	1.849	1.832
1:5	0.897	0.888	1.594	1.610

Dilution ratio of serums in DI water	Horse blood serum (mM)		Rabbit blood serum (mM)	
	1.0NiMn₂O₄/rGOH	Glucometer	1.0NiMn₂O₄/rGOH	Glucometer
Error (%)	1.230		1.197	

3.4. Conclusions

A highly conductive and well-developed 3D structure composed of NiMn₂O₄ and reduced graphene oxide hydrogel was fabricated using a facile solvothermal method followed by thermal annealing under nitrogen. When NiMn₂O₄/rGOH was used for glucose sensing, it showed excellent glucose sensitivity, rapid response time, low detection limit, and long-term stability. In addition, it could determine the glucose concentration of real blood samples with negligible interference. This type of material can become a promising candidate for glucose sensors in many fields.

3.5. Supporting Information

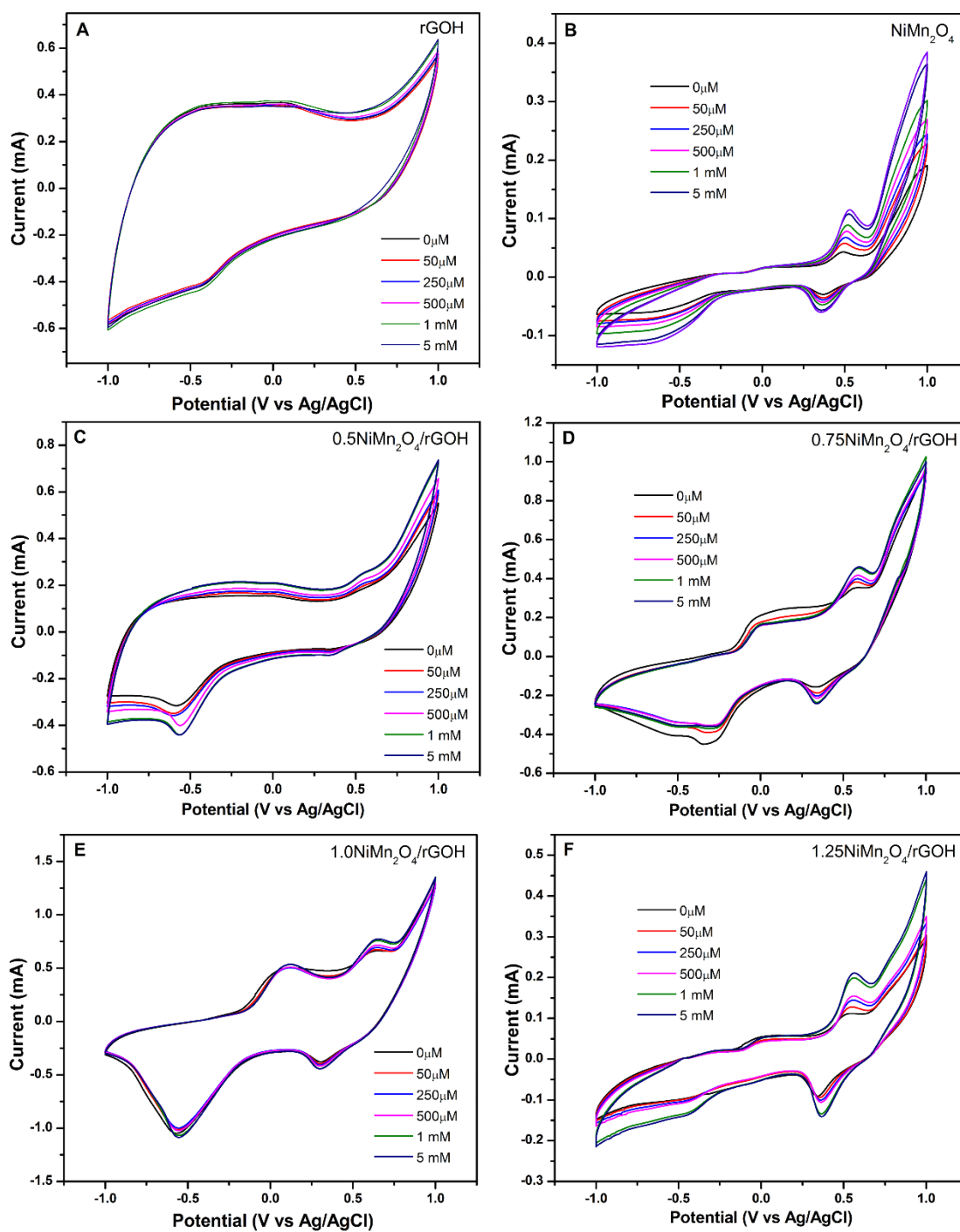


Figure S3.1. (A-F) CV curves of rGOH (A), NiMn₂O₄ (B), and the NiMn₂O₄/rGOHs (C-F) modified electrodes synthesized at different NiMn₂O₄ contents at various glucose concentrations in a 0.1 M NaOH at a scan rate of 50 mV s⁻¹.

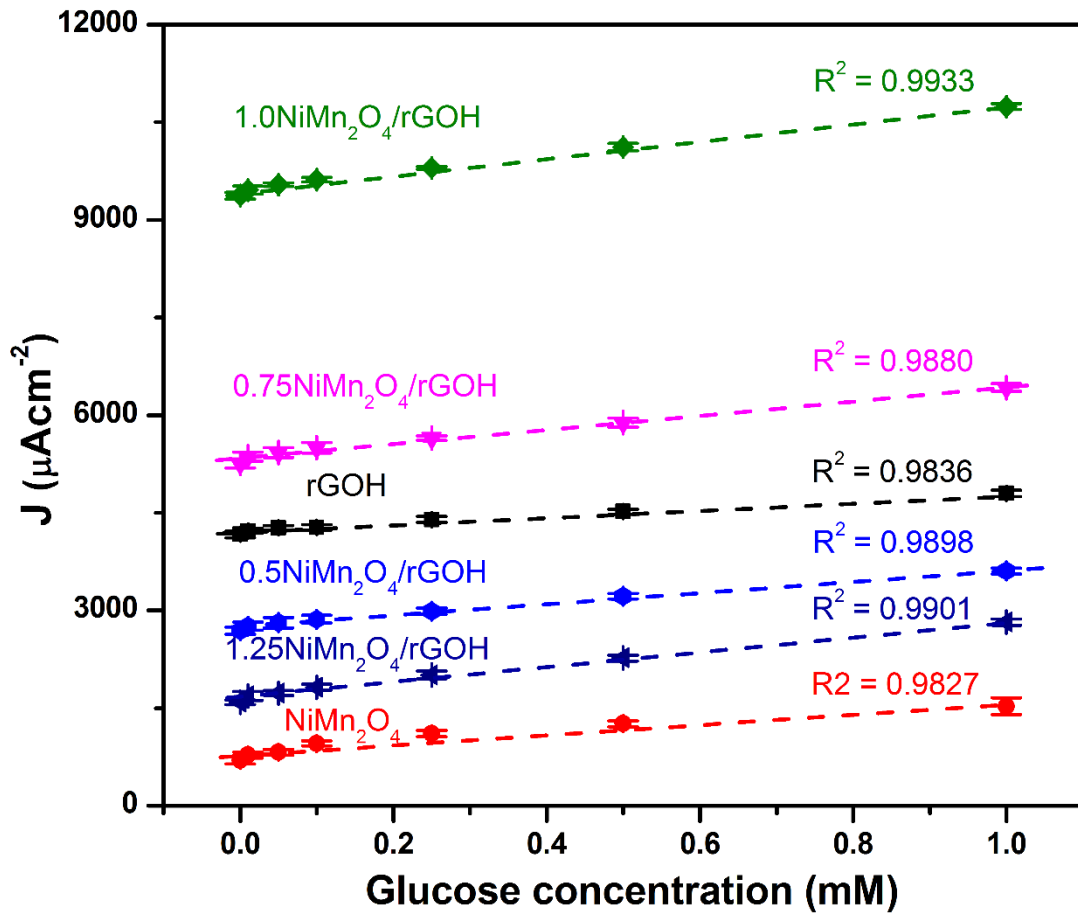


Figure S3.2. Calibration curves of sensitivity vs. concentration of glucose of the NiMn₂O₄/rGOH synthesized at different NiMn₂O₄ contents in a 0.1 M NaOH at a scan rate of 50 mV s⁻¹.

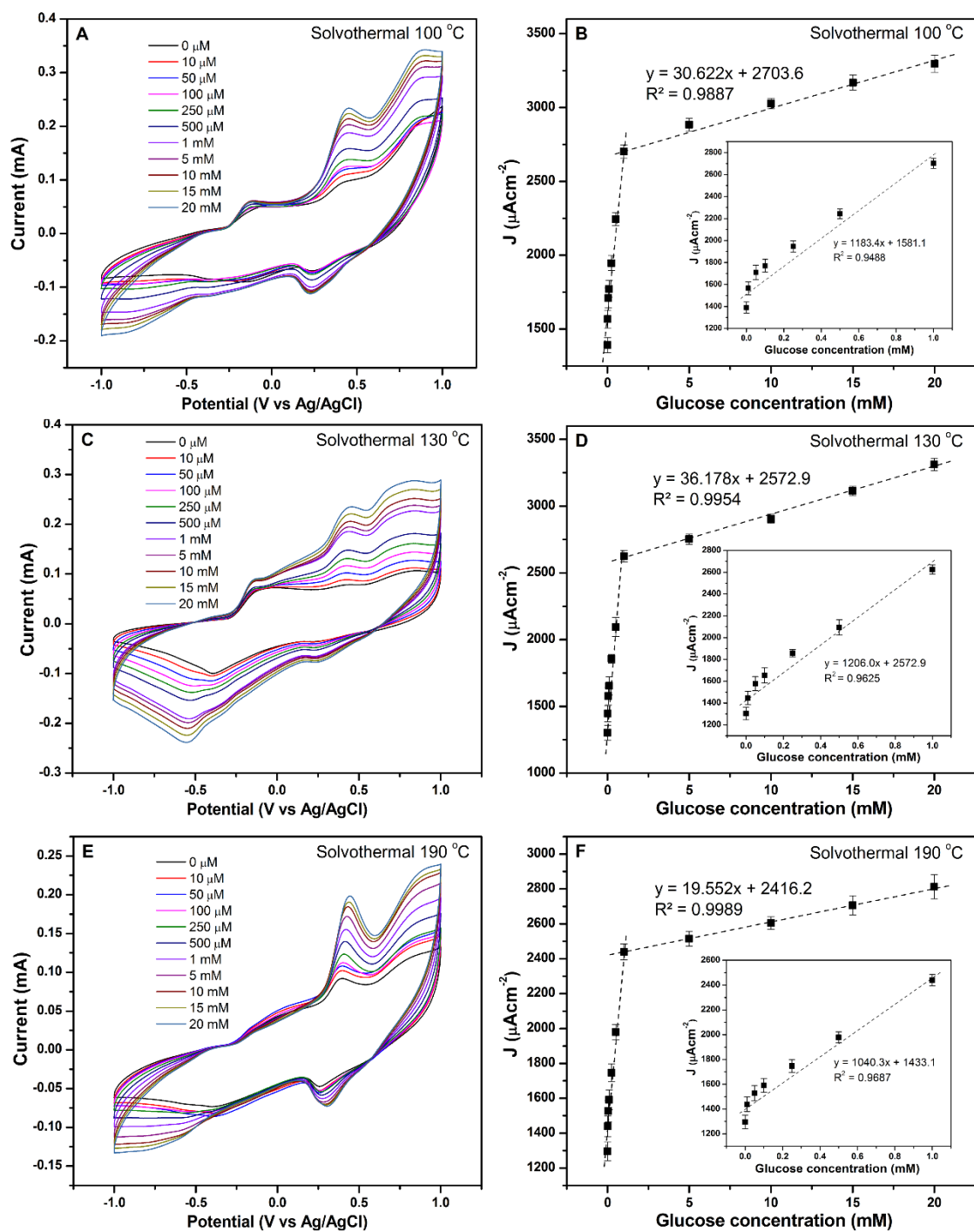


Figure S3.3. (A-C-E) CV curves and (B-D-F) corresponding calibration curves of sensitivity vs. concentration of glucose of the 1.0NiMn₂O₄/rGOH electrodes synthesized at different solvothermal temperature in a 0.1 M NaOH at a scan rate of 50 mV s⁻¹.

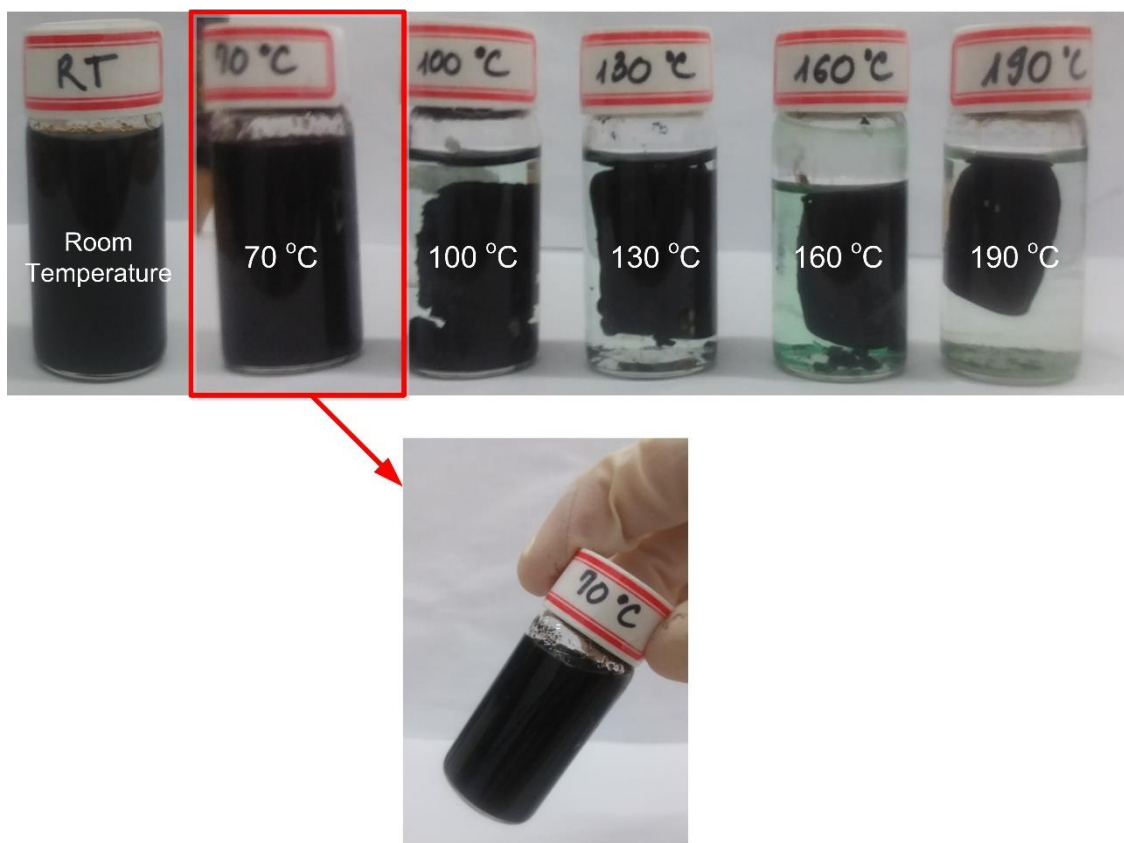


Figure S3.4. The images of various $\text{NiMn}_2\text{O}_4/\text{rGOH}$ prepared at different solvothermal temperature. Only above $130\text{ }^\circ\text{C}$ the hydrogel can be properly formed and at too high temperature hydrogel becomes hard and thus the specific area decreases (Table S3.2). Therefore, we fabricated all samples for further study in this manuscript at $160\text{ }^\circ\text{C}$.

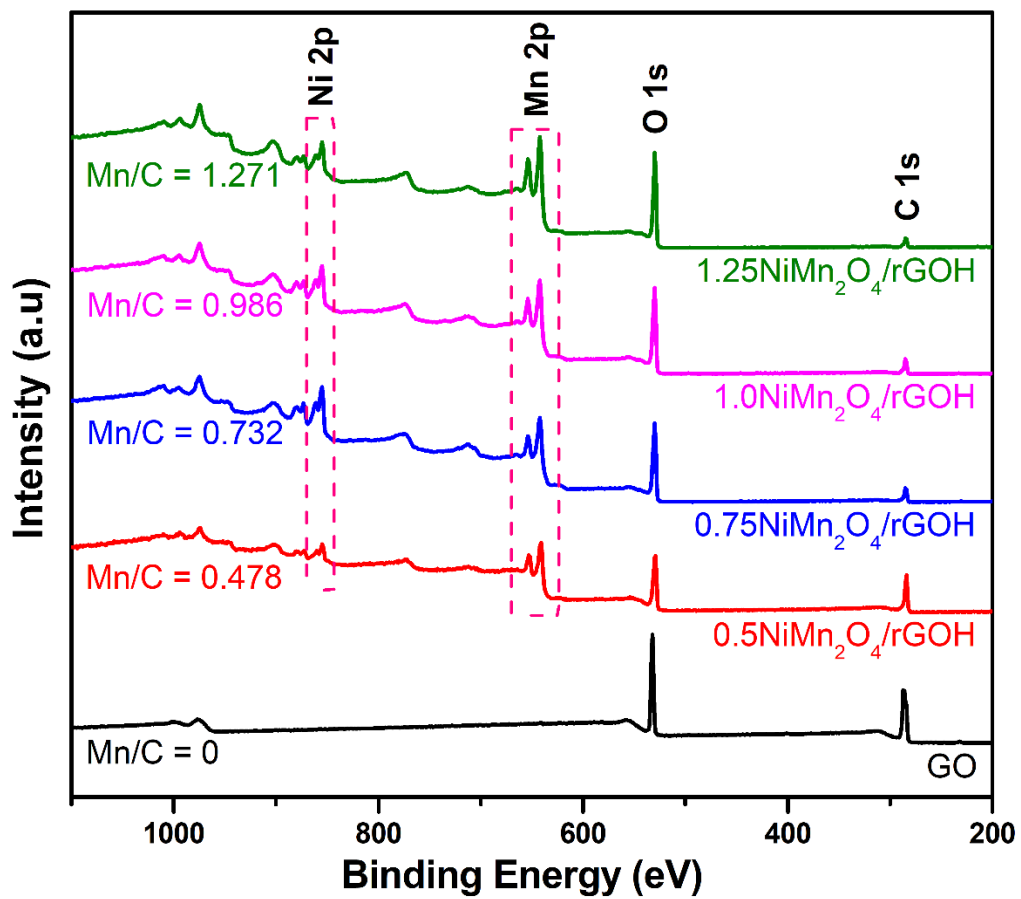


Figure S3.5. The XPS survey spectra of various $x\text{NiMn}_2\text{O}_4/\text{rGOH}$ fabricated at 160 °C.

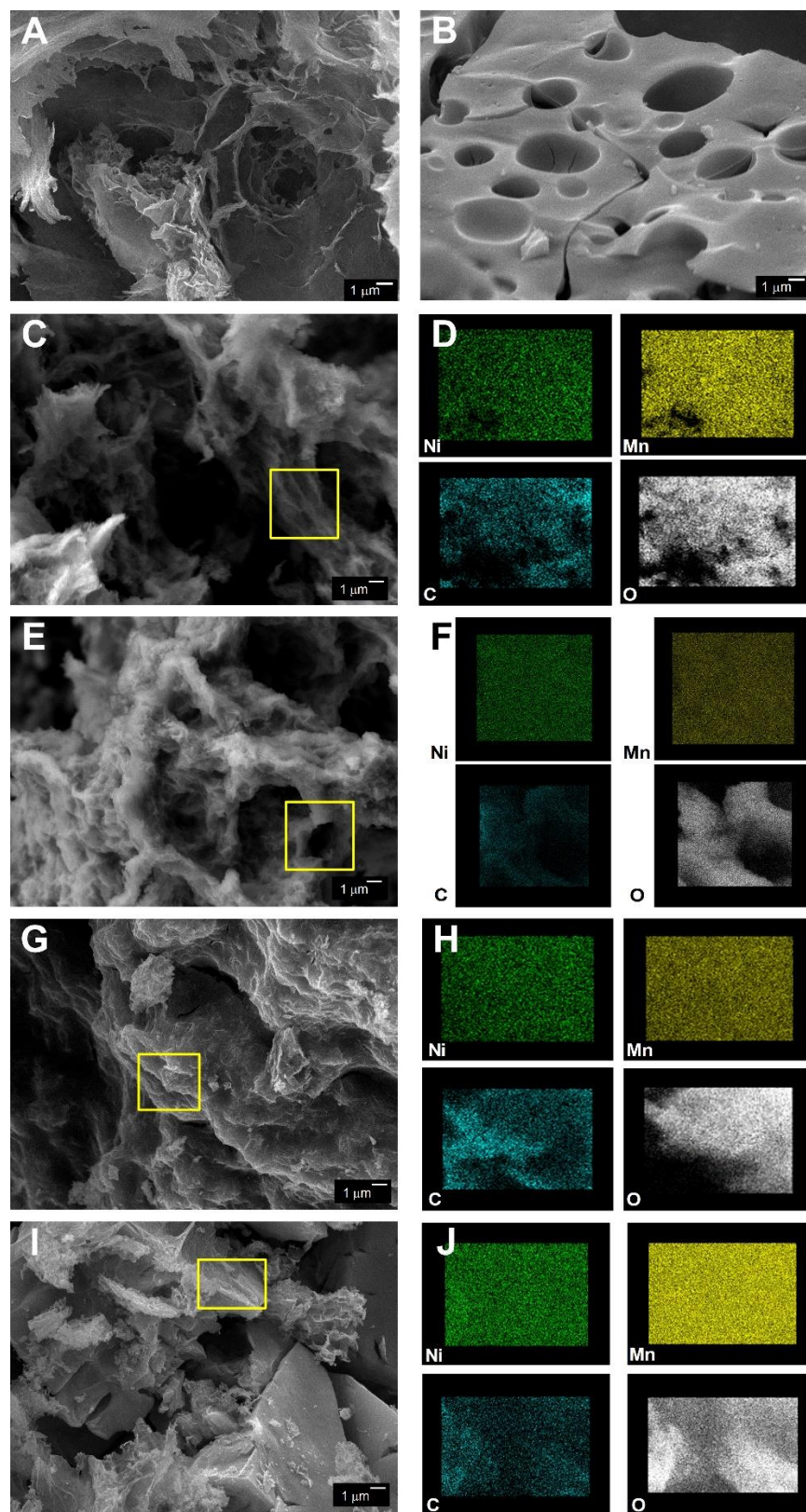


Figure S3.6. FE-SEM images of (A) rGOH, (B) NiMn_2O_4 , and FE-SEM/EDAX images for Ni, Mn, C and O elements of (C-D) $0.5\text{NiMn}_2\text{O}_4/\text{rGOH}$, (E-F) $0.75\text{NiMn}_2\text{O}_4/\text{rGOH}$, (G-H) $1.0\text{NiMn}_2\text{O}_4/\text{rGOH}$ and (I-J) $1.25\text{NiMn}_2\text{O}_4/\text{rGOH}$.

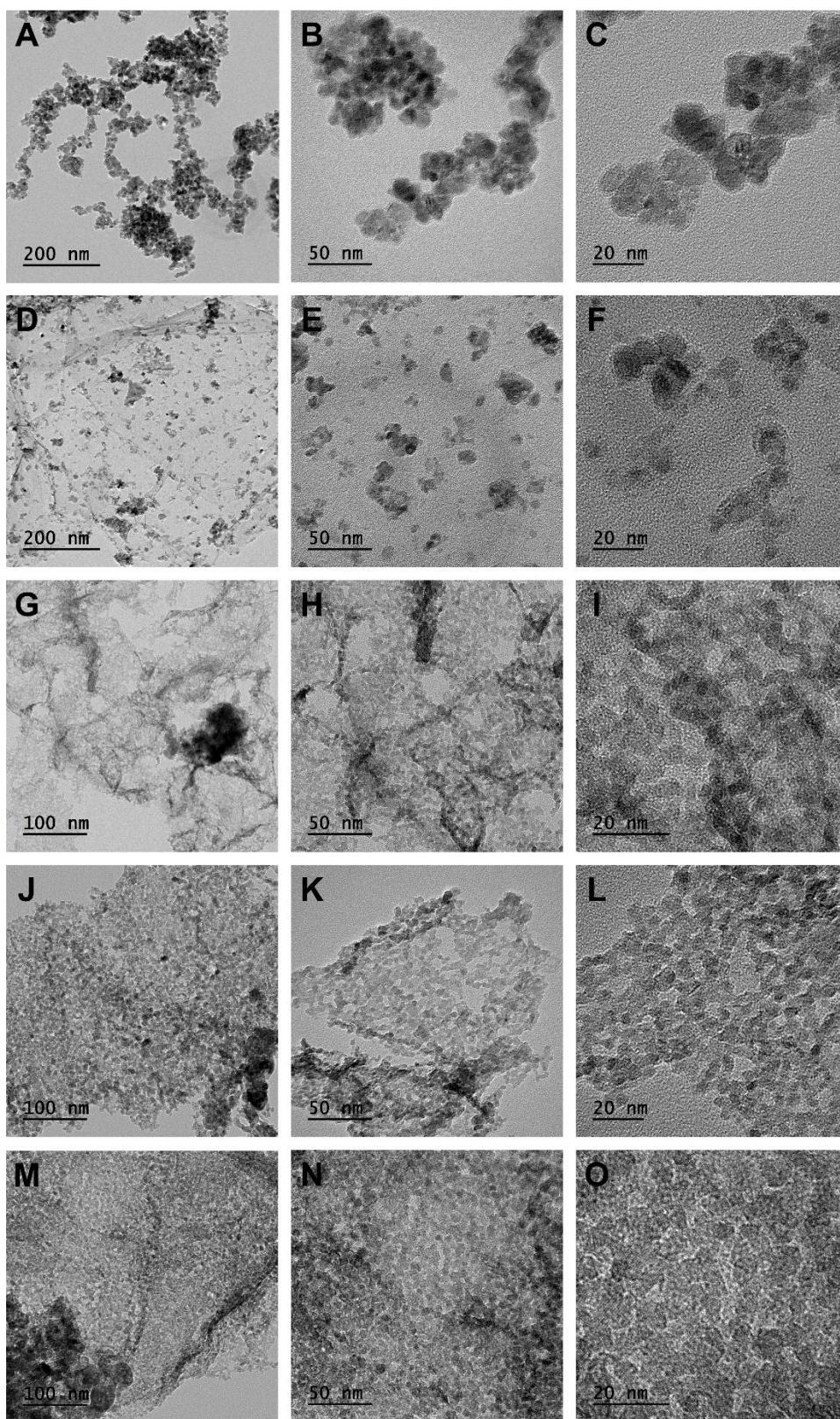


Figure S3.7. HR-TEM images of (A-C) NiMn₂O₄, (D-F) 0.5NiMn₂O₄/rGOH, (G-I) 0.75NiMn₂O₄/rGOH, (J-L) 1.0NiMn₂O₄/rGOH and (M-O) 1.25NiMn₂O₄/rGOH at various resolution.

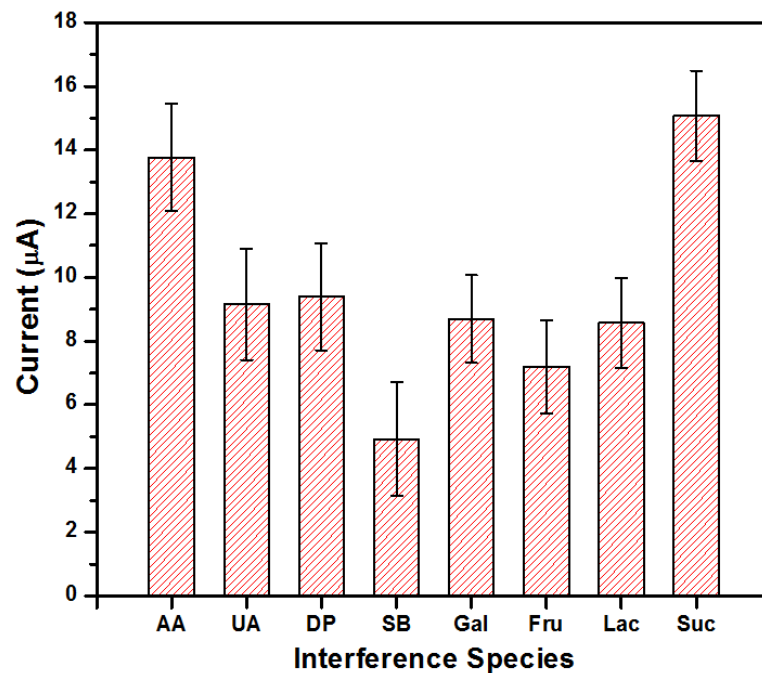


Figure S3.8. The current increase of 1.0NiMn₂O₄/rGOH electrode when 5 mM of each interfering species was injected in 0.1 M NaOH electrolyte at the applied voltage of +0.62 V. The error bars indicate the standard deviation of triplicate determination of each interfering species.

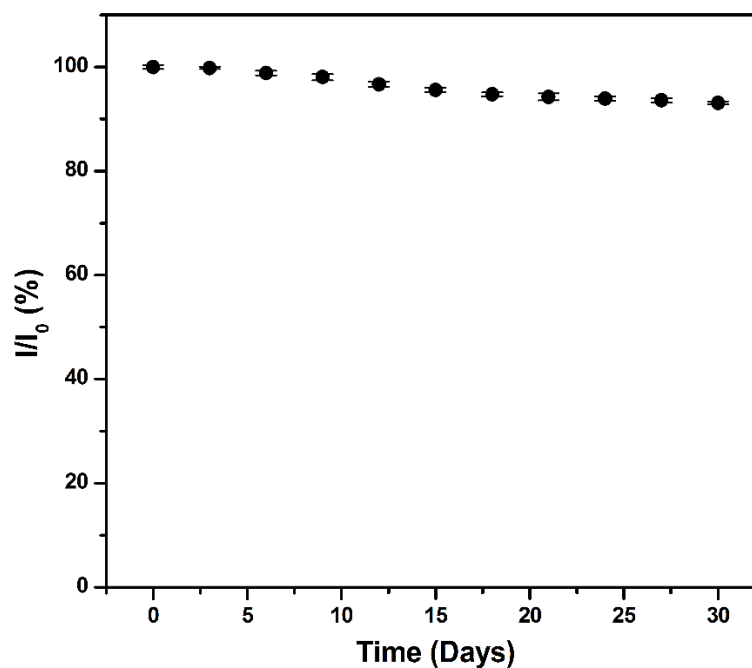


Figure S3.9. Stability of the 1.0NiMn₂O₄/rGOH based on glucose sensor at room temperature. The current was measured every 3 days for one month.

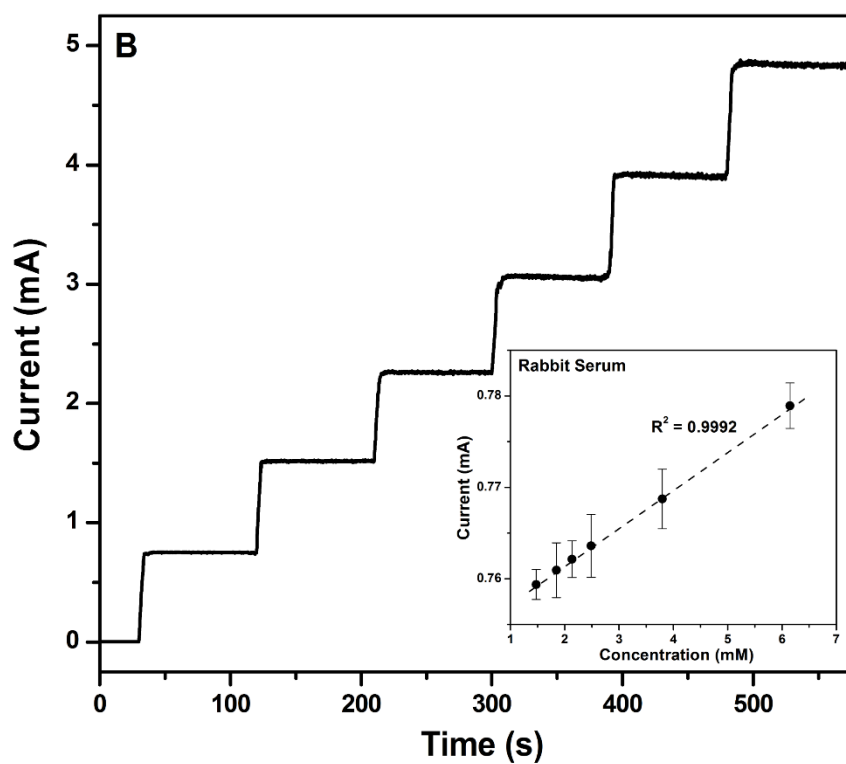
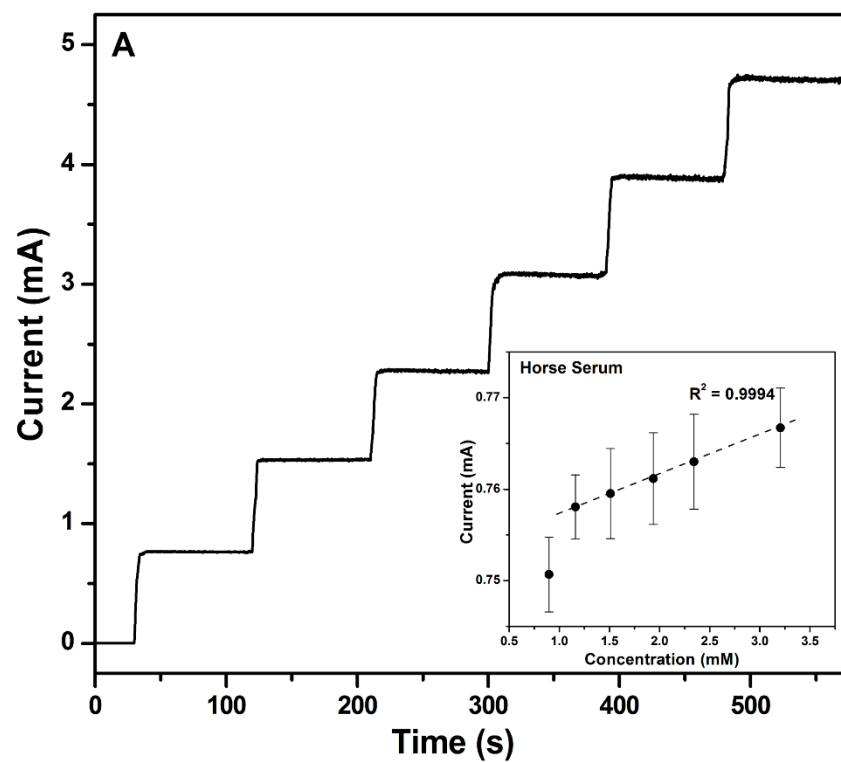


Figure S3.10. Amperometric tests of $1.0\text{NiMn}_2\text{O}_4/\text{rGOH}$ in 0.1 M NaOH at $+0.62\text{ V}$ with the successive addition of (A) Horse and (B) Rabbit serum.

Table S3.1. BET surface area of rGOH, NiMn₂O₄ and various NiMn₂O₄/rGOHs of different NiMn₂O₄ contents.

Sample	Content of NiMn ₂ O ₄ (mmol)	BET surface area (m ² g ⁻¹)
rGOH	0	404.35
NiMn ₂ O ₄	1.00	100.10
0.5NiMn ₂ O ₄ /rGOH	0.50	243.13
0.75NiMn ₂ O ₄ /rGOH	0.75	277.81
1.0NiMn ₂ O ₄ /rGOH	1.00	347.14
1.25NiMn ₂ O ₄ /rGOH	1.25	308.17

Table S3.2. BET surface areas of various 1.0NiMn₂O₄/rGOHs synthesized at different solvothermal temperatures.

Sample	Temperature (°C)	BET surface area (m ² g ⁻¹)
1.0NiMn ₂ O ₄ /rGOH	100	215.16
	130	263.19
	160	347.14
	190	183.20

Table S3.3. The glucose sensing results of our study compared to those of the previous nickel/manganese oxide-based studies.

Material electrode	Linear range	Sensitivity (μA.mM ⁻¹ cm ⁻²)	Low detection limit (LOD)	Response time (s)	Ref.
Hedgehog-NiO	0.1 – 5 μM	1052.8	1.2 μM	–	[64]
NiO/rGO	3.13 μM – 3.05 mM	1087	1 μM	~ 10	[65]
NiO-Nanofibers/rGO	0.002 – 0.6 mM	1100	0.77 μM	< 5	[53]
NiO/MWCNT	0.2 – 12 mM	–	160 μM	10	[95]
Ni/MnO ₂	0.25 μM – 3.5 mM	1040	0.1 μM	~3	[96]

Material electrode	Linear range	Sensitivity ($\mu\text{A}\cdot\text{mM}^{-1}\text{cm}^{-2}$)	Low detection limit (LOD)	Response time (s)	Ref.
MnO ₂ /MWCNT	10 μM – 28 mM	33.19	–	10	[93]
MnO ₂ /Graphene	0.04 – 2 mM	3300	10 μM	10	[97]
NiMn ₂ O ₄ /rGOH	Up to 1 mM	1310.8	1.78 μM	< 3.5	This work
	1 mM – 20 mM	59.24	0.82 mM		

Chapter 4. Highly Sensitive Non-Enzymatic Electrochemical Glucose Sensor based on Multi-functional NiO/g-C₃N₄ Hybrid Nanostructures

4.1. Introduction

Recently, graphitic carbon nitride (g-C₃N₄), a type of 2D material, has become a potential candidate in a range of applications, such as biosensors [98,99], energy storage [100-102], catalysts [103,104], photocatalysts [105], water splitting materials [26], and oxygen reduction reaction materials [106], because of its unique optical properties, thermal/chemical stability, and inexpensive synthesis process. In addition, g-C₃N₄ exhibits excellent electrical conductivity and effective charge transfer with other materials because of the high π -conjugation of the sp²-hybridized N-substituted graphite framework [107]. Therefore, the hybridization of nanomaterials with g-C₃N₄ can enhance their original properties for a range of applications, particularly in electrochemical sensors and energy storage.

In this regard, nanomaterials with high electrocatalytic ability towards glucose oxidation, including metal and their oxide (Ag [108], Au [109], Pt [13], NiO [52], CuO [61], Co₃O₄ [39]...), or composite materials [110,111], have been studied widely as an electrode material for non-enzymatic glucose sensors. Among them, NiO has attracted considerable interest as an electrode material in electrochemical reactions because of its good stability, low cost, and high catalytic activity towards the glucose oxidation reaction [112,113]. Thus far, different morphologies of NiO have been demonstrated using a range of preparation methods and their morphology-dependent properties have also been widely studied [36-38]. On the other hand, the low conductivity and sensitivity of the pristine NiO electrode should be solved before NiO can be used as an electrode material for glucose detection. In this regard, a hybrid of NiO with highly conductive materials can lead to improved electrical and electrochemical properties [74].

Previous studies have shown that the hybridization of electrocatalysts, such as NiMn₂O₄ (Chapter 3) or Co₃O₄ [39] with conductive reduced graphene oxide can strongly improve their

electrocatalytic activity. In this study, the NiO/g-C₃N₄ hybrid structure (NC) was prepared using a controlled thermal treatment under a nitrogen atmosphere. The structure was then employed as an electrode material for non-enzymatic glucose sensors and symmetric supercapacitors. The electrochemical properties of NC were examined by cyclic voltammetry. The NC exhibits extremely high glucose sensitivity, up to 5387.1 $\mu\text{A mM}^{-1}\text{cm}^{-2}$, which is one of the highest values ever reported. This also shows a low detection limit, excellent selectivity, good long-term stability, and rapid response towards glucose. When monitoring the glucose level in real blood serum, the results were comparable to the enzyme-based commercial glucose sensor. A flexible glucose sensor was also fabricated using NC as an electrode material, which could maintain its sensitivity, even after more than 100 severe bending tests.

4.2. Experimental details

4.2.1. Materials

Nickel (II) chloride hexahydrate (NiCl₂·6H₂O), urea (CO(NH₂)₂), melamine, sodium hydroxide (NaOH), ethanol 99.9% (C₂H₅OH), nafion, isopropanol (IPA), carbon (C), D-(+)-glucose, D-(-)-fructose, maltose, lactose, galactose, sucrose, l-cystine (L-cys), glycine (Glys), ascorbic acid (AA), uric acid (UA), sorbitol (Sor), dopamine (DA), horse serum (HS), and rabbit serum (RS) were purchased from Sigma-Aldrich Co. (USA). All reagents were used as received. Deionized (DI) water was used throughout the experiments.

4.2.2. Synthesis of NiO/ g-C₃N₄ hybrid materials

Ni(OH)₂ was fabricated using a facile hydrothermal treatment method. First, 2.5 g of NiCl₂·6H₂O and 1.0 g of CO(NH₂)₂ were dissolved in DI water under stirring until the solution became clear. The solution was then transferred to a Teflon-stainless steel autoclave and kept at 150 °C for 3 h. The green product was washed several times by DI and ethanol and dried overnight at 80 °C.

The NC was fabricated by $\text{Ni}(\text{OH})_2$ and melamine. First, $\text{Ni}(\text{OH})_2$ and melamine were mixed and ground by a mortar for 10 min. The mixture was treated thermally under a nitrogen environment (N_2) up to $370\text{ }^\circ\text{C}$ with a ramping rate of $10\text{ }^\circ\text{C}$ per min. The resulting products were ground again, washed with DI and ethanol, and dried at $80\text{ }^\circ\text{C}$. A range of hybrid materials were fabricated and are labeled as $\text{NC}(x)$, where x indicates the mass ratio of the precursor melamine and $\text{Ni}(\text{OH})_2$. **Figure 4.1** shows the procedure for NC synthesis. The mixing ratio of melamine and $\text{Ni}(\text{OH})_2$ was confirmed by TGA (**Figure S4.1** – Supporting Information).

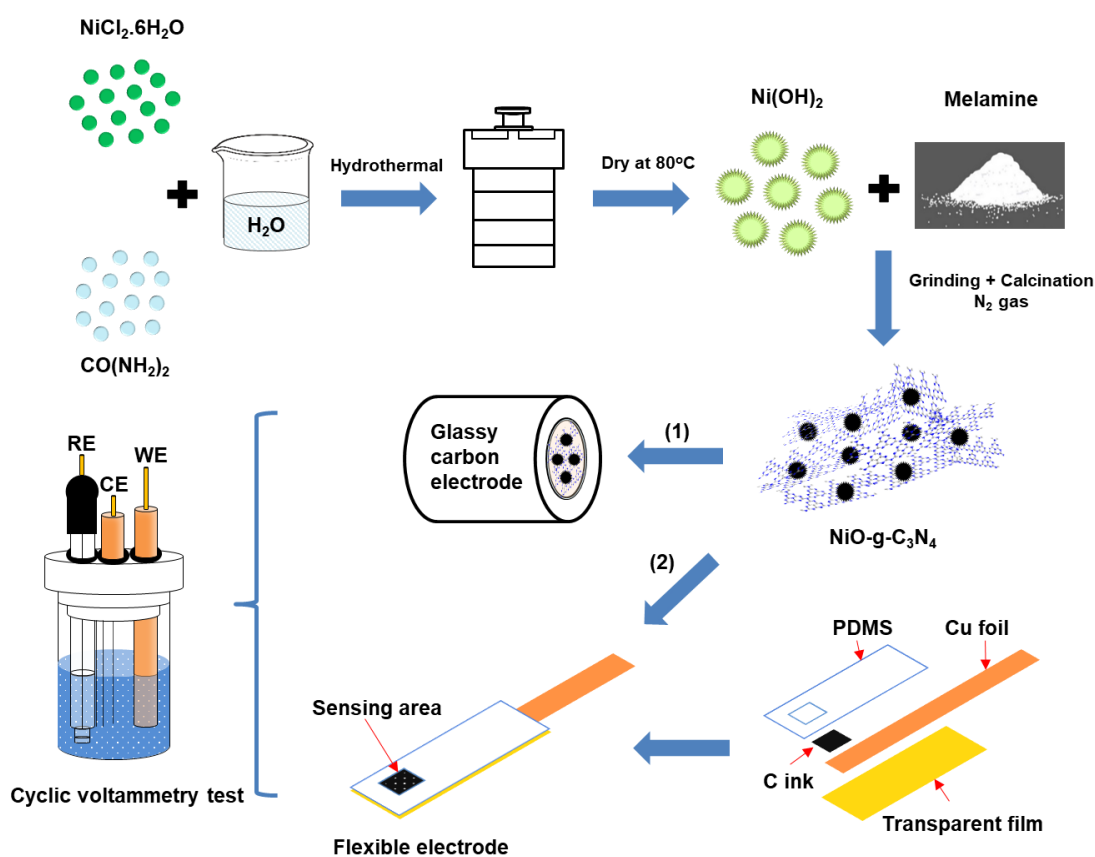


Figure 4.1. Schematic diagram of the preparation process of $\text{NiO/g-C}_3\text{N}_4$ hybrid materials (NC) and NC based electrodes.

4.2.3. Preparation of the $\text{NiO/g-C}_3\text{N}_4$ modified electrodes

The NC was decorated on a glassy carbon electrode (GCE, 3 mm of diameter), which had been polished with alumina and diamond slurries and rinsed with DI water. A NC slurry was prepared by dispersing 1.0 mg of the sample in $50\text{ }\mu\text{L}$ nafion in an isopropanol solution (5 wt.%).

Subsequently, a 10 μL solution was drop-coated on a GCE and dried at room temperature. The flexible NC/GCE working electrode was prepared except that the slurry of the NC composite was decorated onto the C ink/copper foil/transparent film (**Figure S4.8** - Supporting Information).

4.2.4. Instrumental analysis

Field-emission scanning electron microscopy (FE-SEM, JSM-7600F, JEOL, Japan) was carried out at an acceleration voltage of 15 kV. High-resolution transmission electron microscopy (HR-TEM, JEM-2100F, JEOL, USA) images were performed at an accelerating voltage of 100 kV. Fourier transform infrared (FT-IR, Nicolet 380, iS5, Thermo Fisher, USA) spectroscopy was conducted. X-ray diffraction (XRD, Rigaku, Japan) was performed using Cu $K\alpha$ radiation. X-ray photoelectron spectroscopy (XPS, ESCALAB 250Xi, Thermo Fisher Scientific, USA) was conducted using an Al $K\alpha$ X-ray source. Thermogravimetric analysis (TGA, TGA Q50, TA Instruments, USA) was carried out in the nitrogen environment. The specific surface area was measured by nitrogen adsorption/desorption isotherm analysis on a Micromeritics ASAP 2020 (USA) apparatus and calculated using the Brunauer-Emmett-Teller (BET) method.

All electrochemical measurements were performed on an electrochemical workstation (Bio Logic, SP-50, USA) in a standard three-electrode cell. The NC/GCE was used as the working electrode with a platinum wire and Ag/AgCl as the counter and reference electrodes, respectively. The measurements for the glucose sensor were carried out in a 0.1 M NaOH solution at room temperature.

4.3. Results and Discussion

4.3.1. Characterization of pristine g-C₃N₄, NiO and NiO/g-C₃N₄

To investigate the functional groups, the FT-IR spectra of the NC(x) and pristine g-C₃N₄ were recorded, as shown in **Figure 4.2**. The red dashed lines in the range of 1150 – 1630 cm^{-1} represent the typical stretching vibration of the C-N aromatic rings. The absorption peaks centered at 1244, 1322, and 1408 cm^{-1} were assigned to the stretching vibration mode of C-N,

C=N, and C=C in aromatic amine, respectively [114]. The peaks at 1556 and 1630 cm^{-1} correspond to the C=N stretching vibration modes of the tri-s-triazine structure. In addition, the characteristic out-of-plane bending vibration of the tri-s-triazine unit as the main peak was observed at 806 cm^{-1} for all samples, which demonstrates the presence of g- C_3N_4 [105]. As noted by the black-colored line, the peak at 460 cm^{-1} in all the NC(x) corresponds to the Ni-O stretching vibration [115], which confirmed the successful fabrication NiO/g- C_3N_4 hybrid structures.

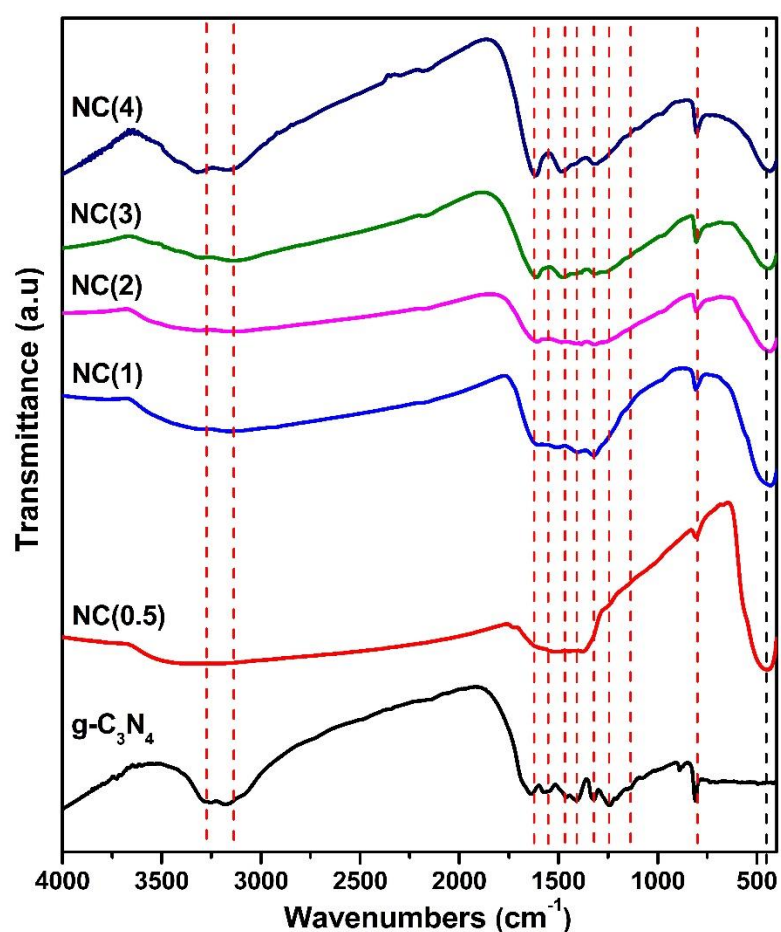


Figure 4.2. FT-IR spectra of pure g- C_3N_4 and NC(x) with various $\text{Ni}(\text{OH})_2$ and melamine mass ratios.

XRD was performed to determine the crystalline and phase structure of NC(x) after the thermal treatment, as shown in **Figure 4.3**. The XRD pattern of g- C_3N_4 heat treated at 370 $^{\circ}\text{C}$ showed many XRD peaks that were similar to those of pristine melamine (**Figure S4.2(A)** – Supporting Information). On the other hand, the XRD pattern of g- C_3N_4 calcined at 550 $^{\circ}\text{C}$

showed a graphitic carbon nitride peak. The characteristic peaks shown in $g\text{-C}_3\text{N}_4$ calcined at $550\text{ }^\circ\text{C}$ at 12.79° and 27.02° 2θ were assigned to the (100) and (002) planes of $g\text{-C}_3\text{N}_4$ (JCPDS Card No 87-1526), which represents the stacking of the motif and conjugated $\pi\text{-}\pi$ systems in the aromatic unit of $g\text{-C}_3\text{N}_4$, respectively [105]. The XRD patterns of $\text{NC}(x)$ exhibited sharper NiO peaks originating from the $\text{Ni}(\text{OH})_2$ precursor (**Figure S4.2(B)** – Supporting Information), which confirms the high crystallinity of NiO after high temperature thermal treatment. The other peaks observed at 44.37° and 51.76° 2θ correspond to the (111) and (200) crystal plane of the Ni phase. Interestingly, the (002) plane can be observed clearly in $\text{NC}(x)$, had been calcined at $370\text{ }^\circ\text{C}$, because of the catalytic effect of NiO, as observed by TGA (**Figure S4.1** – Supporting Information).

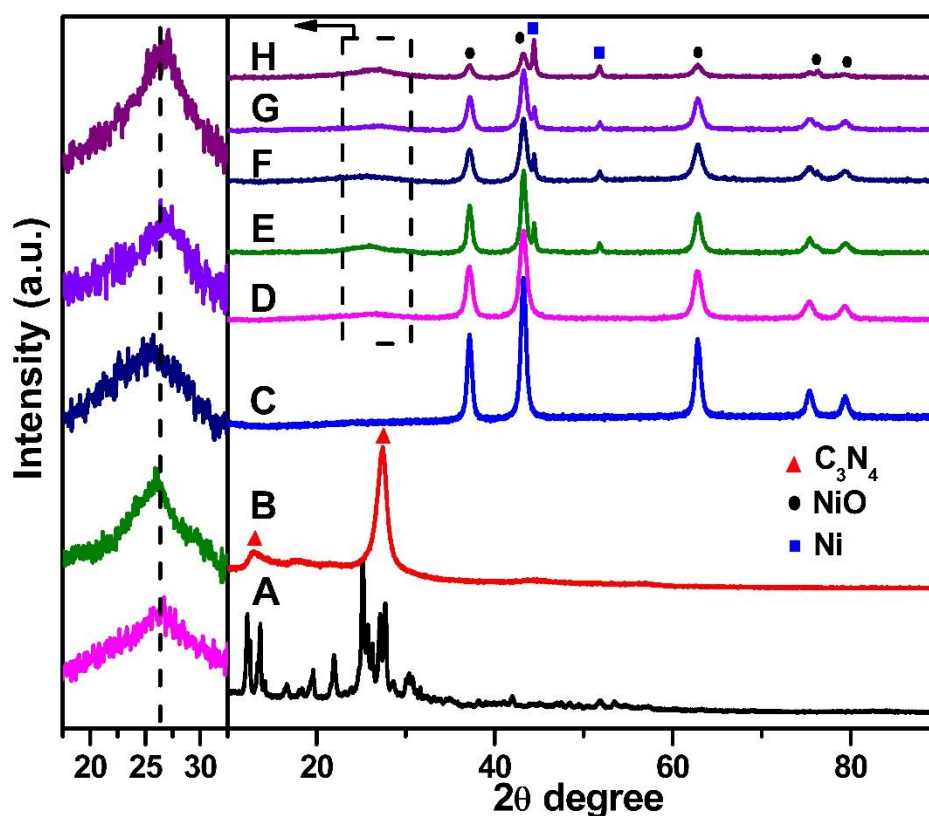


Figure 4.3. XRD patterns of (A) $g\text{-C}_3\text{N}_4$ (calcined at $370\text{ }^\circ\text{C}$), (B) $g\text{-C}_3\text{N}_4$ (calcined at $550\text{ }^\circ\text{C}$), (C) NiO and (D-H) various $\text{NC}(x)$ with $x = 0.5, 1, 2, 3, 4$ corresponding to D, E, F, G and H, respectively.

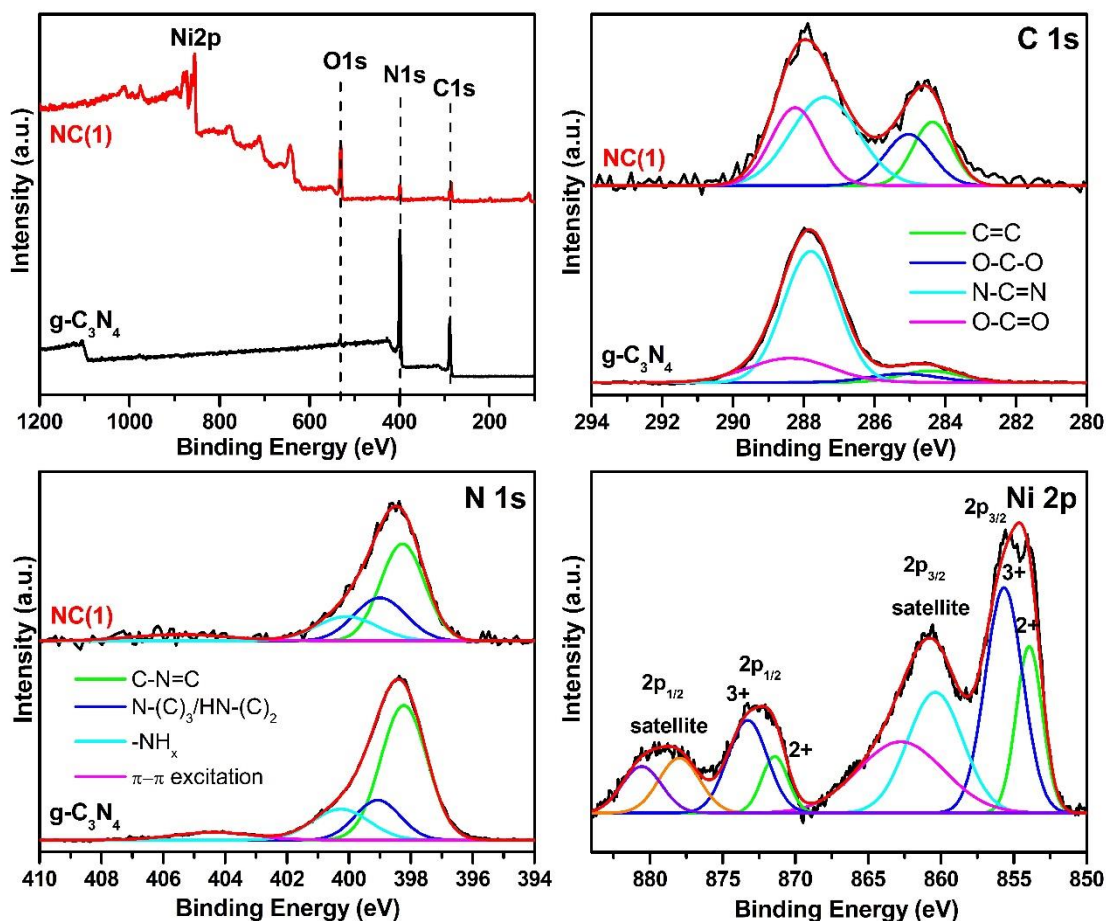


Figure 4.4. (A) XPS survey and high-resolution (B) C 1s, (C) N 1s, and (D) Ni 2p XPS spectra of pristine $g\text{-C}_3\text{N}_4$ and NC(1) composite.

The oxidation state of carbon, nitrogen, and nickel in NC(1) and pure $g\text{-C}_3\text{N}_4$ were examined by XPS. **Figure 4.4** presents the XPS survey and high-resolution spectra of C 1s, N 1s, and Ni 2p of $g\text{-C}_3\text{N}_4$ and NC(1). As shown in **Figure 4.4(A)**, $g\text{-C}_3\text{N}_4$ is composed of only C, N, and O but NC(1) contains Ni. Deconvolution of the C 1s spectrum revealed four peaks centered at 284.5, 287.8, 285.2, and 288.4 eV, which were assigned to sp^2 -hybridized carbon atoms (C=C), tertiary N-C=N coordination, and sp^2 -hybridized carbon with oxygen groups (O-C-O and O-C=O/N-C=O) of the $g\text{-C}_3\text{N}_4$ structure, respectively (**Figure 4.4(B)**) [116]. The high-resolution N 1s spectra (**Figure 4.4(C)**) exhibited typical characteristic peaks at 398.3, 399.0, 400.2, and 404.6 eV, which correspond to sp^2 -hybridized N (C-N=C), sp^3 -hybridized N (N-(C)₃/HN-(C)₂), amino groups with hydrogen (N-H/NH₂ group), and π - π excitation charged of $g\text{-C}_3\text{N}_4$,

respectively. The relative peak area ratio (**Tables S4.1-4.2** – Supporting Information) of C and N bonding obtained from the C 1s and N 1s spectra for the NC(1) was similar to those of g-C₃N₄, which indicates that there are no chemical changes in g-C₃N₄ after hybridization with NiO [100]. The Ni 2p core level spectrum of NC(1) (**Figure 4.4(D)**) showed two major peaks at 854.7 and 872.8 eV, which were assigned to Ni 2p_{3/2} and Ni 2p_{1/2}, respectively. The other peaks at 879.0 eV and 860.6 eV were satellite peaks of Ni 2p_{1/2}. The peaks at 853.9 and 871.4 eV after refined fitting of Ni 2p can be attributed to Ni²⁺, whereas the other peaks at 855.7 and 873.3 eV can be assigned to Ni³⁺ [111].

SEM and TEM images were obtained to examine the morphology. As shown in **Figures. 4.5(A-B)**, the pristine g-C₃N₄ exhibited layer-by-layer stacked structures and the pure NiO revealed particles with an urchin structure. On the other hand, the NiO/g-C₃N₄ hybrid exhibited a flake-like shape with NiO dispersed over the g-C₃N₄ surface (**Figure 4.5(C)**). Similar to the XPS results, only C, O, N, and Ni were observed by EDS (**Figure 4.5(D)**). As shown in **Figure S4.3** and **Table S4.3** (Supporting Information), at a low NiO ratio, the surface area increased due to less stacking of g-C₃N₄ and the reduced agglomeration of NiO particles. At an excessive NiO ratio, however, the structure became more agglomerated and the BET surface area decreased. The maximum BET surface area was as high as 54.74 m² g⁻¹ at a melamine and Ni(OH)₂ precursor ratio of 1:1. As shown in **Figure S4.4** (Supporting Information), in contrast to the pristine g-C₃N₄, NC(1) exhibited type IV (Brunauer, Deming, Deming, and Teller classification) adsorption and desorption behavior, indicating that a wide range of mesopores had formed by the NiO and graphitic carbon nitride nanosheets. A well-developed porous nanostructure can promote an electrochemical reaction, kinetic reversibility, and electrolyte accessibility.

The TEM and HR-TEM (**Figures. 4.5(E-F)**) show that g-C₃N₄ and NiO are mixed together. The Fast Fourier Transform (FFT) of the selected regions clearly show crystal planes corresponding to the (100) and (002) planes of the hexagonal graphitic carbon nitride with a lattice spacing of 2.2 and 3.4 Å, respectively [116,117]. In addition, the (200) plane of the cubic NiO phase (d = 2.0 Å) [110] can be also observed.

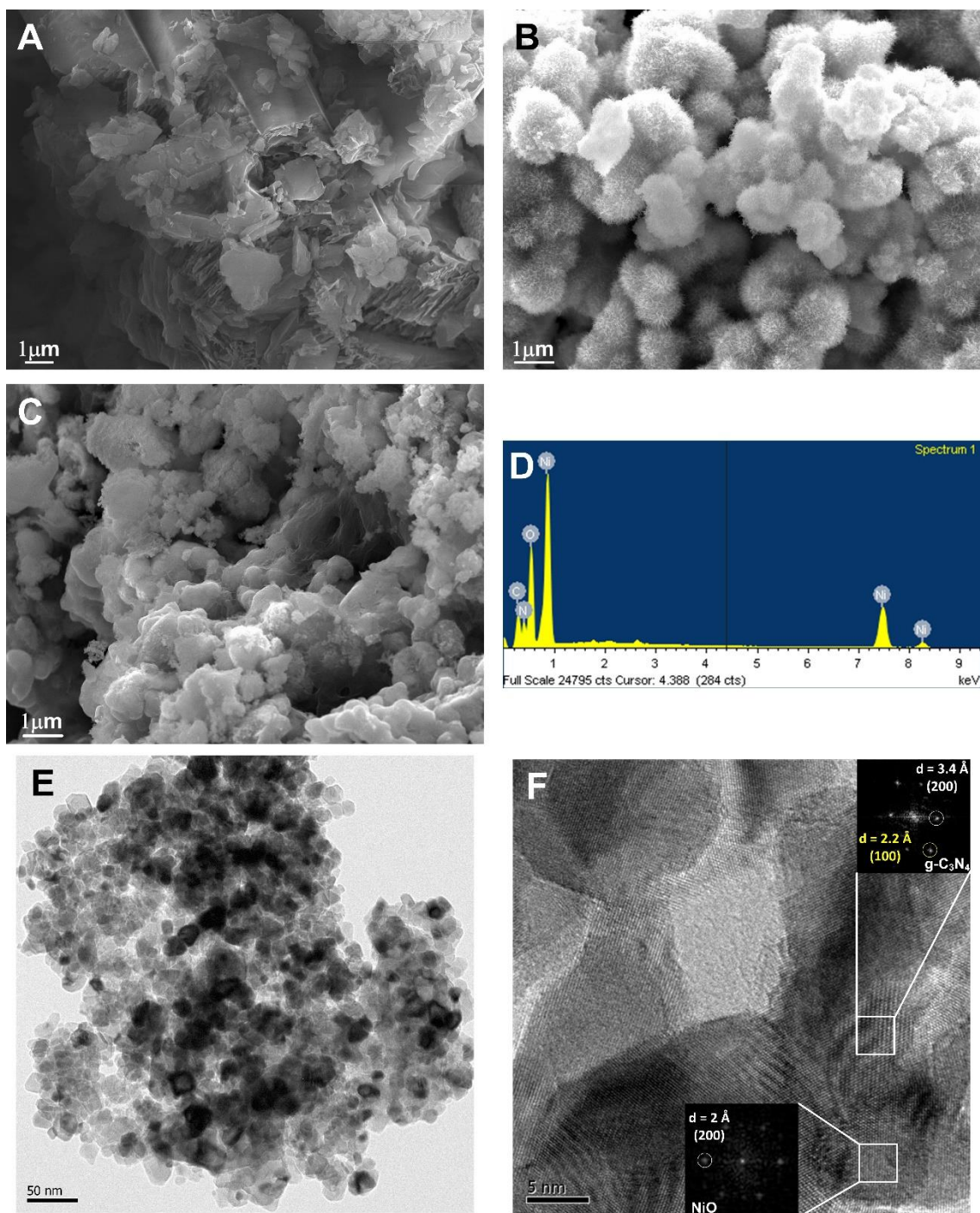


Figure 4.5. FE-SEM images of (A) pristine $g\text{-C}_3\text{N}_4$ (calcined at $370\ ^\circ\text{C}$), (B) NiO and (C) NC(1). (D) EDS spectrum of NC(1). (E) TEM and (F) HR-TEM images of NC(1) and the inset images are the FFT patterns of $g\text{-C}_3\text{N}_4$ and NiO.

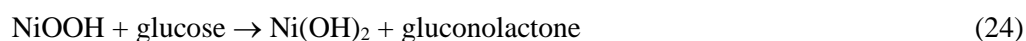
4.3.2. Electrochemical glucose sensing with NiO/g-C₃N₄ electrodes

The electrochemical active surface area (A_e) was estimated by cyclic voltammetry (CV) to evaluate the effective loading of the samples on the GC electrode surface based on the Randles–Sevcik equation [61] (as presented in **Chapter 2**):

$$I_p = 2.69 \times 10^5 \cdot A_e \cdot n^{3/2} \cdot D^{1/2} \cdot \nu^{1/2} \cdot C \quad (i)$$

where I_p is the redox peak current (A); n is the number of electrons participating in the redox reaction ($n = 1$); D is the diffusion coefficient in $K_3(Fe(CN)_6)$ ($0.67 \times 10^{-5} \text{ cm}^2 \text{ s}^{-1}$); ν is the scan rate (mV s^{-1}) and C is the concentration of the redox probe molecule in solution (mol cm^{-3}). The CV curves were obtained in a 0.2 M KCl electrolyte solution containing 5 mM $K_3(Fe(CN)_6)$ at a scan rate of 50 mV s^{-1} . A very high electrochemical active surface area was obtained from NC(1) ($0.733 \times 10^{-3} \text{ cm}^2$), which is five times higher than that of g-C₃N₄ ($0.146 \times 10^{-3} \text{ cm}^2$) and 1.5 times higher than that of NiO ($0.486 \times 10^{-3} \text{ cm}^2$), suggesting the synergetic effects between NiO and g-C₃N₄ for the electrocatalytic reactions.

The electrocatalytic activities of pristine g-C₃N₄, NiO and NC(1) towards glucose were measured by CV in a 0.1 M NaOH electrolyte with and without 500 μM glucose at a scan rate of 50 mV s^{-1} . As shown in **Figure 4.6**, the background current (without glucose) of NC(1) was higher than those of pristine g-C₃N₄ and NiO, which agrees well with the highest electrochemical surface area of NC(1). Pristine g-C₃N₄ showed no noticeable oxidation-reduction (redox) peaks both with and without glucose conditions. On the other hand, neither NC(1) nor NiO exhibited distinct redox peaks at +0.4 and +0.68 V, corresponding to Ni^{2+}/Ni^{3+} redox peaks [53]. The electrochemical oxidation of glucose on the NiO and NC(1) proceeded via two steps involving the formation of strong oxidizing species (Ni^{3+}) that are shown in the following equations:



During the anodic scan, the nickel oxyhydroxide (NiOOH) can oxidize glucose to gluconolactone, leading to an increase in current at a given potential, and vice versa during the cathodic scan [94]. The enhanced electrochemical performance of NiO/g-C₃N₄ compared to bare NiO can be attributed to the high specific surface area, high conductivity, and rapid electron transfer by g-C₃N₄.

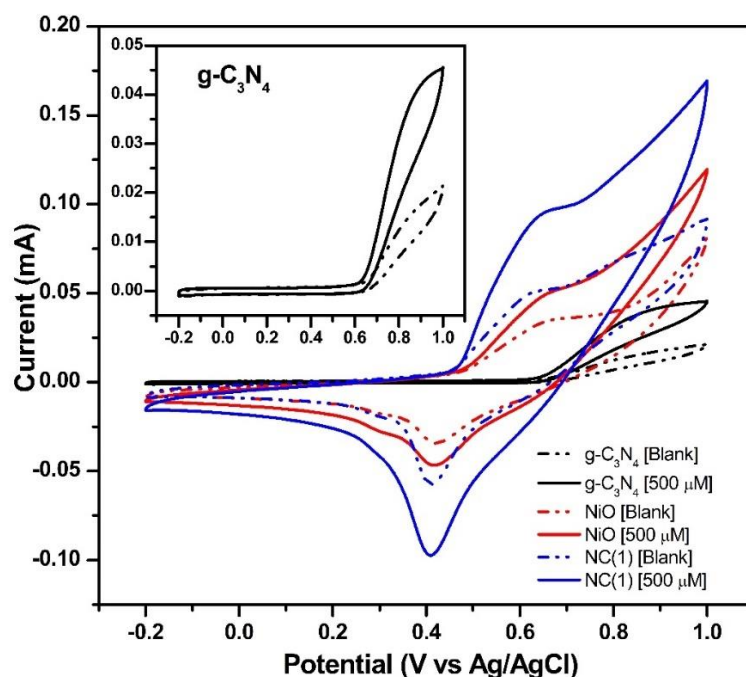


Figure 4.6. CV curves of pure g-C₃N₄, NiO and NC(1) in 0.1 M NaOH at a scan rate of 50 mV s⁻¹ with (solid line) and without (dash dot line) 500 μM glucose, respectively.

To explore the electrochemical redox process, the change in current at various scan rates was studied in the presence of 1 mM glucose. Obviously, the current increased and the peak shifted slightly to a higher potential with increasing scan rate. **Figure 4.7** shows the linear relationship between the currents of the both anodic (oxidation) and cathodic (reduction) peak of NC(1) and the square root of the scan rate in the range of 10 – 100 mV s⁻¹ with a correlation coefficient (R^2) of 0.9998 (I_{pa}) and 0.9984 (I_{pc}), respectively, suggesting that the glucose redox reaction is a typical diffusion-controlled process with rapid electron-transfer from the electrolyte to the electrode surface [66]. In addition, the shift of the anodic and cathodic peak toward the positive and negative sides, respectively, as the scan rate increases further confirms that the

oxidation of glucose on the NiO/g-C₃N₄ proceeds via surface-controlled electrochemical reactions by the adsorption of glucose and oxidized intermediates [63].

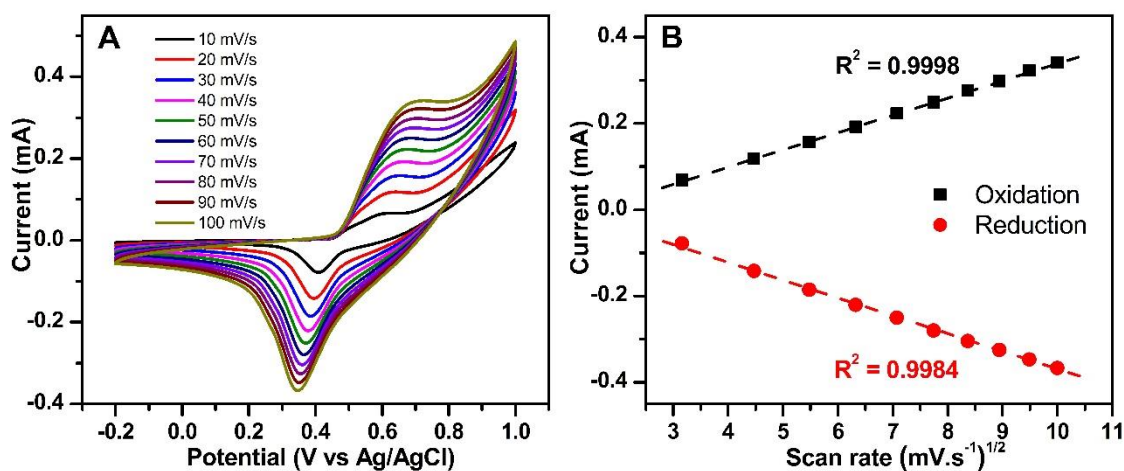


Figure 4.7. (A) CV curves of the NC(1) in 0.1 M NaOH with 1 mM glucose at different scan rates 10 – 100 mV s⁻¹. (B) Plot of the peak current versus the square root of the scan rate at an applied potential of +0.68 V.

Figure 4.8(A) shows the CV curves of the NC(1) electrode at various glucose concentrations. The redox peak currents increased gradually with increasing glucose concentration, whereas the peak potential shifted slightly positively for the oxidation peak and negatively for the reduction peak. This can be attributed to the diffusion controlled reaction at high glucose concentrations, which reveals the excellent electrocatalytic activity of the NiO/g-C₃N₄ fabricated in this study [118]. **Figure 4.8(B)** presents the calibration curve of the anodic peak current with the concentration of glucose obtained from the CV curves in **Figure 4.8(A)**; two linear relationships were defined in the ranges, 500 nM – 100 μM and 100 μM – 20 mM. The sensor based on the NC(1) electrode exhibited a sensitivity as high as 5387.1 μA mM⁻¹ cm⁻², which is one of the highest values ever reported (**Table S4.4** – Supporting Information), as well as a limit of detection (LOD) of 2.30 μM (S/N = 3). **Table S4.3** and **Figure S4.5** (Supporting Information) show the sensitivity towards glucose of pristine g-C₃N₄, NiO and various NC(x).

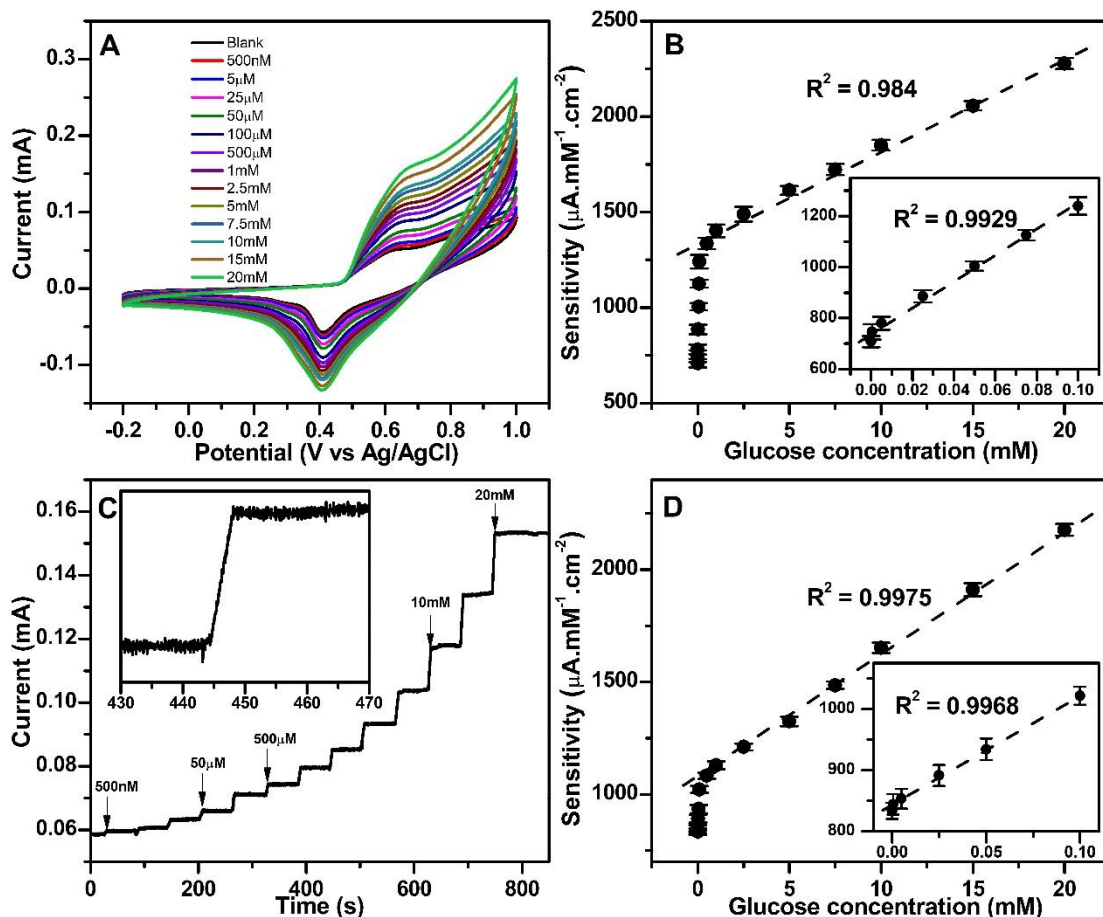


Figure 4.8. (A) CV curves of the NC(1) and (B) calibration curve from CV of NC(1) at a wide range of glucose concentrations from 500 nM to 20 mM. (C) Typical amperometric current response recorded at +0.68 V and (D) calibration curves vs. glucose concentration from amperometric with the successive addition of various glucose concentrations at 60 s intervals. Conditions: scan rate of 50 mV s^{-1} , 0.1 M NaOH electrolyte. Inset: (C) the response time to achieve steady-state current. The error bars indicate the standard deviations for triplicate measurements at each glucose concentration. Inset: (B) and (D) calibration curves at low glucose concentrations.

As summarized in **Table S4.3** (Supporting Information), NC(1) exhibited ~ 5.5 and ~ 28 times higher sensitivity than those of pristine NiO and $g\text{-C}_3\text{N}_4$, which indicates the synergetic effects between them, such as high surface area, enhanced conductivity, and effective charge transfer. As described in the BET results, the sensitivity decreases at an excessively high NiO ratio, which can be due to the agglomeration of NiO particles.

The amperometric response of the NC(1) electrode towards glucose was monitored under a constant potential of +0.68 V with the successive injection of various glucose concentrations into the 0.1 M NaOH electrolyte at 60 s intervals. As shown in **Figure 4.8(C)**, during the successive addition of glucose, a well-defined, stable, and rapid response (< 4s) of NC(1) towards glucose was observed. The amperometric response exhibited a step-like increase in current and a rapid steady-state current upon the addition of glucose. The calibration curve obtained from the amperometric test (**Figure 4.8(D)**) also exhibited excellent linearity and sensitivity as it did from the CV curves.

4.3.3. Stability, reproducibility and anti-interference property of the NiO/g-C₃N₄ electrode

The stability of the NiO/g-C₃N₄-based glucose sensor was examined by measuring its current change towards glucose for a 30 days period. The sensor was exposed to air at room temperature, and its sensitivity was obtained every three days. The current of NC(1) decreased to only 8% compared to its original current after 30 days (**Figure S4.6** – Supporting Information) and the slope became smaller, suggesting that NiO/g-C₃N₄ has good stability under ambient conditions. The reproducibility of NiO/g-C₃N₄ was also evaluated by amperometric test three times; the relative standard deviation (RSD) was 1.53%. In addition, twelve measurements of glucose on one electrode were taken upon the sequential addition of 1.0 mM glucose in 0.1 M NaOH. The RSD was 2.76%, which confirmed that the NiO/g-C₃N₄ fabricated in this study exhibited excellent reproducibility and reliability.

The selectivity of NiO/g-C₃N₄ was examined by adding interference species, including dopamine, ascorbic acid (AA), uric acid (UA), sorbitol, glycine, l-cystine, and other carbohydrate compounds, to the solution. Because the concentration of glucose in human serum is higher than those of the interference species [[53,64,119](#)], an anti-interference test was performed by the successive addition of 1.0 mM glucose and 0.1 mM of various interfering species, respectively.

As shown in **Figure 4.9**, NC(1) exhibited a negligible response towards all interfering species, which indicates the excellent selectivity towards NiO/g-C₃N₄ fabricated in this study.

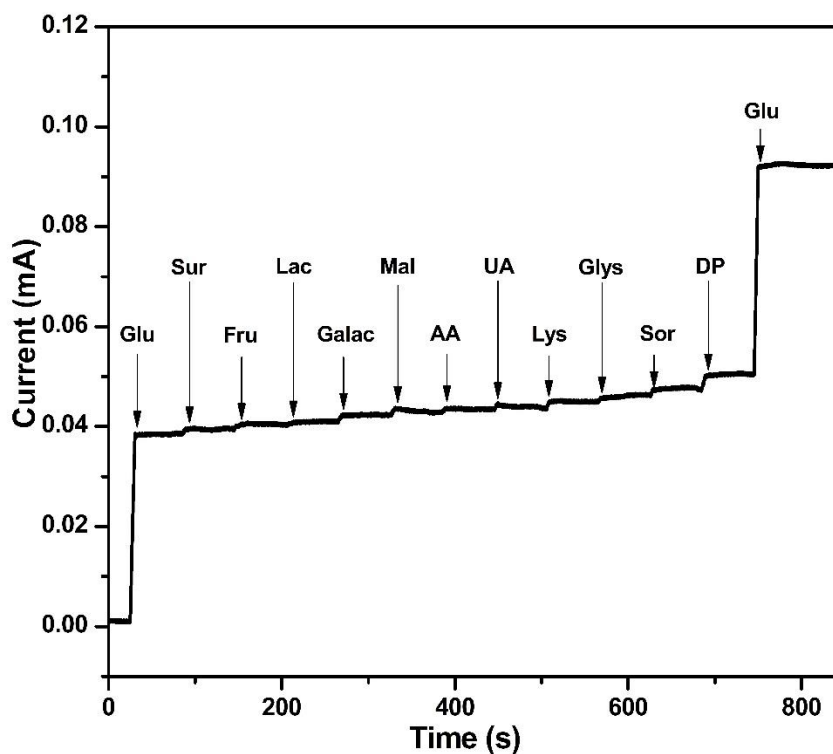


Figure 4.9. Typical amperometric response of NC(1) to the sequential addition of 1 mM glucose and 0.1 mM interferents of UA, AA, Sor, DP, Lys, Glys, galactose, fructose, lactose, maltose, and sucrose in 0.1 M NaOH electrolyte at an applied voltage of + 0.68 V

4.3.4. Real sample test

To evaluate the feasibility of monitoring the glucose level in the in real blood, the amperometric response of NiO/g-C₃N₄ was recorded with the addition of horse and rabbit blood sera, whose glucose concentration is already known from the provider. As shown in **Figure S4.7** (Supporting Information), the current increased linearly with increasing concentration of serum. To evaluate the accuracy of NiO/g-C₃N₄, the glucose concentration in real blood sera was compared with that using a commercial glucometer. **Table 4.1** lists the glucose concentration for real blood serum obtained using both a commercial ACCU-CHEK[®] Performa Blood Glucose Meter and NiO/g-C₃N₄-based glucose sensor. The mean difference was only 1.76% for HS and

3.72% for RS, which demonstrates that NiO/g-C₃N₄ fabricated in this study shows comparable glucose sensing capability to that of a commercial enzymatic glucometer.

Table 4.1. Comparison of the glucose level between NiO/g-C₃N₄ and commercial glucometer.

Dilution ratio of serums in DI water	Horse blood serum (mM)		Rabbit blood serum (mM)	
	NiO/g-C ₃ N ₄	Glucometer	NiO/g-C ₃ N ₄	Glucometer
pure	3.331	3.385	6.200	6.161
1:1	1.964	1.942	3.420	3.497
1:2	1.428	1.443	2.720	2.664
1:3	0.879	0.888	2.092	2.054
Error (%)	1.761		3.722	

4.3.5. Flexible glucose sensor based on NiO/g-C₃N₄

The NiO/g-C₃N₄ flexible glucose sensor was fabricated on PDMS and Cu foil, as shown in **Figure S4.8** (Supporting Information). The electrocatalytic properties of NC(1) on a flexible electrode were investigated by CV in 0.1 M NaOH at a scan rate of 50 mV s⁻¹. As shown in **Figure 4.10(A)**, no redox peaks were observed in the absence of glucose, whereas it exhibited significant redox peaks in the presence of glucose at approximately +0.64 V and +0.34 V, which is in agreement with the NiO/g-C₃N₄ on the GCE electrode. The sensitivity and linear range of the fabricated flexible electrochemical sensor in response to various glucose concentrations from 500 nM to 20 mM at an applied potential of +0.64 V were investigated using amperometry, as shown in **Figure 4.10(B)**. After injecting glucose, the current also increased immediately and maintained a stable current. The sensitivity and LOD of NC(1) on the flexible electrode calculated from the calibration curve shown in **Figure 4.10(C)** were 5001.9 μA mM⁻¹ cm⁻² and 5.1 μM, respectively, which are similar to those of NiO/g-C₃N₄ on the GCE electrode. To evaluate the resistance to the physical stress environment, the current was measured after performing the bending test 140 times (**Figure 4.10(D)**). The bending radius was 5 mm and bending was focused on the NiO/g-C₃N₄ part of the entire flexible electrode. There was no

significant change after bending 40 times and ~ 88.9% of the initial current was maintained after bending 140 times, which implies that NiO/g-C₃N₄ flexible glucose sensor can be used effectively in the wearable healthcare devices that can be exposed to frequent physical stress conditions.

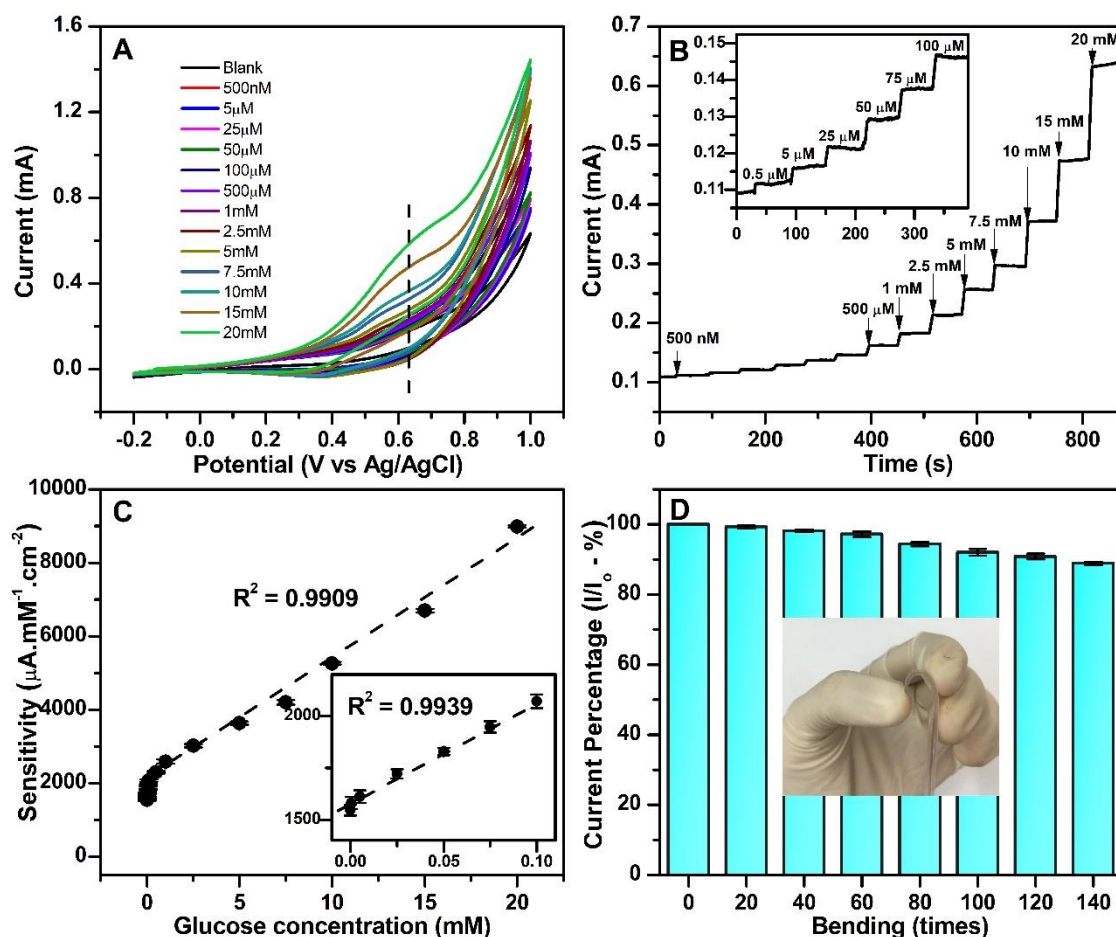


Figure 4.10. (A) CV test of NC(1)/flexible electrode in the presence of various glucose concentrations in 0.1 M NaOH at a scan rate of 50 mV s⁻¹. (B) Amperometric response of NC(1)/flexible sensor at + 0.64 V with the successive addition of glucose in 0.1 M NaOH at every 60 s. (C) Calibration curve of NC(1)/flexible sensor with the linear fitting result. (D) Current response with different bending times in 0.1 M NaOH. The inset shows a digital picture of bent NC(1) electrode.

4.4. Conclusions

A multi-functional NiO/g-C₃N₄ hybrid nanostructure was fabricated by a hydrothermal process followed by a thermal treatment. The as-synthesized NiO/g-C₃N₄-based glucose sensor exhibited an excellent sensitivity, as high as 5387.1 $\mu\text{A mM}^{-1} \text{cm}^{-2}$, wide linear range, low detection limit, rapid response, and high stability. In addition, it exhibited excellent anti-interference properties, mechanical flexibility, and allowed precise monitoring of the glucose level even real blood sera.

4.5. Supporting Information

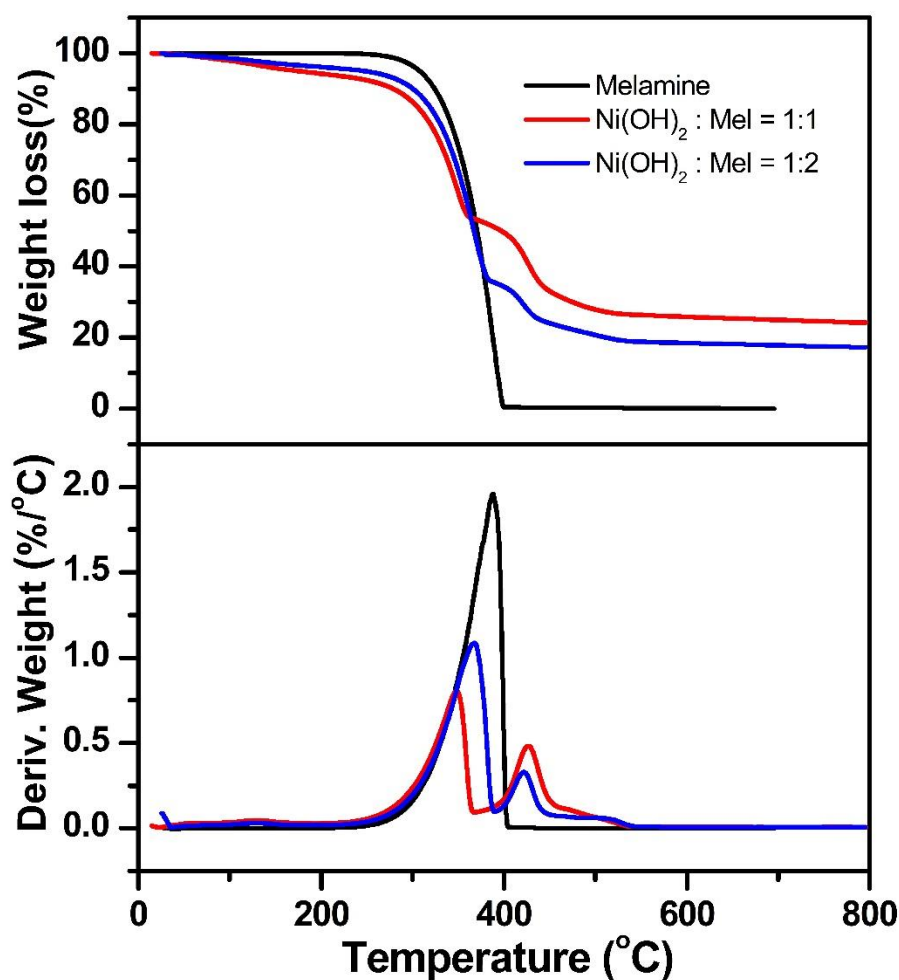


Figure S4.1. Thermal treatment process was simulated under nitrogen flow gas by TGA (top) and (DTA) analyses for melamine and as-synthesized NiO/g-C₃N₄ composites.

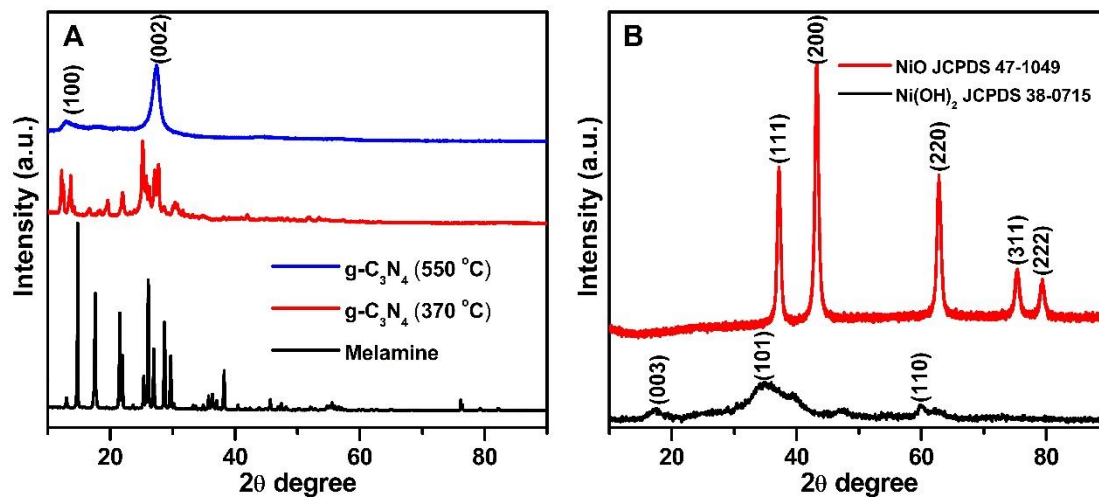


Figure S4.2. XRD patterns of (A) melamine, g-C₃N₄ calcinated at 370 and 500 °C; (B) Ni(OH)₂ and NiO.

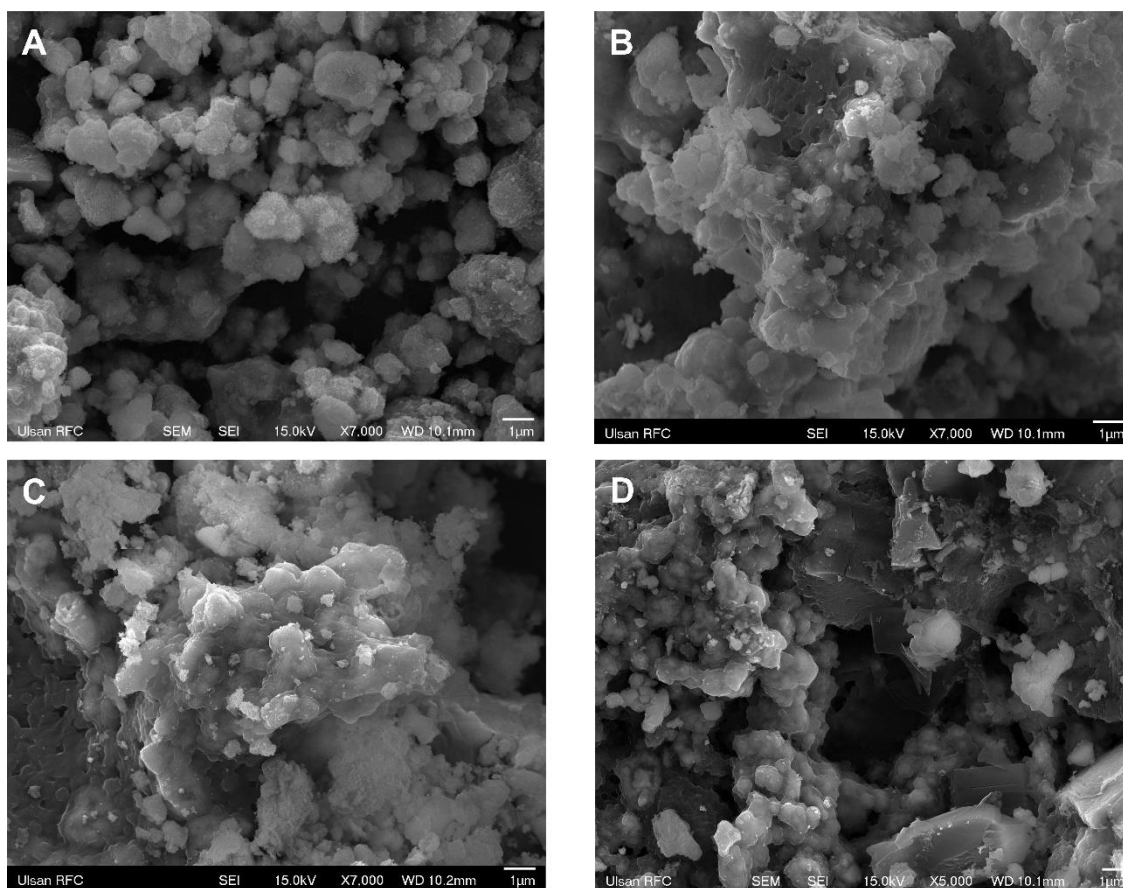


Figure S4.3. FE-SEM images of various composite (A) NC(0.5), (B) NC(2), (C) NC(3) and (D) NC(4).

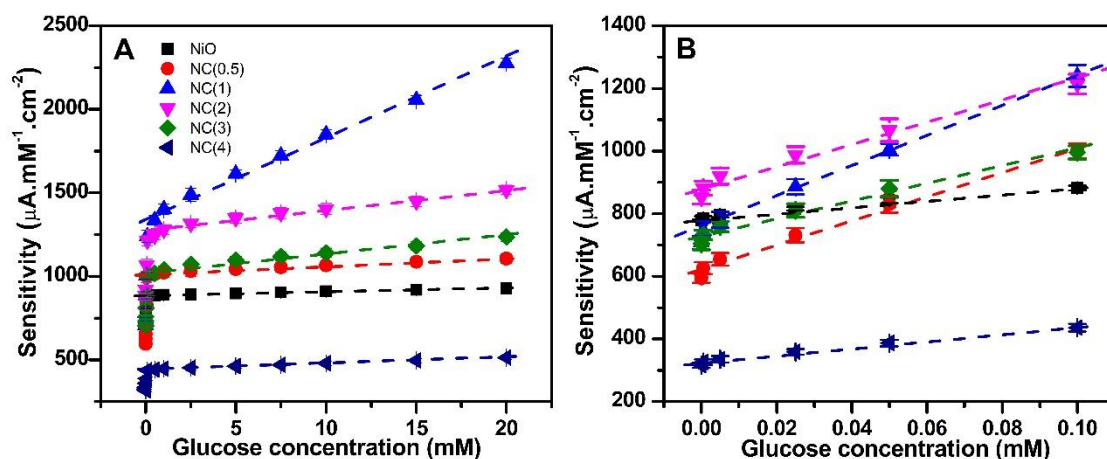


Figure S4.4. (A) N₂ adsorption-desorption (BET isotherm) of g-C₃N₄, NiO, and NC(1); (B) BJH pore size distribution of NC(1).

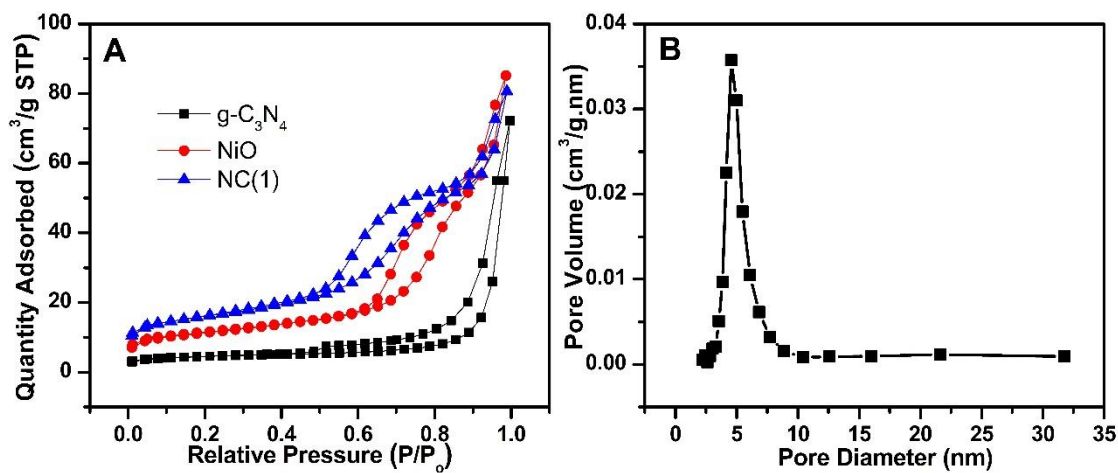


Figure S4.5. Plot of calibration curves of NiO and composites NC(x) with various glucose concentration in 0.1 M NaOH at a scan rate of 50 mV s⁻¹.

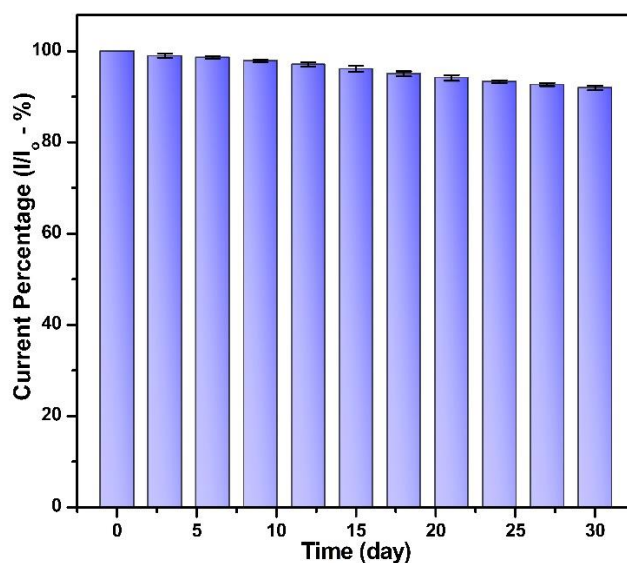


Figure S4.6. Stability of NC(1) based glucose sensor at room temperature. The current was recorded every 3 days in 30 days.

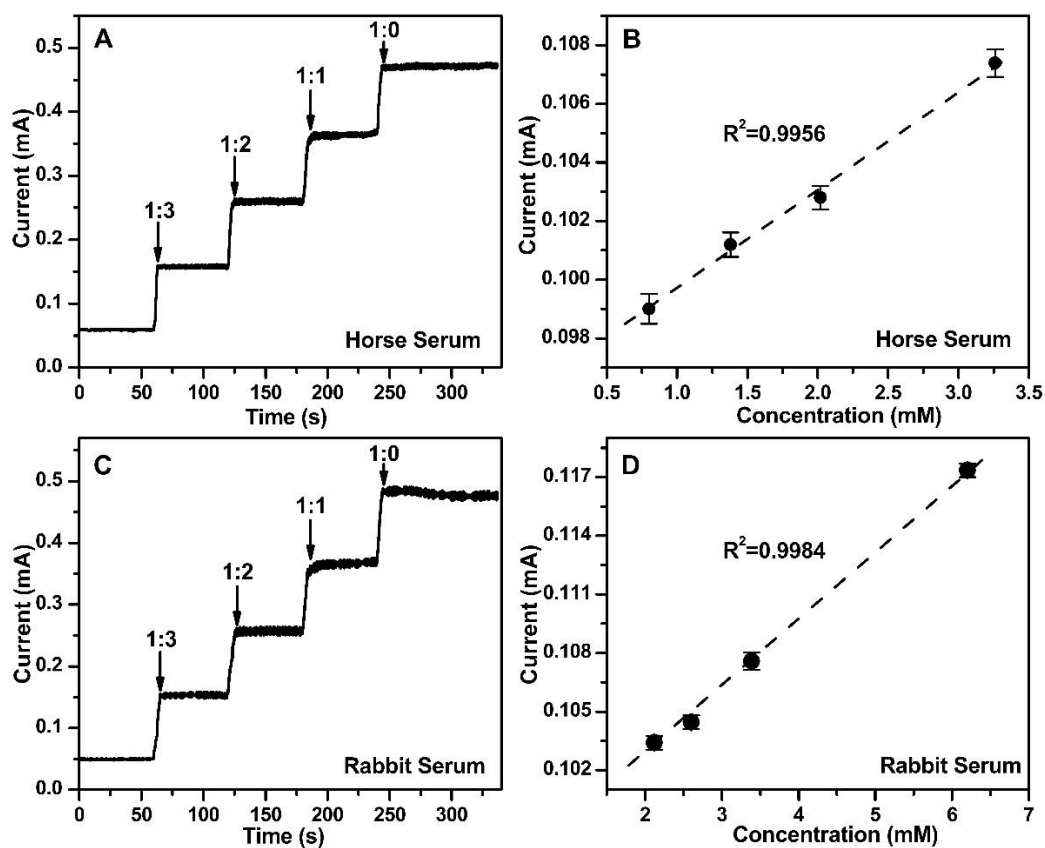


Figure S4.7. Amperometric tests and calibration curves of NC(1) in 0.1 M NaOH at an applied potential +0.68 V with the successive addition real serum samples (A-B) Horse serum and (C-D) Rabbit serum.

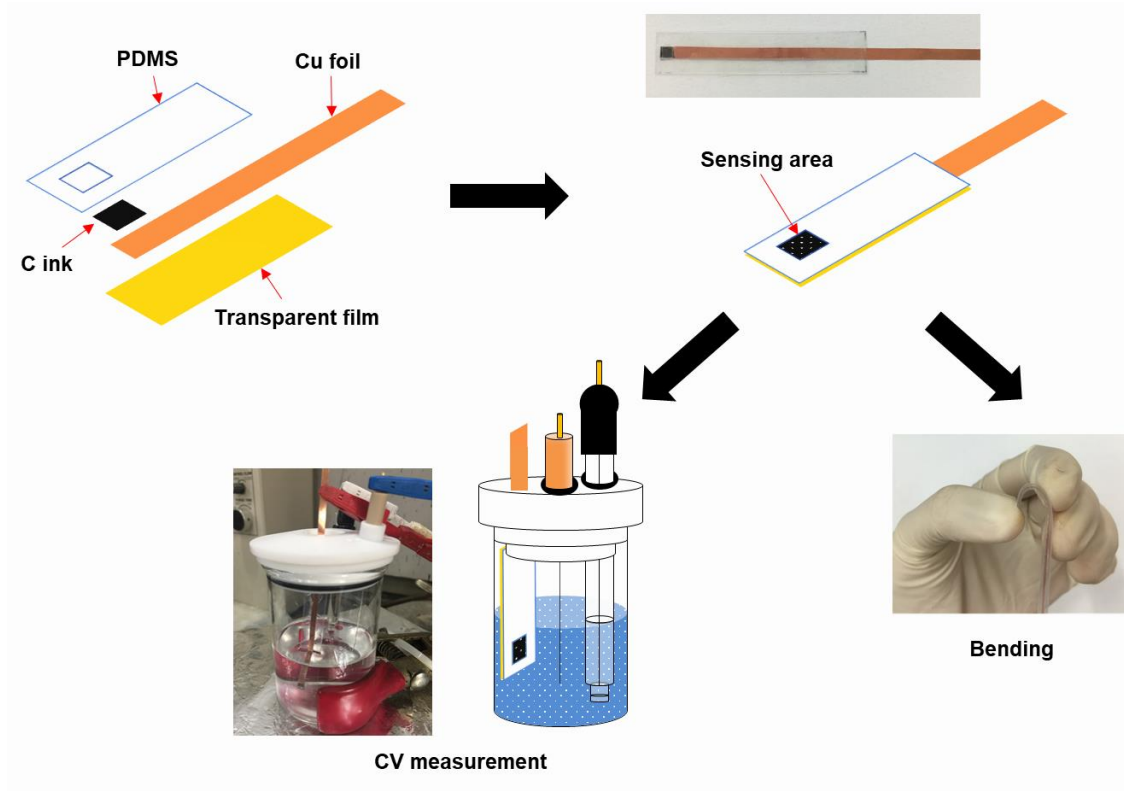


Figure S4.8. Schematic illustration of the fabrication process of flexible NC(1) sensor.

Table S4.1. Relative ratio of C=C, HC-O, N-C=N and N-C=O/O-C=O of all samples by C 1s spectra analysis

Sample	C=C		O-C-O		N-C=N		O-C=O/N-C=O	
	Area	%	Area	%	Area	%	Area	%
g-C ₃ N ₄	965.31	7.54	820.06	6.41	10057.44	78.57	957.01	7.48
NC(1)	922.17	17.03	894.45	16.52	221.69	40.84	1387.43	25.61

Table S4.2. Relative ratio of C-N=C (N₁), N-(C)₃ and HN-(C)₂ (tertiary - N₂), C - NH (quaternary - N₃) of all samples by N 1s spectra analysis

Sample	N ₁		N ₂		N ₃		π - π excitation	
	Area	%	Area	%	Area	%	Area	%
g-C ₃ N ₄	21157.44	59.90	6109.12	17.30	5976.63	16.92	2079.04	5.89
NC(1)	2045.90	49.70	1064.20	25.85	707.00	17.17	299.47	7.28

Table S4.3. The BET surface area and glucose sensitivity of various samples fabricated in this study.

Samples	Ratio of Ni(OH) ₂ : Melamine	S _{BET} (m ² /g)	Pore size (nm)	Sensitivity (μA·mM ⁻¹ ·cm ⁻²)	Correlation coefficient (R ²)
g-C ₃ N ₄	0 : 1	14.50	16.71	194.01*	0.9168
NiO	1 : 0	39.52	10.55	974.31	0.9838
NC(0.5)	1 : 0.5	48.13	8.31	3881.9	0.9884
NC(1)	1 : 1	54.74	6.80	5387.1	0.9929
NC(2)	1 : 2	30.92	8.18	3403.6	0.9792
NC(3)	1 : 3	23.92	10.94	2742.3	0.9784
NC(4)	1 : 4	19.93	11.32	1140.0	0.9850

*The sensitivity of g-C₃N₄ was obtained by CV curves at +0.8 V with the change of current as increasing glucose concentration. Other samples were obtained at the oxidation peak of Ni²⁺/Ni³⁺ at +0.68 V.

Table S4.4. Performance comparison of NiO/g-C₃N₄ based electrode and other non-enzymatic glucose sensor

Material electrode	Linear range	Sensitivity (μA·mM ⁻¹ ·cm ⁻²)	Low detection limit (LOD)	Response time (s)	Ref.
Hedgehog-NiO	0.1 – 5 μM	1052.8	1.2 μM	–	[64]
NiO@Ag NWs	0 – 1.28 mM	67.51	1.01 μM	7	[60]
NiO/rGO	3.13 μM – 3.05 mM	1087	1 μM	~ 10	[65]
NiO/CuO/PANI	20 – 2500 μM	–	2 μM	5	[120]
Ag/NiO/rGO	50 μM – 7.5 mM 10 – 25 mM	1807.2 115.8	2.44 μM 1.22 mM	< 4	[110]
g-C ₃ N ₄ -GOD*	1 – 12 mM	-	11 mM	–	[121]
Cu ²⁺ -C ₃ N ₄ /MWCNT	0.5 μM – 12 mM	929	0.35 μM	<3	[122]

Material electrode	Linear range	Sensitivity ($\mu\text{A}\cdot\text{mM}^{-1}\text{cm}^{-2}$)	Low detection limit (LOD)	Response time (s)	Ref.
AgNPs-CN _x **	0.001 – 0.1 mM	97	0.6 μM	–	[99]
NiO/g-C ₃ N ₄	500 nM – 0.1 mM 0.1 – 20 mM	5387.1 49.06	2.30 μM 1.13 mM	< 4	This work

*GOD – Glucose oxidase; **CN_x – Graphitic carbon nitride

PART III - GLUCOSE-SENSITIVE FLUORESCENCE

SENSOR BASED ON GRAPHITIC CARBON NITRIDE

QUANTUM DOTS

Chapter 5. Highly Biocompatible Phenylboronic acid-functionalized

Graphitic Carbon Nitride Quantum Dots for the Selective

Glucose Sensor

5.1. Introduction

Recently, glucose sensing by the optical methods using fluorescent nanoparticles (NPs) or semiconductor quantum dots (QDs) has attracted considerable attention because of their low toxic and rapid response characteristics [123,124]. On the other hand, the conventional NPs or QDs have many drawbacks, including environmental hazardousness, hydrophobicity, and high cost. Graphitic carbon nitride (g-C₃N₄), which allotropes of carbon nitride and metal-free polymeric semiconductors, have attracted considerable interest because of their excellent properties, such as low toxicity, excellent biocompatibility, eco-friendly, great photostability, and distinct optical features [125]. g-C₃N₄ has a two-dimensional structure (2D) and exhibits a highly π -conjugated electronic structure due to the rigorous C-N plane along the separate layers. Recently, nanoscale g-C₃N₄, such as fluorescent g-C₃N₄ nanosheets (g-CNNS) and g-C₃N₄ quantum dots (CNQDs), have been assessed for various applications, such as biosensors [25,126,127], drug delivery and bioimaging [27,128,129], photocatalysts [24,130], water splitting [26,131], and oxygen reduction reaction [28,132], owing to their bright fluorescence, chemical stability under ambient conditions, and semiconducting properties with a moderate band gap. On the other hand, it still important to fabricate CNQDs, which exhibit improved quantum yield and sensitivity with high selectivity for specific target materials, such as glucose [30].

Boronic acid and various derivatives containing a boronic acid functional group are used widely for fluorescent biosensors to detect glucose based on the fluorescence, UV-Vis absorption, and surface plasmon resonance [32]. Owing to the ability to form a boronate ester via reversible covalent interactions with the position at the cis-1,2- or 1,3-diol, they exhibit a rapid and sensitive response towards glucose by changing the fluorescence intensity of the g-CNQDs through the covalent bonds [34,133,134]. On the other hand, the different structure of similar saccharide molecules can also bind to boronic acid depending on the relative position of the diol group.

This paper reports a highly selective and sensitive glucose sensor based on g-CNQDs/phenyl boronic acid (PBA) using graphitic carbon nitride as a fluorescent and PBA as a quencher and receptor during glucose sensing. The product obtained exhibited the highest quantum yield among fluorescent g-CNQDs ever reported with bright blue emission under UV-lamp in water. The sensor also showed a wide linear range of glucose concentrations from 25 nM – 1 mM with a very low detection limit of 16 nM (S/N = 3). In addition, the g-CNQDs/PBA-based glucose sensor had low toxicity and good biocompatibility in the cell imaging test, highlighting its potential clinical applications.

5.2. Experimental details

5.2.1. Materials

Phenylboronic acid (PBA), melamine, paraformaldehyde (PFA), ascorbic acid (AA), dopamine (DA), uric acid (UA), L-cystine (L-cys), sorbitol (SB), D-(+)-glucose, D-(–)-fructose, galactose, maltose, sucrose, lactose, horse serum (HS), rabbit serum (RS), sodium chloride (NaCl), potassium chloride (KCl), hydrochloric acid (HCl), sodium hydroxide (NaOH), potassium dihydrogen phosphate (KH₂PO₄), di-sodium hydrogen phosphate (Na₂HPO₄), dimethylsulfoxide (DMSO), and 3-(4,5-dimethylthiazol-2-yl)-2,5-diphenyltetrazolium bromide (MTT) were purchased from Sigma-Aldrich Co. (USA). Dulbecco's modified eagle media (DMEM) was obtained from Welgene Company (South Korea) and 4,6-diamidino-2-phenylindole (DAPI) was acquired from Vector Laboratories (USA). Human epithelial

carcinoma (HeLa) cells (ATCC[®] CCL-2[™]) were supplied by American Type Culture Collection (USA). All chemical reagents were used as received. Deionized (DI) water was used for the preparation of the samples in all experiments.

5.2.2. Synthesis of g-CNQDs/PBA

g-C₃N₄ was prepared by heating melamine according to a previous report [24]. Typically, a 10.0 g sample of melamine powder was calcined at 550 °C for 4 h in a muffle furnace. After cooling to room temperature, the yellowish product of g-C₃N₄ was obtained and milled to a powder using an agate mortar. Subsequently, a 40 mg sample of bulk g-C₃N₄ powder was added to 20 mL of DI water and sonicated for 2 h to produce a well-dispersed solution. The g-C₃N₄ nanosheet suspension (2 mg/mL) was transferred to a Teflon–stainless steel autoclave and heated at 180 °C for 8 h to fabricate g-CNQDs. The acquired white solution was centrifuged at approximately 3000 rpm to remove the large particles and washed with DI water. A calculated amount of phenylboronic acid (PBA) was added to the g-CNQDs solution and shaken thoroughly for 1 h at room temperature (IKA KS 130 Basic Orbital Shaker, IKA-Werke GmbH & Co. KG, Germany). Finally, the resulting product was purified with DI water using dialysis tubing with pore size of 1000 Da for 24 h to eliminate all the impurities and remaining chemicals (**Figure 5.1**). The optimal conditions of the hydrothermal process were investigated and optimized using the MATLAB simulation, as shown in **Figures S5.1-S5.3** (Supporting Information).



Figure 5.1. Schematic diagram of g-CNQDs/ PBA fabrication from melamine.

5.2.3. Glucose sensing

To determine the glucose level, various amounts of g-CNQDs/PBA containing solutions were added to 2.34 mL of phosphate buffer solution (PBS, pH = 7.2). After shaking vigorously, the photoluminescence intensity of each sample was measured at 434 nm under an excitation wavelength of 310 nm. The selectivity of glucose detection towards interfering species was examined in a similar manner, as described above except that the interfering species were added to the solution. To detect glucose in real blood serum, the HS and RS were diluted with DI water at ratios from 1:6 to 1:11 (real blood serum:DI) and measured.

5.2.4. Measurement of the quantum yields

The fluorescence quantum yields (QYs) of the g-CNQDs were measured by a relative method according to previous reports [135,136] using quinine sulfate in 0.1 M H₂SO₄ ($\phi = 54\%$) as the fluorescence standards. The fluorescence QYs value of a sample was calculated using the following equation (iii):

$$\phi = \phi_{\text{ref}} \times \frac{I}{A} \times \frac{A_{\text{ref}}}{I_{\text{ref}}} \times \frac{n^2}{n_{\text{ref}}^2} \quad (\text{iii})$$

where ϕ , I, A, and n is the QYs of the sample, integrated emission intensity of the sample, optical density, and refractive index ($n = 1.33$ for DI), respectively. The subscript “ref” refers to the reference fluorophore with a known QYs. The optical density of the sample was kept below 0.1 to minimize the inner-filter effects at the excitation wavelength. **Figure S5.4** (Supporting Information) summarizes the QYs of quinine sulfate and g-CNQDs.

5.2.5. Cell culture and fluorescence imaging

The HeLa cells (approximately 4×10^4 cells/well) were seeded in 24-well plates and cultured in DMEM at 37 °C with a humidified atmosphere containing 5% CO₂ for 24 h to adhere the cells onto the surface. The culture medium was then replaced with 0.5 mL of fresh medium containing 1 mg/mL g-CNQDs, and the cells were incubated for 16 h. Before the confocal

imaging experiments, the cells were washed three times with PBS buffer (pH = 7.2) to eliminate the excess g–CNQDs, followed by fixation with a 4% paraformaldehyde (PFA) solution for 15 min and washing twice with PBS buffers. The cells were then dyed by DAPI for nucleus staining to easily detect the fluorescence. Finally, the fixed cells were observed under 405 nm and 488 nm laser excitation using the confocal fluorescence system

5.2.6. Cytotoxicity assay of g–CNQDs

The cellular toxicity test of g–CNQDs to HeLa cells was performed using a standard MTT assay. The HeLa cells were seeded in 96-well plates at a density of 5×10^4 cells per mL and cultured for 24 h in an incubator (37 °C, 5% CO₂). After incubation, the DMEM medium was discarded and treated with DMEM containing g–CNQDs at different concentrations (0 – 400 µg/mL) for a further 24 h. Subsequently, 20 µL of a 5 mg/mL MTT solution was added to each cell well and incubated for a further 4 h. The culture medium with MTT was removed, followed by the injection of 150 µL DMSO with shaking for 15 min. Finally, the optical density (OD) was recorded at a wavelength of 490 nm using a microplate reader (SpectraMax M2, USA). Each experiment was conducted 3 times, and the data are reported as the average. The cell viability was estimated using the following equation (iv):

$$\text{Cell viability (\%)} = \frac{\text{OD}_{\text{treated}}}{\text{OD}_{\text{control}}} \times 100 \quad (\text{iv})$$

where OD_{control} and OD_{treated} were obtained in the absence and presence of g–CNQDs, respectively.

5.2.7. Instrumental analysis

An ultrasonic treatment was performed using a UPC-10 (Jeio-Tech Co., Ltd., South Korea). Fourier transform infrared (FT-IR, Nicolet iS5, Thermo Fisher Scientific, USA) spectroscopy was carried out to analyze the functional groups. X-ray diffraction (XRD, D/MAZX 2500V/PC model, Rigaku, Japan) was conducted using Cu K α radiation (40 kV, 30 mA, $\alpha =$

1.5415 Å). X-ray photoelectron spectroscopy (XPS Thermo ESCALAB 250 Xi, Thermo Fisher Scientific, USA) was performed using Al K α X-ray radiation (1486.6 eV). High-resolution transmission electron microscopy (HR-TEM, JEM-2100F, JEOL, Japan) images were taken at an operating voltage of 200 kV.

Ultraviolet visible (UV-Vis, SPECORD 210 PLUS, Analytik Jena, Germany) absorption spectroscopy was performed. The photoluminescence spectra (PL) were recorded using a Cary Eclipse fluorescence spectrophotometer (Agilent Technologies, USA) with a 1.0 cm quartz cell. Confocal images were acquired in sequential mode using a 60 \times Plan-Apochromat (1.4 NA) oil objective and the appropriate filter combination on an Olympus 2000 laser-scanning confocal fluorescence microscopy.

5.3. Results and discussion

5.3.1. Characterization of g-CNQDs and g-CNQDs/PBA

The size and morphology of the bulk g-C₃N₄, g-CNQDs, and as-obtained g-CNQDs/PBA were examined by HR-TEM. HR-TEM showed that the bulk g-C₃N₄ had an agglomerated nanosheet structure, approximately 100 nm in size (**Figure 5.2(A)**). The FFT patterns (**Figure 5.2(B)**) were indexed to the (100) and (002) crystal plane of graphitic carbon with inter-planar distances of 2.1 Å and 3.3 Å, respectively. As shown in **Figure 5.2(C)**, after the sonication and hydrothermal treatment, g-C₃N₄ transformed to small particles with a mean diameter of 1.8 nm (**Figure 5.2(D)**). The lattice spacing of g-CNQDs obtained by high-resolution TEM was approximately 0.336 nm (the inset in **Figure 5.2(C)**), which corresponds to the (002) plane of graphitic carbon [30]. The structure of g-CNQDs after mixing with the PBA (**Figure 5.2(E)**) showed an increase in size due to agglomeration, which may cause a decrease in the PL intensity. Interestingly, the Tyndall effect phenomena of an aqueous dispersion of g-CNQDs obtained by light scattering of a laser passing through highlight the colloidal nature of the dispersion (**Figure 5.2(F)**), which indicates the excellent dispersion of g-CNQDs in water [137].

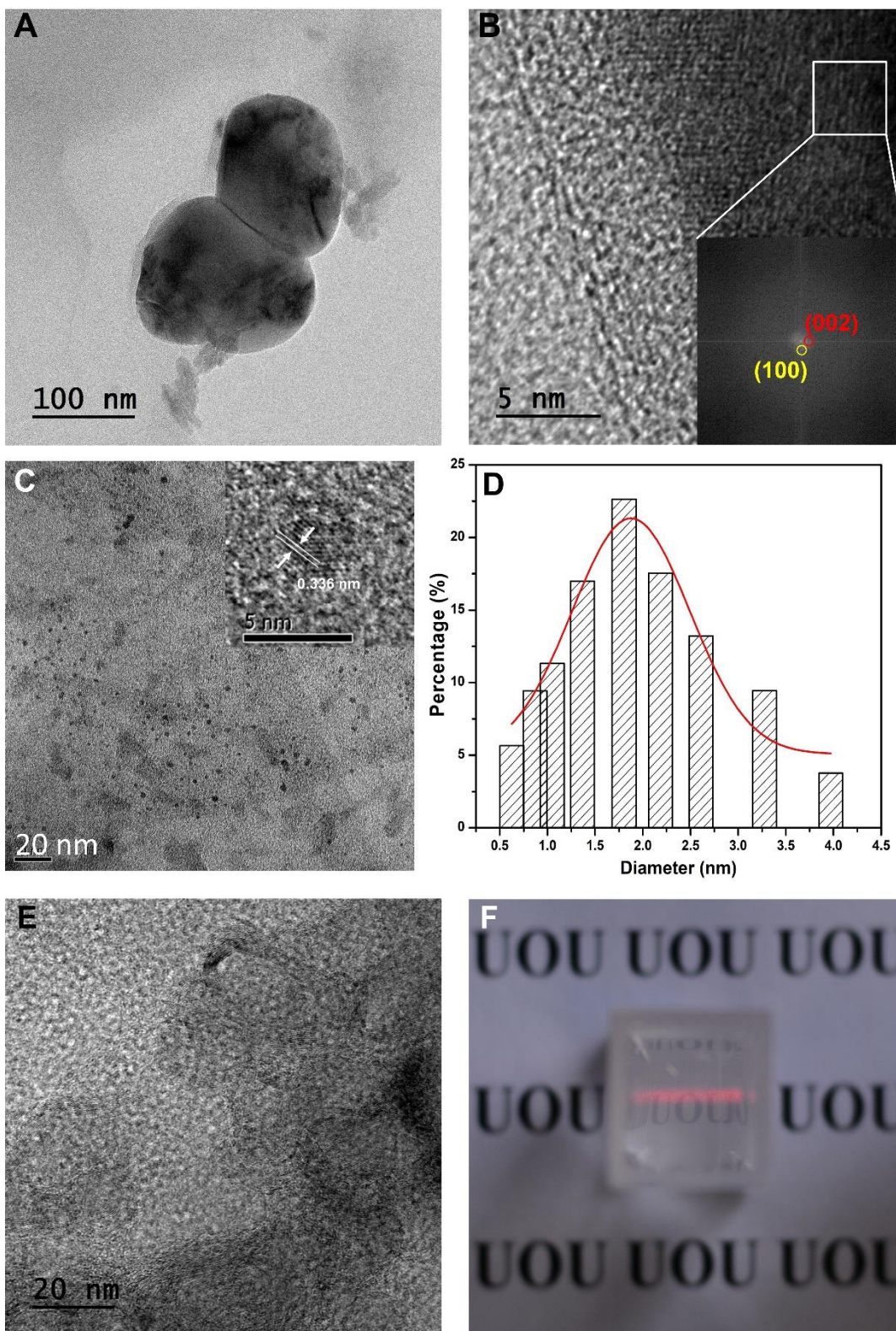


Figure 5.2. TEM images of (A-B) bulk $g\text{-C}_3\text{N}_4$, (C) $g\text{-CNQDs}$, (E) $g\text{-CNQDs/PBA}$. (D) Size distribution of $g\text{-CNQDs}$. (F) Tyndall effect of $g\text{-CNQDs}$ dispersion with the red laser light passing through. Inset: (B) FFT patterns of $g\text{-C}_3\text{N}_4$, (C) HR-TEM images of $g\text{-CNQDs}$.

XRD was conducted to obtain information of the crystallographic phase of the samples. As shown in **Figure 5.3**, the bulk $g\text{-C}_3\text{N}_4$ exhibited two prominent peaks at 13.08° and 27.25° 2θ , which were assigned to the periodic in-plane structural packing motif (100) and the interplanar stacking peak of graphitic-like carbon systems (002), respectively [138,139]. After the ultrasonication and hydrothermal treatments, the intensity of the (002) peak decreased and the position shifted to 27.42° 2θ ($g\text{-CNQDs}$), indicating the successful formation of layered-nanoscale $g\text{-CNQDs}$ from $g\text{-C}_3\text{N}_4$ [140]. The disappearance of the (100) peak at 13.08° 2θ was attributed to the decreased planar size of the layers after the hydrothermal process.

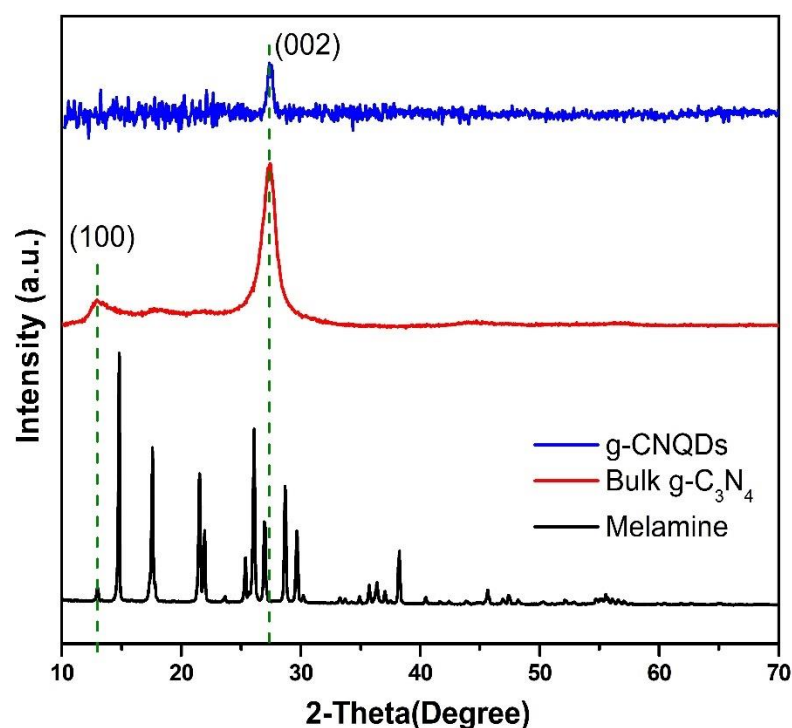


Figure 5.3. XRD patterns of melamine, bulk $g\text{-C}_3\text{N}_4$ and $g\text{-CNQDs}$.

The composition and chemical structure of bulk $g\text{-C}_3\text{N}_4$, $g\text{-CNQDs}$ and $g\text{-CNQDs/PBA}$ were examined further by FT-IR spectroscopy. As shown in **Figure 5.4**, all the samples showed the typical IR spectra of graphitic carbon nitride. The sharp absorption peak at 810 cm^{-1} was attributed to the out-of-plane ring bending vibration modes that are characteristic of tri-s-triazine units. The other peaks present in a wide region from approximately 1100 to 1750 cm^{-1} correspond to the typical stretching vibration modes of C-N heterocycles. The peaks at approximately 1333

and 1259 cm^{-1} clearly indicate the presence of secondary and tertiary amine fragments, respectively [141]. The broad peak between $3600\text{--}3000\text{ cm}^{-1}$ was assigned to the stretching vibration of the hydroxyl group (νOH) and the sharp peaks at $3300\text{--}3400\text{ cm}^{-1}$ and 3056 cm^{-1} were assigned to the stretching vibration of the terminal amino group ($\nu\text{N-H}$ or NH_2) of $\text{g-C}_3\text{N}_4$ and the stretching vibration of C-H, respectively [142]. After mixing with PBA, the new peaks at 850 cm^{-1} , 1347 cm^{-1} , and 1089 cm^{-1} , which correspond to the symmetric and asymmetric B-O stretching vibrations of PBA, and stretching vibration modes of B-C, respectively, indicates the successful modification of g-CNQDs with PBA [143].

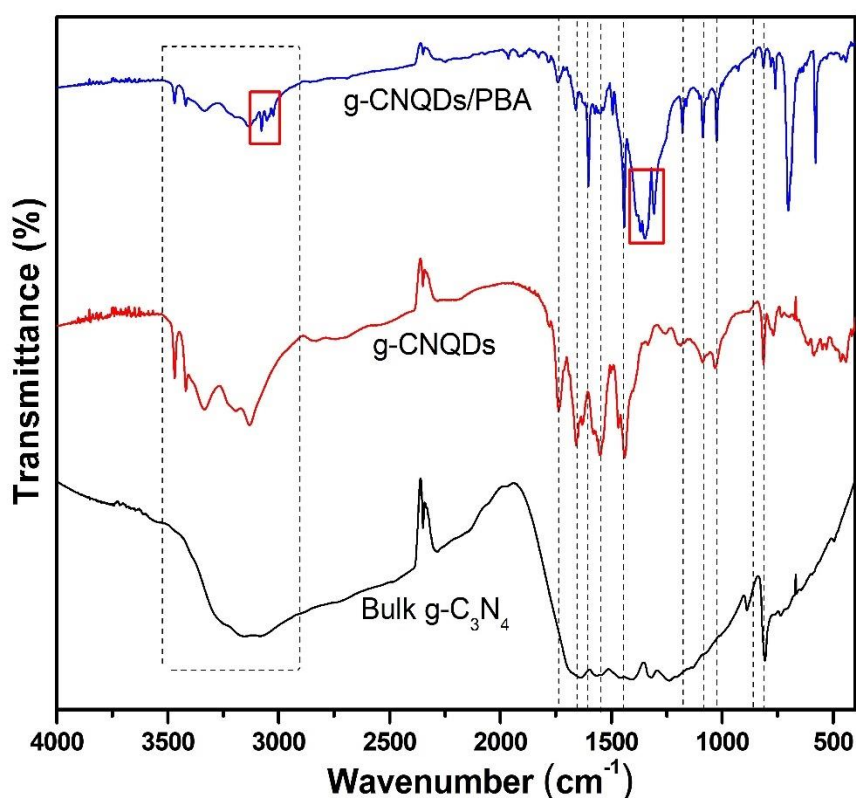


Figure 5.4. FT-IR spectra of bulk $\text{g-C}_3\text{N}_4$, g-CNQDs and g-CNQDs/PBA .

XPS was used to investigate the oxidation state of each element in the samples. Melamine and bulk $\text{g-C}_3\text{N}_4$ showed peaks corresponding to C, N, and O. A new peak corresponding to B was observed in the g-CNQDs and g-CNQDs/PBA , as shown in **Figure 5.5(A)**. High-resolution XPS of C 1s, N 1s, O 1s and B 1s was also performed, as shown in **Figures 5.5(B-E)** and **Figure S5.5** (Supporting Information). The C 1s spectrum exhibited four

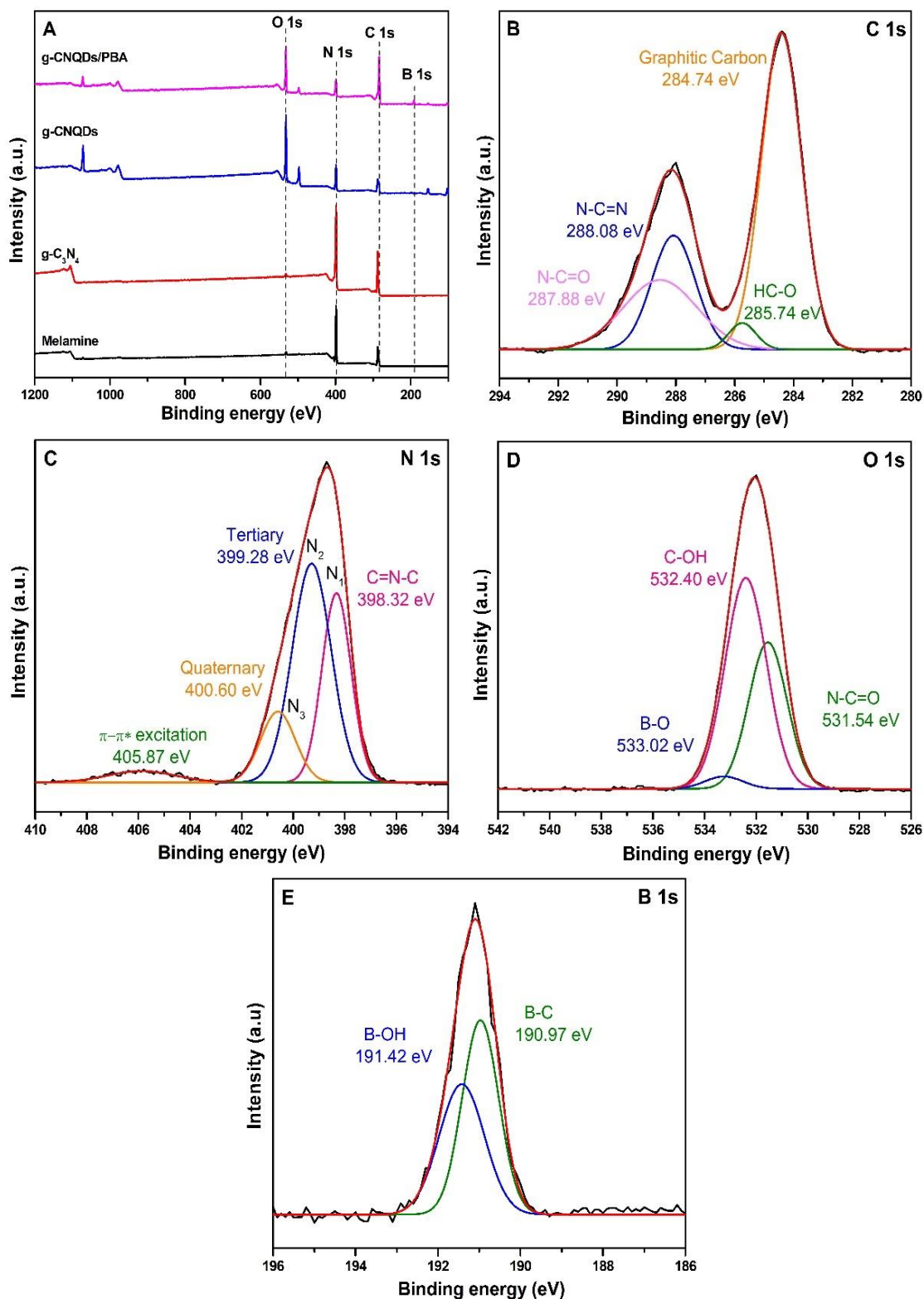


Figure 5.5. (A) XPS survey spectra of melamine, bulk $g\text{-C}_3\text{N}_4$, $g\text{-CNQDs}$, and $g\text{-CNQDs/PBA}$. The high-resolution XPS spectra of (B) C 1s, (C) N 1s, (D) O 1s, and (E) B 1s for $g\text{-CNQDs/PBA}$.

peaks centered at 284.41, 285.74, 288.08, and 288.56 eV, which were assigned to graphitic carbon C=C, sp³-bonded carbon with oxygen (HC–O), sp²-hybridized carbon with nitrogen (N–C=N), and oxygen (N–C=O), respectively.

The N 1s spectra in **Figure 5.5(C)** can be resolved into four peaks. Two peaks labeled as N₁ and N₂ at 398.32 and 399.28 eV were ascribed to the sp²-hybridized aromatic nitrogen bonded to carbon atom (C=N–C) and the tertiary nitrogen N–(C)₃ and HN–(C)₂ groups, respectively. Both groups involved the tri-s-triazine heterocyclic ring units to form the basic substructure units of the graphitic carbon along with sp²-hybridized carbon with N (288.08 eV). The final peak tagged as N₃ at 400.6 eV is related to the quaternary nitrogen, which is also known as graphitic nitrogen. The weak peak centered at 405.87 eV indicated charging effects or π electron delocalization in the heterocycles [130,144]. In **Figure 5.5(D)**, the O 1s spectrum revealed three peaks centered at 531.54, 532.40 and 533.02 eV, which correspond to N–C=O, C–OH, and B–O (of PBA) bonds, respectively. The B 1s spectrum could also be deconvoluted into two peaks at 190.97 and 191.42 eV, corresponding to B–C and B–OH bonds, respectively (**Figure 5.5(E)**). XPS confirmed the existence of a tri-s-triazine ring-based graphitic carbon structure in g–CNQDs and the successful functionalization of PBA on g–CNQDs.

5.3.2. Fluorescence properties of g–CNQDs

UV–Vis absorption and PL spectroscopy were conducted to investigate the optical properties of the g–CNQDs. The UV-Visible spectra of g–CNQDs shown in **Figure 5.6(A)**, exhibited a strong peak at 280 nm and weak shoulder peaks at 310 and 365 nm. The peak at 280 nm was attributed to π – π^* electronic transitions for carbon nitride containing s-triazine rings [144] and the small peak at 310 nm was assigned to the n– π^* electronic transitions of the C=N and C=O bonds in g–CNQDs [145]. The photoluminescence excitation (PLE) spectrum showed a peak at 434 nm when excited at 310 nm, which can be due to the transition between the δ^* conduction band and the lone pair valence band corresponding to the sp² C–N band [145,146]. The inset in **Figure 5.6(A)** shows that the g–CNQDs solution is slightly whitish opaque under

visible light, whereas it shows bright blue fluorescence under UV light with a wavelength of 365 nm. As shown in **Figure 5.6(B)**, the PL emission spectra are strongly dependent on the excitation wavelength. The emission intensity initially increased gradually and then decreased when the excitation wavelength was higher than 310 nm, but there was no noticeable change in peak position. To further examine the fluorescence properties of g-CNQDs, the relative quantum yield (QYs) was also measured using quinine sulfate as a standard (QYs 54%) with excitation at 310 nm. As shown in **Figure S5.4** (Supporting Information), the QYs of g-CNQDs fabricated in this study was as high as 67%, which to the best of the authors' knowledge, is the highest QYs value for the fluorescent g-CNQDs ever reported [30,144,147,148].

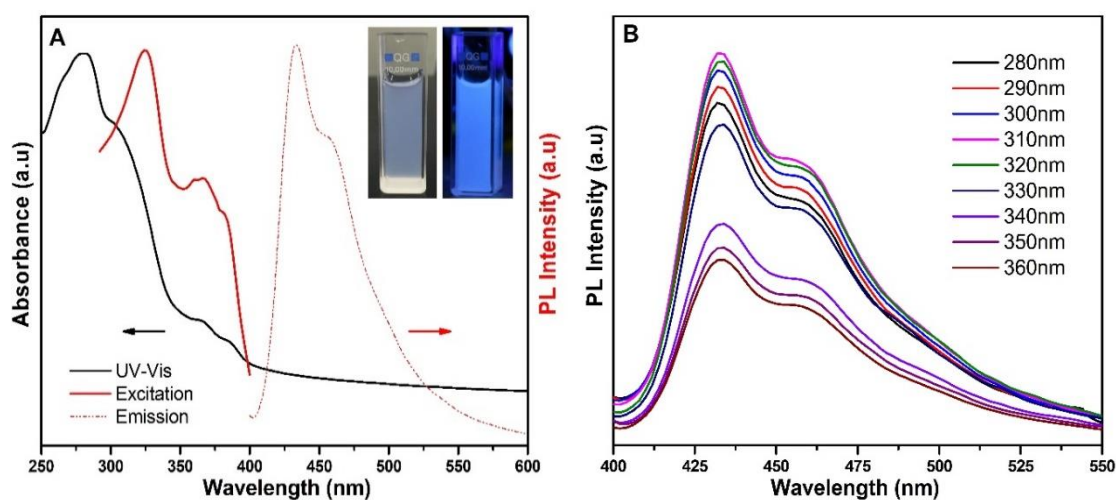


Figure 5.6. UV-Vis absorption and photoluminescence (PL) emission and excitation spectra of g-CNQDs; the inset shows a digital photo of g-CNQDs under visible (left) and UV lights (right). (B) PL spectra of g-CNQDs at various excitation wavelengths.

To determine the optimal conditions for sensing applications, the influence of the pH of g-CNQDs on the PL intensity were investigated. As shown in **Figure S5.6** (Supporting Information), only a small change in PL intensity was observed over the pH range, 4 to 10, indicating the stable sensing characteristics of g-CNQDs over a wide pH range. The decrease in PL intensity at high pH can be explained by the fluorescent species probably having more acidic sites in g-CNQDs that decrease in quantity in a basic environment [144]. Based on the

fluorescence features of the g-CNQDs, all sensing experiments were carried out in a neutral PBS solution of pH = 7.2.

As shown in **Figure S5.2** (Supporting Information), the fluorescent intensity of g-CNQDs decreased gradually with increasing PBA concentration but it became saturated after the addition of 0.225 M PBA. The Stern-Volmer plot of the F_0/F ratio versus PBA concentration shown in the inset in **Figure S5.2(B)** (Supporting Information) revealed good linearity with a high correlation coefficient (R^2) of 0.995. In theory, the fluorescence quenching mechanism could be explained by energy or electron transfer. The emission spectrum of g-CNQDs does not overlap with the absorption of PBA (**Figure S5.7** - Supporting Information), which suggests that fluorescence resonance energy transfer from g-CNQDs to PBA can be rejected [149]. The PL intensity of g-CNQDs is quenched in the presence of PBA due to some molecular interactions such as π - π stacking interaction between triazine rings of g-CNQDs and benzene rings of PBA, and hydrogen bonding occurred between the hydroxyl (-OH) on the PBA and the various functional groups such as -NH₂, -NH-, -COOH and -OH on the surface of electron-rich g-CNQDs, results in enhanced electron transfer from the g-CNQDs molecule to PBA [22,140,150]. Thus, the favorable interaction indicated that the g-CNQDs exhibited an excellent fluorescence quenching response toward PBA.

5.3.3. Glucose sensing of g-CNQDs/PBA

Glucose can interact with PBA through the formation of a covalent bond [34], which can recover the PL intensity of g-CNQDs quenched by PBA, as shown in **Figure 5.7**. When glucose was added to a g-CNQDs/PBA solution, the boronic acid molecules were converted to more tetrahedral anionic glucoboronate esters, which formed the negatively charged boronate complexes that removed the quencher from the vicinity of the g-CNQDs, leading to effective recovery of the PL intensity of g-CNQDs [149].

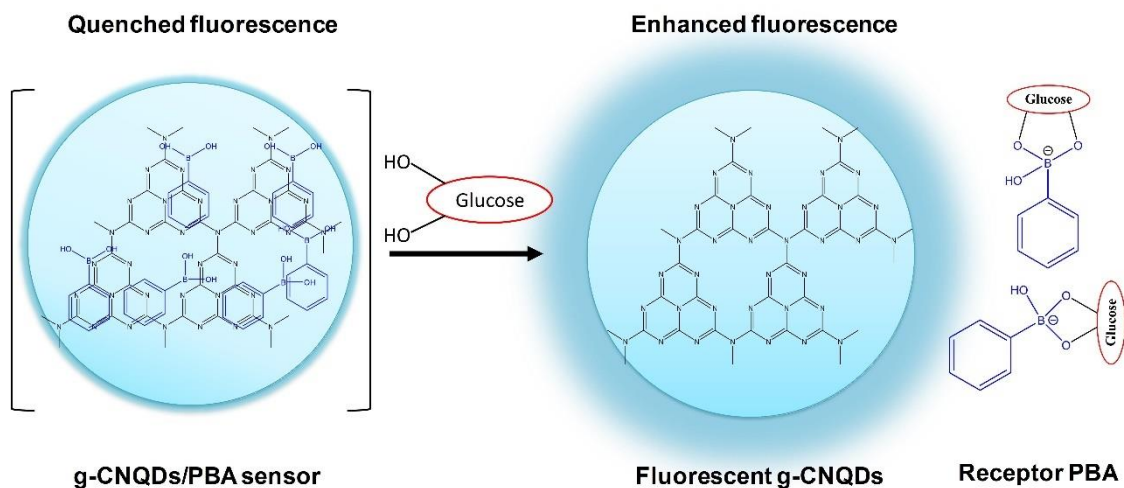


Figure 5.7. Proposed glucose-sensing mechanism based on g-CNQDs/PBA as a fluorescent and PBA as a receptor.

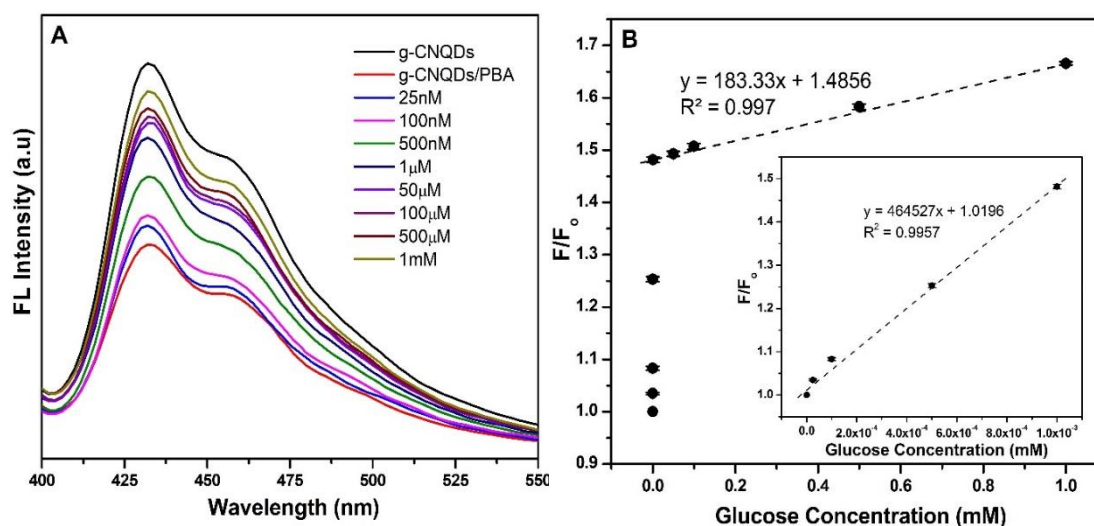


Figure 5.8. (A) PL emission spectra of g-CNQDs and g-CNQDs/PBA at various glucose concentrations (from bottom to top: 0 – 1 mM). (B) Plots of the relative PL intensity (F/F_0) versus glucose concentration. F and F_0 are the PL intensity of g-CNQDs/PBA in the absence and presence of glucose, respectively. The inset shows a linear curve over the concentration range from 25 nM to 1 μ M. Measurement conditions: g-CNQDs = 2 mg/mL, PBA = 0.25 M, pH = 7.2, and λ_{ex} = 310 nm. The error bars imply the standard deviations for triplicate determinations at each concentration.

As shown in **Figure 5.8(A)**, the PL intensity increased gradually with increasing glucose concentration. A Stern-Volmer plot of the relative PL intensity versus the glucose concentration shown in **Figure 5.8(B)** shows that the fluorescence intensity is strongly dependent on the glucose concentration. Two good line ranges from 25 nM to 1 μ M ($R^2 = 0.996$) and 1 μ M to 1 mM ($R^2 = 0.997$) were observed with a very low detection limit of 16 nM ($S/N = 3$). Compared to the boronic acid/ quantum dot-based sensing systems reported previously (**Table S5.1** – Supporting Information), g-CNQDs/PBA shows highly improved sensitivity, linear range, and detection limit, which can be due to the excellent QYs of g-CNQDs fabricated in this study.

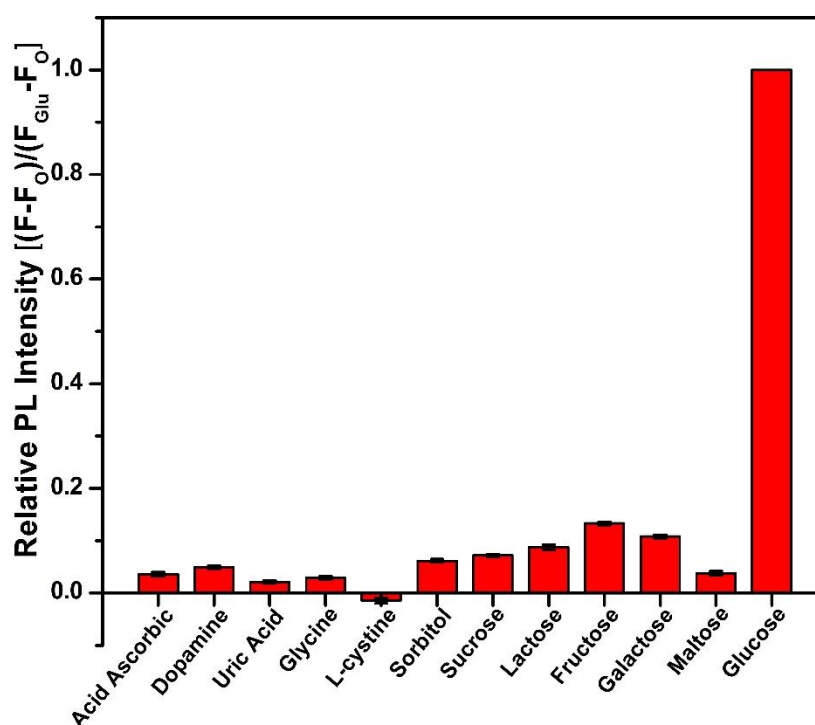


Figure 5.9. Relative PL intensity $((F-F_0)/(F_{\text{Glu}}-F_0))$ of g-CNQDs/PBA in the presence of various interfering species. F and F_0 represent the PL intensity of g-CNQDs/PBA with and without 5 mM of interfering species, respectively. F_{Glu} is the PL intensity at 1 mM of glucose. The data shown here describe the average of three experiments for each interfering species.

To evaluate the selectivity of g-CNQDs/PBA during the diagnosis of diabetes, the effects of various interfering species, such as ascorbic acid, dopamine, uric acid, glycine, l-cystine, sorbitol and other saccharides present in real blood were studied. As shown in **Figure**

5.9, all interfering species showed no significant response to g–CNQDs/PBA, even at a 5 times higher concentration than that of glucose, which can be due to the specific reaction between glucose and PBA by the presence of a pair of cis-diol units at the 1,2 – and 5,6 – positions in glucose. Other saccharides also had a negligible effect on the PL intensity of g–CNQDs/ PBA due to the absence of such a specific structure that can release PBA from the g–CNQDs/PBA [151].

5.3.4. Detection of glucose in real blood

To evaluate the feasibility of g–CNQDs/PBA in measuring the glucose concentration in real blood, experiments are carried out using horse (HS) and rabbit serum (RS), of which the glucose concentrations were known. First, the calibration curve of the PL intensity using g–CNQDs/PBA at various diluted HS and RS solutions was obtained, as shown in **Figure S5.8** (Supporting Information), each calculated concentration was then compared with those obtained by the commercial glucometer (ACCU-CHECK® Blood Glucose Meter). As summarized in **Table 5.1**, the differences in the glucose concentration in real blood measured by g–CNQDs/PBA and between commercial glucometer are only 0.51 to 0.85 %, which strongly indicates that the g–CNQDs/PBA fabricated in this study can measure the concentration of glucose precisely, even in real blood and its accuracy is similar to that of the commercial enzymatic glucose sensor.

Table 5.1. Comparison of the glucose concentration between the commercial glucometer and g–CNQDs/PBA measured at various glucose concentrations

Dilution ratio of serum in DI water	Horse blood serum (mM)		Dilution ratio of serum in DI water	Rabbit blood serum (mM)	
	g-CNQDs/PBA	Glucometer		g-CNQDs/PBA	Glucometer
1:8	0.944	0.940	1:6	0.722	0.715
1:9	0.777	0.782	1:7	0.666	0.673
1:10	0.721	0.726	1:8	0.611	0.613

Dilution ratio of serum in DI water	Horse blood serum (mM)		Dilution ratio of serum in DI water	Rabbit blood serum (mM)	
	g-CNQDs/PBA	Glucometer		g-CNQDs/PBA	Glucometer
1:11	0.611	0.608	1:9	0.555	0.549
Error (%)	0.51		0.85		

5.3.5. Bio-imaging and Cytotoxicity test

The cytotoxicity at different doses of g-CNQDs was investigated using a standard MTT assay with HeLa cells. As shown in **Figure S5.9** (Supporting Information), the results confirmed that g-CNQDs/PBA has low cytotoxicity to HeLa cells, in which approximately 91.74 % cell viability was observed, even at concentrations of up to 400 $\mu\text{g}/\text{mL}$ after incubation for 24 h. This high stability, low cytotoxicity, and good biocompatibility of g-CNQDs make it a promising material for bio-imaging applications. As shown in the confocal microscopy images (**Figure 5.10**), the HeLa cells emitted bright blue and green fluorescent after incubation with g-CNQDs for 16 h when excited with 405 and 488 nm, respectively. The emission was observed mainly in the membrane and cytoplasmic region of cells, suggesting that g-CNQDs molecules cannot enter the inner nuclei but it can pass through the nucleus. Therefore, these results demonstrate the excellent biocompatibility of g-CNQDs as a promising sensing and imaging material for biomedical applications in the future.

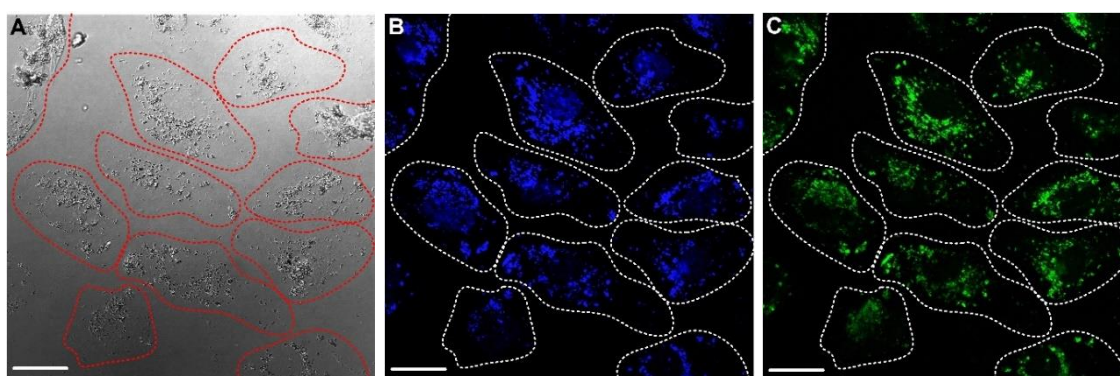


Figure 5.10. Confocal fluorescence images of HeLa cells incubated with g-CNQDs under (A) bright field, and excitation at (B) 405 nm, and (C) 488 nm. The scale bar represents 30 μm .

5.4. Conclusions

A photoluminescence sensor based on g-CNQDs/PBA was synthesized for the selective glucose sensing with a wide detection range and a low detection limit. The obtained g-CNQDs/PBA exhibited high glucose sensitivity and excellent selectivity against various interfering species, which were attributed to the very high quantum yield of g-CNQDs and the specific reaction of PBA with glucose, respectively. In addition, it showed excellent bio-imaging features and low cytotoxicity, even at very high g-CNQDs/PBA concentrations, which can be due to the green synthesis process used in this study.

5.5. Supporting Information

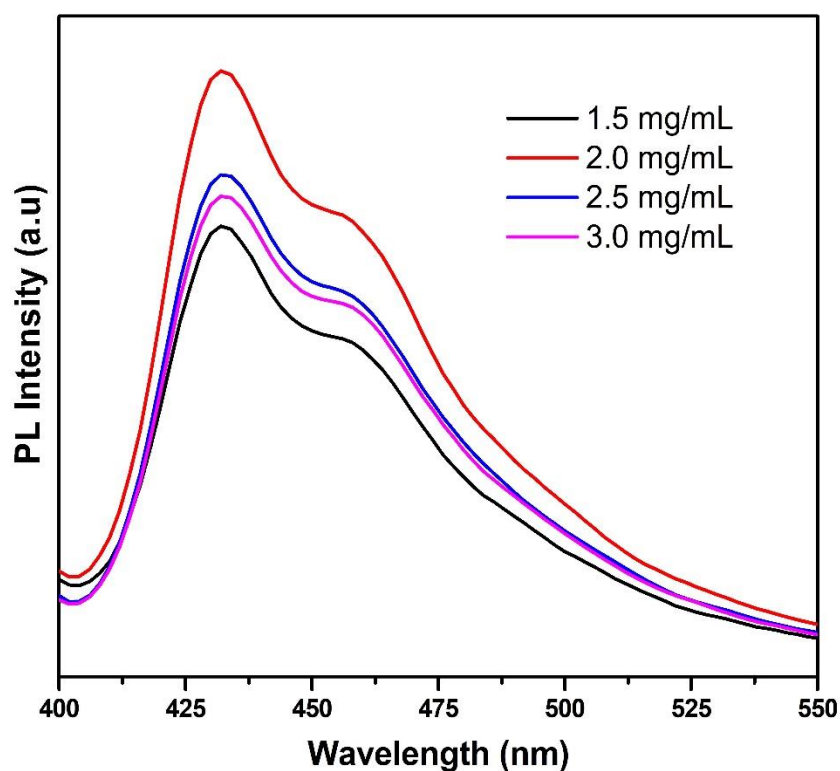


Figure S5.1. The optimized concentration of g-C₃N₄. PL emission spectra of g-CNQDs with different concentrations of g-C₃N₄ under excitation wavelength at 310 nm, buffer pH = 7.2.

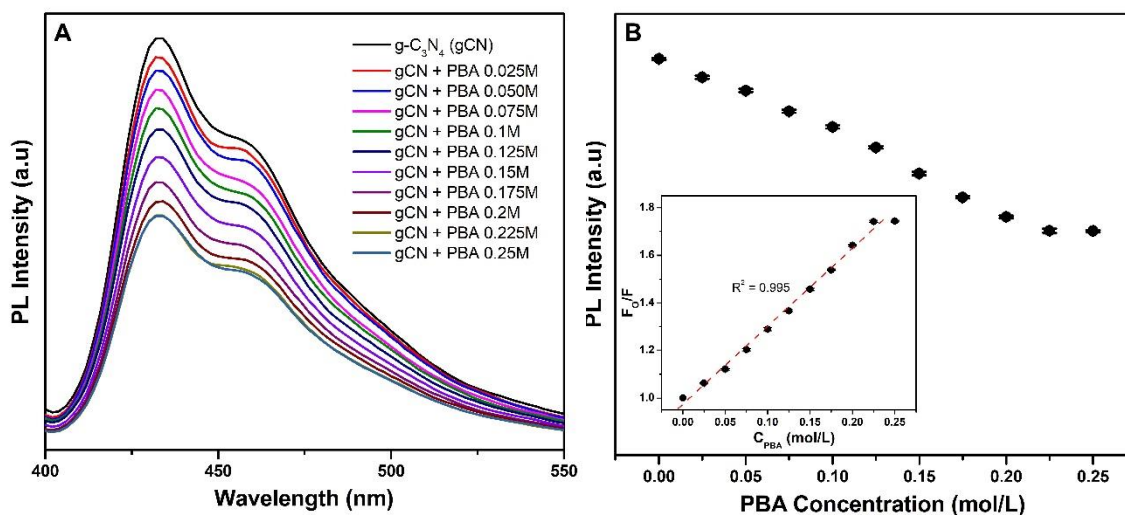


Figure S5.2. The optimized concentration of PBA. (A-B) PL emission spectra of g-CNQDs/PBA in PBS buffer with the addition of various PBA concentrations increasing from 0 to 0.25 M (top to bottom). Inset: the linear plot of the PL intensity for g-CNQDs/PBA versus the PBA concentration. The PL spectra were recorded using 2 mg/mL g-CNQDs in PBS buffer (pH 7.2) under $\lambda_{ex} = 310$ nm, $\lambda_{em} = 434$ nm. The error bars imply the standard deviations for triple measurement at each concentration.

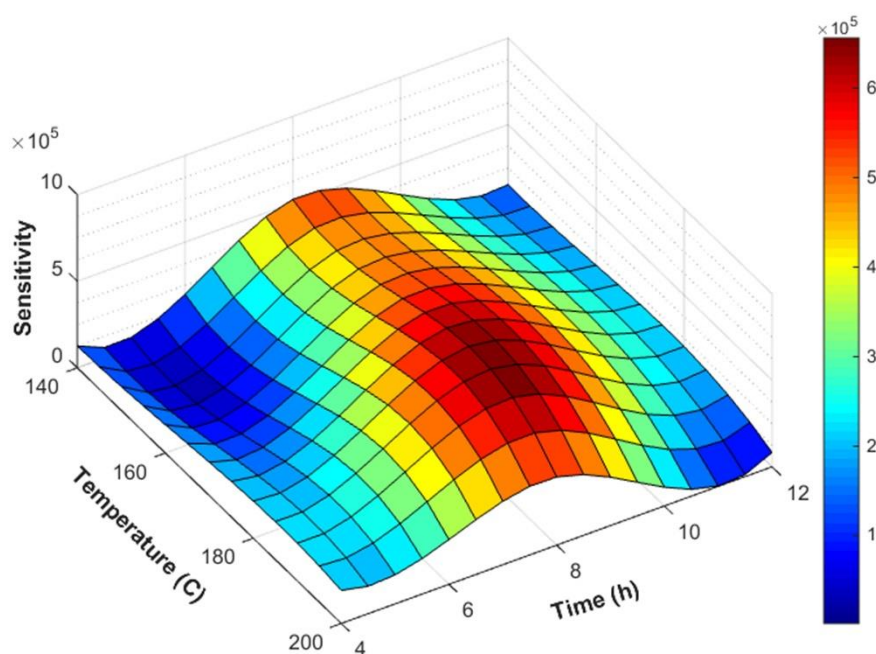
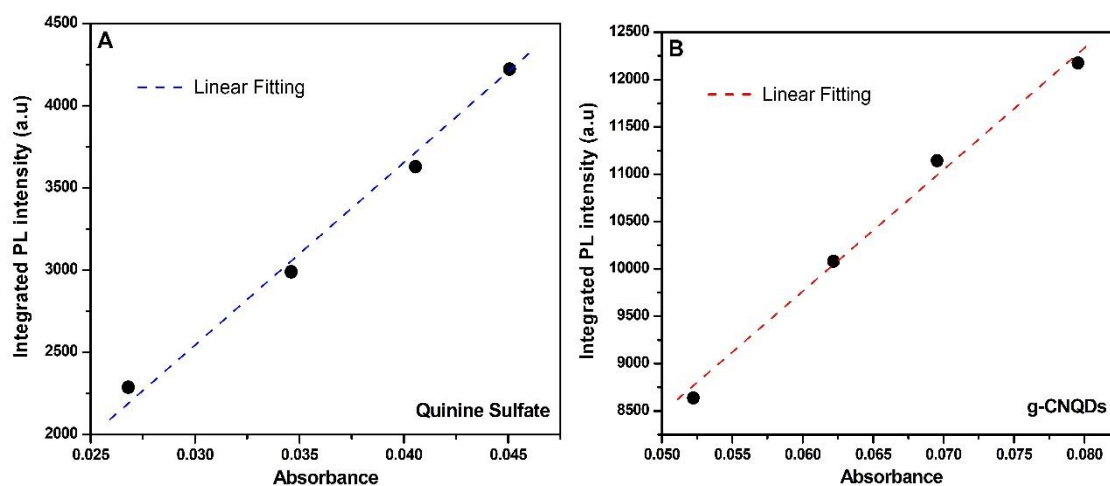


Figure S5.3. Simulated the optimized conditions including temperature and time for hydrothermal process by MATLAB simulation of the 3D-scattering intensity distribution.



	Quinine sulfate				g-CNQDs			
Abs	0.0268	0.0346	0.0406	0.0451	0.0522	0.0622	0.0696	0.0795
Integrated PL	2286.99	2989.26	3629.85	4222.73	8637.23	10079.74	11143.71	12173.32
Slope	105055				130549			
QY (%)	54				67.1			

Figure S5.4. Plots integrated PL intensity of g-CNQDs and quinine sulfate (reference dye) as a function of optical absorbance at 310 nm and relevant data.

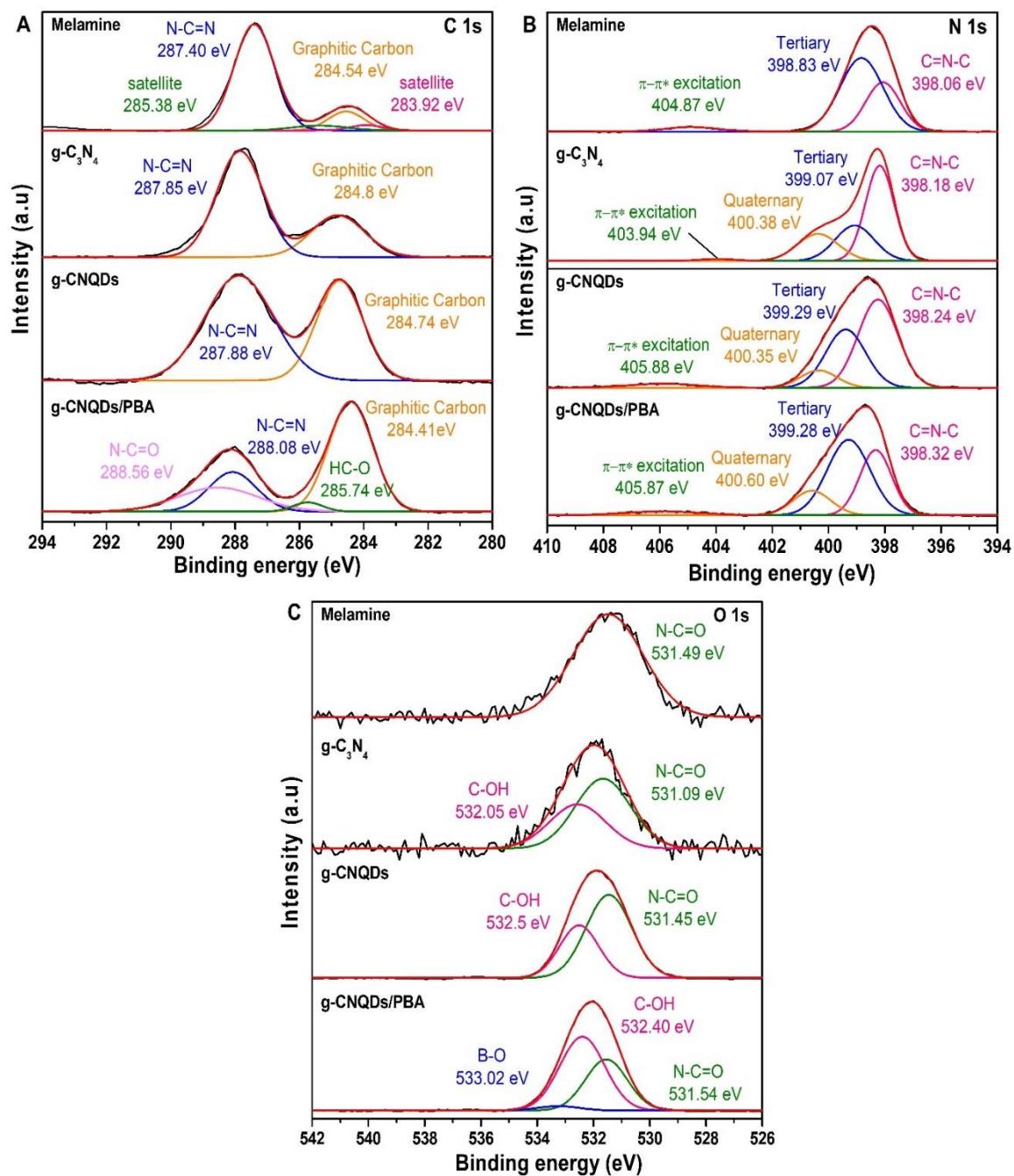


Figure S5.5. The XPS spectrum (A) C 1s, (B) N 1s, (C) O 1s of melamine, bulk g-C₃N₄, g-CNQDs and g-CNQDs/PBA.

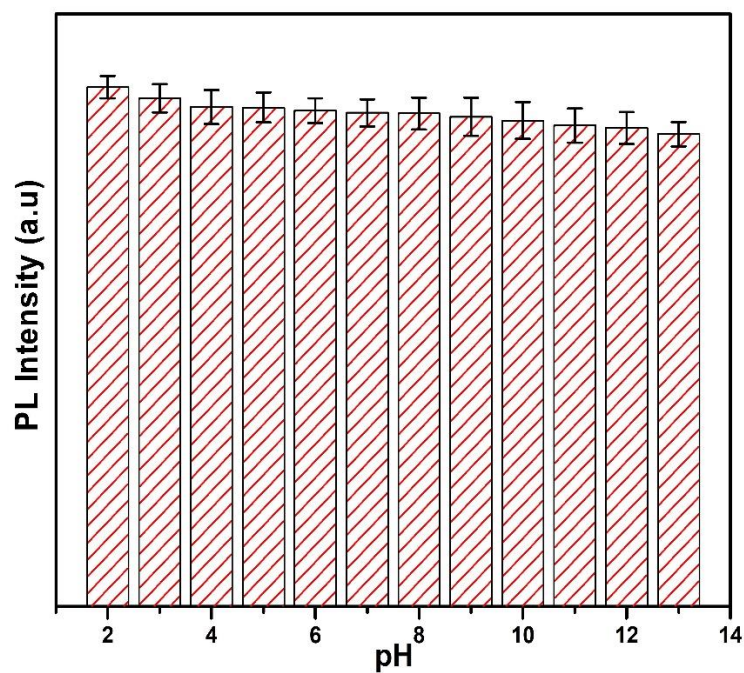


Figure S5.6. The effect of pH on the PL intensity of g-CNQDs in the range from 2 to 13. The experiment was measured in g-CNQDs (2 mg/mL) solution at excitation wavelength of 310 nm. The error bars imply the standard deviations for triple measurement at each pH value.

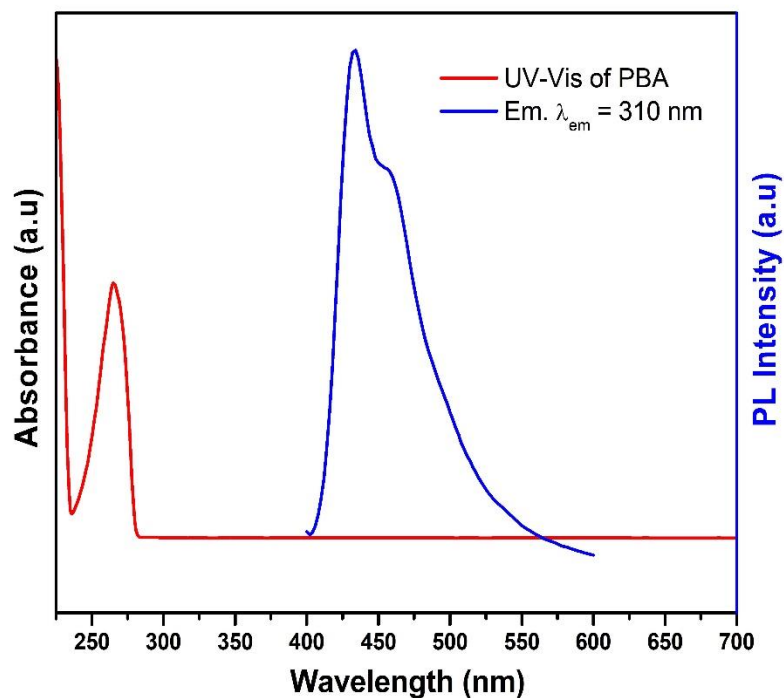


Figure S5.7. The UV-vis spectrum of PBA (red curve), and emission spectrum of the g-CNQDs ($\lambda_{ex} = 310$ nm) (black curve).

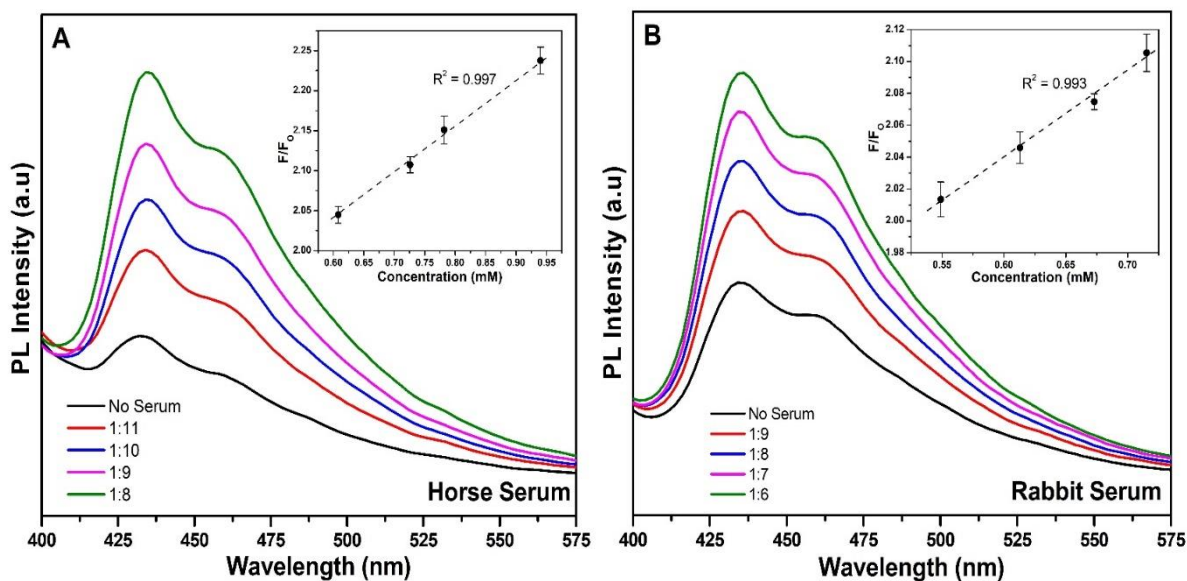


Figure S5.8. PL emission spectra of g-CNQDs/PBA towards the real serum (A) Horse serum, (B) Rabbit serum. The inset pictures show the relative PL intensity vs various concentration of serum. The error bars imply the standard deviations for triple determination at each concentration.

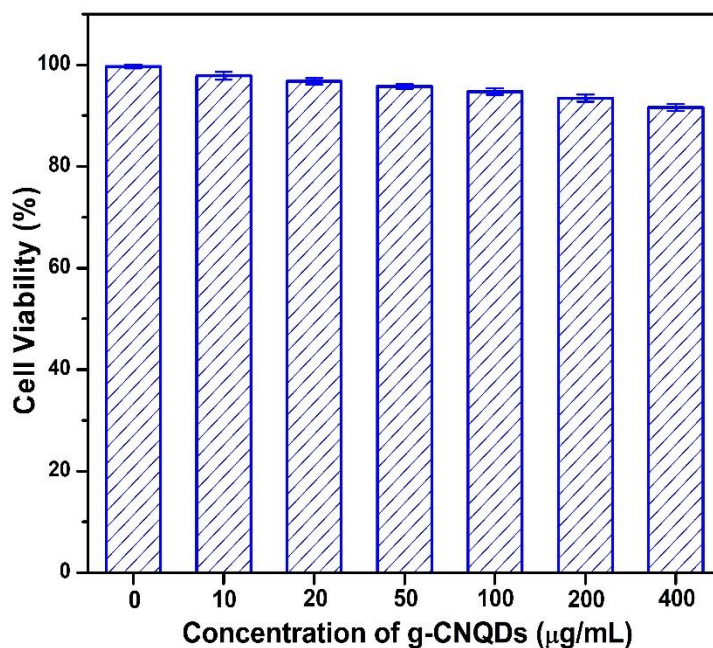


Figure S5.9. Cellular cytotoxicity of g-CNQDs towards HeLa cells evaluated by using the MTT assay.

Table S5.1. Comparison of performance of some previous studies based on fluorescent sensor for glucose.

Material	Type of sensor	Linear range	Low detection limit (LOD)	Ref.
BBV-GQDs	Fluorescent sensor	1 mM – 60 mM	–	[149]
PBS-GODs	Fluorescent sensor	4 – 40 mM	3 mM	[123]
3APBA-GODs	Fluorescent sensor	0.1 – 10 mM	5 μ M	[32]
g-C ₃ N ₄ /HRP/OPD/ GOx	Fluorescent sensor	0 – 0.1 mM 1 – 4 mM	0.4 μ M	[126]
g-C ₃ N ₄ -GOx	Colorimetric sensor	5 – 100 μ M	1 μ M	[152]
g-C ₃ N ₄ -WO ₃	Non-enzymatic sensor	0.01 – 7.12 mM	0.1 μ M	[153]
Ag ⁺ / g-CNQDs	Non-enzymatic sensor	100 μ M – 2 mM 2 – 30 mM	15 μ M	[99]
g-CNQDs-PBA	Fluorescent sensor	25 nM – 1 μ M 1 μ M – 1 mM	16 nM	This work

*Note: BBV – Bipyridinium salt, GQDs - Graphene quantum dots, PBS – Phenylboronic acid sodium salt, 3APBA – 3 Amino phenylboronic acid, HRP - Horseradish peroxidase, OPD – o-phenylenediamine, GOx – Glucose Oxidase, g-CNQDs – Graphitic carbon nitride quantum dots, PBA – Phenylboronic acid.

Chapter 6. Aminoboronic Acid-functionalized Graphitic Carbon Nitride Quantum Dots for the Photoluminescence Multi-chemical Sensing Probe

6.1. Introduction

Considerable efforts on glucose sensing have been made, including electrochemical, photo-electrochemical, colorimetric, and fluorescence methods [99,128]. Currently, practical glucose sensors have been designed based on optical methods using fluorescent quantum dots (QDs) because they show low toxicity and rapid responses with excellent sensitivity and selectivity [123,124]. Similar to graphene as a two-dimensional structure (2D), graphitic carbon nitride (g-C₃N₄) has a tunable electronic structure with a N-rich carbonaceous structure along the distinct layers, resulting in a high π -conjugation [154]. g-C₃N₄ is one of the most well-known materials with many excellent characteristics, such as eco-friendly synthetic routes, outstanding chemical stability, excellent optical properties, great biocompatibility, and low-cost [155]. Recently, g-C₃N₄ was successfully demonstrated as a fluorescent material for various potential applications in water splitting [156,157], photocatalysts [105,158], bio-sensors [126,159], bio-imaging [145,160], degradation of organic pollutants [161], and oxygen reduction reaction [28,132], owing to its unique optical features, thermal/chemical stability, and moderate band gap [103]. Furthermore, the size and surface properties are significant for determining the applications of g-C₃N₄. Therefore, they can be used as glucose sensing materials after the appropriate modification of surface functional groups [30].

To improve glucose detection, researchers have replaced the enzymes (such as glucose oxidase) with chemical ligands, which are more stable, easier to control, and inexpensive compared to enzyme-based sensors [162-164]. Many boronic acids and various derivatives containing the boronic acid group can rapidly and reversibly form a cyclic boronate ester with 1,2- and 1,3-diols located through covalent bonds [34,133,134], which enable their use in selective glucose detection when introduced to the nanostructured g-C₃N₄.

A previous study reported the successful fabrication of a glucose sensor based on g-C₃N₄ and phenylboronic acid (PBA) as a fluorescent and glucose detector, respectively [116]. By introducing properly designed chemical bonding to this structure, more chemicals can be detected by the “on-off-on” mechanism. Thus, this paper reports an effective fluorescence “on-off-on” sensor for the determination of glucose and propylene glycol based on the reversible covalent bonds of 3-aminophenylboronic acid (3APBA) with 1,2-diol groups. The highly sensitive and selective glucose sensing materials based on 3APBA-functionalized g-CNQDs were fabricated by a simple two-step process from melamine and 3APBA. The g-CNQDs/3APBA fabricated in this study exhibited strong blue emission with the highest quantum yields reported thus far. The g-CNQDs/3APBA – based sensor showed a wide detection range (25 nM – 10 mM) and a very low detection limit (42 nM). In addition, it also exhibited excellent selectivity, good biocompatibility, and low cytotoxicity in the cell-imaging test.

6.2. Experimental details

6.2.1. Materials

Melamine, sulfuric acid 98% (H₂SO₄), nitric acid 70% (HNO₃), 3-aminophenylboronic acid (3APBA), N-ethyl-(3-Dimethylaminopropyl)-N'-carbodiimide (EDC), di-sodium hydrogen phosphate (Na₂HPO₄), sodium hydroxide (NaOH), sodium chloride (NaCl), potassium chloride (KCl), potassium dihydrogen phosphate (KH₂PO₄), 37% hydrochloric acid (HCl), dimethylsulfoxide (DMSO), and 3-(4,5-dimethylthiazol-2-yl)-2,5-diphenyltetrazolium bromide (MTT), dopamine (DA), sorbitol (SB), ascorbic acid (AA), uric acid (UA), l-cystine (L-cys), D-(+)-glucose, galactose, fructose, maltose, lactose, sucrose, rabbit serum (RS) and horse serum (HS) were purchased from Sigma-Aldrich Co. (USA). Human epithelial carcinoma (HeLa) cells (ATCC[®] CCL-2[™]) were obtained from American Type Culture Collection (USA). 4,6-Diamidino-2-phenylindole (DAPI) was acquired from Vector Laboratories (USA) and a dulbecco's modified eagle media (DMEM) was supplied by Welgene Co. (Republic of Korea).

All reagents were used as received. Deionized (DI) water was used for all experiments in this research.

6.2.2. g-CNQDs/3APBA quantum dots preparation

Bulk g-C₃N₄ was fabricated using the previously reported procedure from melamine [24]. The highly water dispersible g-C₃N₄ can be prepared by chemically oxidizing the melamine with concentrated HNO₃ and H₂SO₄. Briefly, 0.05 g of bulk g-C₃N₄ powder was suspended in the concentrated HNO₃ and H₂SO₄ (volume ratio of 3:1) mixture, and followed by an ultrasonic treatment (UPC-10, Jeio-Tech Co., Ltd., Korea) in an ice bath for 10 hr. The yellowish solution was then poured into a beaker containing 500 mL of DI water and cooled to room temperature. Through the acid treatment, the surface of g-C₃N₄ can be functionalized and the size of g-C₃N₄ can be reduced to quantum dot size. The product was then filtered through a 0.2 μm microporous membrane and washed with DI water until the pH reached 7.0. The white product was dispersed in 40 mL DI water and sonicated for 10 min to produce a homogeneous solution (g-C₃N₄ (at)).

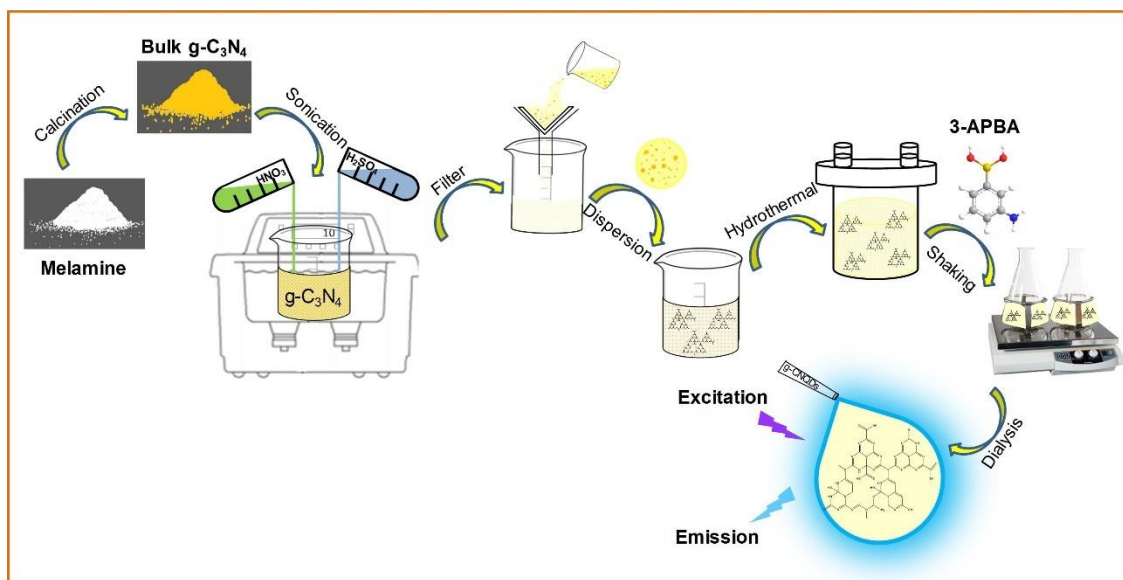


Figure 6.1. Schematic diagram of g-CNQDs/ 3APBA synthesis process from melamine.

Subsequently, 10 mL of g-C₃N₄ (at) suspension (0.25 mg/mL) was transferred to a Teflon autoclave and heated to 160 °C for 6 h to fabricate the g-CNQDs. After the hydrothermal process, 12 mg of 3-APBA and 16 mg of EDC were added to the g-CNQDs and a phosphate buffer

solution (PBS) (pH = 7.2) with a volume ratio of 1:1. The solution was shaken thoroughly for 17 h at room temperature using a Basic Orbital Shaker (IKA KS 130, Germany). To purify the sample, the final product (g-CNQDs/3APBA) was dialyzed in a dialysis bag with a pore size of 500-1000 Da for 1 day to remove the residue chemicals (see **Figure 6.1**). The MATLAB simulation was used to find the optimal condition for the hydrothermal process, as displayed in **Figure S6.1** (Supporting Information).

6.2.3. Detection of Glucose

The fluorescent solution was prepared by adding 60 μL of as-prepared g-CNQDs/3APBA to 3.08 mL of a PBS solution (pH = 10). The targeted concentration of glucose was then added to this fluorescent solution. The mixture was shaken vigorously at room temperature for 20 min, and the PL spectra of each sample was recorded under an excitation wavelength of 320 nm. To measure the selectivity of this sensor, the glucose solution was replaced with various interfering species and all other procedures were carried out in the same manner, as described above. The detection of glucose sensing towards real blood serum samples was also examined using HS and RS serum.

6.2.4. Instrumental analysis

The functional groups were examined by Fourier transform infrared (FT-IR, Nicolet 380 Thermo Fisher Scientific iS5, USA) spectroscopy. The structure and morphology were examined by high-resolution transmission electron microscopy (HR-TEM, JEM-2100F, JEOL, Japan) at an accelerating voltage of 200 kV. The chemical bonding states and electronic state of the elements were analyzed by X-ray photoelectron spectroscopy (XPS, ESCALAB 250 Xi, Thermo Fisher Scientific, USA) using Al K α X-ray radiation (1486.6 eV). The photoluminescence (PL, Cary Eclipse, Agilent Technologies, Santa Clara, USA) were obtained. Ultraviolet visible (UV-Vis SPECORD 210 PLUS, Analytik Jena, Germany) absorption spectroscopy was conducted. Time-resolved fluorescence decay spectra were obtained using a fluorescence spectrofluorometer FS5 (Edinburgh Instruments, UK). Cellular imaging was performed with a confocal laser

fluorescence microscope in sequential mode using a 60 × Plan-Apochromat (1.4 NA) oil objective.

6.3. Results and discussion

6.3.1. Characterization of quantum dots

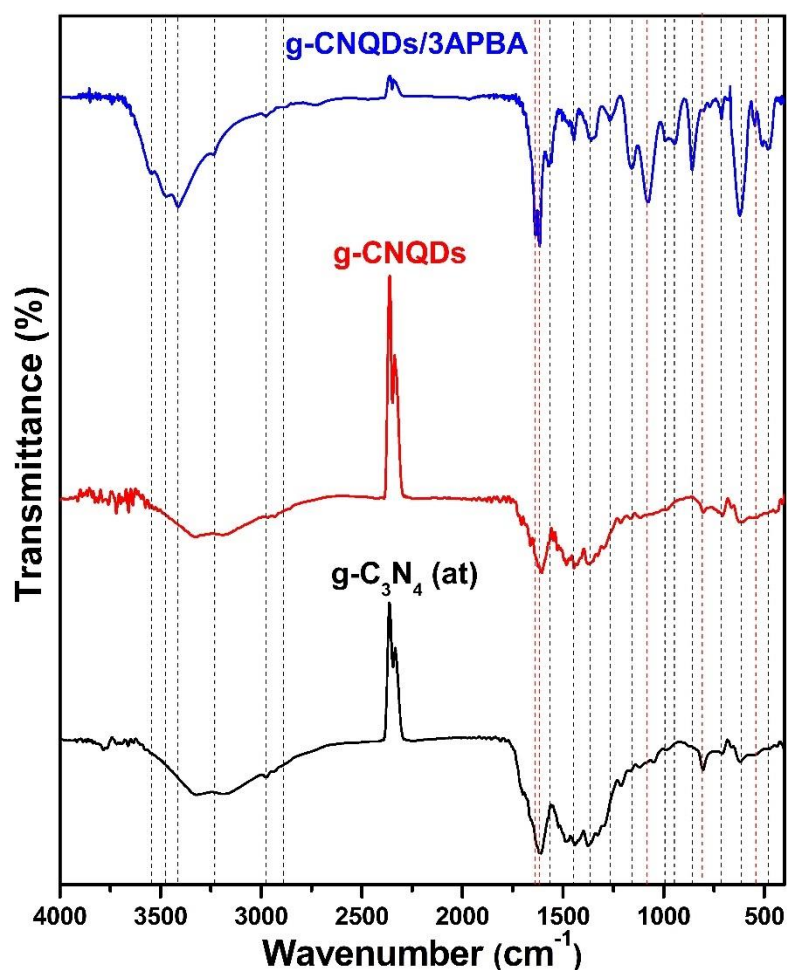


Figure 6.2. FT-IR spectra of g-C₃N₄ (at), g-CNQDs and g-CNQDs/3APBA.

FT-IR spectroscopy was used to characterize the structure and composition of the as-synthesized products. As shown in **Figure 6.2**, the sharp peak at 807 cm⁻¹ was assigned to the breathing vibration of tri-s-triazine, which is one typical out-of-plane ring bending vibration modes of g-C₃N₄, indicating that the basic structure of g-CNQDs fabricated in this study was the carbon nitride form. The absorption peaks at ~ 1267, 1364, and 1450 cm⁻¹ were assigned to the C-N, C=N, and C=C stretching bands for an aromatic amine, respectively [155]. The broad peak

at 1560–1750 cm^{-1} were assigned to the typical of C=N stretching vibration in the amide group, and the many peaks between 2850–3550 cm^{-1} were attributed to the stretching vibrations of aliphatic $-\text{CH}_2$ (νCH), hydroxyl group (νOH), and terminal amino ($\nu\text{N}-\text{H}$ or NH_2) groups of graphitic carbon nitride [142]. The new peaks at 540, 861, and 1084 cm^{-1} after the reaction with 3APBA were assigned to the symmetric and asymmetric B-O stretching vibrations of 3APBA, and the stretching vibration modes of B-C, respectively [143], indicating the successful incorporation of 3APBA to the g-CNQDs surface. Furthermore, the sharp peaks at 1569 and 1638 cm^{-1} were assigned to the stretching vibration of C=N of amide II ($-\text{CONH}$) and the stretching vibration of C=O in amide I groups, respectively [165], which confirms the formation of amide covalent bonds between g-CNQDs and 3APBA. All FT-IR peaks were assigned and the detailed information is summarized in **Table S6.1** (Supporting Information).

XPS was performed to investigate the chemical composition and oxidation state of each element. All samples exhibited several peaks related to C, N and O, as shown in **Figure 6.3(A)**. The high-resolution C 1s XPS spectra of g-C₃N₄ (at) and g-CNQDs in **Figure 6.3(B)** exhibited four peaks centered at approximately 283.6, 284.7, 287.0, and 288.0 eV, which were assigned to the sp² graphitic carbon (C-C or C=C), sp³-bonded carbon with oxygen (HC-O), sp²-hybridized carbon atoms with nitrogen in the graphite skeleton (N-C=N), and oxygen (N-C=O), respectively [166]. Interestingly, the relative ratio corresponding to the sp²-hybridized carbon with nitrogen and oxygen were decreased compared with those of C=C and HC-O bonding in the C 1s spectrum of g-CNQDs/3APBA as presented in **Table S6.2** (Supporting Information). This can be attributed to the chemical bonding of g-CNQDs with 3-APBA, which has abundant C=C bonding in its structure.

As presented in **Figure 6.3(C)**, the N 1s XPS spectra can be resolved into four sub-peaks. Three main ones centered at ~398.5 (N₁), ~400.0 (N₂), and ~401.0 eV (N₃) originated from pyridinic, pyrrolic, and quaternary and amide nitrogen atoms, respectively. **Table S6.3** (Supporting Information) shows the peak area and relative ratio of all peaks in the N 1s spectrum.

The relative ratio of peak N₃ of g-CNQDs/3APBA significantly increased when compared to pure g-CNQDs, because of the formation of amide groups between g-CNQDs and 3APBA [165]. The weak peak at ~ 405.6 eV was assigned to the charging effects or π electron (positive charge localization) delocalization in the heterocycles [130,144].

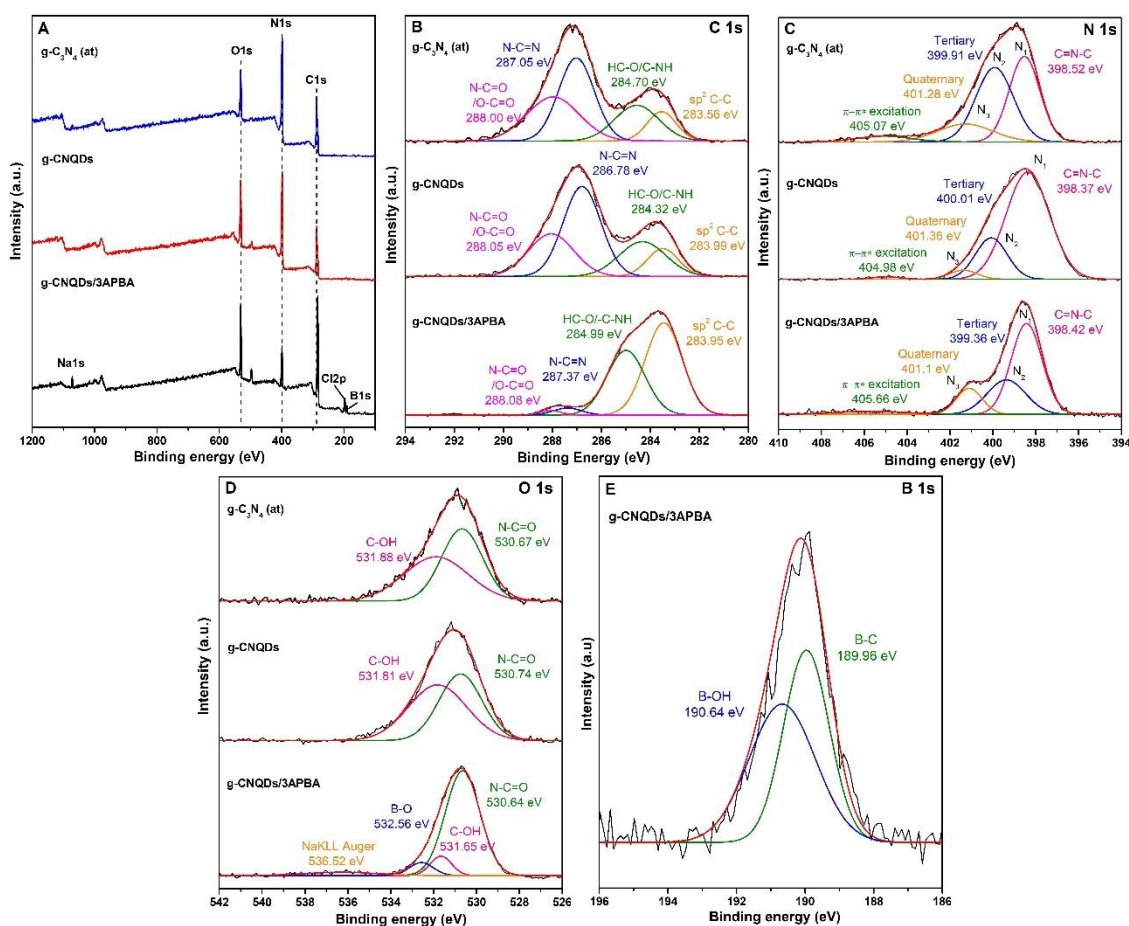


Figure 6.3. (A) XPS survey spectra and high-resolution XPS spectra of (B) C 1s, (C) N 1s, (D) O 1s of g-C₃N₄ (at), g-CNQDs, and g-CNQDs/3APBA and (E) B 1s of g-CNQDs/3APBA.

Figure 6.3(D) shows that the O 1s of g-C₃N₄ and g-CNQDs can be divided into two peaks centered at ~530.65 and ~531.70 eV, which were assigned to N-C=O and C-OH bonds, respectively. On the other hand, g-CNQDs/3APBA exhibited two new peaks centered at 532.56 eV and 536.32 eV, which were attributed to B-O bonds of 3-APBA functionalized g-CNQDs and O-F_x (Sodium Auger peak NaKLL) of PBS, respectively. In addition, as shown in **Figure 6.3(E)**, B 1s can be deconstructed into two peaks centered at 189.96 and 191.64 eV, which

correspond to B–C and B–OH bonds, respectively. The O 1s and B 1s XPS spectra of g-CNQDs/3APBA clearly indicate that 3-APBA had been attached successfully to the g-CNQDs.

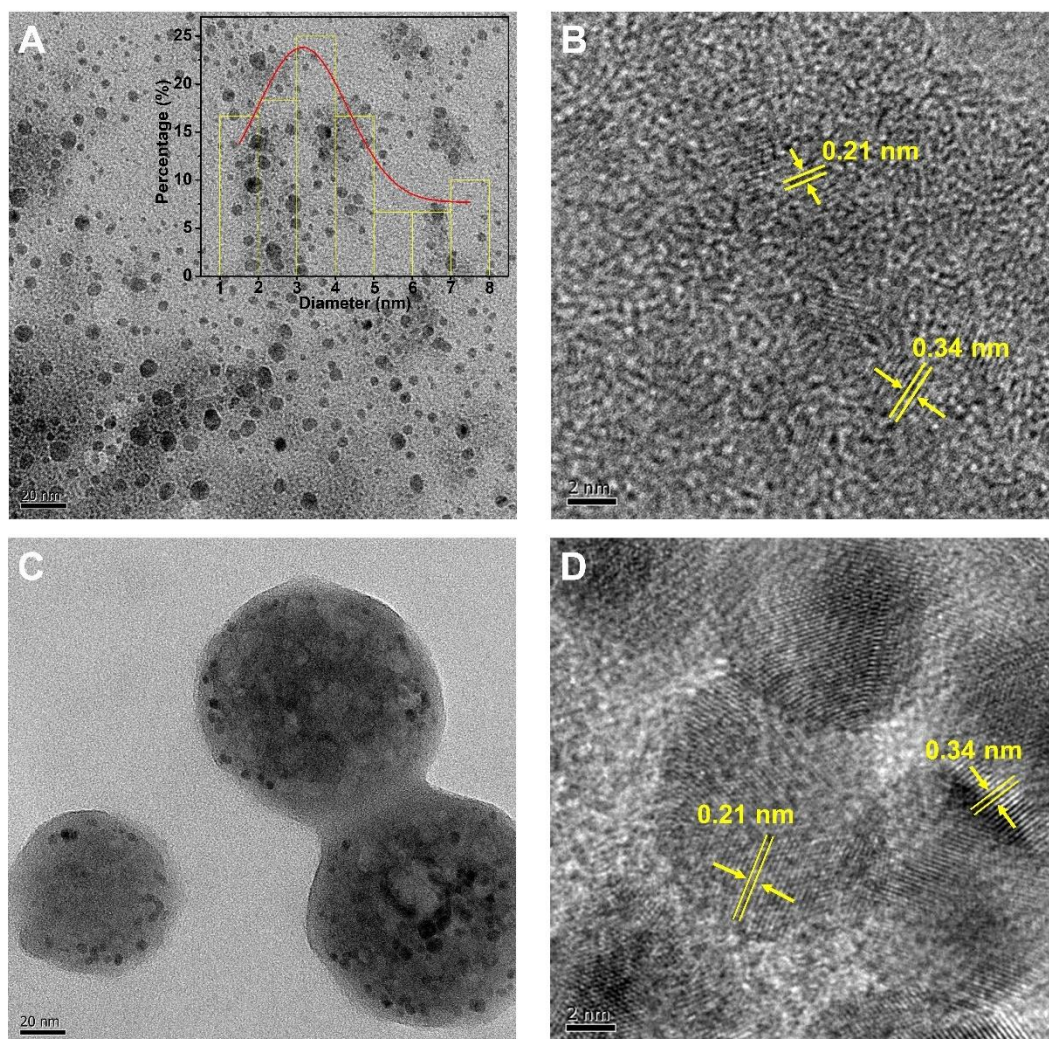


Figure 6.4. TEM images of (A) g-CNQDs, (C) g-CNQDs/3APBA. HR-TEM images of (B) g-CNQDs and (D) g-CNQDs/3APBA.

The morphology and size of g-C₃N₄ (at), g-CNQDs, and g-CNQDs/3APBA were investigated by TEM and HR-TEM, as shown in **Figure S6.2** (Supporting Information) and **Figure 6.4**. The TEM image of the g-CNQDs (**Figure 6.4(A)**) indicated that the nanodots were well dispersed without agglomeration. The diameter of the as-prepared g-CNQDs were in the range of 1–8 nm with a mean diameter of 3.5 nm when 200 random dots were measured (Inset of **Figure 6.4(A)**). The lattice spacings of g-CNQDs shown in **Figure 6.4(B)** were approximately 0.21 and 0.34 nm, which are consistent with those of the (100) and (002) crystal planes of

graphitic carbon nitride, respectively [30]. As shown in **Figure 6.4(C)**, the structure of g-CNQDs/3APBA had a secondary structure, both agglomerates and aggregates form, but the g-CNQDs maintained a spherical shape with a similar size to the original g-CNQDs. The existence of secondary structure of g-CNQDs/3APBA can be explained that the distribution of van der Waals forces among the g-CNQDs molecules, and formation of the covalent bonds with 3APBA in the presence of EDC/PBS solution [167-169]. In addition, the lattice spacing of g-CNQDs/3APBA was the same as that of the original g-CNQDs, which indicates that the basic structure of g-CNQDs remains the same even after the reaction with 3APBA and mixing with PBS (**Figure 6.4(D)**).

6.3.2. Optical properties of g-CNQDs/3APBA

The optical properties of g-CNQDs/3APBA were investigated by UV-vis absorption and PL spectroscopy. As shown in **Figure S6.3** (Supporting Information), the UV-vis spectrum of g-CNQDs/3APBA exhibited two strong peaks at 250 nm and 300 nm, which were assigned to $\pi-\pi^*$ electronic transitions for carbon nitride containing s-triazine rings and the electron transition of $n-\pi^*$ for the C=N and C=O bonds in g-CNQDs/3APBA, respectively [170]. Interestingly, the photoluminescence emission spectra showed an excitation wavelength-independent emission peak at ~ 374 nm, owing to the transition between the δ^* conduction band and the lone pair valence band attributed to the sp^2 C-N band [145,146]. As distinct from most previous studies based on g-CNQDs with blue fluorescence [144,145,171], the emission peak of g-CNQDs/3APBA is in the ultraviolet region. The blue-shift of emission peak of g-CNQDs/3APBA can be described to the quantum confinement effect with the conduction and valence band shifting in the opposite directions [171-173]. The digital photographs shown in the inset of **Figure S6.3(A)** (Supporting Information) suggest that the g-CNQDs/ 3APBA solution is whitish opaque under visible light excitation but recognizes blue fluorescence under UV irradiation with a wavelength of 365 nm. Moreover, the emission wavelength observed was almost constant (**Figure S6.3(B)** - Supporting Information), which indicates that the as-fabricated g-CNQDs has a single emitter with main emission is blue color.

The relative quantum yields (QYs) were measured using quinine sulfate as a reference (QYs = 54%) with an excitation wavelength of 320 nm. In **Figure S6.4** (Supporting Information), the QYs of the as-obtained g-CNQDs/3APBA was as high as 78.5%, which is the highest QYs for fluorescence sensors based on g-CNQDs reported thus far, as summarized in **Table S6.4** (Supporting Information). The time-resolved fluorescence decay spectra of g-CNQDs/3APBA was investigated as shown in **Figure S6.5** (Supporting Information). Emission decay curve for g-CNQDs/3APBA is fit to double-exponential decay that indicated the presence of two emitting components with different lifetimes. The faster component has a shorter lifetime ($\tau_1 = 0.58$ ns) and the slower component has a longer lifetime ($\tau_2 = 5.94$ ns). The lifetimes and the corresponding fractional contributions are summarized in the inset **Figure S6.5** (Supporting Information). Because $^1(\pi,\pi^*)$ and $^1(n,\pi^*)$ are close to each other in the presence of polar solvent like water, the (π,π^*) level would be lower than (n,π^*) level, this would cause high fluorescence with short lifetime [144]. Furthermore, the photograph of the Tyndall effect of a diluted dispersion of g-CNQDs/3APBA acquired by red laser light scattering passing through the solution revealed the colloidal nature of the dispersion (**Figure S6.6** – Supporting Information), demonstrating the excellent dispersion of g-CNQDs/3APBA in the solvent [137].

6.3.3. Fluorescence glucose detection of g-CNQDs/3APBA

To determine the optimal pH for glucose sensing, the sensing properties were analyzed at pH = 7 and 10, as shown in **Figure S6.7** (Supporting Information). 3-APBA is a Lewis acid with vacant p orbitals that can accept the lone pair of a Lewis base, such as hydroxyl groups in glucose, to form the boronate form [164]. The change in PL intensity of g-CNQDs/3APBA was significantly higher at pH = 10 than at pH = 7 when the same amount of glucose was added. Generally, boronic acid can produce bonds with diols that have a 1,2-diol group, such as glucose. The structure can be either a trigonal neutral boronate form, where the boron atom is in sp^2 hybridization, or tetrahedral anionic boronate form, where the boron atom is in sp^3 form, which depends strongly on the pH of the solution [174]. When the pH of an aqueous solution is close

to the pK_a of boronic acid, the concentration of the boronic acid form is equal to the concentration of the boronate form. As the reported pK_a of 3-APBA is approximately 8.8, boronate ester formation is not favored at neutral pH [174]. When glucose is added, the boronate can bind the hydroxyl group of glucose to form an ester, leading to a lower concentration of the boronate form. This causes a decrease in the boronic acid form to maintain the acid-base equilibrium, resulting in a decrease in apparent pK_a [164,175,176]. Moreover, as the neutral boronate ester is generally more Lewis acidic than the initial boronic acid, boronate ester formation is favored at a higher pH to form the tetrahedral anionic boronate ester, which results in much stronger binding with diols of D-glucose than that with the trigonal neutral form [177]. Based on these results, all experiments were carried out in a PBS solution at pH = 10.

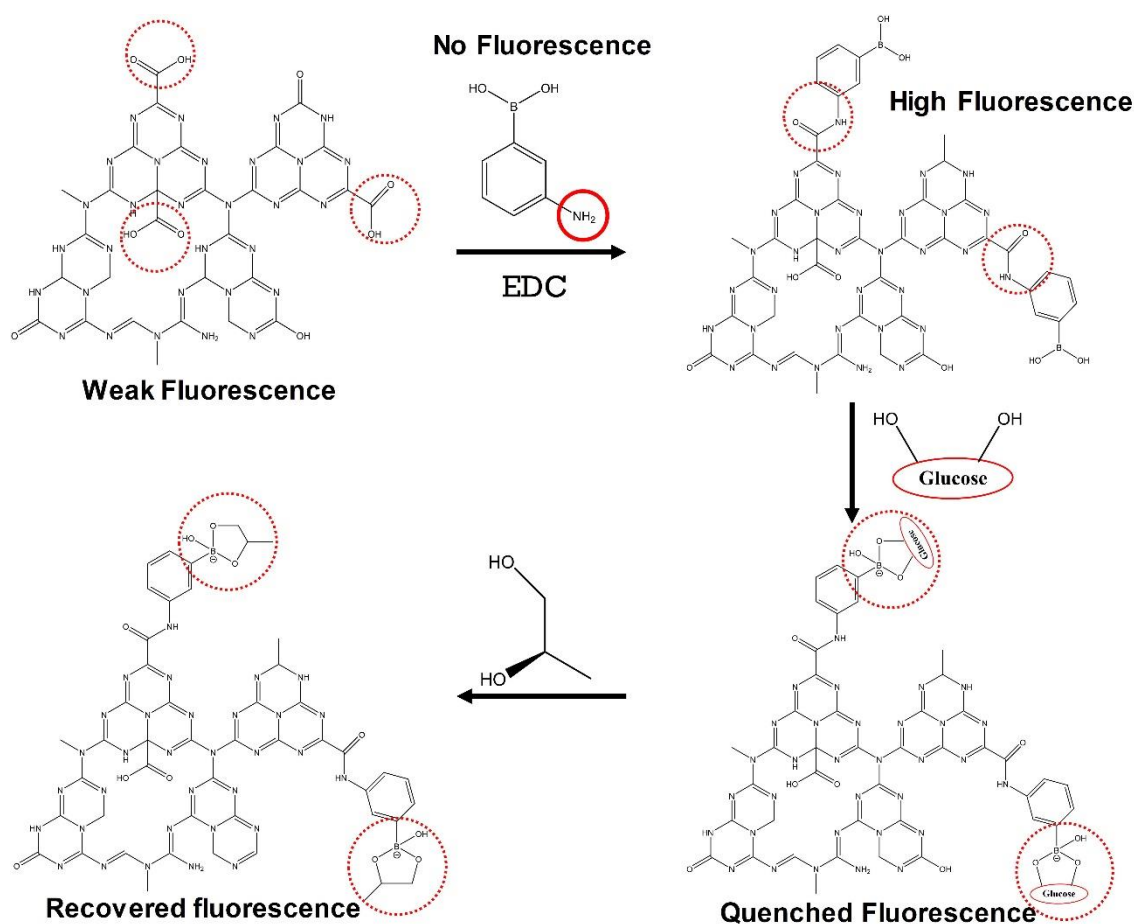


Figure 6.5. Sensing mechanism of g-CNQDs/3APBA based fluorescence sensor “on-off” for glucose and “on-off-on” for propylene glycol.

Figure 6.5 presents the reaction between g-CNQDs and 3-APBA in the presence of an EDC catalyst. The PL intensity of g-CNQDs after the hydrothermal process is very low, as shown in **Figure S6.8** (Supporting Information). Indeed, the functional group on g-CNQDs surface especially is -COOH, tends to withdraw electrons from the conduction band of the C-N electronic structure, such that the fluorescence of g-CNQDs may be quenched [178]. The addition of 3-APBA to an EDC/PBS solution containing g-CNQDs causes strong enhancement of the fluorescent intensity. This can be attributed to the suppression of photo-induced electron transfer (PET) due to efficient formation of the fluorescent structure between the protonated tertiary amino group and the negatively charge on the hydroxylated boronic acid ester by hydrolysis in the PBS buffer solution [179].

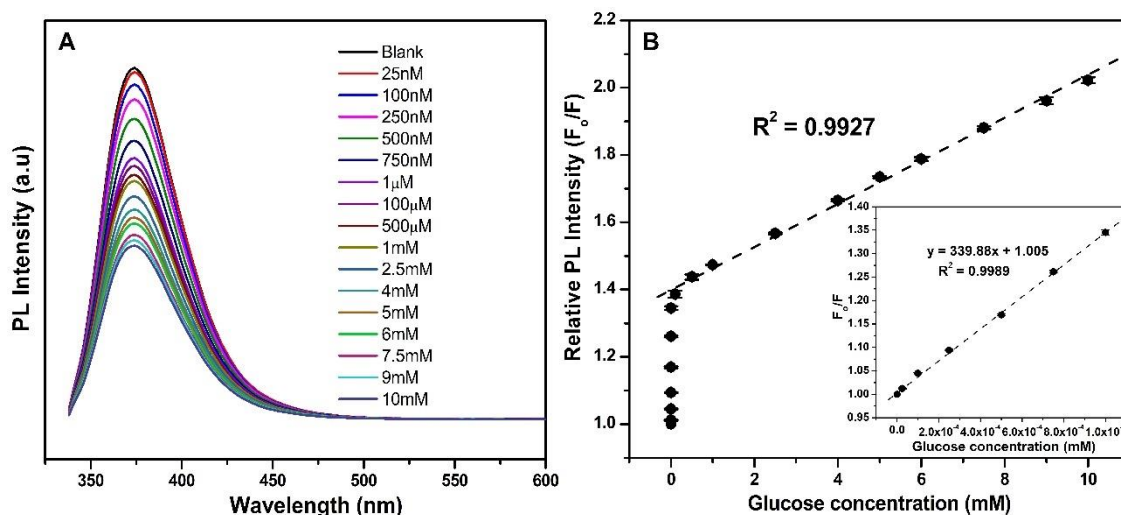


Figure 6.6. (A) PL emission spectra of g-CNQDs/3APBA in the presence of different glucose concentrations. (B) Plots of the relationship between the relative PL intensity (F_0/F) and glucose concentration. F_0 and F are the PL intensity of g-CNQDs/3APBA in the absence and presence of glucose, respectively. The inset shows a linear curve over the concentration range from 25 nM to 1 μ M. Measurement conditions: g-CNQDs/3APBA = 0.5 mg/mL, pH = 10, and λ_{ex} = 320 nm.

As shown in **Figure 6.6(A)**, the PL of g-CNQDs/3APBA decreased gradually with increasing glucose concentration, even at a low concentration of 25 nM, which indicates the excellent sensitivity of g-CNQDs/3APBA towards glucose. The PL quenching of g-

CNQDs/3APBA by glucose can be due to the formation of tetragonal anionic glucoboronate ester bonds between the boronic acids and 1,2-diols of glucose [175,177]. In addition, boronate ester formation results in the introduction of electron-withdrawing substituents on the glucoboronate ester, leading to the enhanced Lewis acidic nature of boron atoms and consequently decreased PL intensity [179], as illustrated in **Figure 6.5**. The Stern-Volmer plot shown in **Figure 6.6(B)** indicates that the PL intensity is strongly dependent on the glucose concentration. Wide linear ranges from 25 nM to 1 μ M ($R^2 = 0.9989$) and 1 μ M to 10 mM ($R^2 = 0.9927$) were observed with a limit of detection (LOD) as low as 42 nM (signal-to-noise ratio of 3). Compared to a previous report of a boronic acid/quantum dot-based glucose sensor (**Table S6.5** – Supporting Information), the present results showed excellent glucose sensing properties, such as a very wide linear range and extremely low detection limit with high sensitivity. This was attributed to the excellent QYs and well-designed glucose specific surface functional groups of g-CNQDs/3APBA fabricated in this research.

The detection selectivity of the g-CNQDs/3APBA towards various interfering species in blood, such as uric acid, ascorbic acid, dopamine, sorbitol, glycine, l-cystine, and other saccharides, was investigated under the same experimental conditions. As shown in **Figure S6.9** (Supporting Information), g-CNQDs/3APBA exhibited excellent selectivity towards glucose over other interfering species, which can be due to the specific reaction between the 1,2-diols of glucose and the boronic acid of 3-APBA. The very low response of g-CNQDs/3APBA towards other saccharides can be attributed to the absence of such key structural features that can interact with boronic acid [151].

A simple 1,2-diol compound was tested to verify the glucose effect on the quenching of g-CNQDs/3APBA. 1,2-Propanediol is one type of 1,2-diol compounds, which is a substance commonly used as a cosmetic and food additives [176]. As shown in **Figure 6.7**, the PL intensity of glucose-added g-CNQDs/3APBA increased with increasing 1,2-propanediol concentration, which can be due to the hydrolysis of glucoboronate ester in the presence of 1,2-propanediols at the boronic acid sites of g-CNQDs/3APBA. This can be applied to the 1,2-propanediol sensor.

Two good linear regions were observed between the PL intensity and propylene glycol concentration, ranging from 100 nM to 5 mM with a very low LOD of 85 nM. As shown in **Figure S6.10** (Supporting Information), when only 1,2-propanediol is added to the glucose-bonded g-CNQDs/3APBA, the PL is recovered almost up to the original intensity, which suggests that boronic acid can effectively bind with only 1,2-diol compounds. In addition, the diol itself and the chemical structure of glucose plays an important role in the PL quenching of g-CNQDs/3APBA.

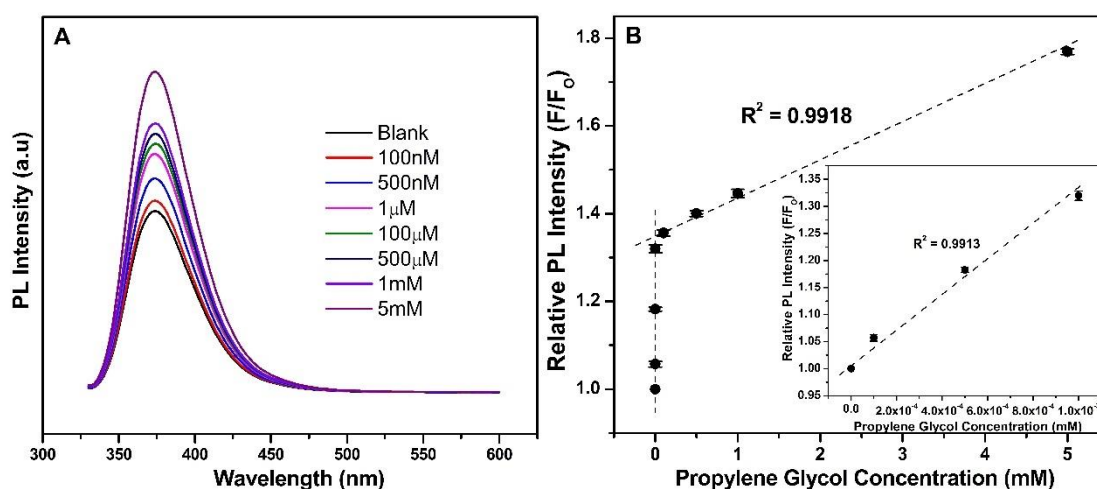


Figure 6.7. (A) PL response of g-CNQDs/3APBA in the presence of 10 mM glucose and different concentrations of propylene glycol. (B) Plot of the linear range of relative PL intensity (F/F_0) vs concentration of propylene glycol, with F_0 and F being the PL intensity in the absence and presence of propylene glycol.

6.3.4. Measurement of the glucose concentration in real blood serums

The glucose concentration in real blood was examined using the g-CNQDs/3APBA fabricated in this study. The experiments were carried out under the same conditions of glucose monitoring using horse serum (HS) and rabbit serum (RS), whose glucose concentrations are known clearly. The calibration curve of the relative intensity of g-CNQDs/3APBA at several diluted HS and RS serum solutions was produced and each concentration calculated from the plot was then compared with those obtained using a commercial glucometer (ACCU-CHECK®).

Blood Glucose Meter). As shown in **Table 6.1** and **Figure S6.11** (Supporting Information), the errors of the glucose concentrations in real blood serum between the g-CNQDs/3APBA-based sensor and commercial glucometer were less than 1% at all concentrations, which indicates that the as-prepared g-CNQDs/3APBA can be used for real blood monitoring with excellent accuracy.

Table 6.1. Comparison of a commercial glucometer with the sensor based on g-CNQDs/3APBA for glucose determination at various serum concentrations.

Dilution ratio of serum in DI water	Horse blood serum (mM)		Rabbit blood serum (mM)	
	g-CNQDs/3APBA	Glucometer	g-CNQDs/3APBA	Glucometer
1:0	3.541	3.552	6.675	6.716
1:1	2.170	2.165	3.723	3.719
1:2	1.560	1.554	3.330	3.275
1:3	1.157	1.166	1.893	1.887
1:4	1.002	0.999	1.719	1.721
1:5	0.837	0.833	1.548	1.550
Error (%)	0.41		0.51	

6.3.5. Cell imaging and cytotoxicity test

A standard MTT assay was used to investigate the cell viability at various concentration of the g-CNQDs/3APBA on HeLa cells. The g-CNQDs/3APBA showed a more than 85% cell viability rate at the concentrations up to 250 $\mu\text{g/mL}$ after 24 h incubation, which demonstrates that the g-CNQDs/3APBA exhibits a very low cytotoxicity to HeLa cells (**Figure 6.8**). Owing to the low cytotoxicity, high PL stability, and good biocompatibility, the g-CNQDs/3APBA can be a promising candidate for bio-imaging applications. The HeLa cells emitted strong blue and green fluorescence after incubation with g-CNQDs/3APBA for 8 h upon irradiation with a wavelength of 405 and 488 nm, respectively (**Figure 6.9**). The fluorescence emission was observed mainly in the membrane and cytoplasmic region of the cells, indicating that although g-CNQDs/3APBA molecules can enter the nucleus, it cannot permeate into the inner nuclei, further confirmed that it presents low cytotoxicity on the cells. Thus, all these results suggest g-CNQDs/3APBA can be

a promising material with the excellent biocompatibility for the biomedical applications such as bio-imaging.

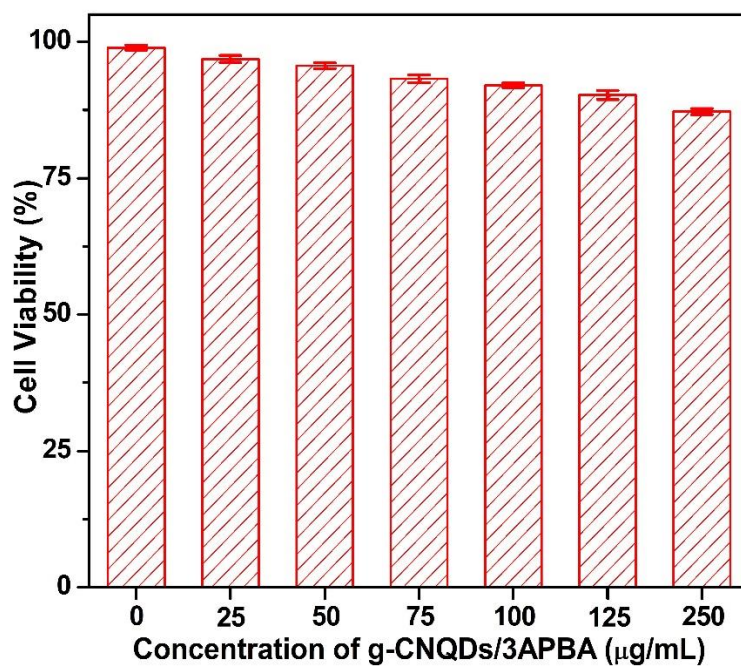


Figure 6.8. Cellular cytotoxicity of g-CNQDs/3APBA towards HeLa cells evaluated by using the MTT assay.

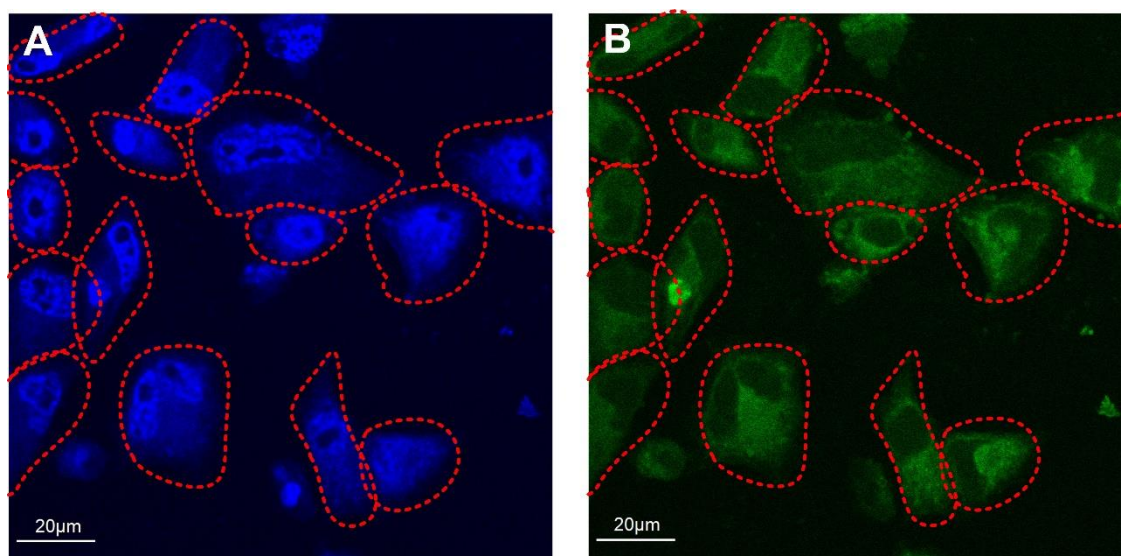


Figure 6.9. Confocal fluorescence images of HeLa cells under laser excitation at (A) 405 nm, and (B) 488 nm of g-CNQDs/3APBA. The scale bar represents 20 μm .

6.3.6. Paper-based glucose sensor

For the easy monitoring of glucose, the cellulose filter paper coated with the g-CNQDs/3APBA was used as a glucose-sensing device. Typically, the g-CNQDs/3APBA sample was dropped on the test paper, DI and glucose were then added to each side of the paper, which was noted as “S” and “S+G” on the paper, respectively (**Figure 6.10(A)**). After 20 min, the paper was placed under a 365 nm UV lamp (**Figure 6.10(B)**). The PL quenching can be observed clearly, even by the naked eye, which suggests that this type of sensing paper can be used very easily for rough monitoring of the glucose level. To obtain the PL quenching quantitatively, the level of corrected total cell fluorescence (CTCF) was determined using ImageJ software. The CTCF was then calculated using the following equation [180,181]:

$$CTCF = \text{Integrated Density} - (\text{Area of selected cell} \\ \times \text{Mean fluorescence of background readings}) \quad (v)$$

Where, the integrated density is the sum of density of all the pixels for one selected area. The mean fluorescence of background readings is the average signal per pixel for a region just beside selected area without fluorescence emission.

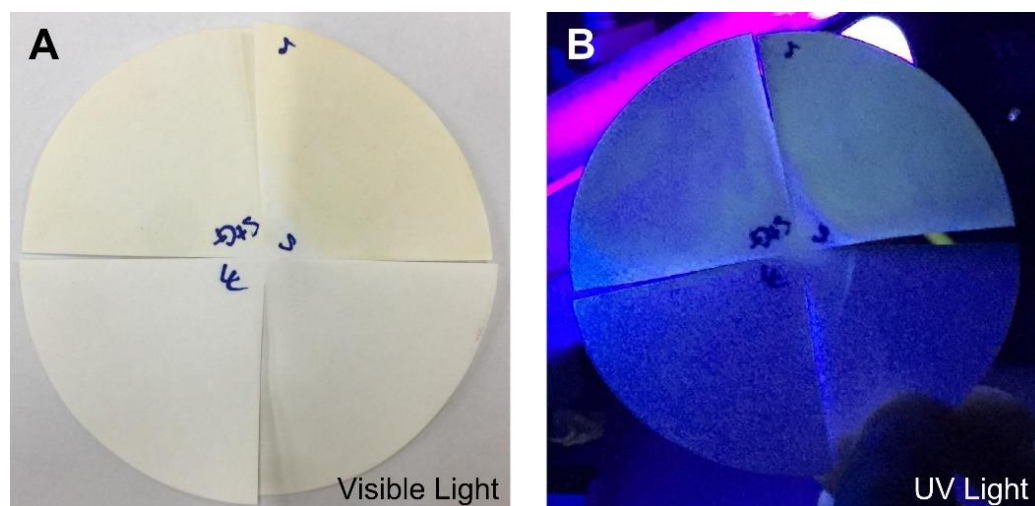


Figure 6.10. Fluorescence images of test paper in the absence and presence of glucose under visible light and a 365 nm UV lamp.

As shown in **Figure 6.11**, the decrease in CTCF after glucose addition to the sensing papers was relatively constant at various samples, from which the level of PL quenching by the glucose can be similar when quenching is monitored by the naked eye.

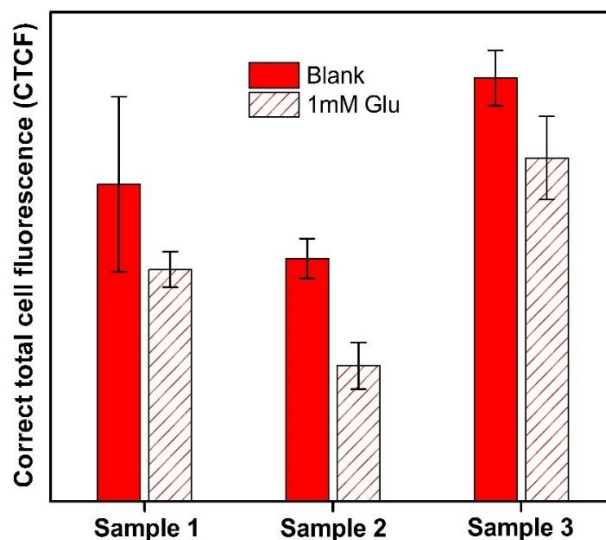


Figure 6.11. Correct total cell fluorescence (CTCF) of each sample. The bar describes the average of three experiments for each sample.

6.4. Conclusions

Well-designed high quantum yields fluorescent carbon nitride quantum dots (g-CNQDs) were fabricated from melamine and 3-aminophenylboronic acid (3APBA) in the presence of a N-ethyl-(3-dimethylaminopropyl)-N'-carbodiimide (EDC) catalyst. The excellent quantum yield of g-CNQDs/3APBA was attributed to the suppression of photo-induced electron transfer (PET) due to the efficient formation of a fluorescent structure between the protonated tertiary amino group and negatively charged hydroxylated boronic acid ester by hydrolysis in a PBS buffer solution. They exhibited high sensitivity and excellent selectivity with a low detection limit and wide linear detection range in glucose detection due to the specific chemical bonding between the boronic acids of g-CNQDs/3APBA. Using the hydrolysis of glucoboronate ester in the presence of diols, glucose-saturated g-CNQDs/3APBA can be also used as an effective 1,2-propanediol sensor with a wide detection range and low detection limit. The g-CNQDs/3APBA also exhibited excellent bio-imaging properties and low cytotoxicity.

6.5. Supporting Information

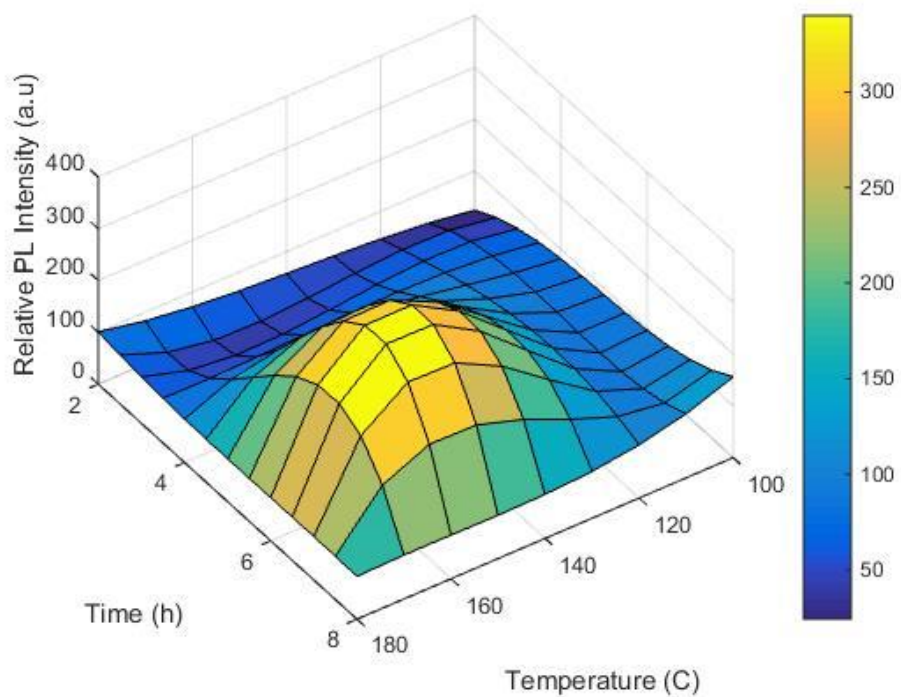


Figure S6.1. Simulated the optimize conditions including temperature and time for hydrothermal process for fabricated g-CNQDs/3APBA by MATLAB simulation of the 3D-scattering intensity distribution.

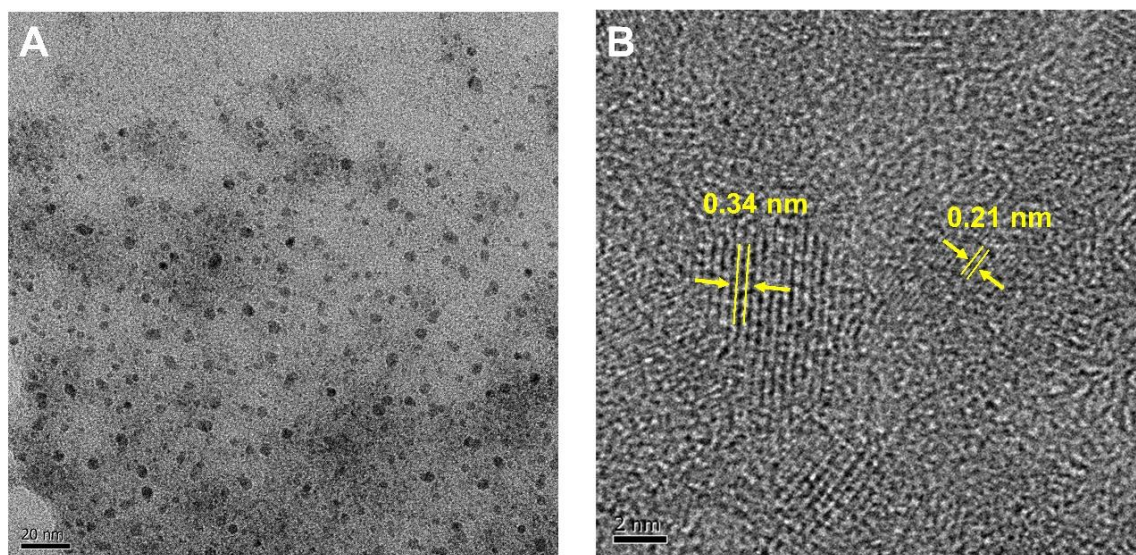


Figure S6.2. TEM and HR-TEM image of g-C₃N₄ after acid treatment process.

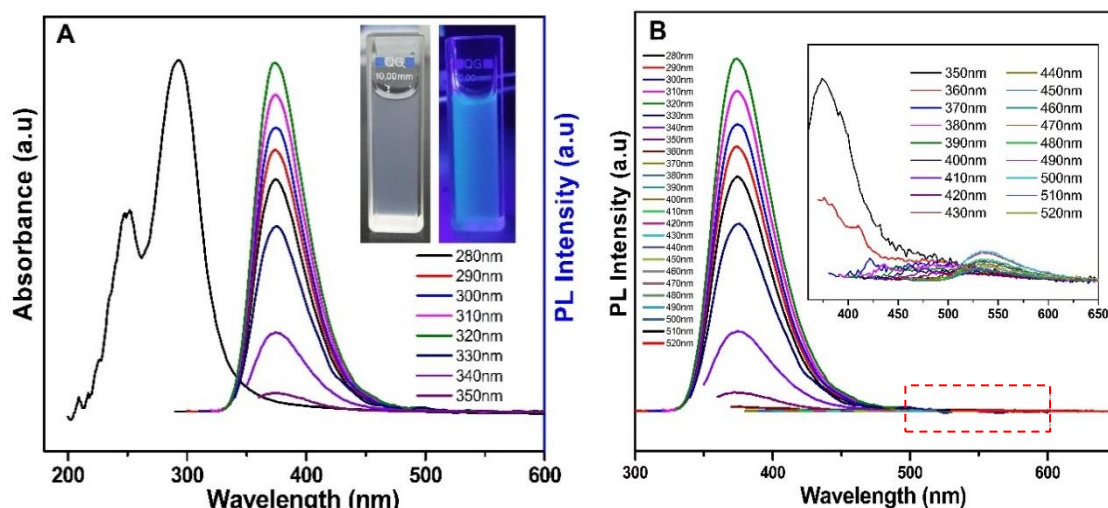


Figure S6.3. (A) UV-Vis absorption and photoluminescence (PL) emission spectra of g-CNQDs/3APBA at various excitation wavelengths; the inset photo represents the g-CNQDs/3APBA suspension under visible (left) and UV light (right). (B) PL emission spectra at the wide range of excitation wavelength from 280 – 520 nm.

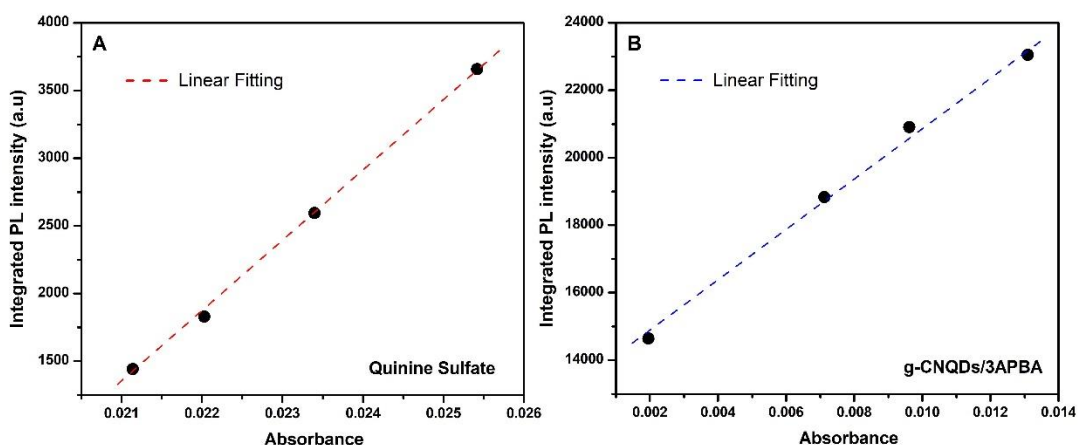


Figure S6.4. Plots integrated PL intensity of quinine sulfate (reference dye) and g-CNQDs/3APBA as a function of optical absorbance at 320 nm and relevant data.

	Quinine sulfate				g-CNQDs/3APBA			
Abs	0.0211	0.0220	0.0234	0.0254	0.0020	0.0071	0.0096	0.0131
Integrated PL	1441.2	1829.3	2594.5	3658.0	14642.9	18832.3	20905.5	23051.4
Slope	524047				762607			
QY (%)	54				78.58			

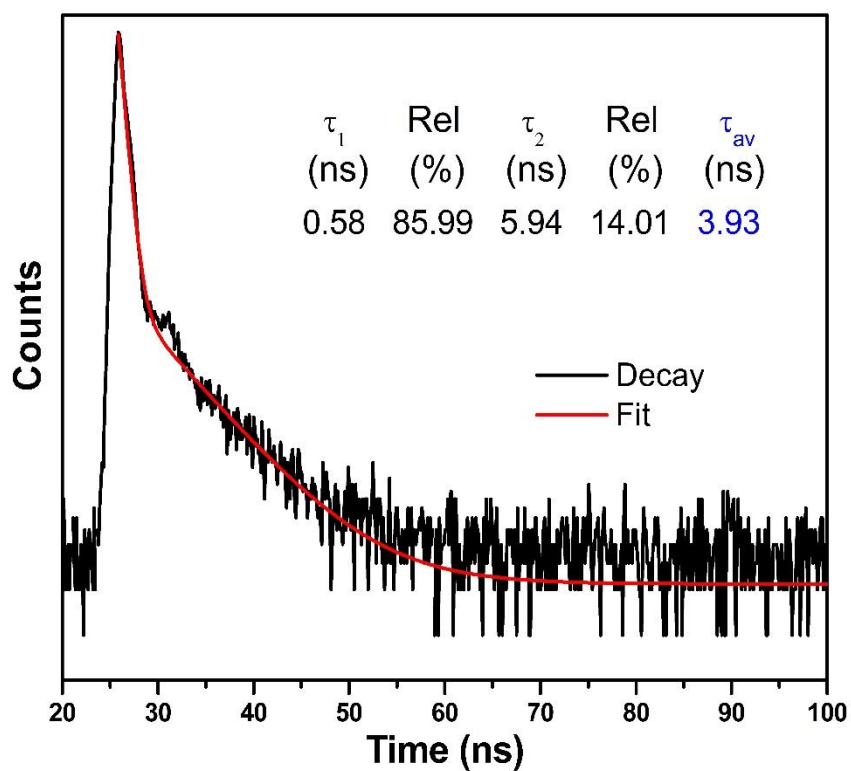


Figure S6.5. Time-resolved fluorescence decay spectra of g-CNQDs/3APBA and inserted shows two-exponential analysis results.

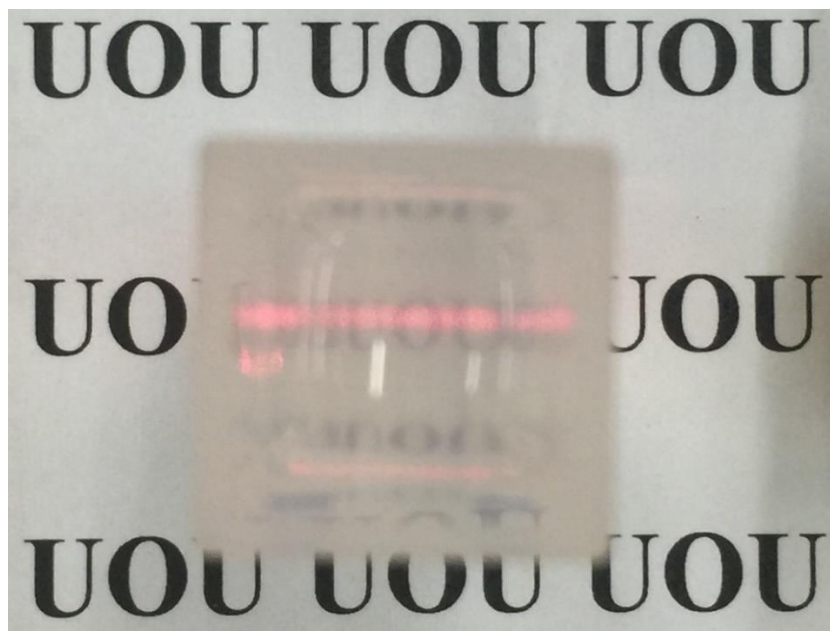


Figure S6.6. Tyndall effect of g-CNQDs/3APBA in the aqueous dispersion obtained by red laser passing through solution.

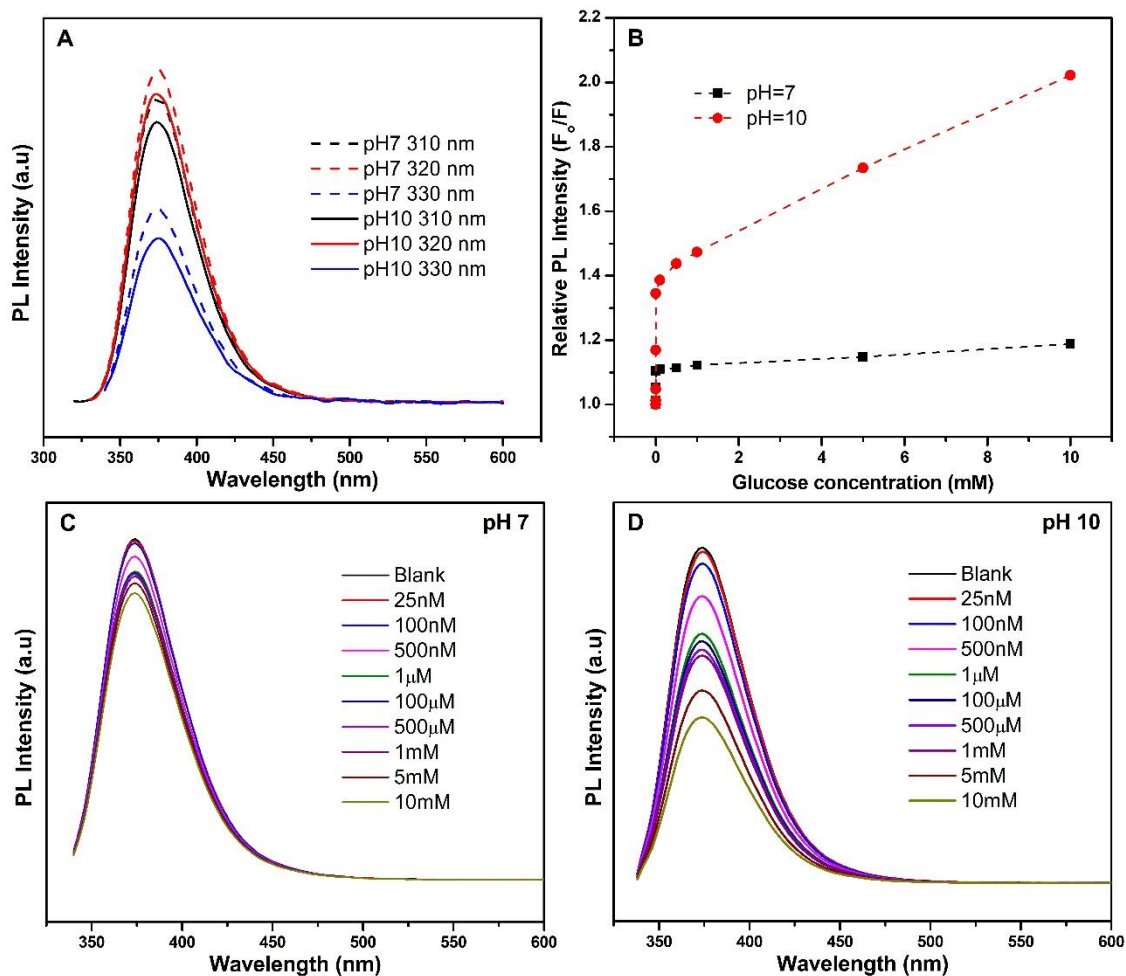


Figure S6.7. (A) PL emission spectra of g-CNQDs/3APBA in PBS solution with pH = 7 and 10; (B) the relative PL intensity of g-CNQDs/3APBA versus the glucose concentration; (C-D) PL emission of g-CNQDs/3APBA with the addition of various glucose concentration increasing from 25 nM to 10 mM in PBS pH = 7 and 10, respectively. The PL spectra was by using 0.5 mg/mL g-CNQDs/3APBA recorded in PBS buffer under $\lambda_{\text{ex}} = 320 \text{ nm}$, $\lambda_{\text{em}} = 374 \text{ nm}$.

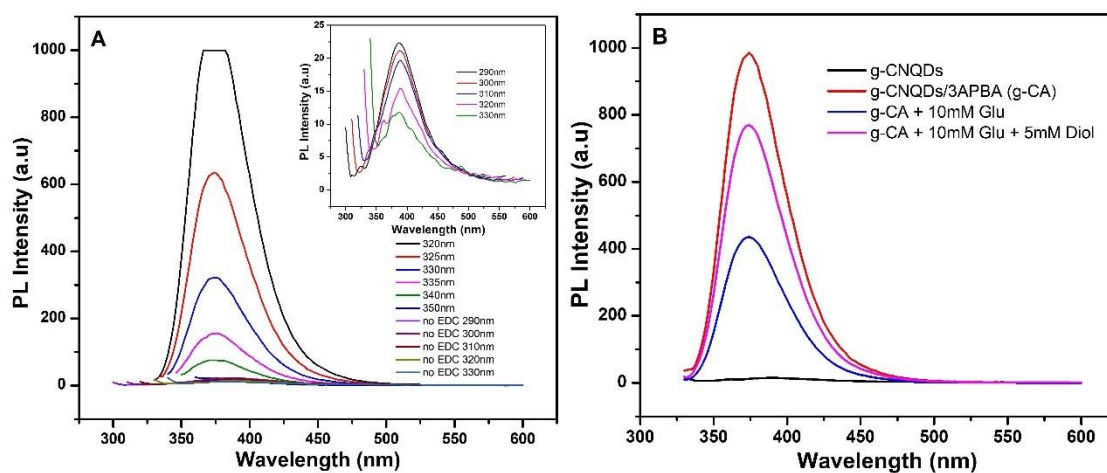


Figure S6.8. (A) PL emission spectra of g-CNQDs and g-CNQDs/3APBA/EDC at the various excitation wavelength; (B) The PL emission of g-CNQDs, g-CNQDs/3APBA, g-CNQDs/3APBA with glucose and g-CNQDs/3APBA/Glucose with propylene glycol (diol).

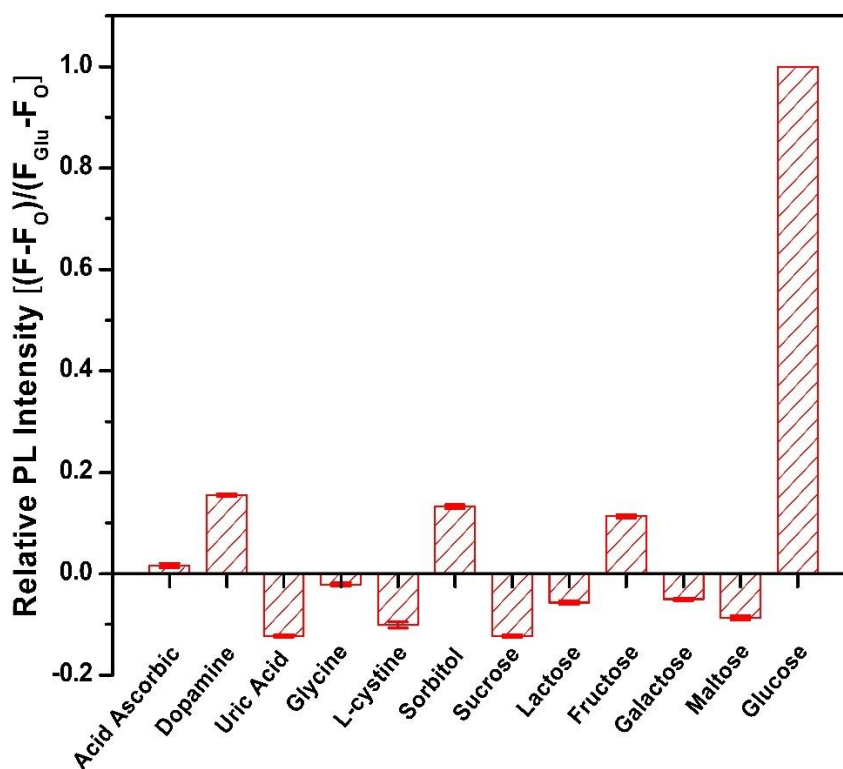


Figure S6.9. Relative PL intensity $\frac{(F-F_0)}{(F_{Glu}-F_0)}$ of g-CNQDs/3APBA after the addition of various interfering species. F and F_0 represent the PL intensity of g-CNQDs/3APBA with and without 5 mM of interfering species, respectively. F_{Glu} is the PL intensity at 1 mM of glucose.

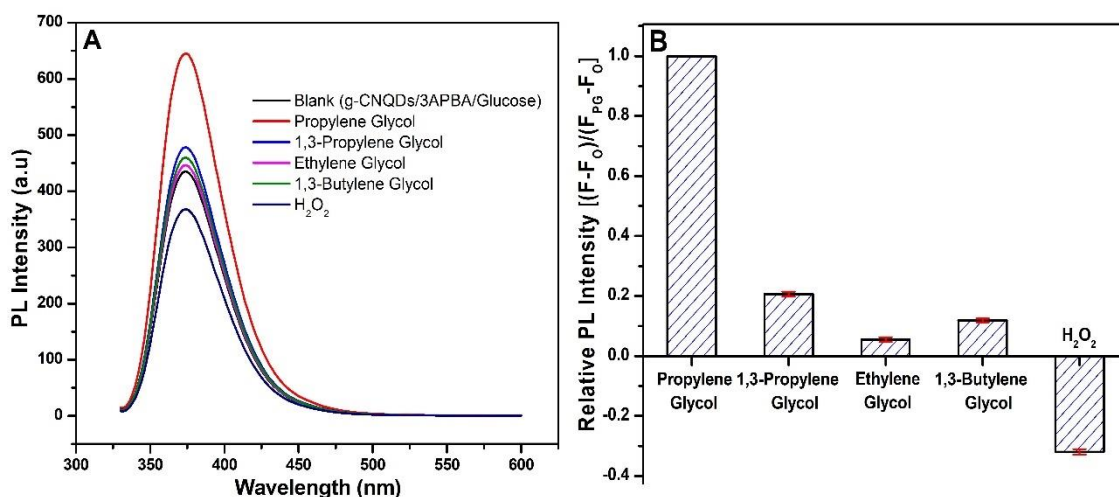


Figure S6.10. (A) PL emission spectra and (B) Relative PL intensity $((F-F_0)/(F_{PG}-F_0))$ of g-CNQDs/3APBA/Glucose in the presence of different diol groups. F and F₀ represent the PL intensity of g-CNQDs/3APBA/Glucose with and without 1 mM of interfering species, respectively. F_{PG} is the PL intensity at 1 mM of propylene glycol. The data shown here describe the average of three experiments for each interfering species.

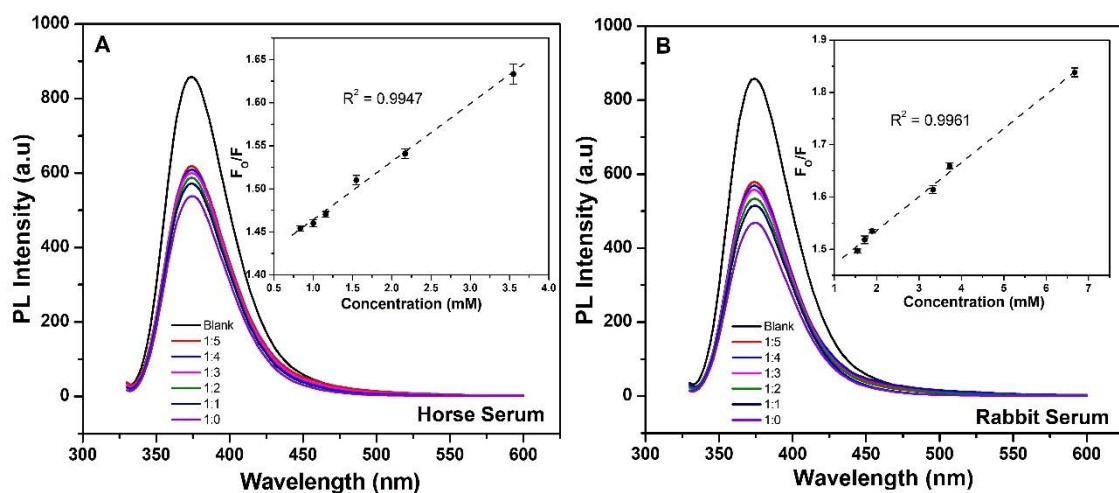


Figure S6.11. PL emission spectra of g-CNQDs/3APBA towards the real serum (A) Horse serum, (B) Rabbit serum. The inset pictures show the relative PL intensity vs various concentration of serum. The error bars imply the standard deviations for triple measurement at each concentration.

Table S6.1. Detail of functional groups in FT-IR results of g-CNQDs/3APBA.

No.	Bond	Absorption bands	Assignment
1	C-H stretching	474.2	ρ CH – Out of plan deformation
2	BO ₂ stretching	550	δ BO ₂ - In plane bending BO ₂ deformation
3	C–C stretching	615-585	α CCC – In plane deformation (benzene ring vibration)
4	C–C stretching	713	ϕ CCC – Out of plane deformation (benzene ring vibration)
5	N–H stretching	812-802	Heptazine ring unit (C ₆ N ₇)
6	C–H bending	858	C–H - Out of plane bending
7	O–H bending	948	Hydroxyl group
8	C–H bending	994.5	Trans = C–H out of plane bending
9	B–C stretching	1075	B–C stretching vibration
10	–C–O–C– stretching	1164	Asymmetric C–O–C vibration
11	C–H bending/ C–O stretch/ C– N stretching	1261	β CH – In plane deformation/ C–O phenols/ aromatic amines
12	C=N	1346-1325	Amines (reveal the existence of N)
13	C=C/C–N stretching	1450	Aromatic ring
14	N–H bending/ – COO [–] stretching	1562	Amide II/ Asymmetric stretching of the carboxylate anions
15	R– CONH–R'/ C=O	1710-1665 and 1640-1610	Amide I / α , β -unsaturated aldehydes and ketones
16	C–H stretching	2982 and 2890	–CH ₂ asymmetric and symmetric stretching
17	N–H stretching	3410-3240	NH ₂ amines (1° amine)
18	–O–H stretching	3550-3450	Hydroxyl group

Table S6.2. Relative ratio of C=C, HC-O, N-C=N and N-C=O of all samples by C 1s spectra analysis.

Sample	C=C		HC-O		N-C=N		N-C=O	
	Area	%	Area	%	Area	%	Area	%
g-C ₃ N ₄ (at)	1828.2	11.07	3378.5	20.45	6360.8	38.51	4949.6	29.97
g-CNQDs	1619.2	11.09	3041.6	20.83	6335.5	43.38	3605.0	24.70
g-CNQDs/3APBA	14002.4	55.32	10112.0	39.95	808.3	3.19	387.62	1.54

Table S6.3. Relative ration of C-N=C (N₁), N-(C)₃ and HN-(C)₂ (tertiary - N₂), C - NH (quaternary - N₃) of all samples by N 1s spectra analysis.

Sample	N ₁		N ₂		N ₃		π - π excitation	
	Area	%	Area	%	Area	%	Area	%
g-C ₃ N ₄ (at)	11742.0	39.11	12458.9	41.50	4410.4	14.69	1409.8	4.70
g-CNQDs	20842.2	74.12	5864.7	20.86	1106.8	3.94	305.0	1.08
g-CNQDs/3APBA	5399.8	56.03	2540.0	26.36	1296.5	13.45	400.4	4.16

Table S6.4. Comparison of quantum yield performance based on g-CNQDs.

No.	Material	Quantum yield (%)	Ref.
1	Fluorescent carbon nitride dots (CNDs)	9.0	[148]
2	Photoluminescent carbon nitride dots (CNDs)	11.0	[147]
3	Oxygen and sulfur co-doped graphitic carbon nitride quantum dots (OS-GCNQDs)	14.5	[182]
4	Ultrathin Graphitic-Phase C ₃ N ₄ Nanosheets (g-C ₃ N ₄)	19.6	[171]
5	g-CNQDs (by solid-phase hydrothermal method)	22.0	[183]
6	CNQDs (by a facile microwave-assisted solvothermal method)	27.1	[184]
7	g-CNQDs (by simple microwave method)	29.0	[144]
8	g-CNQDs (by a facile microwave method)	35.0	[185]
9	g-CNQDs (by a low-temperature solid-phase method)	42.0	[30]
10	CNQDs (by chemical tailoring)	46.0	[172]
11	Phenyl-gCNQDs	48.4	[186]
12	g-CNQDs (by hydrothermal method)	67.0	[116]
13	g-CNQDs/3APBA	78.5	This study

Table S6.5. Comparison of performance of some previous studies based on g-C₃N₄ for glucose sensor.

Material	Type of sensor	Linear range	Low detection limit (LOD)	Ref.
PBS-GODs	Fluorescent sensor	4 – 40 mM	3 mM	[123]
3APBA-GODs	Fluorescent sensor	0.1 – 10 mM	5 μM	[32]
g-C ₃ N ₄ /HRP/OPD/ GOx	Fluorescent sensor	0 – 0.1 mM; 1 – 4 mM	0.4 μM	[126]
PBA/g-CNQDs	Fluorescent sensor	25 nM – 1 μM; 1 μM – 1 mM	16 nM	[116]
g-C ₃ N ₄ -GOx	Colorimetric sensor	5 – 100 μM	1 μM	[152]
g-C ₃ N ₄ -Fe	Colorimetric sensor	0.5 μM – 0.01mM	0.5 μM	[187]
g-C ₃ N ₄ -WO ₃	Non-enzymatic sensor	0.01 – 7.12 mM	0.1 μM	[153]
Ag ⁺ / g-CNQDs	Non-enzymatic sensor	100 μM – 2 mM; 2 – 30 mM	15 μM	[99]
g-CNQDs/3APBA	Fluorescent sensor	25 nM – 1 μM; 1 μM – 10 mM	42 nM	This study

*Note: GQDs - Graphene quantum dots, PBS – Phenylboronic acid sodium salt, 3APBA – 3 Amino phenylboronic acid, HRP - Horseradish peroxidase, OPD – o-phenylenediamine, GOx – Glucose Oxidase, g-CNQDs – Graphitic carbon nitride quantum dots.

PART IV - SUMMARY

In summary, this research is based on the idea of developing a highly sensitive non-enzymatic glucose sensor based on the key factors:

- Longer storage lifetimes compared with an enzyme-based sensor,
- The multi-dimensional nanostructure to avoid bulk/surface charge recombination.

We investigated the chemical-physical properties of hybrid graphitic carbon with metal/metal oxide and their applications in non-enzymatic glucose sensor. Basic characterizations were carried out by FT-IR, Raman, XRD, FE-SEM, and HR-TEM to determine the chemical composition and their morphology in materials. The interactions between different components within the materials were identified by XPS core level spectra. One of the important properties of the electrochemical glucose sensor, electrochemical properties, were evaluated by the cyclic voltammetry. On the other hand, the optical properties of fluorescence glucose sensor were examined by UV-Vis and PL spectroscopy.

The hybridizing of metal (Ag)/ metal oxide (NiO, NiMn₂O₄) with graphitic carbon material as well as the synergistic effect between metal/metal oxide and graphitic carbon in the composite, significantly enhanced the electrocatalytic activity due to enhancing charge transfer during the electro-redox reaction and increasing specific surface area. The multi-dimensional 5Ag/NiO/rGO (5 mol% of AgNO₃ to NiO) composite-based sensor could detect glucose over the wide range of glucose concentrations from 50 μM to 7.5 mM with high sensitivity as 1869.4 $\mu\text{A mM}^{-1} \text{cm}^{-2}$ and LOD of 2.44 μM (S/N = 3). Instead of using noble metal, we synthesized the composite of spinel oxide NiMn₂O₄ (combination of two oxides NiO and Mn₂O₃) and rGO hydrogel with porous structure. The well-developed 3D NiMn₂O₄/rGOH-based sensing material showed excellent glucose sensitivity, rapid response time, low detection limit and long-term stability. In another story, the as-prepared composite with graphitic carbon nitride exhibited an excellent sensitivity, as high as 5387.1 $\mu\text{A mM}^{-1} \text{cm}^{-2}$, which is one of the highest values ever reported, as well as a limit of detection of 2.30 μM (S/N = 3). The loading of metal/metal oxide

was induced not only enhancing charge transfer but also improving the long-term stability of sensor. Meanwhile, the presence of graphitic carbon structure (rGO and g-C₃N₄) in composite inhibited the agglomeration of metal/metal oxide particles on the composite surface, resulting in nanocomposite structure size and enhancing glucose adsorption, charge transfer, and electrical conductivity.

On the other hand, glucose sensing by the optical methods using the fluorescent quantum dots has investigated because of their low toxic and rapid response with excellent sensitivity. In addition, boronic acid derivatives offer a promising alternative as enzyme-free-based glucose sensors. The interaction between boronic acid and g-CNQDs leads to affect optical properties. The fluorescence (PL) intensity of g-CNQDs is quenched in the presence of PBA due to some molecular interaction and hydrogen bonding from g-CNQDs and PBA molecules. Herein, glucose can interact PBA through the formation of a covalent bond, which can recover the PL intensity of g-CNQDs. A fluorescent glucose sensor based on g-CNQDs/PBA exhibited high glucose sensitivity with a very low LOD of 16 nM (S/N = 3) and against various interfering species. Whereas, the addition of 3-APBA in the presence of EDC into g-CNQDs causes strong enhancement of fluorescent intensity. It was attributed to the suppression of photo-induced electron transfer due to the efficient formation of fluorescent structure between the protonated tertiary amino group and the negative charged hydroxylated boronic acid ester. The g-CNQDs/3APBA showed high sensitivity, excellent selectivity and bio-imaging, low cytotoxicity, wide range and low detection limit. Moreover, using the competitive binding with the boronic group, we demonstrated the effective fluorescence “on-off-on” sensor for the determination of glucose and propylene glycol-based on the reversible covalent bonds of 3APBA with 1,2-diol groups.

PART V - RECOMMENDATIONS FOR FUTURE WORK

Graphitic carbon structure – based glucose sensor exhibited high glucose sensitivity, low detection limit and fast response time. Thus, improving nanomaterial – based on its are necessary for further research.

- ❖ For intensive research, there are some directions for enhancing the sensitivity and improving the lifetime:
 - Expanding the compositing of graphitic carbon nanostructure with other metal/metal oxide or organic chemical (g-C₃N₄/NiO, rGO/boronic acid derivatives, etc.)
 - Determining the low limit detection of glucose can detect glucose in the sweat.
- ❖ For extensive research, some of these points necessary for long-term studying such as:
 - Further develop the electrochemical, fluorescence sensor with extreme sensitivity, especially colorimetric glucose sensor for sweat, urine glucose monitoring application.
 - Develop the app on the smartphone to determine glucose level through colorimetric glucose sensor.
 - Investigate to avoid interferences related to the foreign body reaction, skin irritation and bioelectricity within the human body.

REFERENCES

- [1] E. Makrantonaki, D. Jiang, A.M. Hossini, G. Nikolakis, M. Wlaschek, K. Scharffetter-Kochanek, et al., Diabetes mellitus and the skin, *Rev. Endocr. Metab. Disord.* (2016) 1-14.
- [2] H.-C. Wang, A.-R. Lee, Recent developments in blood glucose sensors, *J. Food Drug. Anal.* 23(2015) 191-200.
- [3] W.H.O. (WHO), Global report on diabetes, WHO publications 2016.
- [4] J. Wang, Electrochemical Glucose Biosensors, *Chem. Rev.* 108(2008) 814-25.
- [5] N.S. Oliver, C. Toumazou, A.E.G. Cass, D.G. Johnston, Glucose sensors: a review of current and emerging technology, *Diabet. Med.* 26(2009) 197-210.
- [6] A.L. Galant, R.C. Kaufman, J.D. Wilson, Glucose: Detection and analysis, *Food Chem.* 188(2015) 149-60.
- [7] L.C. Clark, C. Lyons, Electrode Systems For Continuous Monitoring In Cardiovascular Surgery, *Ann. N. Y. Acad. Sci.* 102(1962) 29-45.
- [8] C. Chen, Q. Xie, D. Yang, H. Xiao, Y. Fu, Y. Tan, et al., Recent advances in electrochemical glucose biosensors: a review, *RSC Adv.* 3(2013) 4473-91.
- [9] D.-W. Hwang, S. Lee, M. Seo, T.D. Chung, Recent advances in electrochemical non-enzymatic glucose sensors – A review, *Anal. Chim. Acta* 1033(2018) 1-34.
- [10] G.G. Guilbault, G.J. Lubrano, An enzyme electrode for the amperometric determination of glucose, *Anal. Chim. Acta* 64(1973) 439-55.
- [11] K.E. Toghill, R.G. Compton, Electrochemical non-enzymatic glucose sensors: a perspective and an evaluation, *Int. J. Electrochem. Sci* 5(2010) 1246-301.
- [12] Z. Zhu, L. Garcia-Gancedo, A.J. Flewitt, H. Xie, F. Moussy, W.I. Milne, A Critical Review of Glucose Biosensors Based on Carbon Nanomaterials: Carbon Nanotubes and Graphene, *Sensors* 12(2012) 5996-6022.

- [13] Y.-Y. Song, D. Zhang, W. Gao, X.-H. Xia, Nonenzymatic Glucose Detection by Using a Three-Dimensionally Ordered, Macroporous Platinum Template, *Chem. Eur. J.* 11(2005) 2177-82.
- [14] V. Singh, D. Joung, L. Zhai, S. Das, S.I. Khondaker, S. Seal, Graphene based materials: Past, present and future, *Prog. Mater. Sci.* 56(2011) 1178-271.
- [15] S. Stankovich, D.A. Dikin, G.H.B. Dommett, K.M. Kohlhaas, E.J. Zimney, E.A. Stach, et al., Graphene-based composite materials, *Nature* 442(2006) 282-6.
- [16] S. Gadipelli, Z.X. Guo, Graphene-based materials: Synthesis and gas sorption, storage and separation, *Prog. Mater. Sci.* 69(2015) 1-60.
- [17] Z. Liu, J.T. Robinson, X. Sun, H. Dai, PEGylated Nanographene Oxide for Delivery of Water-Insoluble Cancer Drugs, *J. Am. Chem. Soc.* 130(2008) 10876-7.
- [18] J. Chen, B. Yao, C. Li, G. Shi, An improved Hummers method for eco-friendly synthesis of graphene oxide, *Carbon* 64(2013) 225-9.
- [19] T. Chen, B. Zeng, J.L. Liu, J.H. Dong, X.Q. Liu, Z. Wu, et al., High throughput exfoliation of graphene oxide from expanded graphite with assistance of strong oxidant in modified Hummers method, *J. Phys. Conf. Ser.* 188(2009) 012051.
- [20] J. Zhu, P. Xiao, H. Li, S.A.C. Carabineiro, Graphitic Carbon Nitride: Synthesis, Properties, and Applications in Catalysis, *ACS Appl. Mater. Interfaces* 6(2014) 16449-65.
- [21] J. Sehnert, K. Baerwinkel, J. Senker, Ab Initio Calculation of Solid-State NMR Spectra for Different Triazine and Heptazine Based Structure Proposals of g-C₃N₄, *J. Phys. Chem. B* 111(2007) 10671-80.
- [22] G. Dong, Y. Zhang, Q. Pan, J. Qiu, A fantastic graphitic carbon nitride (g-C₃N₄) material: Electronic structure, photocatalytic and photoelectronic properties, *J. Photoch. Photobio. C* 20(2014) 33-50.

- [23] B.V. Lotsch, W. Schnick, From Triazines to Heptazines: Novel Nonmetal Tricyanomelaminates as Precursors for Graphitic Carbon Nitride Materials, *Chem. Mater.* 18(2006) 1891-900.
- [24] W.-J. Ong, L.-L. Tan, Y.H. Ng, S.-T. Yong, S.-P. Chai, Graphitic Carbon Nitride (g-C₃N₄)-Based Photocatalysts for Artificial Photosynthesis and Environmental Remediation: Are We a Step Closer To Achieving Sustainability?, *Chem. Rev.* 116(2016) 7159-329.
- [25] M. Rong, L. Lin, X. Song, Y. Wang, Y. Zhong, J. Yan, et al., Fluorescence sensing of chromium (VI) and ascorbic acid using graphitic carbon nitride nanosheets as a fluorescent “switch”, *Biosens. Bioelectron.* 68(2015) 210-7.
- [26] J. Ehrmaier, T.N.V. Karsili, A.L. Sobolewski, W. Domcke, Mechanism of Photocatalytic Water Splitting with Graphitic Carbon Nitride: Photochemistry of the Heptazine–Water Complex, *J. Phys. Chem. A* 121(2017) 4754-64.
- [27] L.-S. Lin, Z.-X. Cong, J. Li, K.-M. Ke, S.-S. Guo, H.-H. Yang, et al., Graphitic-phase C₃N₄ nanosheets as efficient photosensitizers and pH-responsive drug nanocarriers for cancer imaging and therapy, *J. Mater. Chem. B* 2(2014) 1031-7.
- [28] H. Zhang, L.-H. Guo, L. Zhao, B. Wan, Y. Yang, Switching Oxygen Reduction Pathway by Exfoliating Graphitic Carbon Nitride for Enhanced Photocatalytic Phenol Degradation, *J. Phys. Chem. Lett.* 6(2015) 958-63.
- [29] Z. Zhao, Y. Sun, F. Dong, Graphitic carbon nitride based nanocomposites: a review, *Nanoscale* 7(2015) 15-37.
- [30] J. Zhou, Y. Yang, C.-y. Zhang, A low-temperature solid-phase method to synthesize highly fluorescent carbon nitride dots with tunable emission, *Chem. Commun.* 49(2013) 8605-7.
- [31] R. Nishiyabu, Y. Kubo, T.D. James, J.S. Fossey, Boronic acid building blocks: tools for sensing and separation, *Chem. Commun.* 47(2011) 1106-23.

- [32] Z.-b. Qu, X. Zhou, L. Gu, R. Lan, D. Sun, D. Yu, et al., Boronic acid functionalized graphene quantum dots as a fluorescent probe for selective and sensitive glucose determination in microdialysate, *Chem. Commun.* 49(2013) 9830-2.
- [33] H.S. Mader, O.S. Wolfbeis, Boronic acid based probes for microdetermination of saccharides and glycosylated biomolecules, *Microchim. Acta* 162(2008) 1-34.
- [34] X. Wu, Z. Li, X.-X. Chen, J.S. Fossey, T.D. James, Y.-B. Jiang, Selective sensing of saccharides using simple boronic acids and their aggregates, *Chem. Soc. Rev.* 42(2013) 8032-48.
- [35] M. Fleischmann, K. Korinek, D. Pletcher, The oxidation of organic compounds at a nickel anode in alkaline solution, *J. Electroanal. Chem.* 31(1971) 39-49.
- [36] H. Mohammad Shiri, M. Aghazadeh, Synthesis, Characterization and Electrochemical Properties of Capsule-Like NiO Nanoparticles, *J. Electrochem. Soc.* 159(2012) E132-E8.
- [37] C. Heyser, R. Schrebler, P. Grez, New route for the synthesis of nickel (II) oxide nanostructures and its application as non-enzymatic glucose sensor, *J. Electroanal. Chem.* 832(2019) 189-95.
- [38] M. El-Kemary, N. Nagy, I. El-Mehasseb, Nickel oxide nanoparticles: Synthesis and spectral studies of interactions with glucose, *Mater. Sci. Semicond. Process.* 16(2013) 1747-52.
- [39] L.T. Hoa, J.S. Chung, S.H. Hur, A highly sensitive enzyme-free glucose sensor based on Co₃O₄ nanoflowers and 3D graphene oxide hydrogel fabricated via hydrothermal synthesis, *Sensor. Actuat. B-Chem.* 223(2016) 76-82.
- [40] L.-C. Jiang, W.-D. Zhang, A highly sensitive nonenzymatic glucose sensor based on CuO nanoparticles-modified carbon nanotube electrode, *Biosens. Bioelectron.* 25(2010) 1402-7.
- [41] H. Quan, S.-U. Park, J. Park, Electrochemical oxidation of glucose on silver nanoparticle-modified composite electrodes, *Electrochim. Acta* 55(2010) 2232-7.
- [42] F. Kurniawan, V. Tsakova, V.M. Mirsky, Gold Nanoparticles in Nonenzymatic Electrochemical Detection of Sugars, *Electroana.* 18(2006) 1937-42.

- [43] A. Nirmala Grace, K. Pandian, Synthesis of gold and platinum nanoparticles using tetraaniline as reducing and phase transfer agent—A brief study and their role in the electrocatalytic oxidation of glucose, *J. Phys. Chem. Solids* 68(2007) 2278-85.
- [44] P. Holt-Hindle, S. Nigro, M. Asmussen, A. Chen, Amperometric glucose sensor based on platinum–iridium nanomaterials, *Electrochem. Commun.* 10(2008) 1438-41.
- [45] L.-M. Lu, L. Zhang, F.-L. Qu, H.-X. Lu, X.-B. Zhang, Z.-S. Wu, et al., A nano-Ni based ultrasensitive nonenzymatic electrochemical sensor for glucose: Enhancing sensitivity through a nanowire array strategy, *Biosens. Bioelectron.* 25(2009) 218-23.
- [46] C.-H. Wang, S.-W. Lee, C.-J. Tseng, J.-W. Wu, I.M. Hung, C.-M. Tseng, et al., Nanocrystalline Pd/carbon nanotube composites synthesized using supercritical fluid for superior glucose sensing performance, *J. Alloys Compd.* 615, Supplement 1(2014) S496-S500.
- [47] F. Gao, Q. Wei, J. Yang, H. Bi, M. Wang, Synthesis of graphene/nickel oxide composite with improved electrochemical performance in capacitors, *Ionics* 19(2013) 1883-9.
- [48] L.T. Hoa, H.N. Tien, V.H. Luan, J.S. Chung, S.H. Hur, Fabrication of a novel 2D-graphene/2D-NiO nanosheet-based hybrid nanostructure and its use in highly sensitive NO₂ sensors, *Sensor. Actuat. B-Chem.* 185(2013) 701-5.
- [49] Z. Cui, H. Yin, Q. Nie, Controllable preparation of hierarchically core–shell structure NiO/C microspheres for non-enzymatic glucose sensor, *J. Alloys Compd.* 632(2015) 402-7.
- [50] J.H. Pan, Q. Huang, Z.Y. Koh, D. Neo, X.Z. Wang, Q. Wang, Scalable Synthesis of Urchin- and Flowerlike Hierarchical NiO Microspheres and Their Electrochemical Property for Lithium Storage, *ACS Appl. Mater. Interfaces* 5(2013) 6292-9.
- [51] S.K. Yadav, P. Jeevanandam, Synthesis of NiO–Al₂O₃ nanocomposites by sol–gel process and their use as catalyst for the oxidation of styrene, *J. Alloys Compd.* 610(2014) 567-74.
- [52] S. Liu, B. Yu, T. Zhang, A novel non-enzymatic glucose sensor based on NiO hollow spheres, *Electrochim. Acta* 102(2013) 104-7.

- [53] Y. Zhang, Y. Wang, J. Jia, J. Wang, Nonenzymatic glucose sensor based on graphene oxide and electrospun NiO nanofibers, *Sensor. Actuat. B-Chem.* 171–172(2012) 580-7.
- [54] K. Tian, M. Prestgard, A. Tiwari, A review of recent advances in nonenzymatic glucose sensors, *Mater. Sci. Eng., C* 41(2014) 100-18.
- [55] Y.-L.T. Ngo, S.H. Hur, Low-temperature NO₂ gas sensor fabricated with NiO and reduced graphene oxide hybrid structure, *Mater. Res. Bull.* 84(2016) 168-76.
- [56] Y. Ding, Y. Wang, L. Su, H. Zhang, Y. Lei, Preparation and characterization of NiO–Ag nanofibers, NiO nanofibers, and porous Ag: towards the development of a highly sensitive and selective non-enzymatic glucose sensor, *J. Mater. Chem.* 20(2010) 9918-26.
- [57] L.M. Malard, M.A. Pimenta, G. Dresselhaus, M.S. Dresselhaus, Raman spectroscopy in graphene, *Phys. Rep.* 473(2009) 51-87.
- [58] K. Kaviyarasu, E. Manikandan, J. Kennedy, M. Maaza, Synthesis and analytical applications of photoluminescent carbon nanosheet by exfoliation of graphite oxide without purification, *J. Mater. Sci. - Mater. Electron.* 27(2016) 13080-5.
- [59] C. Van der Horst, B. Silwana, E. Iwuoha, V. Somerset, Synthesis and Characterization of Bismuth-Silver Nanoparticles for Electrochemical Sensor Applications, *Anal. Lett.* 48(2015) 1311-32.
- [60] J. Song, L. Xu, R. Xing, W. Qin, Q. Dai, H. Song, Ag nanoparticles coated NiO nanowires hierarchical nanocomposites electrode for nonenzymatic glucose biosensing, *Sensor. Actuat. B-Chem.* 182(2013) 675-81.
- [61] P. Zhang, L. Zhang, G. Zhao, F. Feng, A highly sensitive nonenzymatic glucose sensor based on CuO nanowires, *Microchim. Acta* 176(2012) 411-7.
- [62] L. Shahriary, A.A. Athawale, Electrochemical deposition of silver/silver oxide on reduced graphene oxide for glucose sensing, *J. Solid. State. Electrochem.* 19(2015) 2255-63.

- [63] M. Li, X. Bo, Z. Mu, Y. Zhang, L. Guo, Electrodeposition of nickel oxide and platinum nanoparticles on electrochemically reduced graphene oxide film as a nonenzymatic glucose sensor, *Sensor. Actuat. B-Chem.* 192(2014) 261-8.
- [64] R.A. Soomro, Z.H. Ibupoto, Sirajuddin, M.I. Abro, M. Willander, Electrochemical sensing of glucose based on novel hedgehog-like NiO nanostructures, *Sensor. Actuat. B-Chem.* 209(2015) 966-74.
- [65] B. Yuan, C. Xu, D. Deng, Y. Xing, L. Liu, H. Pang, et al., Graphene oxide/nickel oxide modified glassy carbon electrode for supercapacitor and nonenzymatic glucose sensor, *Electrochim. Acta* 88(2013) 708-12.
- [66] T. Marimuthu, S. Mohamad, Y. Alias, Needle-like polypyrrole–NiO composite for non-enzymatic detection of glucose, *Synth. Met.* 207(2015) 35-41.
- [67] M. Zhang, S. Guo, L. Zheng, G. Zhang, Z. Hao, L. Kang, et al., Preparation of NiMn₂O₄ with large specific surface area from an epoxide-driven sol–gel process and its capacitance, *Electrochim. Acta* 87(2013) 546-53.
- [68] Y. Guan, C. Yin, X. Cheng, X. Liang, Q. Diao, H. Zhang, et al., Sub-ppm H₂S sensor based on YSZ and hollow balls NiMn₂O₄ sensing electrode, *Sensor. Actuat. B-Chem.* 193(2014) 501-8.
- [69] D. Mehandjiev, A. Naydenov, G. Ivanov, Ozone decomposition, benzene and CO oxidation over NiMnO₃-ilmenite and NiMn₂O₄-spinel catalysts, *Appl. Catal., A-Gen.* 206(2001) 13-8.
- [70] J. Ryu, K.-Y. Kim, J.-J. Choi, B.-D. Hahn, W.-H. Yoon, B.-K. Lee, et al., Highly Dense and Nanograined NiMn₂O₄ Negative Temperature coefficient Thermistor Thick Films Fabricated by Aerosol-Deposition, *J. Am. Ceram. Soc.* 92(2009) 3084-7.
- [71] S. Åsbrink, A. Waśkowska, M. Drozd, E. Talik, Physical properties and X-ray diffraction of a NiMn₂O₄ single crystal below and above the ferrimagnetic transition at T_c = 145 K, *J. Phys. Chem. Solids* 58(1997) 725-9.

- [72] Y. Ouyang, Y. Feng, H. Zhang, L. Liu, Y. Wang, Designing Sandwiched and Crystallized NiMn₂O₄/C Arrays for Enhanced Sustainable Electrochemical Energy Storage, ACS Sustain. Chem. Eng. 5(2017) 196-205.
- [73] H. Nan, W. Ma, Z. Gu, B. Geng, X. Zhang, Hierarchical NiMn₂O₄@CNT nanocomposites for high-performance asymmetric supercapacitors, RSC Adv. 5(2015) 24607-14.
- [74] J. Luo, L. Cheng, Y. Xia, LiMn₂O₄ hollow nanosphere electrode material with excellent cycling reversibility and rate capability, Electrochem. Commun. 9(2007) 1404-9.
- [75] Y. Huang, X. Dong, Y. Shi, C.M. Li, L.-J. Li, P. Chen, Nanoelectronic biosensors based on CVD grown graphene, Nanoscale 2(2010) 1485-8.
- [76] A.K. Geim, K.S. Novoselov, The rise of graphene, Nat. Mater. 6(2007) 183-91.
- [77] H. Xu, Z. Zhang, Z. Wang, S. Wang, X. Liang, L.-M. Peng, Quantum Capacitance Limited Vertical Scaling of Graphene Field-Effect Transistor, ACS Nano 5(2011) 2340-7.
- [78] F. Schwierz, Graphene transistors, Nat. Nano. 5(2010) 487-96.
- [79] J.K. Wassei, R.B. Kaner, Graphene, a promising transparent conductor, Mater. Today 13(2010) 52-9.
- [80] H. Park, P.R. Brown, V. Bulović, J. Kong, Graphene As Transparent Conducting Electrodes in Organic Photovoltaics: Studies in Graphene Morphology, Hole Transporting Layers, and Counter Electrodes, Nano Lett. 12(2012) 133-40.
- [81] Z. Wu, S. Bai, J. Xiang, Z. Yuan, Y. Yang, W. Cui, et al., Efficient planar heterojunction perovskite solar cells employing graphene oxide as hole conductor, Nanoscale 6(2014) 10505-10.
- [82] J.D. Roy-Mayhew, D.J. Bozym, C. Punckt, I.A. Aksay, Functionalized Graphene as a Catalytic Counter Electrode in Dye-Sensitized Solar Cells, ACS Nano 4(2010) 6203-11.
- [83] S.H. Hur, J.-N. Park, Graphene and its application in fuel cell catalysis: a review, Asia-Pac. J. Chem. Eng. 8(2013) 218-33.

- [84] H. Yuan, Z. He, Graphene-modified electrodes for enhancing the performance of microbial fuel cells, *Nanoscale* 7(2015) 7022-9.
- [85] V.H. Luan, H.N. Tien, L.T. Hoa, N.T.M. Hien, E.-S. Oh, J. Chung, et al., Synthesis of a highly conductive and large surface area graphene oxide hydrogel and its use in a supercapacitor, *J. Mater. Chem. A* 1(2013) 208-11.
- [86] R. Raccichini, A. Varzi, S. Passerini, B. Scrosati, The role of graphene for electrochemical energy storage, *Nat. Mater.* 14(2015) 271-9.
- [87] F. Wang, L. Liu, W.J. Li*, Graphene-Based Glucose Sensors: A Brief Review, *IEEE T. NanoBiosci.* 14(2015) 818-34.
- [88] Y. Chang, Y. Yao, B. Wang, H. Luo, T. Li, L. Zhi, Reduced Graphene Oxide Mediated SnO₂ Nanocrystals for Enhanced Gas-sensing Properties, *J. Mater. Sci. Technol.* 29(2013) 157-60.
- [89] X.-J. Zhu, J. Hu, H.-L. Dai, L. Ding, L. Jiang, Reduced graphene oxide and nanosheet-based nickel oxide microsphere composite as an anode material for lithium ion battery, *Electrochim. Acta* 64(2012) 23-8.
- [90] M.H.-S. Ouaguenouni, A. Benadda, A. Kiennemann, A. Barama, Preparation and catalytic activity of nickel–manganese oxide catalysts in the reaction of partial oxidation of methane, *C. R. Chim.* 12(2009) 740-7.
- [91] N. Watanabe, H. Nakayama, K. Fukao, F. Munakata, Transport and x-ray photoelectron spectroscopy properties of (Ni_{1-x}Cu_x)Mn₂O₄ and Ni(Mn_{2-y}Cu_y)O₄, *J. Appl. Phys.* 110(2011) 023519-.
- [92] C. Batchelor-McAuley, L. Shao, G.G. Wildgoose, M.L.H. Green, R.G. Compton, An electrochemical comparison of manganese dioxide microparticles versus [small alpha] and [small beta] manganese dioxide nanorods: mechanistic and electrocatalytic behaviour, *New J. Chem.* 32(2008) 1195-203.

- [93] J. Chen, W.-D. Zhang, J.-S. Ye, Nonenzymatic electrochemical glucose sensor based on MnO₂/MWNTs nanocomposite, *Electrochem. Commun.* 10(2008) 1268-71.
- [94] L. Burke, Premonolayer oxidation and its role in electrocatalysis, *Electrochim. Acta* 39(1994) 1841-8.
- [95] M. Shamsipur, M. Najafi, M.-R.M. Hosseini, Highly improved electrooxidation of glucose at a nickel(II) oxide/multi-walled carbon nanotube modified glassy carbon electrode, *Bioelectrochem.* 77(2010) 120-4.
- [96] Y. Wang, W. Bai, F. Nie, J. Zheng, A Non-Enzymatic Glucose Sensor Based on Ni/MnO₂ Nanocomposite Modified Glassy Carbon Electrode, *Electroana.* 27(2015) 2399-405.
- [97] Y. Liu, X. Zhang, D. He, F. Ma, Q. Fu, Y. Hu, An amperometric glucose biosensor based on a MnO₂/graphene composite modified electrode, *RSC Adv.* 6(2016) 18654-61.
- [98] S. Zhang, J. Li, M. Zeng, J. Xu, X. Wang, W. Hu, Polymer nanodots of graphitic carbon nitride as effective fluorescent probes for the detection of Fe³⁺ and Cu²⁺ ions, *Nanoscale* 6(2014) 4157-62.
- [99] M.K. Kundu, M. Sadhukhan, S. Barman, Ordered assemblies of silver nanoparticles on carbon nitride sheets and their application in the non-enzymatic sensing of hydrogen peroxide and glucose, *J. Mater. Chem. B* 3(2015) 1289-300.
- [100] H.-L. Zhu, Y.-Q. Zheng, Mesoporous Co₃O₄ anchored on the graphitic carbon nitride for enhanced performance supercapacitor, *Electrochim. Acta* 265(2018) 372-8.
- [101] Q. Liang, L. Ye, Q. Xu, Z.-H. Huang, F. Kang, Q.-H. Yang, Graphitic carbon nitride nanosheet-assisted preparation of N-enriched mesoporous carbon nanofibers with improved capacitive performance, *Carbon* 94(2015) 342-8.
- [102] J. Chen, Z. Mao, L. Zhang, D. Wang, R. Xu, L. Bie, et al., Nitrogen-Deficient Graphitic Carbon Nitride with Enhanced Performance for Lithium Ion Battery Anodes, *ACS Nano* 11(2017) 12650-7.

- [103] A. Wang, C. Wang, L. Fu, W. Wong-Ng, Y. Lan, Recent Advances of Graphitic Carbon Nitride-Based Structures and Applications in Catalyst, Sensing, Imaging, and LEDs, *Nano-Micro Lett.* 9(2017) 47.
- [104] S. An, G. Zhang, T. Wang, W. Zhang, K. Li, C. Song, et al., High-Density Ultra-small Clusters and Single-Atom Fe Sites Embedded in Graphitic Carbon Nitride (g-C₃N₄) for Highly Efficient Catalytic Advanced Oxidation Processes, *ACS Nano* 12(2018) 9441-50.
- [105] T.-T. Pham, E.W. Shin, Influence of g-C₃N₄ Precursors in g-C₃N₄/NiTiO₃ Composites on Photocatalytic Behavior and the Interconnection between g-C₃N₄ and NiTiO₃, *Langmuir* 34(2018) 13144-54.
- [106] Z. Wei, M. Liu, Z. Zhang, W. Yao, H. Tan, Y. Zhu, Efficient visible-light-driven selective oxygen reduction to hydrogen peroxide by oxygen-enriched graphitic carbon nitride polymers, *Energy Environ. Sci.* 11(2018) 2581-9.
- [107] I.S. Pieta, A. Rathi, P. Pieta, R. Nowakowski, M. Hołdyski, M. Pisarek, et al., Electrocatalytic methanol oxidation over Cu, Ni and bimetallic Cu-Ni nanoparticles supported on graphitic carbon nitride, *Appl. Catal. B* 244(2019) 272-83.
- [108] J. Chen, C. Liu, Y.-T. Huang, H. Lee, S.-P. Feng, Study of the growth mechanisms of nanoporous Ag flowers for non-enzymatic glucose detection, *Nanotechnology* 29(2018) 505501.
- [109] Y. Li, Y.-Y. Song, C. Yang, X.-H. Xia, Hydrogen bubble dynamic template synthesis of porous gold for nonenzymatic electrochemical detection of glucose, *Electrochem. Commun.* 9(2007) 981-8.
- [110] Y.-L.T. Ngo, L.T. Hoa, J.S. Chung, S.H. Hur, Multi-dimensional Ag/NiO/reduced graphene oxide nanostructures for a highly sensitive non-enzymatic glucose sensor, *J. Alloys Compd.* 712(2017) 742-51.
- [111] Y.-L.T. Ngo, L. Sui, W. Ahn, J.S. Chung, S.H. Hur, NiMn₂O₄ spinel binary nanostructure decorated on three-dimensional reduced graphene oxide hydrogel for bifunctional materials in non-enzymatic glucose sensor, *Nanoscale* 9(2017) 19318-27.

- [112] N. Pal, S. Banerjee, A. Bhaumik, A facile route for the syntheses of Ni(OH)₂ and NiO nanostructures as potential candidates for non-enzymatic glucose sensor, *J. Colloid Interface Sci.* 516(2018) 121-7.
- [113] M. Baghayeri, A. Amiri, Z. Alizadeh, H. Veisi, E. Hasheminejad, Non-enzymatic voltammetric glucose sensor made of ternary NiO/Fe₃O₄-SH/para-amino hippuric acid nanocomposite, *J. Electroanal. Chem.* 810(2018) 69-77.
- [114] Y.-L. Thi Ngo, J.S. Chung, S.H. Hur, Aminoboronic acid-functionalized graphitic carbon nitride quantum dots for the photoluminescence multi-chemical sensing probe, *Dyes Pigm.* 168(2019) 180-8.
- [115] F. Motahari, M.R. Mozdianfard, M. Salavati-Niasari, Synthesis and adsorption studies of NiO nanoparticles in the presence of H₂acacen ligand, for removing Rhodamine B in wastewater treatment, *Process Saf. Environ.* 93(2015) 282-92.
- [116] Y.-L.T. Ngo, W.M. Choi, J.S. Chung, S.H. Hur, Highly biocompatible phenylboronic acid-functionalized graphitic carbon nitride quantum dots for the selective glucose sensor, *Sensor. Actuat. B-Chem.* 282(2019) 36-44.
- [117] N. Cheng, P. Jiang, Q. Liu, J. Tian, A.M. Asiri, X. Sun, Graphitic carbon nitride nanosheets: one-step, high-yield synthesis and application for Cu²⁺ detection, *Analyst* 139(2014) 5065-8.
- [118] J. Yang, M. Cho, C. Pang, Y. Lee, Highly sensitive non-enzymatic glucose sensor based on over-oxidized polypyrrole nanowires modified with Ni(OH)₂ nanoflakes, *Sensor. Actuat. B-Chem.* 211(2015) 93-101.
- [119] M. Wu, S. Meng, Q. Wang, W. Si, W. Huang, X. Dong, Nickel–Cobalt Oxide Decorated Three-Dimensional Graphene as an Enzyme Mimic for Glucose and Calcium Detection, *ACS Appl. Mater. Interfaces* 7(2015) 21089-94.
- [120] K. Ghanbari, Z. Babaei, Fabrication and characterization of non-enzymatic glucose sensor based on ternary NiO/CuO/polyaniline nanocomposite, *Anal. Biochem.* 498(2016) 37-46.

- [121] J. Tian, Q. Liu, C. Ge, Z. Xing, A.M. Asiri, A.O. Al-Youbi, et al., Ultrathin graphitic carbon nitride nanosheets: a low-cost, green, and highly efficient electrocatalyst toward the reduction of hydrogen peroxide and its glucose biosensing application, *Nanoscale* 5(2013) 8921-4.
- [122] W. Zheng, Y. Li, M. Liu, C.-S. Tsang, L.Y.S. Lee, K.-Y. Wong, Cu²⁺-doped Carbon Nitride/MWCNT as an Electrochemical Glucose Sensor, *Electroana.* 30(2018) 1446-54.
- [123] M. Shehab, S. Ebrahim, M. Soliman, Graphene quantum dots prepared from glucose as optical sensor for glucose, *J. Lumin.* 184(2017) 110-6.
- [124] J. Zhao, G. Chen, L. Zhu, G. Li, Graphene quantum dots-based platform for the fabrication of electrochemical biosensors, *Electrochem. Commun.* 13(2011) 31-3.
- [125] H. Zhang, Y. Huang, S. Hu, Q. Huang, C. Wei, W. Zhang, et al., Fluorescent probes for "off-on" sensitive and selective detection of mercury ions and l-cysteine based on graphitic carbon nitride nanosheets, *J. Mater. Chem. C* 3(2015) 2093-100.
- [126] J.-W. Liu, Y. Luo, Y.-M. Wang, L.-Y. Duan, J.-H. Jiang, R.-Q. Yu, Graphitic Carbon Nitride Nanosheets-Based Ratiometric Fluorescent Probe for Highly Sensitive Detection of H₂O₂ and Glucose, *ACS Appl. Mater. Interfaces* 8(2016) 33439-45.
- [127] Q. Zhao, W. Wu, X. Wei, S. Jiang, T. Zhou, Q. Li, et al., Graphitic carbon nitride as electrode sensing material for tetrabromobisphenol-A determination, *Sensor. Actuat. B-Chem.* 248(2017) 673-81.
- [128] K. Hu, T. Zhong, Y. Huang, Z. Chen, S. Zhao, Graphitic carbon nitride nanosheet-based multicolour fluorescent nanoprobe for multiplexed analysis of DNA, *Microchim. Acta* 182(2015) 949-55.
- [129] H. Li, F.-Q. Shao, H. Huang, J.-J. Feng, A.-J. Wang, Eco-friendly and rapid microwave synthesis of green fluorescent graphitic carbon nitride quantum dots for vitro bioimaging, *Sensor. Actuat. B-Chem.* 226(2016) 506-11.

- [130] L. Lin, H. Ou, Y. Zhang, X. Wang, Tri-s-triazine-Based Crystalline Graphitic Carbon Nitrides for Highly Efficient Hydrogen Evolution Photocatalysis, *ACS Catal.* 6(2016) 3921-31.
- [131] Q. Han, F. Zhao, C. Hu, L. Lv, Z. Zhang, N. Chen, et al., Facile production of ultrathin graphitic carbon nitride nanoplatelets for efficient visible-light water splitting, *Nano. Res.* 8(2015) 1718-28.
- [132] Z. Pei, J. Zhao, Y. Huang, Y. Huang, M. Zhu, Z. Wang, et al., Toward enhanced activity of a graphitic carbon nitride-based electrocatalyst in oxygen reduction and hydrogen evolution reactions via atomic sulfur doping, *J. Mater. Chem. A* 4(2016) 12205-11.
- [133] W. Yang, J. Yan, G. Springsteen, S. Deeter, B. Wang, A novel type of fluorescent boronic acid that shows large fluorescence intensity changes upon binding with a carbohydrate in aqueous solution at physiological pH, *Bioorg. Med. Chem. Lett.* 13(2003) 1019-22.
- [134] A.L. Chibac, V. Melinte, T. Buruiana, E.C. Buruiana, Fluorescent polymeric sensors containing boronic acid derivatives for sugars and dopamine detection. Sensing characteristics enhancement by Au NPs, *Sensor. Actuat. B-Chem.* 253(2017) 987-98.
- [135] D.K. Dang, C. Sundaram, Y.-L.T. Ngo, J.S. Chung, E.J. Kim, S.H. Hur, One pot solid-state synthesis of highly fluorescent N and S co-doped carbon dots and its use as fluorescent probe for Ag⁺ detection in aqueous solution, *Sensor. Actuat. B-Chem.* 255(2018) 3284-91.
- [136] J.R. Lakowicz, *Principles of Fluorescence Spectroscopy*, 3 ed., USA: Springer; 2006.
- [137] N. Cheng, J. Tian, Q. Liu, C. Ge, A.H. Qusti, A.M. Asiri, et al., Au-Nanoparticle-Loaded Graphitic Carbon Nitride Nanosheets: Green Photocatalytic Synthesis and Application toward the Degradation of Organic Pollutants, *ACS Appl. Mater. Interfaces* 5(2013) 6815-9.
- [138] S. Zhou, Y. Liu, J. Li, Y. Wang, G. Jiang, Z. Zhao, et al., Facile in situ synthesis of graphitic carbon nitride (g-C₃N₄)-N-TiO₂ heterojunction as an efficient photocatalyst for the selective photoreduction of CO₂ to CO, *Appl. Catal. B* 158-159(2014) 20-9.

- [139] S.-Z. Wu, Y.-X. Yu, W.-D. Zhang, Processing graphitic carbon nitride for improved photocatalytic activity, *Mater. Sci. Semicond. Process.* 24(2014) 15-20.
- [140] M. Rong, L. Lin, X. Song, T. Zhao, Y. Zhong, J. Yan, et al., A Label-Free Fluorescence Sensing Approach for Selective and Sensitive Detection of 2,4,6-Trinitrophenol (TNP) in Aqueous Solution Using Graphitic Carbon Nitride Nanosheets, *Anal. Chem.* 87(2015) 1288-96.
- [141] W. Bian, H. Zhang, Q. Yu, M. Shi, S. Shuang, Z. Cai, et al., Detection of Ag⁺ using graphite carbon nitride nanosheets based on fluorescence quenching, *Spectrochim. Acta. Part A* 169(2016) 122-7.
- [142] W. Zhang, Q. Zhang, F. Dong, Z. Zhao, The Multiple Effects of Precursors on the Properties of Polymeric Carbon Nitride, *Int. J. Photoenergy* 2013(2013) 9.
- [143] J.A. Faniran, H.F. Shurvell, Infrared spectra of phenylboronic acid (normal and deuterated) and diphenyl phenylboronate, *Can. J. Chem.* 46(1968) 2089-95.
- [144] S. Barman, M. Sadhukhan, Facile bulk production of highly blue fluorescent graphitic carbon nitride quantum dots and their application as highly selective and sensitive sensors for the detection of mercuric and iodide ions in aqueous media, *J. Mater. Chem.* 22(2012) 21832-7.
- [145] Y. Zhan, Z. Liu, Q. Liu, D. Huang, Y. Wei, Y. Hu, et al., A facile and one-pot synthesis of fluorescent graphitic carbon nitride quantum dots for bio-imaging applications, *New J. Chem.* 41(2017) 3930-8.
- [146] M. Rong, X. Song, T. Zhao, Q. Yao, Y. Wang, X. Chen, Synthesis of highly fluorescent P,O-g-C₃N₄ nanodots for the label-free detection of Cu²⁺ and acetylcholinesterase activity, *J. Mater. Chem. C* 3(2015) 10916-24.
- [147] S. Liu, J. Tian, L. Wang, Y. Luo, J. Zhai, X. Sun, Preparation of photoluminescent carbon nitride dots from CCl₄ and 1,2-ethylenediamine: a heat-treatment-based strategy, *J. Mater. Chem.* 21(2011) 11726-9.

- [148] S. Liu, L. Wang, J. Tian, J. Zhai, Y. Luo, W. Lu, et al., Acid-driven, microwave-assisted production of photoluminescent carbon nitride dots from N,N-dimethylformamide, *RSC Adv.* 1(2011) 951-3.
- [149] Y.-H. Li, L. Zhang, J. Huang, R.-P. Liang, J.-D. Qiu, Fluorescent graphene quantum dots with a boronic acid appended bipyridinium salt to sense monosaccharides in aqueous solution, *Chem. Commun.* 49(2013) 5180-2.
- [150] G. Kaur, N. Lin, H. Fang, B. Wang, Boronic Acid-Based Fluorescence Sensors for Glucose Monitoring, in: C.D. Geddes, J.R. Lakowicz (Eds.), *Glucose Sensing*, Springer US, Boston, MA, 2006, pp. 377-97.
- [151] Y. Liu, C. Deng, L. Tang, A. Qin, R. Hu, J.Z. Sun, et al., Specific Detection of d-Glucose by a Tetraphenylethene-Based Fluorescent Sensor, *J. Am. Chem. Soc.* 133(2011) 660-3.
- [152] T. Lin, L. Zhong, J. Wang, L. Guo, H. Wu, Q. Guo, et al., Graphite-like carbon nitrides as peroxidase mimetics and their applications to glucose detection, *Biosens. Bioelectron.* 59(2014) 89-93.
- [153] D. Chen, D. Jiang, X. Du, L. Zhou, L. Huang, J. Qian, et al., Engineering efficient charge transfer based on ultrathin graphite-like carbon nitride/WO₃ semiconductor nanoheterostructures for fabrication of high-performances non-enzymatic photoelectrochemical glucose sensor, *Electrochim. Acta* 215(2016) 305-12.
- [154] H. Yuan, J. Liu, H. Li, Y. Li, X. Liu, D. Shi, et al., Graphitic carbon nitride quantum dot decorated three-dimensional graphene as an efficient metal-free electrocatalyst for triiodide reduction, *J. Mater. Chem. A* 6(2018) 5603-7.
- [155] N. Wang, Z. Han, H. Fan, S. Ai, Copper nanoparticles modified graphitic carbon nitride nanosheets as a peroxidase mimetic for glucose detection, *RSC Adv.* 5(2015) 91302-7.
- [156] J. Ehrmaier, W. Domcke, D. Opalka, Mechanism of Photocatalytic Water Oxidation by Graphitic Carbon Nitride, *J. Phys. Chem. Lett.* 9(2018) 4695-9.

- [157] M. Volokh, G. Peng, J. Barrio, M. Shalom, Carbon Nitride Materials for Water Splitting Photoelectrochemical Cells, *Angew. Chem. Int. Ed* 0.
- [158] X. Kang, Y. Kang, X. Hong, Z. Sun, C. Zhen, C. Hu, et al., Improving the photocatalytic activity of graphitic carbon nitride by thermal treatment in a high-pressure hydrogen atmosphere, *Prog. Nat. Sci-Mater.* 28(2018) 183-8.
- [159] M.-H. Xiang, J.-W. Liu, N. Li, H. Tang, R.-Q. Yu, J.-H. Jiang, A fluorescent graphitic carbon nitride nanosheet biosensor for highly sensitive, label-free detection of alkaline phosphatase, *Nanoscale* 8(2016) 4727-32.
- [160] Q. Zhuang, P. Guo, S. Zheng, Q. Lin, Y. Lin, Y. Wang, et al., Green synthesis of luminescent graphitic carbon nitride quantum dots from human urine and its bioimaging application, *Talanta* 188(2018) 35-40.
- [161] Y. Cui, Z. Ding, P. Liu, M. Antonietti, X. Fu, X. Wang, Metal-free activation of H₂O₂ by g-C₃N₄ under visible light irradiation for the degradation of organic pollutants, *Phys. Chem. Chem. Phys.* 14(2012) 1455-62.
- [162] G. Springsteen, B. Wang, A detailed examination of boronic acid–diol complexation, *Tetrahedron* 58(2002) 5291-300.
- [163] L.R. Jones, J.A. Riddick, Colorimetric Determination of 1,2-Propanediol and Related Compounds, *Anal. Chem.* 29(1957) 1214-6.
- [164] Y. Egawa, R. Miki, T. Seki, Colorimetric Sugar Sensing Using Boronic Acid-Substituted Azobenzenes, *Materials (Basel, Switzerland)* 7(2014) 1201-20.
- [165] M. Brahmayya, S.A. Dai, S.Y. Suen, Synthesis of 5-substituted-3H-[1,3,4]-oxadiazol-2-one derivatives: a carbon dioxide route (CDR), *RSC Adv.* 5(2015) 65351-7.
- [166] T.S. Miller, A.B. Jorge, T.M. Suter, A. Sella, F. Corà, P.F. McMillan, Carbon nitrides: synthesis and characterization of a new class of functional materials, *Phys. Chem. Chem. Phys.* 19(2017) 15613-38.

- [167] C.A. Andersen, B. Rost, Secondary structure assignment, *Structural bioinformatics* 44(2009) 459-84.
- [168] A. Schreiber, F. Witte, 13 - Immune response to nanobiomaterials, in: M. Razavi, A. Thakor (Eds.), *Nanobiomaterials Science, Development and Evaluation*, Woodhead Publishing 2017, pp. 249-60.
- [169] D. Walter, Primary Particles – Agglomerates – Aggregates, *Nanomaterials*, Deutsche Forschungsgemeinschaft (DFG) (Ed.) 2013.
- [170] H. Nie, M. Li, Q. Li, S. Liang, Y. Tan, L. Sheng, et al., Carbon Dots with Continuously Tunable Full-Color Emission and Their Application in Ratiometric pH Sensing, *Chem. Mater.* 26(2014) 3104-12.
- [171] X. Zhang, X. Xie, H. Wang, J. Zhang, B. Pan, Y. Xie, Enhanced Photoresponsive Ultrathin Graphitic-Phase C_3N_4 Nanosheets for Bioimaging, *J. Am. Chem. Soc.* 135(2013) 18-21.
- [172] Z. Zhou, Y. Shen, Y. Li, A. Liu, S. Liu, Y. Zhang, Chemical Cleavage of Layered Carbon Nitride with Enhanced Photoluminescent Performances and Photoconduction, *ACS Nano* 9(2015) 12480-7.
- [173] Z. Song, T. Lin, L. Lin, S. Lin, F. Fu, X. Wang, et al., Invisible Security Ink Based on Water-Soluble Graphitic Carbon Nitride Quantum Dots, *Angew. Chem. Int. Ed* 55(2016) 2773-7.
- [174] B. Pappin, M. J. T. A, *Boron-Carbohydrate Interactions* 2012.
- [175] C. Bromba, P. Carrie, J.K.W. Chui, T.M. Fyles, Phenyl boronic acid complexes of diols and hydroxyacids, *Supramol. Chem.* 21(2009) 81-8.
- [176] B. Wang, K. Yoshida, K. Sato, J.-i. Anzai, Phenylboronic Acid-Functionalized Layer-by-Layer Assemblies for Biomedical Applications, *Polymers* 9(2017).
- [177] K. Kur-Kowalska, M. Przybyt, E. Miller, The study of phenylboronic acid optical properties towards creation of a glucose sensor, (2014).

- [178] N. Dhenadhayalan, K.-C. Lin, R. Suresh, P. Ramamurthy, Unravelling the Multiple Emissive States in Citric-Acid-Derived Carbon Dots, *J. Phys. Chem. C* 120(2016) 1252-61.
- [179] Y. Ooyama, K. Uenaka, A. Matsugasako, Y. Harima, J. Ohshita, Molecular design and synthesis of fluorescence PET (photo-induced electron transfer) sensors for detection of water in organic solvents, *RSC Adv.* 3(2013) 23255-63.
- [180] R.A. McCloy, S. Rogers, C.E. Caldon, T. Lorca, A. Castro, A. Burgess, Partial inhibition of Cdk1 in G2 phase overrides the SAC and decouples mitotic events, *Cell cycle* 13(2014) 1400-12.
- [181] O. Gavet, J. Pines, Progressive activation of CyclinB1-Cdk1 coordinates entry to mitosis, *Dev. Cell* 18(2010) 533-43.
- [182] Y.-C. Lu, J. Chen, A.-J. Wang, N. Bao, J.-J. Feng, W. Wang, et al., Facile synthesis of oxygen and sulfur co-doped graphitic carbon nitride fluorescent quantum dots and their application for mercury(ii) detection and bioimaging, *J. Mater. Chem. C* 3(2015) 73-8.
- [183] M.-H. Chan, C.-W. Chen, I.J. Lee, Y.-C. Chan, D. Tu, M. Hsiao, et al., Near-Infrared Light-Mediated Photodynamic Therapy Nanoplatform by the Electrostatic Assembly of Upconversion Nanoparticles with Graphitic Carbon Nitride Quantum Dots, *Inorg. Chem.* 55(2016) 10267-77.
- [184] X. Cao, J. Ma, Y. Lin, B. Yao, F. Li, W. Weng, et al., A facile microwave-assisted fabrication of fluorescent carbon nitride quantum dots and their application in the detection of mercury ions, *Spectrochim. Acta. Part A* 151(2015) 875-80.
- [185] Y. Tang, Y. Su, N. Yang, L. Zhang, Y. Lv, Carbon Nitride Quantum Dots: A Novel Chemiluminescence System for Selective Detection of Free Chlorine in Water, *Anal. Chem.* 86(2014) 4528-35.
- [186] Q. Cui, J. Xu, X. Wang, L. Li, M. Antonietti, M. Shalom, Phenyl-Modified Carbon Nitride Quantum Dots with Distinct Photoluminescence Behavior, *Angew. Chem. Int. Ed* 55(2016) 3672-6.

[187] J. Tian, Q. Liu, A.M. Asiri, A.H. Qusti, A.O. Al-Youbi, X. Sun, Ultrathin graphitic carbon nitride nanosheets: a novel peroxidase mimetic, Fe doping-mediated catalytic performance enhancement and application to rapid, highly sensitive optical detection of glucose, *Nanoscale* 5(2013) 11604-9.

LIST OF PUBLICATIONS

1. Yen-Linh Thi Ngo, Seung Hyun Hur, Low-temperature NO₂ gas sensor fabricated with NiO and reduced graphene oxide hybrid structure, *Materials Research Bulletin*, 84(2016) 168-76.
2. Yen-Linh Thi Ngo, Le Thuy Hoa, Jin Suk Chung, Seung Hyun Hur, Multi-dimensional Ag/NiO/reduced graphene oxide nanostructures for a highly sensitive non-enzymatic glucose sensor, *Journal of Alloys and Compound*, 712(2017) 742-51.
3. Le Thuy Hoa, Yen-Linh Thi Ngo, Jin Suk Chung, Seung Hyun Hur, Green synthesis of silver nanoparticle-decorated porous reduced graphene oxide for antibacterial non-enzymatic glucose sensors, *Ionics*, 6(2017) 1525-32.
4. Sundaram Chandrasekaran, Yen-Linh Thi Ngo, Lijun Sui, Eui Jung Kim, Dinh Khoi. Dang, Jin Suk Chung, Seung Hyun Hur, Highly enhanced visible light water splitting of CdS by green to blue upconversion, *Dalton Transactions*, 46(2017) 13912-9.
5. Yen-Linh Thi Ngo, Lijun Sui, Wei Ahn, Jin Suk Chung, Seung Hyun Hur, NiMn₂O₄ spinel binary nanostructure decorated on three-dimensional reduced graphene oxide hydrogel for bifunctional materials in non-enzymatic glucose sensor, *Nanoscale*, 9(2017) 19318-27.
6. Dinh Khoi Dang, Sundaram Chandrasekaran, Yen-Linh Thi Ngo, Jin Suk Chung, Eui Jung Kim, Seung Hyun Hur, One pot solid-state synthesis of highly fluorescent N and S co-doped carbon dots and its use as fluorescent probe for Ag⁺ detection in aqueous solution, *Sensors and Actuators B: Chemical*, 255(2018) 3284-91.
7. Yen-Linh Thi Ngo, Won Mook Choi, Jin Suk Chung, Seung Hyun Hur, Highly biocompatible phenylboronic acid-functionalized graphitic carbon nitride quantum dots for the selective glucose sensor, *Sensors and Actuators B: Chemical*, 282(2019) 36-44.
8. Dinh Khoi Dang, Chandrasekaran Sundaram, Yen-Linh Thi Ngo, Won Mook Choi, Jin Suk Chung, Eui Jung Kim, Seung Hyun Hur, Pyromellitic acid-derived highly fluorescent N-

doped carbon dots for the sensitive and selective determination of 4-nitrophenol, *Dyes and Pigments*, 165(2019), 327-34.

9. Yen-Linh Thi Ngo, Jin Suk Chung, Seung Hyun Hur, Aminoboronic acid-functionalized graphitic carbon nitride quantum dots for the photoluminescence multi-chemical sensing probe, *Dyes and Pigments*, 168(2019), 180-8.
10. Hye Jin Lee, Jayasmita Jana, Yen-Linh Thi Ngo, Lin Lin Wang, Jin Suk Chung, Seung Hyun Hur, The effect of solvent polarity on emission properties of carbon dots and their uses in colorimetric sensors for water and humidity, *Materials Research Bulletin*, 119(2019), 110564.
11. Chatchai Rodwihok, Duangmanee Wongratanaphisan, Yen-Linh Thi Ngo, Mahima Khandelwal, Seung Hyun Hur, Jin Suk Chung, Effect of GO Additive in ZnO/rGO Nanocomposites with Enhanced Photosensitivity and Photocatalytic Activity, *Nanomaterials*, 9(2019), 1441.